OHIO UNIVERSITY

COLLEGE OF ARTS AND SCIENCES

REPORT OF THE ORAL THESIS EXAMINATION/DISSERTATION DEFENSE

Michael Sumption is seeking
(student's name)

____ Master of ____ degree,

_X_ Doctor of Philosophy degree

with a major in Physics.

Exact wording of thesis/dissertation title: Proximity Effect Magnetization and Energy Loss in Multifilamentary Composites: Influence of Strand Design and Sample Geometry.

Satisfactory _✓_ or letter grade ____ or unsatisfactory ____

COMMITTEE SIGNATURES:

Ronald Cappiello
(Thesis/Dissertation Director)

Roger Rollins

F.W. Callerman

N.J. Carron Jr.

Howard J. Arnold
(Graduate Faculty Representative - Dissertation Only)

Date: March 12 1992

Earle R. Hunt
(Signature, Graduate Chair)

This report should be signed and filed as soon as FINAL approval is given for the (corrected) dissertation/thesis). It must be submitted to the Dean's Office before the dissertation can be accepted.

One copy to the Departmental file
One copy to the Office of Arts and Sciences
One copy to the student

(10/84)

A&S #8

PROXIMITY EFFECT MAGNETIZATION AND ENERGY LOSS IN MULTIFILAMENTARY COMPOSITES: INFLUENCE OF STRAND DESIGN AND SAMPLE GEOMETRY

A dissertation presented to

The Graduate Faculty of

The College of Arts and Sciences of Ohio University

In partial fulfillment

of the requirements for the degree

Doctor of Philosophy

Michael D. Sumption

March 1992

Sumption, Michael, D., Ph.D. March, 1992. Physics

Proximity Effect Magnetization and Energy Loss in Multifilamentary Composites: Influence of Strand Design and Sample Geometry

Flux trapping and cycling energy losses were studied by vibrating sample magnetometry in fine multifilamentary Nb-Ti superconductive strands for which proximity effect coupling between the filaments is significant. Measurements were made to determine the influence of helical twist about the strand axis as well as sample length for strands experiencing varying levels of proximity effect coupling. The proximity effect strength was varied by investigating strands with a range of filament diameters, as well as by the addition of magnetic impurities to the interfilamentary medium (the matrix) to suppress the proximity effect. Critical currents and fields for the matrix were extracted from the measurements. The reduction of cycling loss[1] and magnetization[2] previously found was confirmed. Additionally, these measurements were extended to strands where little twist was applied, and the magnetization and cyclic loss were found to saturate.

Bean-like models for anisotropic media introduced by Carr[1] and later Harada[2] were further developed to calculate magnetization and penetration fields in these strands over a large range of twist pitch values. A calculation of magnetic hysteresis loops was also made for short strand samples. These models provide a good qualitative understanding of the observed behavior and lead to useful predictions for applications.

1. W.J. Carr, J. Appl. Phys. 54, 6549 (1983).

2. N. Harada, Y. Mawatari, O. Miura, Y. Tanaka, and K. Yamafuji, Cryogenics 31, 183 (1991).

Approved_____

Professor of Physics

ACKNOWLEDGEMENTS

I would like to thank all those who have I have worked with over the past five years. I have enjoyed much friendship during that time, especially that of Hui Li and Sukesh Mahajan -- the other student members of the "superconductivity group". Thanks to Betty Craddock for her help with Battelle contract details, and Tom Tigner for his instruction in OP-AMP electronics, as well as the use of his lab. I would like to thank Ralph Smith for his help in acclimating to the atmosphere at Battelle, and for specific suggestions about sample preparation. Also, I want to mention my appreciation of Judy Ward for her very long hours and gorgeous pictures.

I would like to thank Dr. R. Rollins for his tutorials on critical state models, and Dr. A. Markworth for his comments and help on various calculations and models. Thanks to Dr. K.R. Marken Jr. for teaching me how to use the magnetometer, as well as other aspects of the Battelle superconductivity lab. Also, I would like to acknowledge Dr. W.J. Carr Jr. for his pointers in the calculation of magnetic moments, and his helpful discussions of PE theory.

I have had the good fortune to have two advisors on this thesis project. Dr. R.L. Cappelletti was a great help during many of my years at O.U.; his demonstration of experimental technique, along with his help in calculation as well as concept were vital. His insistence on a clear examination of the problem at hand, as well as his concern for

his students, is sincerely appreciated. I would like to thank Dr. E.W. Collings for the opportunity to work with him in the Battelle Lab. His eternal optimism and energy were and are invigorating. Also, his various suggestions and ideas were indispensable, and I thank him for the very question which this thesis answers.

My entire family has been absolutely supportive, for which I am very grateful. Lastly, and most importantly, I want to thank my wife Denise for giving me the quiet space to complete this, and the encouragement to do so, at a time when this attaining this goal might have seemed unlikely.

Financial support for this research was provided by the U.S. Department of Energy, Division of High Energy Physics, under Contract Number DE-AC02-86ER40296.

TABLE OF CONTENTS

LIST OF TABLES

LIST OF FIGURES

SYMBOLS

$\hat{a}_{1\text{-}3}$ = Unit vectors describing the filament geometry.

$\hat{a}_{\rho,\theta,z}$ = Unit vectors describing the strand geometry (conventional cylindrical coordinates, with the z-axis along the strand).

$A_{1,2}$ = Fitting parameters in Mota et al.'s expression for H_b (related to $H_{c1,prox}$).

A_z = Cross sectional area over which z-currents flow in the heuristic short sample model (cf. Sec. 5.2).

B = Internal magnetic flux density (since we have described the system as an anisotropic continuum this will refer to an average, valid over lengths large compared to the filament diameter).

$B_{x,y,z}$ = B field along the $\hat{a}_x$, $\hat{a}_y$, and $\hat{a}_z$ directions respectively.

$C_{1,2}$ = Fitting parameters in the exponential expression for J_{cp}.

d = Width of short sample in the model which describes the PE transfer length (rectangular geometry version).

d_f = Filament diameter.

d_N = Thickness of the normal conductor (in the case of thin films, it is the thickness of the normal metal overlayer, while in 3-D cases, it is set to 1/2 of the interfilament spacing).

d_T = Distance that the flux front moves in across the sample width, at full penetration, for short samples modeled with a rectangular geometry. This is analogous to L_T, below, but for the case $L < L_T$.

d_{T1} = d_T for less than full penetration (i.e. $H < H_{p,prox}$).

$d\tau$ = Volume element of integration.

$(dH/dt)_c$ = Ramp rate for continuous M-H loop.

$(dH/dt)_{eff}$ = Effective ramp rate for a stepping M-H loop.

$(dH/dt)_r$ = Ramp rate during the ramp time of the ramp-hold procedure of the stepping M-H loop. G = Constant of proportionality, used to connect M_E and Q_E to dH/dt.

h = Dimensionless penetration field; defined as $H_{p,prox}/H_{p,prox,sat}$.

H = External magnetic field intensity.

H_b = Breakdown field of the superconductive matrix, valid for small κ_N.

H_{c1} = General expression for the lower critical field of a superconductor material.

$H_{c1,NbTi}$ = Value of H_{c1} for the bare NbTi conductor. (this value is enhanced because of the small diameter of the filaments). This is measured by subtracting the initial slope from the initial permeability data, and then noting the first deviation from linearity in the M-H for a virgin sample.

$H_{c1,prox}$ = Field below which the field is totally excluded from the conductor bundle. This field should correspond to H_b, the breakdown field of the Cu as measured in thin films. Experimentally, it was determined by measuring the initial deviation from linearity in the M-H for a virgin sample.

H_{c2} = General expression for the upper critical field of a superconductor material.

H_{ex} = Applied field at which M_{ex} occurs.

H_m = Field sweep amplitude.

H_p = General expression for the penetration field of a superconductor material.

$H_{p,NbTi}$ = Penetration field of the NbTi filaments, defined as that point (in H) at which the initial magnetization line meets the fully penetrated loop (for a conductor with no PE). $H_{p,prox}$ = Field at which, for heavily proximity-effected conductors where $H_{c1,NbTi}$ has been exceeded, the flux fronts which form across the diameter of the strand meet in the center of the conductor, in analogy to penetration fields in bulk superconductors.

$H_{p,proxL}$ = Field at which, for proximity effected conductors where $H_{c1,NbTi}$ has not been exceeded, the flux fronts which form across the diameter of the strand meet in the center of the conductor. This is similar to the definition for $H_{p,prox}$ except that the NbTi filaments are not in the mixed state.

$H_{p,prox,sat}$ = $H_{p,prox}$ in the limit of L_p --> infinity. For transverse fields applied to long conductors this is $0.8\lambda J_{cfil}R$.

$H_{p0,\ NbTi}$ = Field at which the first derivative of the initial magnetization goes through zero for a bare NbTi sample. This would be equivalent to $H_{p,NbTi}$ for a field-independent-J_c conductor.

$H_{p0,\ prox}$ = Field at which the first derivative of the initial magnetization curve goes to zero in regions of the initial magnetization where the PE is apparent, and $H > H_{c1,NbTi}$.

$H_{p0,proxL}$ = Field at which the first derivative of the initial magnetization curve goes to zero when also $H < H_{c1,prox}$.

H_{PA} = Contribution to $H_{p,prox}$ from the part of strand obeying Eq. 5.1.2.2 (a).

H_{PB} = Contribution to $H_{p,prox}$ from the part of strand obeying Eq. 5.1.2.2 (b).

H_0 = Normalizing parameter used in Ghosh's equation which describes the field

dependence of the PE (cf. Sec. 1.3).

$I_{1,2,3..}$ = Denotes various integrals (used in App. G).

IM = Initial magnetization portion of the virgin M-H loop.

J = Current density.

J_c = Critical current density.

J_{cfil} = Critical current density of the filaments.

J_{cp} = Critical current density of the proximity-effected matrix.

J_{cz} = Critical current density along the z-axis (along the length) of the conductor.

$J_{c1,2,3}$ = Critical currents for the composite, defined with respect to coordinates connected to the filament geometry.

$J_{c\rho,\theta,z}$ = Critical current densities for the composite, defined with respect to coordinates connected to the strand geometry (conventional cylindrical coordinates).

$J_{x,y,z}$ = Current densities for the composite, defined with respect to coordinates used for the rectangular geometry short sample model.

$J_{1,2,3}$ = Current densities for the composite, defined with respect to coordinates connected to the filament geometry.

$J_{\rho,\theta,z}$ = Current densities for the composite, defined with respect to coordinates connected to the strand geometry.

k_B = Boltzmann's constant (1.380×10^{-16} erg K^{-1}).

K_N^{-1} = Pair penetration depth, a constant, the characteristic distance over which Cooper pairs "decay" into the normal metal.

l_N = Mean free path in the normal metal.

L = Sample length.

L_c = Cable pitch of strand. (e.g. if a number of strands are wound together to form a cable this will be the period of the helix formed by any given strand).

L_{eff} = Effective pitch, determined by the interaction between L_c and L_p (see App. H).

L_g = Length over which flux gradients form in the proximity-effected matrix.

L_p = Twist pitch of strand; the period of the helixes formed by each of the filaments in the strand.

L_{pc} = Twist pitch for a given helix radius for which the helix pitch angle α is equal to the critical value ($\equiv 2\pi\rho\lambda J_{cfil}/J_{cp}$).

L_{pcm} = Critical twist pitch for a helix of radius equal to the strand radius ($\equiv 2\pi R\lambda J_{cfil}/J_{cp}$).

L_T = Transfer length; a measure of the length (along the conductor) which is required for the current cross over (the matrix) at the conductor ends.

L_{T1} = Transfer length for $H < H_{p,prox}$, for the case $J_{cp}L > \lambda J_{cfil}d/2$.

M = Magnetization.

M_{ex} = Maximum in excess PE magnetization (i.e. the magnetization maximum (of an M-H loop) which is directly attributable to PE).

M_E = Eddy current magnetization.

M_{E0} = Eddy current magnetization at the initial point in a decay curve.

M_h = NbTi hysteretic magnetization (that part due solely to the NbTi).

M_{PE} = Proximity effect related magnetization ($\equiv M_S - M_h$).

M_S = Static magnetization.

M_T = Total magnetization.

$M_{x,y,z}$ = Magnetization along the $\hat{a}_x$, $\hat{a}_y$, and $\hat{a}_z$ directions respectively.

M-H = Complete magnetization loop.

n = Total number of points in a stepping M-H loop.

N = Normal metal.

p = Fraction of t_{tot} devoted to ramping (cf. App. B).

P = Probability of finding a Cooper pair a distance x_N into the normal conductor.

PE = Proximity effect.

Q = DC energy loss, defined by the area of an M-H loop (energy/cycle).

Q_E = Eddy current energy loss (energy/cycle).

Q_h = NbTi hysteretic (static) energy loss (energy/cycle).

Q_{PE} = Proximity effect enhanced energy loss, where $Q_{PE} \equiv Q_S - Q_h$ (energy/cycle).

Q_S = Total static energy loss (energy/cycle).

Q_T = Total energy loss (energy/cycle).

r = Radial distance, as defined in spherical polar coordinates.

R = Strand radius.

R_e = Penetration distance of the field into the strand for heuristic short sample model.

s = Interfilament spacing (shortest distance between two filaments).

S = Superconducting metal.

s_L = One half of integration distance along the z-axis for the short samples, in the rectangular geometry model (the limit is taken as $s_L \rightarrow \infty$).

SSB = Short sample, bare.

SSC = Short sample, clad.

t = time.

$\hat{t}$ = Unit vector which traces out the helix.

T = Temperature, in K.

T_c = General expression for the superconducting transition temperature.

T_{CN} = Superconductive transition temperature of the "normal" metal.

T_{CNS} = Superconductive transition temperature of the superconductive-normal metal pair.

T_{CS} = Superconductive transition temperature of the superconductive metal.

t_r = Ramp time during a stepping hysteresis loop measurement (cf. App. B).

t_h = Hold time during a stepping hysteresis loop measurement (cf. App. B).

t_{tot} = Total time for a measurement segment during the field stepping runs (M-H loop time/n).

v_N = Fermi velocity in the normal metal.

V = Sample volume.

VL = Variable length sample.

VP = Variable Pitch sample.

VSM = Vibrating sample magnetometer.

w = Width of the current saturated region in model describing non-axial currents (cf. App. D).

x = x variable, cartesian coordinates.

x_e = Distance into the conductor that the field penetrates along the x-axis during the IM (rectangular SS).

x_{er} = For $H_m > H_{p,prox}$, on the initial reversal branch, this is the point (as measured from

the sample x-boundary) at which the bean current reverse direction.

x_{e1} = For $H_m < H_{p,prox}$, on the initial reversal branch, this is the point (as measured from the x-boundary) at which the bean currents reverse directions.

x_N = Distance into a metal overlayer, as measured from the S-N boundary (1-D case).

y_{e2} = For $H_m < H_{p,prox}$, on the initial reversal branch, this is the distance into the conductor along the x-direction that the field penetrates.

y = y variable, cartesian coordinates.

y_e = Distance into the conductor that the field penetrates along the y-axis during the IM (rectangular SS).

y_{er} = For $H_m > H_{p,prox}$, on the initial reversal branch, this is the point (as measured from the sample y-boundary) at which the bean currents reverse direction.

y_{e1} = For $H_m < H_{p,prox}$, on the initial reversal branch, this is the point (as measured from the y- boundary) at which the bean currents reverse directions.

y_{e2} = For $H_m < H_{p,prox}$, on the initial reversal branch, this is the distance into the conductor along the y-direction that the field penetrates.

z = z variable, cartesian coordinates, cylindrical polar coordinates.

GREEK SYMBOLS

α = Pitch angle of a helix; the angle between a vector tangent to a helix winding and a line parallel to the helix axis.

α_c = Critical helix pitch; the angle at which both critical currents J_{c1} and J_{c3} are saturated.

$\beta_C = \lambda J_{cfil}/J_{cp}$.

$\beta_\rho = L_p/2\pi\rho$.

$\beta_R = \beta_\rho(\rho = R)$.

ΔM = Difference between shielding and trapping segment of loop at a given field.

ΔM_h = ΔM due to the NbTi hysteresis.

ΔM_{PE} = ΔM due to proximity effect related coupling ($\Delta M_{PE} \equiv \Delta M_S - \Delta M_h$).

ΔM_S = Total static ΔM ($\Delta M_{PE} + \Delta M_h$).

ΔM_{sat} = Saturation value of ΔM, given by $(4/15\pi)\lambda J_{cfil} R$ for a long conductor in a transverse field.

$\Delta\mu = \Delta M/\Delta M_{sat}$.

θ = Angular variable in cylindrical polar coordinates.

θ_s = Angular orientation of sample with respect to field, 0° is $\theta_\parallel$, 90° is $\theta_\perp$.

$\theta_\perp$ = Denotes the sample orientation in which H is applied transverse to cylindrical sample.

$\theta_\parallel$ = Denotes the sample orientation in which H is applied along the cylindrical axis of symmetry of the sample.

$\kappa_N(x_N)$ = Ginzburg-Landau parameter for the normal metal, a variable, defined as $\kappa = \lambda_N(x_N)/\xi_N$.

$\kappa_{N,x_N=0}$ = $\kappa_N(x_N)$ evaluated at the superconductor-normal metal interface.

λ = NbTi filling factor = NbTi volume/filamentary volume.

λ_{eff} = Parameter describing field penetration in normal metal, used in Takàcs expression for H_b.

λ_p = Matrix filling factor = matrix volume/filamentary volume (cf. App. D).

$\lambda_N(x_N)$ = Superconductive penetration depth in the normal metal.

$\lambda_{N,x_N=0}$ = $\lambda_N(x_N)$ evaluated at the superconductive-normal metal interface.

ξ = Angle between x-y plane (or ρ-θ plane) and $\hat{a}_r$, such that $\sin\xi = \rho/r$.

ξ_N = Superconductive coherence length in the proximity-effected normal metal.

ρ = Radial distance in the strand, from definition of cylindrical polar coordinates.

ρ' = Boundary between regions in strand described by Eq. 5.1.2.2 (a) and 5.1.2.2 (b); equal to ρ_c when $L_p < L_{pcm}$, and equal to R when $L_p > L_{pcm}$.

ρ_c = Critical radius which, for a given L_p, marks the boundary between regions in a strand described by Eq. 5.1.2.2 (a) and 5.1.2.2 (b). At this radius $\alpha = \alpha_c$.

ρ_s = Screening depth in the proximity-effected normal metal, a constant defined by $\lambda_N(\rho_s) = \xi_N$.

τ_d = Eddy current decay constant.

Φ_0 = The magnetic flux quantum in a superconductor (2.07×10^{-7} G cm^2).

CHAPTER 1: INTRODUCTION

1.1 Fine Filamentary Composite Strands

Filamentary subdivision of superconductive wires, originally used to increase flux jump stability and decrease energy loss, has been extended to very fine filament diameters (10 nm to 1 μm)[1-6]. The use of these wires in precision dipole magnet applications requires low filamentary magnetization and decay[7-10]. This is because strand magnetization causes distortions in the field produced by dipoles wound from these strands. Additionally, this magnetization decays with time, making it more difficult to compensate for these distortions. This problem has an obvious solution, which is to continue to decrease the filament diameter, and thus the magnetization. The lower energy losses experienced by these wires is, of course, an added benefit. Additionally, for the ultra-fine filaments (10 nm to 100 nm), pinning on the filament/matrix interface becomes significant, so that these materials can be viewed as forming artificial pinning centers[3-6]. Several new effects accompany reduction of filament diameter, included in these are: (1) anomalous reversible magnetization, (2) critical field enhancement due to "magnetic volume erosion", (3) surface pinning and loss, and (4) proximity effects (PE). The first two of these generally reduce losses to below the expected level[11-13], while the second two increase them[14-17], at least for the higher field sweep regime. For a recent description

of the properties of ultra-fine filamentary materials see Ref. 18. This thesis, however, focusses attention on the type of strand that is used in accelerator-dipole-magnet applications, and specifically the proximity effects in these strands.

Composite strands intended for accelerator-magnet applications consist of NbTi filaments embedded in a Cu (or Cu + solute) matrix so that the filaments form a hexagonal pattern (ideally). The interfilament spacing to filament diameter ratio, s/d_f, is kept small so as to reduce filament-diameter modulation (sausaging). Additionally, thin Nb sheaths typically surround the filaments to prevent the formation of intermetallics during precipitation heat treatment. In order to reduce eddy currents and/or proximity effects (PE), various solute additions to the copper matrices have been considered, including Ni, Mn and V[19-22]. Eddy currents are also traditionally minimized by applying a twist to these strands, such that the filaments form helices. If we use cylindrical coordinates to describe the conductor with z along the length of the conductor, then the distance in z over which a 2π revolution in θ occurs is denoted the twist pitch (L_p).

1.2 The Superconductive Proximity Effect: Experiments on and Theory of Fundamental Properties

1.2.1 General Theory

The PE, as it manifests itself in thin films, is well understood (see Refs. 23 and 24, which this development closely follows). A normal metal (or a superconductive metal above its transition temperature) will become superconducting over a distance of order

ξ_N from the surface of a superconductive metal against which it is placed in intimate contact. This is caused by the "leakage" of Cooper pairs from the superconductor into the normal metal. The probability of finding a Cooper pair a distance $|x_N| >> K_N^{-1}$ from the S-N boundary is[23]

$$P \propto \exp\left(-\frac{|x_N|}{K_N^{-1}}\right)$$ for a thick metal overlayer, where K_N^{-1} is the pair penetration depth.

where

$$K_N^{-1} = \frac{\hbar v_N}{2\pi k_B T}$$ for a clean normal metal ($l_N >> \xi_N$),

and

$$K_N^{-1} = \left(\frac{\hbar v_N l_N}{6\pi k_B T}\right)^{1/2}$$ for a dirty normal metal ($l_N << \xi_N$).

Here l_N and v_N are the mean free path and Fermi velocity in the normal metal, respectively, $\hbar$ is Planck's constant divided by 2π, and ξ_N is the normal metal coherence length. These expressions are in cgs-practical units, as are all equations in this thesis. Note that if T_{CN} is zero $K_N^{-1} = \xi_N$ in the dirty limit, while in the clean limit $K_N^{-1} \approx \xi_N$. Both the superconductive energy gap and Ginzburg-Landau wave function decay rapidly with increasing distance into the normal region. The penetration depth in the normal material (defined locally) is also dependent on the distance from the interface (as in Fig.

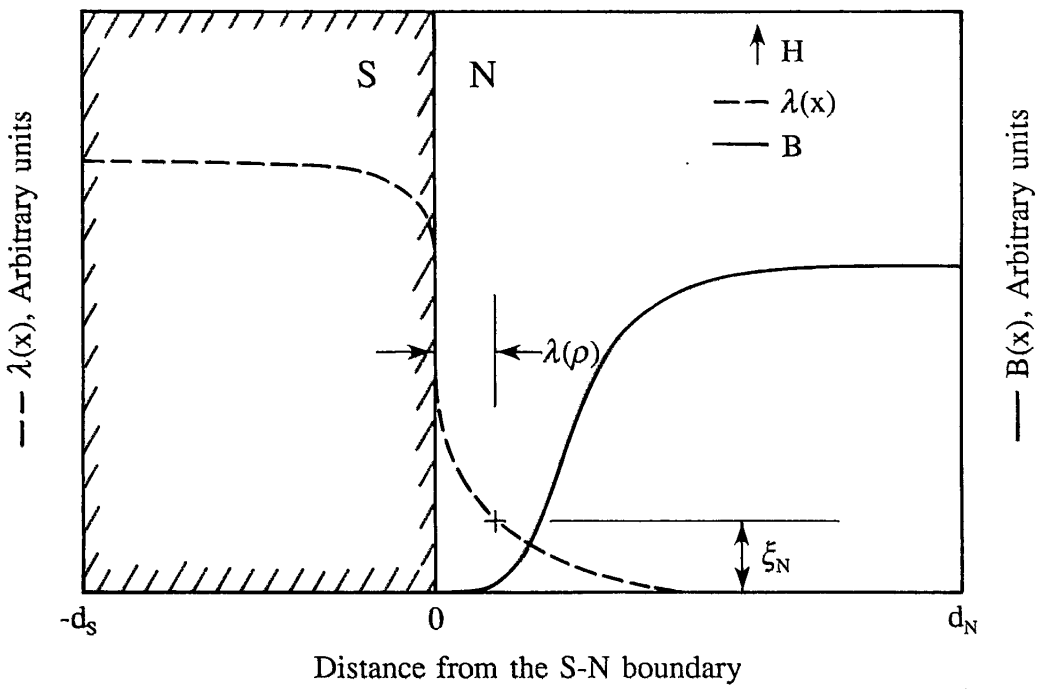

Fig. 1.2.1.1 B(x) and $\lambda_N(x)$ for an S-N interface

1.2.1.1), so that a screening depth, ρ_s, may be defined by $\lambda_N(x_N = \rho_s) \equiv K_N^{-1}$, where $\lambda_N(x_N)$ is the superconductive penetration depth in the normal metal. Since[23] $\lambda_N \propto 1/P$,

$$\lambda_N(\rho_s) = \lambda_{N,x_N=0}\exp\left(\frac{\rho_s}{K_N^{-1}}\right) \equiv K_N^{-1}$$

where $\lambda_{N,x_N=0}$ is the local penetration depth in N at the S-N interface. This implies

$$\rho_s = K_N^{-1}\log\left(\frac{K_N^{-1}}{\lambda_{N,x=0}}\right) = K_N^{-1}\log\left(\frac{1}{\kappa_{N,x=0}}\right).$$

where we have used $\kappa_N(x_N) = \lambda_N(x_N)/K_N^{-1}$ as the Ginzburg-Landau parameter of the

normal metal, and $\kappa_{N,x_N=0}$ as the value of this parameter at $x_N = 0$ (note that log denotes base e logarithm). A more precise calculation gives[23]

$$\rho_s = K_N^{-1}\left[\log\left(\frac{1}{\kappa_{N,x=0}}\right) - 0.116\right].$$

This screening depth will be valid for magnetic fields which are small compared to the field for complete destruction of superconductivity in the normal metal, H_b. Note that since $K_N^{-1} \propto 1/T$, and λ_N is large near T_{CNS} (the critical temperature for the S-N composite)

$$\kappa_N \rightarrow \infty \text{ for } T \rightarrow T_{CNS}$$

and

$$\kappa_N \rightarrow 0 \text{ for } T \rightarrow T_{CN}$$

where T_{CN} is the critical temperature of the "normal" metal when not in the presence of a superconductor.

Deutscher and DeGennes [23] have derived equations which describe the field dependence of the PE for a dirty normal metal ($l_N << K_N^{-1}$). They find that for small κ_N, ρ_s remains relatively constant with H until a certain field, H_b, is reached, above which ρ_s decreases rapidly. There is no exact, general equation for H_b, but in two extreme cases reasonable approximations can be made[23], viz:

$$H_b = \left(\frac{\phi_0}{2\pi\lambda_{N,x=0} K_N^{-1}}\right) \quad \text{for thick metal overlayers} \quad (d_N >> K_N^{-1})$$

and

$$H_b = 3.8\left(\frac{\phi_0 K_N^{\,2}}{2\pi\kappa_{N,x=0}}\right)\exp\left(\frac{-d_N}{K_N^{-1}}\right) \quad \text{for thin metal overlayers} \quad (d_N \approx K_N^{-1})$$

where Φ_0 is the flux quantum. These equations have traditionally been used to describe PEs in thin films.

1.2.2 Monofilaments and Multifilaments in the Clean Limit

As noted by Mota et al. , the equations derived above are only good for the dirty limit, however, NbTi/Cu wires are described by the clean limit[24]. Mota et al. have measured the breakdown fields of monofilaments of Nb and NbTi with varying Cu overlayer thicknesses. Their experimental result is

$$H_b = \left(\frac{A_1}{d_N}\right)\exp\left(\frac{-Td_N}{A_2}\right)$$

where for NbTi in Cu: A_1 = 19 Oe μm, A_2 = 0.6 K μm, and H_b is in Oe. In these samples the filament diameters were in the 30 μm to 500 μm range, and the overlayers were in the 2.5 μm to 100 μm range. All of the measurements were made with the applied field parallel to the filament axis. The temperature in these experiments ranged

from several mK up to about 2 K. Tàkacs[25] has calculated that the breakdown field of a 1-D structure in the clean limit, for small layer spacings, is given by

$$H_b = \frac{\phi_0\ 40}{2\pi\lambda_{eff} d_N}$$

Where an average penetration depth, λ_{eff}, is used. This expression gives an average H_b that is somewhat higher than that calculated from any of the previous expressions.

1.3 Local Proximity Effects in Multifilamentary Composites

The first investigations of PEs in multifilamentary composites occurred in the early 80's. These included studies of T_c and H_{c2} suppression[26], as well as the measurement of J_cs[2,26-28], AC susceptibility[20,27,29,30], calorimetric AC loss[31,32], and DC magnetization[1,2,19,21,25,33-36]. T_c and H_{c2} suppression studies showed that the filamentary T_c and H_{c2} began to decrease at interfilamentary distances of about 0.1 μm (for a pure Cu matrix)[26]. J_c studies generally found a minimum in J_c as a function of filament diameter, although enhanced pinning via surface effects[26] or because of the low dimensionality[2,25,26,33,37] also tend to cause such minimums. The AC susceptibility experiments fell into two categories. In the first, the susceptibility was measured as a function of temperature, as a result of which a flux exclusion volume comparable to the composite volume was found, along with a double transition[29,30]. The second type focussed on the AC loss, finding a minimum of loss as a function of filament diameter

in the vicinity of 1 μm[20,27]. The calorimetric studies gave similar loss-versus-filament diameter results[31]. A number of papers reporting on DC magnetization found a similar enhancement of the DC loss (as measured by the area of the M-H loop) for small filament diameters[1,2,19,21,25,31-36]. Ghosh and Sampson[20] found an exponential dependence of the magnetization on both interfilamentary distance and applied field of the form

$$M \propto \exp(-d_N K_N) \qquad and \qquad M \propto \exp(-H/H_0)$$

where, paralleling the above expressions for P and H_b, K_N^{-1} is the pair penetration depth in the normal metal. Here, however, d_N is the interfilamentary distance, H is the applied field, and H_0 is a normalizing parameter. Collings et al.[1,19,21], and others[20] added Mn to the interfilamentary matrix to reduce the PE magnetization, and thereby provided additional evidence for a PE interpretation. Mn, having a magnetic moment in Cu, is a magnetic scatterer. Its presence in low concentrations ($\leq 1\%$) greatly reduces ξ_N (and thus PE) without significantly increasing the matrix resistivity. This is an important point, since it allows thermal stability to be maintained. Our group applied the technique of matrix etching to both Cu and CuMn matrix strands, in order to give a more direct comparison of the PEs in these strands[21].

While the anomalous magnetization and loss in these strands where quite clearly PE related, there were questions about the nature of the PE in these composites. The exponential dependence of the anomalous magnetization and loss on magnetic field and interfilamentary spacing seemed to fit quite nicely with a conventional PE interpretation. Similarly, the use of Mn additions to reduce the loss was suggested with conventional PEs

in mind. However, the sheer magnitude of the excess loss and magnetization were surprising, since only small modifications of the magnetization would be expected based on S-N bilayer and multilayer studies.

1.4 Non-Local Proximity Effects in Multifilamentary Composites

All of the work mentioned above viewed the PEs in these composites from a "local" perspective, ignoring the influence of strand topology. However, Carr's work in in-situ conductors, performed just subsequent to the earliest continuous filament PE studies, showed that topology was an integral part of the PE enhanced loss in multifilamentary composites. He developed a theory in which the critical current, and its associated DC loss, were proportional to twist pitch (L_p)[38]. Pan's experiments showed that the PE in in-situ strands behaved differently in different field sweep amplitude (H_m) regimes, and exhibited a variation of the penetration field ($H_{p,prox}$) with L_p[39] (which was consistent with Carr's theory). Recently, Harada et al. found an L_p dependence for the DC magnetization in continuous filamentary material[9], and have subsequently used Carr's equations to describe their results[40]. A publication of our group confirmed this behavior (in CuMn as well as Cu matrices), and showed a similar dependence on sample length (L), in analogy with eddy current effects[41]. In a separate publication we have studied the interaction of PE and eddy coupling currents, noting strong similarities, as well as a competition for current paths[42]. Also noted in Yamafuji's work[9], as well as a recent paper from our group[43] was the possibility of PE enhanced flux creep.

This thesis is a compilation of work done over the last two years. Some of it has already been published in the above referenced papers, but the bulk of the more recent work is, as yet, unpublished. While to some extent the focus of PE investigation is beginning to shift to the dynamic properties of these materials[9,42,43], it seems that a coherent, organized, and expanded view of the static properties would be useful.

CHAPTER 2: SUMMARY OF THE RESEARCH

2.1 The Problem

The purpose of using fine filaments is to reduce the hysteretic loss and magnetization, but the small interfilament spacings used in these composites cause the emergence of PE related magnetization (M_{PE}). The goal of this thesis is to measure and model M_{PE} and its associated loss (Q_{PE}) as a function of twist pitch (L_p) and length (L) for multifilamentary samples experiencing varying degrees of PE. In this way we hope not only to be able to predict the occurrence and magnitude of the PE, but also suggest ways to reduce it. Note that we define loss as

$$Q = \int M dH$$

which is just the area of a DC M-H loop. The total loss (Q_T) has the components

$$Q_T = Q_S + Q_E$$

where Q_S is the static component of the loss and Q_E is the eddy current contribution. Q_S can be further separated as

$$Q_S = Q_h + Q_{PE}$$

where Q_h is the NbTi contribution and Q_{PE} is the PE induced loss. The magnetization breaks up into analogous components (cf. Chap. 5).

To display the multifilamentary PE, we refer to Fig. 2.1.1, where we can see the intermediate H_m M-H for a bare/clad sample pair made from proximity-effected strand. These data were taken on the short sample NTCU20-SS-B and -C (for sample descriptions and specifications see Chapter 3) with H applied transverse to the filament axis of symmetry (z-axis). We note that ΔM for the clad sample is greater than that for the bare sample at lower fields, while for higher fields this difference decreases. Here we have defined ΔM as the difference between the trapping and shielding magnetizations at a

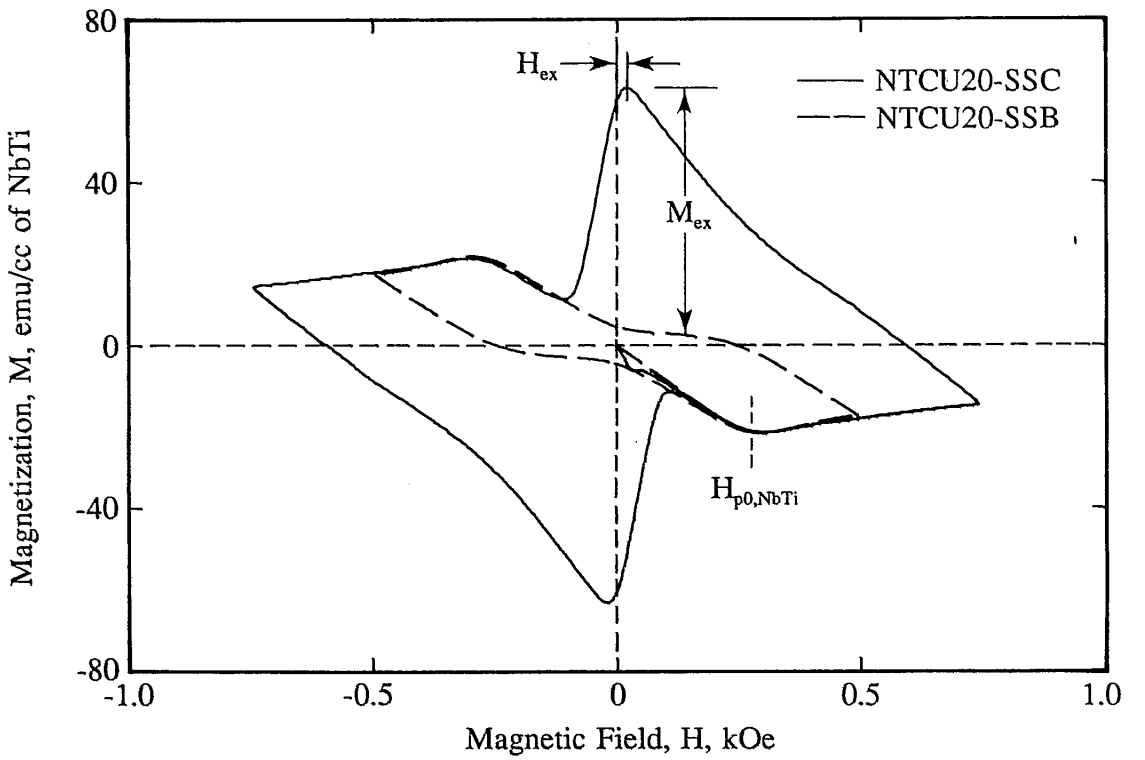

Fig. 2.1.1 Intermediate H_m M-H for bare and clad short samples of NTCU20, indicating the definition of M_{ex}, H_{ex}, and $H_{p0,NbTi}$

given field. This type of data, and the proximity effect interpretations, have been investigated by several authors[1,2,21,36]. It has also been shown, as mentioned earlier, that ΔM is suppressed with the addition of Mn. This clearly indicates that PEs are responsible for the enhanced M-H. The existence of PEs in the low field regime can be seen in Fig. 2.1.2. were we note a somewhat different character than is present for large H_m. In particular note the presence of a low field PE related lower critical field ($H_{c1,prox}$) and penetration ($H_{p0,prox}$) (cf. Sec. 4.3.2 and 5.1.1). In previous publications we have investigated the M-H of proximity-effected short samples as a function of H_m, using the maximum height of the proximity effect magnetization (M_{ex}) and the H-position of this

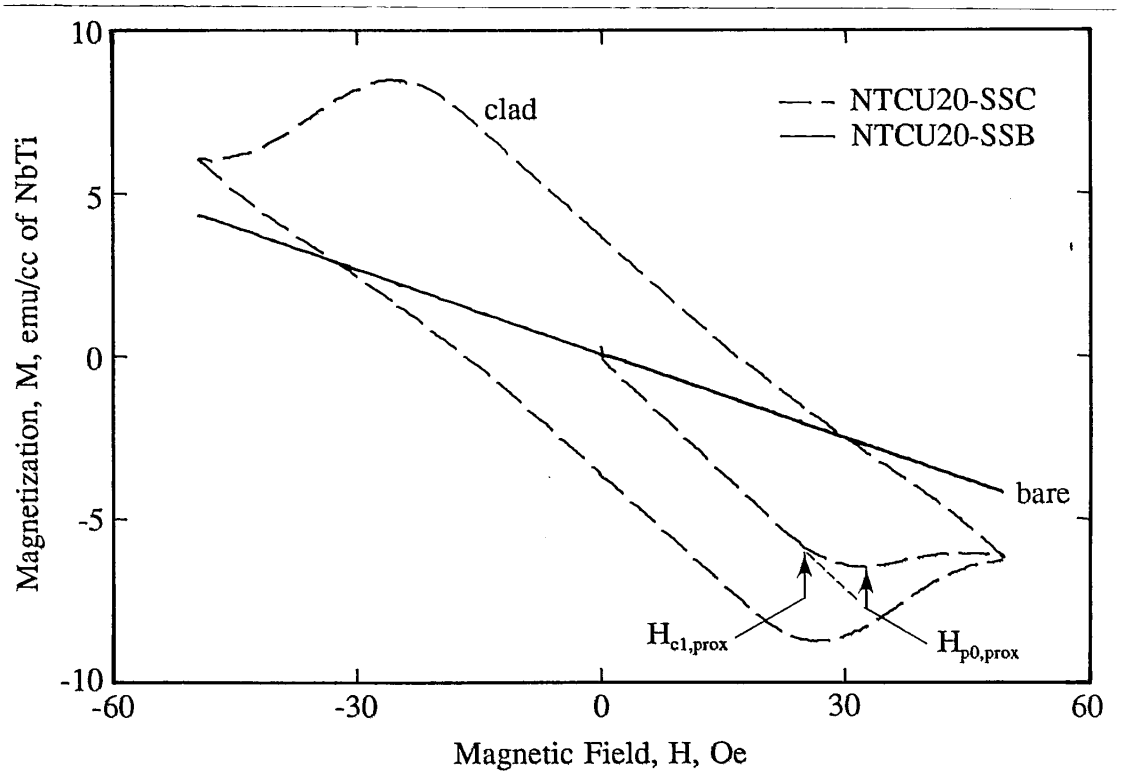

Fig. 2.1.2 Small H_m M-H for bare and clad short samples of NTCU20, indicating the definition of $H_{c1,prox}$ and $H_{p0,proxL}$

maximum (H_{ex}) as shown in Figure 2.1.1[21,44]. These parameters behave differently in different H_m regimes[44]. In the particular case of short samples these regimes turn out to be well defined by $H_{c1,NbTi}$ and $H_{p,NbTi}$[44]. This behavior will be explained in Section 5.2.

While this research was in progress Harada et al.[40] showed that the PE magnetization is twist pitch dependent. We went on to confirm their results and to extend the work into the realm of large twist pitch lengths using both Cu and CuMn strands. Additionally, we looked at the length dependence of PE in untwisted strands. We now attempt to approach this problem from a general point of view, measuring and describing the M-H loops of these strands as a function of both strand design and sample geometry.

2.2 The Experimental Approach

We decided to attack this problem from three directions: (1) bare/clad short-sample pairs, (2) variable length (VL) samples, and (3) variable pitch (VP) samples. Bare/clad short-sample pairs, because of their simple geometry and absence of long time constants, provided an overview of the PE strength for all strand types. Additionally, the bare samples give a baseline NbTi measurement for comparison to all samples -- VL and VP as well as short samples. Initial magnetization (IM) measurements were performed on all short samples with the field applied along the axis of cylindrical symmetry, in an attempt to extract a proximity effect J_c from measurements in this relatively simple geometry. Lastly, M-H measurements for one short-sample pair as a function of angle were also made to provide additional insight into the topological dependence of the

problem.

Point by point, stepping M-H half-loop measurements were performed on VL and VP samples prepared from strands NTCU20, NTCM20, NTCU07, and NTCM07. These data were then used to show the variation of the M-H, ΔM_S, and Q with L and L_p. Additionally, continuous M-H loops were taken on a variety of samples as a function of H_m, and were recast as Q_T versus H_m. General trends were noted, and connections were made between the coil and the short sample results.

2.3 A Theoretical Model

The starting point of our theoretical analysis was a model developed by Carr for in-situ conductors in which he shows that the critical currents, and the associated shielding, are proportional to L_p[38]. This model has been subsequently used by Harada et al. to describe the magnetization and penetration fields of these conductors in the small L_p regime[40]. In Chapter 5 we extend these ideas to a more general equation for ΔM_S (ΔM static), which includes saturation effects. A similar calculation for $H_{p,prox}$ (the PE enhanced penetration field) is also included. For simplicity we focus attention first of all on axial currents in a transverse field. Later (cf. App. D) we consider the possibility of non-axial currents. In addition, the effects of having finite strand lengths is explored, and a heuristic model is developed which gives qualitatively correct predictions. This approach is complemented by the adoption of a model originally developed in the context of high T_c superconductors.

2.4 Conclusions

The magnetization and loss as a function of L_p and L for PE coupled multifilamentary superconductive composites have been measured. The measurements were performed on samples with a range of interfilamentary spacings and with interfilamentary matrices of both Cu and CuMn (0.5 wt. %). The results have been modeled phenomenologically in an attempt to describe the dependence of PEs on strand design and sample geometry. Also, an attempt is made to investigate the connection between these technologically important manifestations of the PE and its traditional occurrence in thin-film sandwiches and bilayers. More detailed conclusions, as well as implications of this work and directions for future research are given in Chapter 6.

CHAPTER 3: EXPERIMENTAL APPROACH

3.1 Equipment

All measurements were made with a computerized PAR-EG&G Model 4500 vibrating sample magnetometer (VSM) in conjunction with a 17 kG iron-core electromagnet, powered by a ±65 A bipolar, field-controlled power supply. All data consisted of sets of magnetization (M) and magnetic field (H) data pairs. The random error in field is 0.15 gauss. The error in M has several components: (a) systematic error due to electronic instrument drift; this is minimized by frequent calibration with a Ni standard, and (b) noise in the moment measurements which is somewhat variable, and in the neighborhood of 0.5 to 1 milliemu. All measurements except those especially noted were run in liquid helium, so that for these measurements no temperature errors occurred. For the variable temperature runs, errors were mostly due to temperature control uncertainty, which is typically ±0.05 K.

Three kinds of M-H runs were performed: (1) initial magnetizations (the M-H recorded during the initial H upsweep for a virgin sample), (2) continuous M-H loops, and (3) stepping M-H loops. Initial magnetizations were performed on most samples, and were used to determine H_p and H_{c1}. These runs were 10 minutes in duration and 1000 points long. The H-field sweep was a single, continuous upward ramp at a constant rate.

The continuous M-H loops were 10 minutes in duration and 1000 points long, with a triangular H versus t profile. These loops were used to measure samples that had small decay time constants (τ_d). The largest contribution to the sweep-rate dependence is eddy current generation, although there are others[42].

The VL and VP samples had long time constants, so that in order to measure static properties it was necessary to use a very low field sweep rate (dH/dt). This was done using a stepping method in the following way: (1) the field was rapidly ramped and then held constant, (2) after 5 minutes the magnetization value was taken, and (3) this step-wise procedure was continued so as to define a magnetization loop. Since this procedure was time intensive, it was deemed sufficient to record only half a hysteresis loop, of H_m = 17 kOe, and consisting of 30 to 40 data points. This stepping procedure allowed the measurement of essentially static M-H loops for samples with long time constants. Our $(dH/dt)_{eff}$s ranged from ≈ 0.08 Oe/s (for the longest L_p samples) down to essentially zero (for short samples). Some recent papers have suggested[9,43] that PE magnetization creeps or drifts more rapidly than has usually been observed in conventional low temperature superconductors. If true, this would introduce some error into the results because of a violation of the implicit assumption above, viz: that the magnetization at long times after a field step is essentially the static magnetization. However, we think that for the time constants of our samples, a 5 minute delay gives a reasonable compromise between eddy current and creep effects. The calculation of the effective sweep rate, $(dH/dt)_{eff}$, associated with a stepping M-H procedure is shown in App. B. Other relevant details are also presented there.

3.2 Strands

All of the samples used in these experiments were very fine filament multifilamentary NbTi superconductive composite strands. Eight different strand types were investigated. The strands were made from a matched pair of billets, consisting of NbTi rods imbedded in two different types of matrix material (Cu and Cu-Mn(0.5 wt %)). These two billets were drawn down to strands with four different filament diameters, ranging from 2.0 μm to 0.7 μm. These sizes were selected primarily with interfilamentary spacing in mind, and were designed to achieve various degrees of PE coupling. Each strand had about 5000 filaments, with a filament-spacing-to-diameter ratio of about 0.2. This ratio was kept low to prevent diameter modulation (sausaging) of the filaments during the wire drawing process. The strands were fully filamentary, having no central copper core. Both strands had an outer copper shell, and their filaments lacked the Nb jackets which are typically used to control the formation of intermetallics during precipitation heat treatment. These strands received no heat treatment, and no twist has been deliberately introduced. Detailed strand specifications are provided in Table 3.2.1, and SEM photographs are displayed in App. A. The strand and sample codes are explained in Fig. 3.2.1.

The strands listed in Table 3.2.1 were actually members of a four-billet set, two billets of which exactly matched these in matrix composition and filament diameter, but the filamentary material was Nb. The Nb-filament strands were intended for heat-capacity measurements, which are still to be performed.

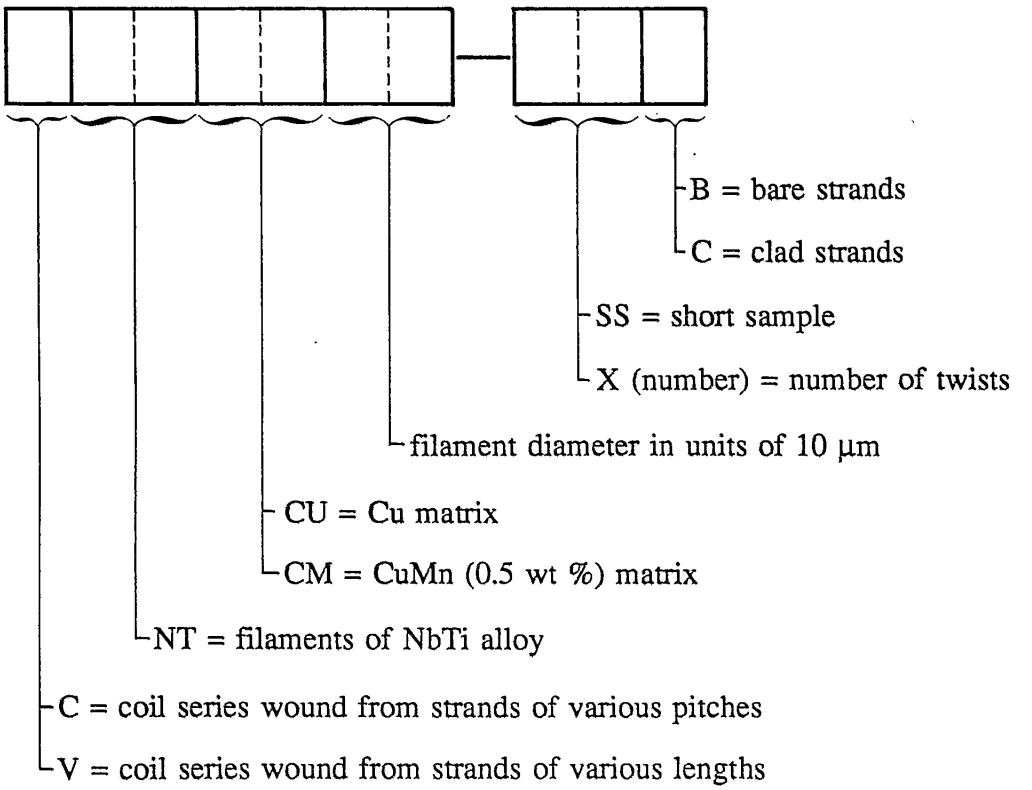

Fig. 3.2.1 Explanation of strand and sample codes

Tab. 3.2.1 Strand Specifications

Strand Code	Strand diameter (mm) nom.	Filament diameter (μm)	Number of filaments	NbTi mass per strand cm (mgs)
NTCU20	0.26	2.03	4395†	0.8706
NTCU14	0.16	1.50	4395	0.4762
NTCU10	0.11	1.17	4395	0.2855
NTCU07	0.081	0.83	4395	0.1450
NTCM20	0.26	1.90	5355‡	0.9274
NTCM14	0.16	1.41	5355	0.5065
NTCM10	0.11	0.96	5355	0.2381
NTCM07	0.081	0.73	5355	0.1383

† Error in the number of filaments for the Cu strands is ± 7.
‡ Error in the number of filaments for the CuMn strands is ± 30.

3.3 Sample Preparation

Three sample types were constructed: (1) a cylindrical bundle of straight short lengths of strand imbedded in epoxy, (2) coil samples of a certain constant length of strand given variable twist pitches (VP), and (3) coil samples of nominally untwisted strand, of varying length (VL). Short samples were made from all strands, while both VL and VP samples were wound only from strands with the largest and smallest filament diameters.

3.3.1 Short Samples

Short cylindrical samples were prepared both from as-received strands, as well as from strands from which the copper had been etched away (using nitric acid), giving a total of 16 samples. In order to make the samples the strands were wound around 2 pegs approximately 2" apart, epoxied, and then were more tightly packed by lassoing with nylon string, taking care to retain parallelism (see Fig. 3.3.1.1). For the bare samples a nitric acid etch was applied after winding but before the application of epoxy. After cutting to the desired length, these samples were recast in epoxy in a teflon mold for ease in attachment to the VSM rod. Figs. 3.3.1.2 (a) and (b) show length-wise cut-aways, displaying the amount of clad and bare filament parallelism and regularity. Additionally, the ends of the clad samples were ground and polished to avoid possible mechanical connection between the filaments. The dimensions of the short samples are given in Table 3.3.1.1.

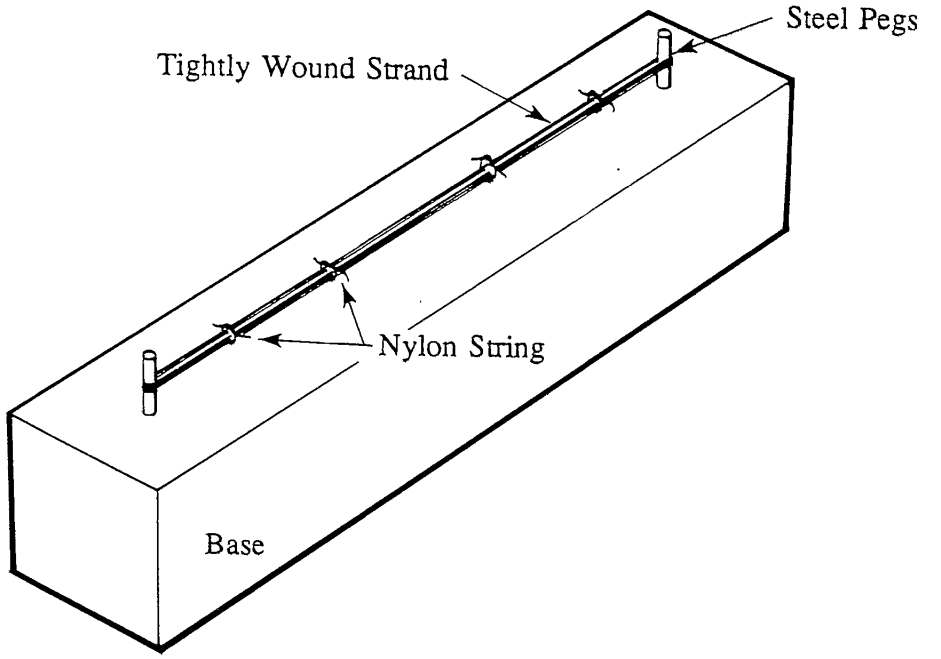

Fig. 3.3.1.1 Apparatus for making the short samples

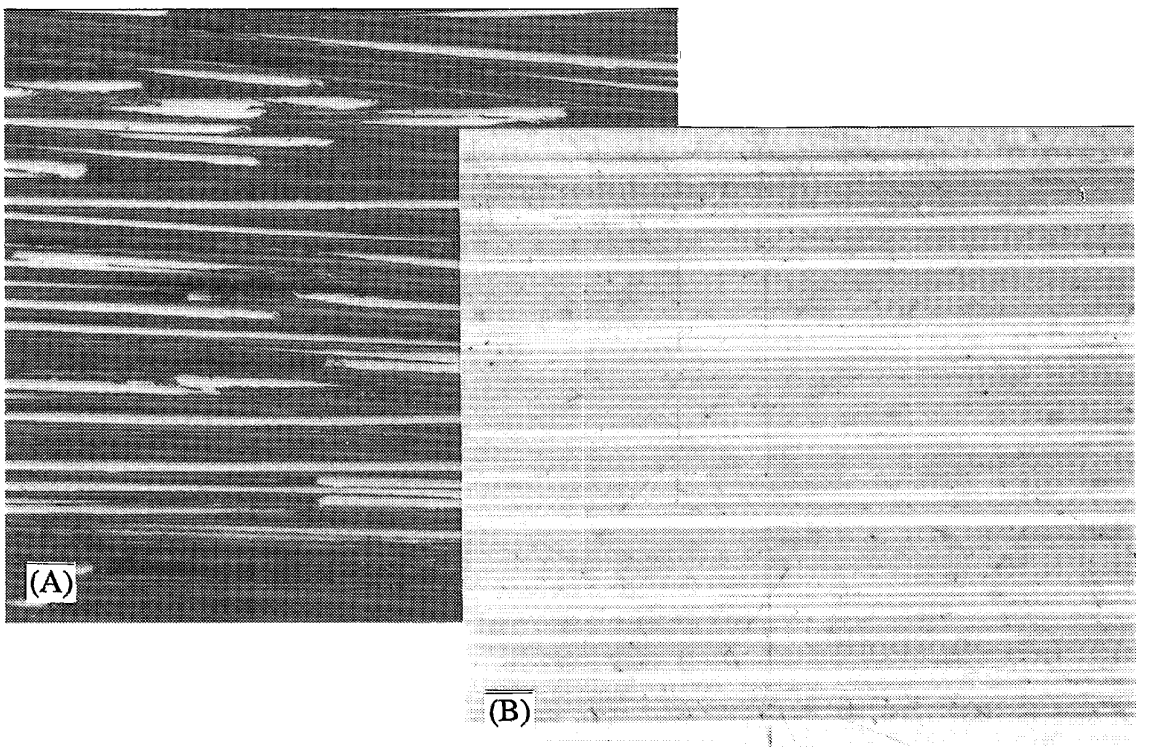

Fig. 3.3.1.2 Optical micrographs of bare and clad short samples showing the parallelism and regularity of (A) the bare filaments, (B) the clad filaments

Tab. 3.3.1.1 Short Sample Specifications

Sample Code	Filament Diam. (μm)	No. of Strands	Sample Length (mm)	NbTi Volume V_{NbTi} (10^{-3} cm^3)	Filamentary Region Volume $V_{Fil.}$ (10^{-3} cm^3)
NTCU20-SSC	2.03	60	3.66	3.13	4.85
NTCU20-SSB	2.03	59	5.40	4.55	- -
NTCM20-SSC	1.90	40	5.38	3.27	4.85
NTCM20-SSB	1.90	40	5.04	3.20	- -
NTCU14-SSC	1.50	100	5.38	4.20	6.50
NTCU14-SSB	1.50	110	5.47	4.69	- -
NTCM14-SSC	1.41	100	5.45	4.56	6.76
NTCM14-SSB	1.41	110	5.28	4.83	- -
NTCU10-SSC	1.17	150	5.37	3.77	5.85
NTCU10-SSB	1.17	150	5.39	3.78	- -
NTCM10-SSC	0.96	150	4.96	2.91	4.31
NTCM10-SSB	0.96	150	5.38	3.15	- -
NTCU07-SSC	0.83	250	5.39	3.21	4.97
NTCU07-SSB	0.83	250	5.21	3.10	- -
NTCM07-SSC	0.73	250	5.29	3.00	4.44
NTCM07-SSB	0.73	250	5.46	3.09	- -

3.3.2 Variable Pitch (VP) Coil Samples

The VP coil samples were formed by wrapping the strands into oval coils approximately 10 mm x 0.3 mm x 0.2 mm as shown in Fig. 3.3.2.1. Using strands NTCU20, NTCU07, NTCM20, and NTCM07, four sets of coils were made. Within each set 1 to 128 twists were administered to the strand (for specifics see Table 3.3.2.1).

The twist was introduced in the following way: (1) An appropriate amount of strand was stretched between two vices and inserted through the hole in the oval coil holder (see Figs. 3.3.2.2 and 3.3.2.3). (2) This strand was then secured to the holder with epoxy. (3) By sliding the strand through Vice 1 a length of strand was measured out, Vice 1 was closed, and the strand was marked with a black marker on the top side. (4) Twist was introduced by rotating Vice 2 around the axis of the strand an integral number of times. (5) The twist length and twist uniformity where checked with the aid of the marking made in stage 3. (6) The oval coil holder was released from Vice 2 and the strand was "rolled" onto it, after which the strand was cut and secured to the coil with cryogenic tape. (7) The coil was inserted into the housing (see Fig. 3.3.2.3) for attachment to the VSM rod. In a test for possible error caused by mechanical damage to the sample ends, two identical coils were made -- one with ends polished, one without -- and M-H loops taken on these samples showed no difference between them. Having failed to discern any difference between their magnetizations, further end polishing was abandoned for these long samples.

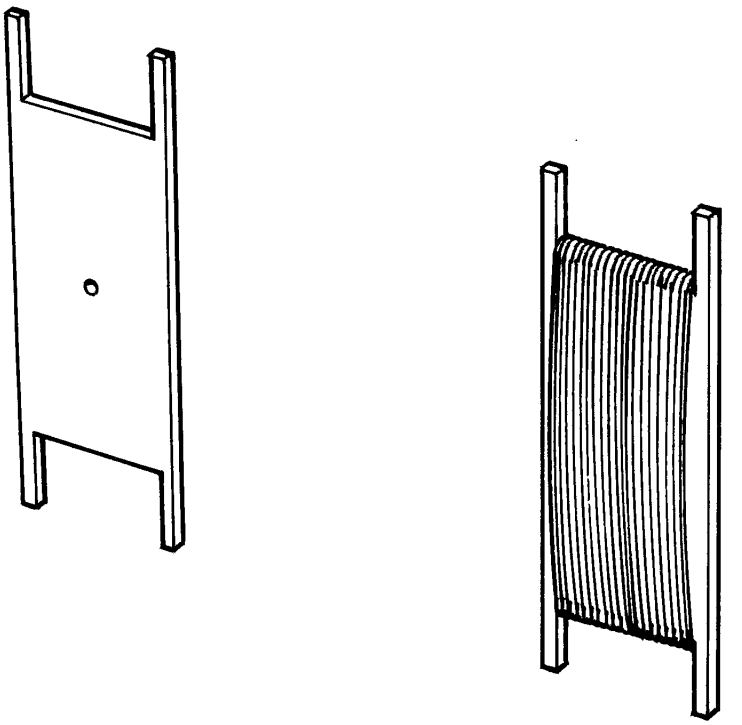

Fig. 3.3.2.1 Oval coil holder

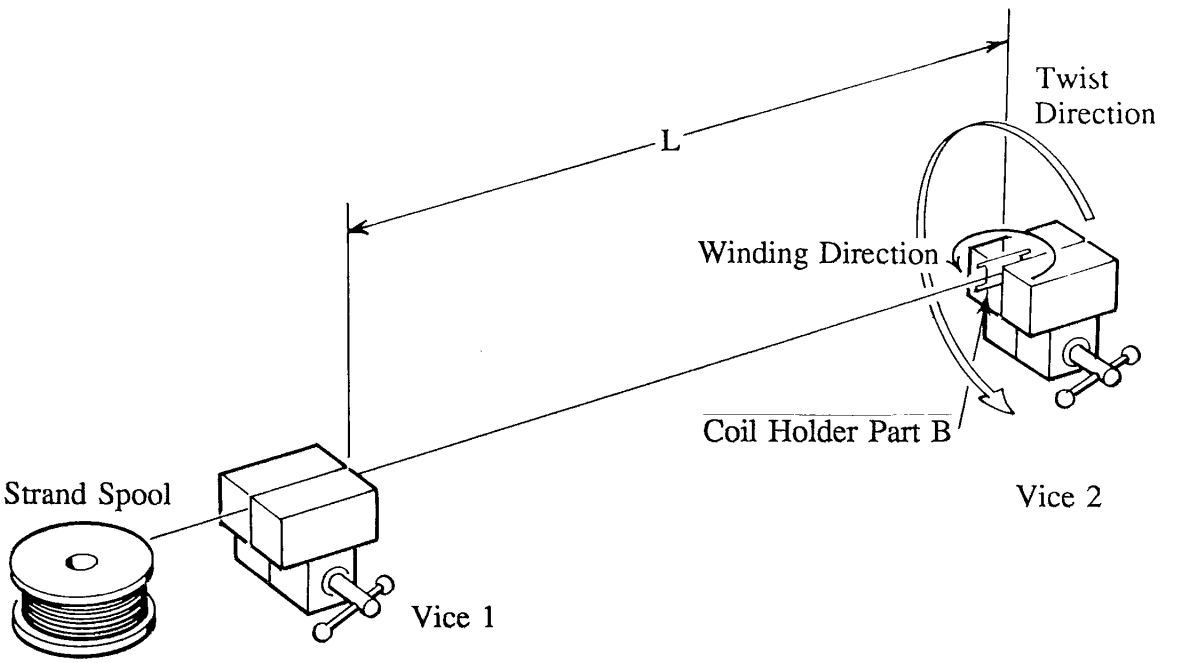

Fig. 3.3.2.2 Apparatus for making the VP samples

Tab. 3.3.2.1: VP Coil Sample Specifications

Coil Name	V_{NbTi} ($10^{-3}cm^3$)	$V_{FIL,\ REG.}$ ($10^{-3}cm^3$)	L_{TOT} (cm)	n	L_P (cm)
CNTCU20-2	10.15	15.73	71.1*	2	35.56
CNTCU20-4	10.15	15.73	71.1	4	17.78
CNTCU20-8	10.15	15.73	71.1	8	8.89
CNTCU20-16	10.15	15.73	71.1	16	4.44
CNTCU20-32	10.15	15.73	71.1	32	2.22
CNTCU20-64	10.15	15.73	71.1	64	1.111
CNTCU07-1	3.383	5.24	142.2**	1	142.2
CNTCU07-2	3.383	5.24	142.2	2	71.12
CNTCU07-4	3.383	5.24	142.2	4	35.56
CNTCU07-16	3.383	5.24	142.2	16	8.89
CNTCU07-32	3.383	5.24	142.2	32	4.44
CNTCU07-128	3.383	5.24	142.2	128	1.111
CNTCM20-0	12.431	18.428	81.724†	0	∞‡
CNTCM20-4	10.81	16.03	71.1	4	17.78
CNTCM20-64	10.81	16.03	71.1	64	1.111
CNTCM07-1	3.225	4.78	142.2	1	142.24
CNTCM07-8	3.225	4.78	142.2	8	17.78
CNTCM07-128	3.225	4.78	142.2	128	1.111

* All values for the 71.1 cm length samples were known to 0.4%, except for n, which was exact.

** All values for the 142.2 cm length samples were known to 0.2%, except for n, which was exact.

† for this sample, measured by weighing, the length, and thus all other values were known to 0.01% (except for n which was exact).

‡i.e., no twist was applied. From the Morgan model $L_p \approx 2$ L.

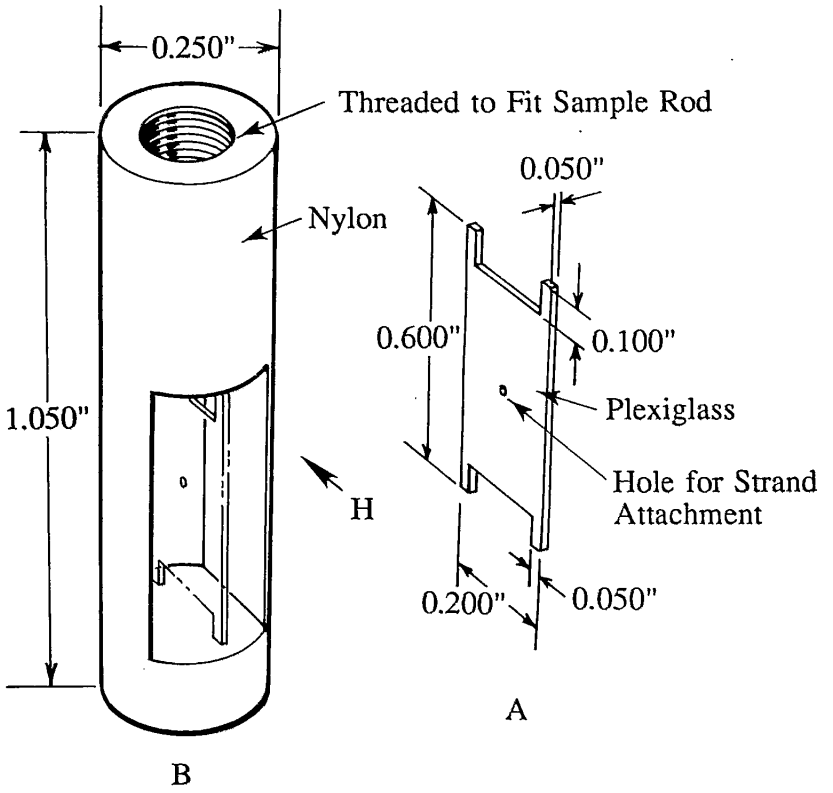

Fig. 3.3.2.3 Coil holder (A) and housing (B)

3.3.3 Variable Length (VL) Coil Samples

The VL coil samples were prepared from strands NTCU20 and NTCU07. Two sets were made, consisting of three samples for NTCU20, and four samples for NTCU07. The strand lengths ranged from 1 cm to 142 cm (see Table 3.3.3.1). To maintain sensitivity, each coil contained about the same mass of strand. Accordingly, the coils generally had multiple strands of the same length in parallel.

The strands were initially wound onto a two-pegged holder, in the manner of the short straight sample preparation (Fig. 3.3.1.1). The peg separation was adjusted to

Tab. 3.3.3.1 VL Coil Sample Specifications

Coil Name	V_{NbTi} ($10^{-3}cm^3$)	$V_{FIL.\ REG.}$ ($10^{-3}cm^3$)	Sample Length (cm)	No. wires
VNTCU20-1	4.25	6.58	1.03*	29
VNTCU20-2	3.64	5.64	1.91	13
VNTCU20-8	6.56	10.17	7.66	6
VNTCU07-2	6.73	10.42	2.04	139
VNTCU07-4	7.85	12.31	4.23	79
VNTCU07-8	4.43	6.86	7.46	25
VNTCU07-32	6.22	9.63	32.7	8

* Error in length is estimated to be 0.01 cm for all samples except VNTCM07-32, for which it is taken to be 0.1 cm.

fit the desired strand length for a given sample. Since the strands needed to remain untwisted, they had to be immobilized during polishing. Accordingly, they were set with Duco cement, and cut to the appropriate length. The ends were then dipped in acetone to dissolve the Duco cement, and recast in epoxy. A representative mold is shown in Fig. 3.3.3.1. To eliminate any possibility of end effects due to mechanical damage, the ends of all the VL samples were polished. In order to do this the samples were fit into the special holder (shown in Fig. 3.3.3.2) for grinding and polishing. Optical micrographs of the polished ends were taken, and a representative sample end is shown in Fig. 3.3.3.3. The remaining Duco cement was then removed with acetone, and the samples were wound (without the introduction of twist) onto coil holder A, above.

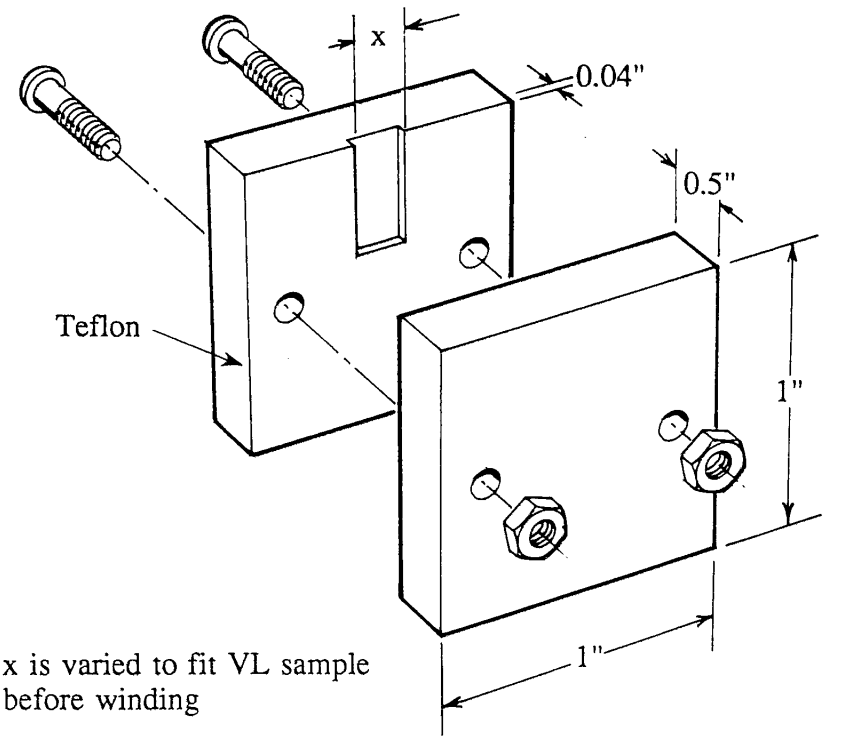

Fig. 3.3.3.1 VL sample end mold

3.4 Design of the experimental program

Short sample measurements had three purposes: (1) a quick overview of the variation of the proximity effect with filament diameter and matrix type, (2) investigation of the angular dependence of the PE, and (3) measurement of the intrinsic properties of the proximity effected copper. Short samples were mounted in holders like that shown in Fig. 3.4.1, which permitted rotation of the sample (hence filament) axis with respect to the applied field. For the short straight samples, the decay time constants were sufficiently small that IM and M-H runs that were 10 minutes in duration measured only the static curve.

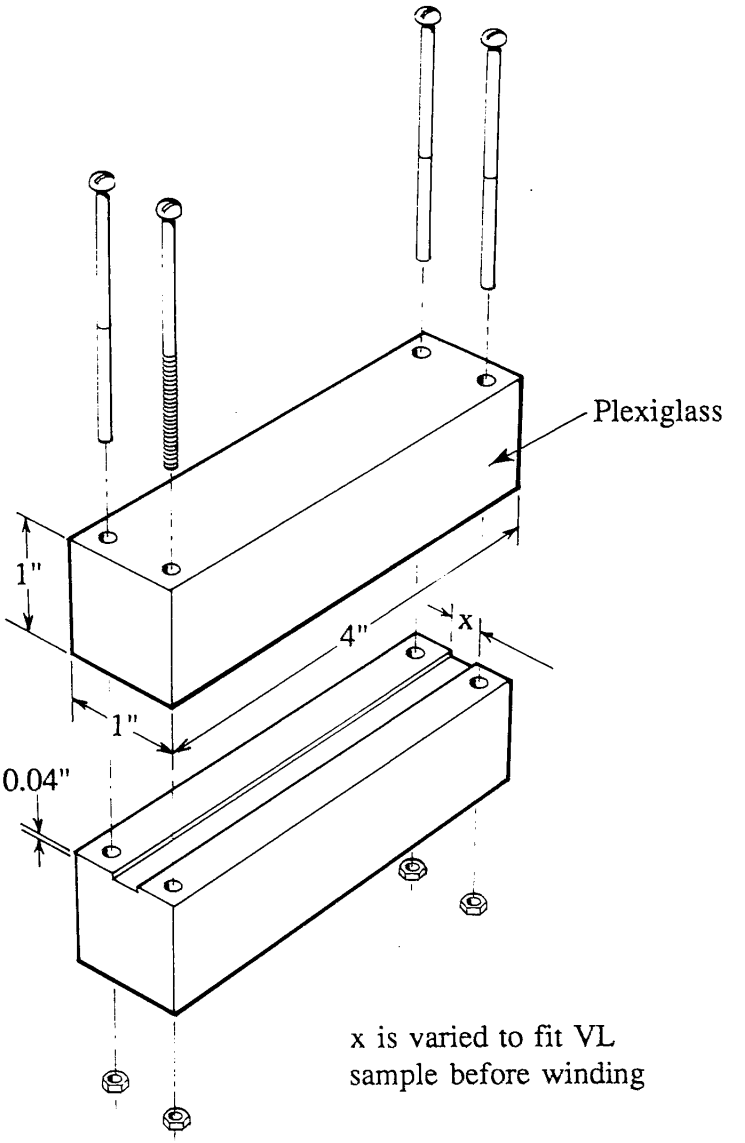

Fig. 3.3.3.2 VL sample polishing holder

The VP samples were used to investigate the effect of various L_ps on the M-H and Q. We applied the magnetic field along the axis of solenoidal symmetry since this is equivalent (geometrically, with respect to L_p) to applying the field transversely to a long straight strand. The true axis orientation was determined by looking for the point of symmetry (usually the maximum) in the total loss (Q_T) versus θ_s near the orientation where the field is applied along the solenoidal symmetry axis.

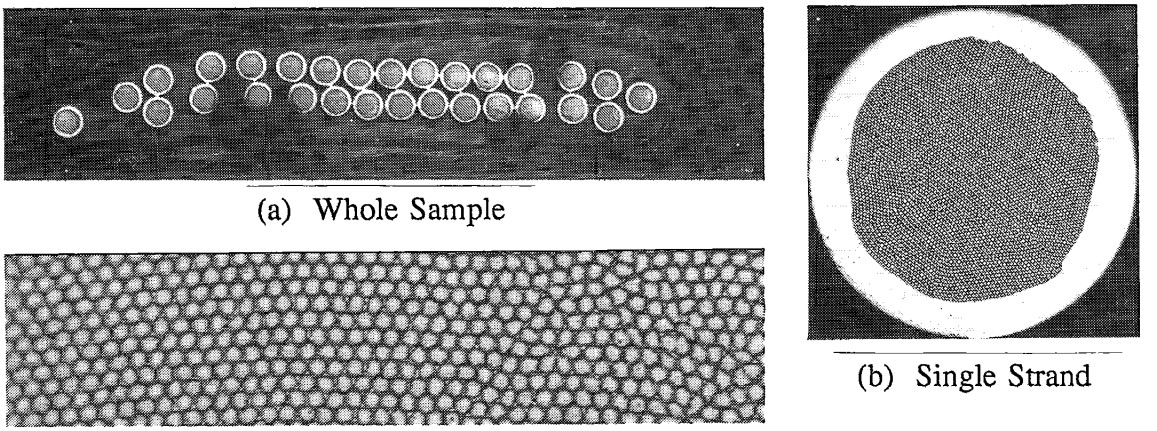

(a) Whole Sample

(b) Single Strand

(c) Detail of Filamentary Part of Strand

Fig. 3.3.3.3 Optical micrograph of the ends of sample VNTCU20-1, showing the absence of filament shorting

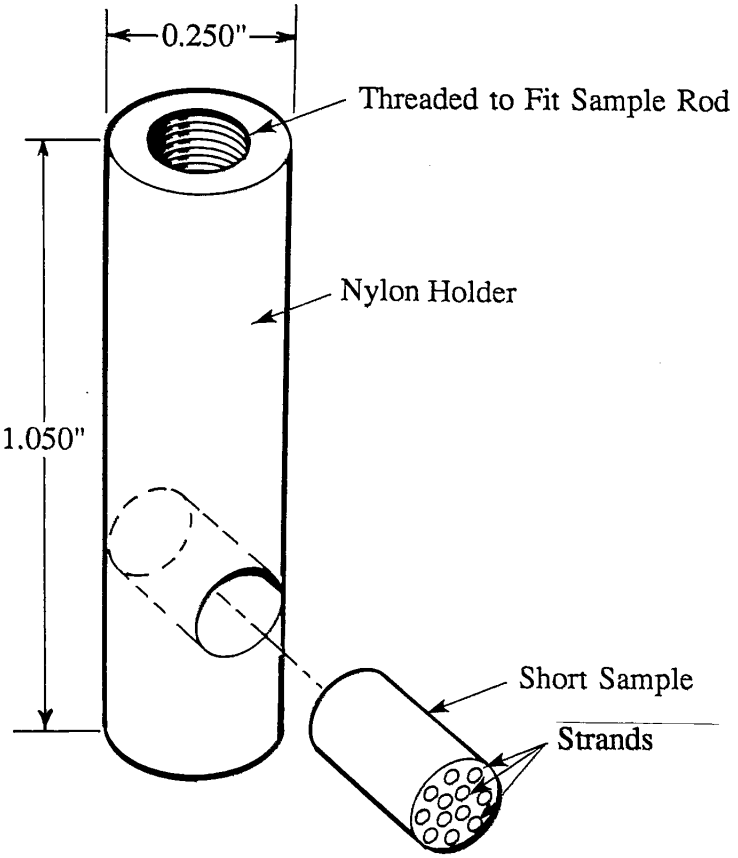

Fig. 3.4.1 Short sample holder

The VL samples were used to investigate the effect of different lengths on M-H and Q, and so it was necessary to apply the field along the solenoidal axis here too. Samples were oriented in the same way as above.

There are differences in the properties of the PE in the various H_m regimes, as described above, and these differences change with L and L_p. Therefore, it was decided to look at large and small H_m regimes (well above and just below the H_{c1} of the NbTi) for all samples, and to look at the detailed M-H versus H_m behavior for only a few samples. Below is a general outline of the measurements made.

CATALOG OF MEASUREMENTS

Large H_m Coil Measurements (Sec. 4.1):

VP Coils

Cu and CuMn 2.0 μm, 71 cm (NTCU20 and NTCM20)

Cu and CuMn 0.7 μm, 142 cm (NTCU07 and NTCM07)

VL Coils

Cu, 2.0 μm and 0.7 μm (NTCU20 and NTCU07)

Small H_m Coil Measurements (Sec. 4.2): M-H and IM.

Short Sample Measurements (Sec. 4.3):

±17 kOe M-H for all strand diameters in both transverse and longitudinal orientation.

$H_{c1,prox}$ and J_{cp} extracted from low field IM in longitudinal field orientation.

M-H versus H_m (Sec. 4.4): For various samples, both coil and short sample

Angular Behavior of Large H_m M-H for Short Sample NTCU20 (Sec. 4.5).

Loss versus L_p, L, and H_m for Both Coil and Short Sample (Sec. 4.6).

CHAPTER 4: RESULTS

4.1 Large H_m M-H and ΔM for the VP and VL coils

4.1.1 Variable Pitch (VP) Coil Results

Large H_m M-H loops as a function of L_p for Cu matrix VP samples of strand NTCU20 are shown in Fig. 4.1.1.1. In this figure the M-H loop of the bare-filament short sample of the appropriate filament diameter is superimposed onto the coil loops to show the extent of PE coupling magnetization and loss. Because these loops were measured

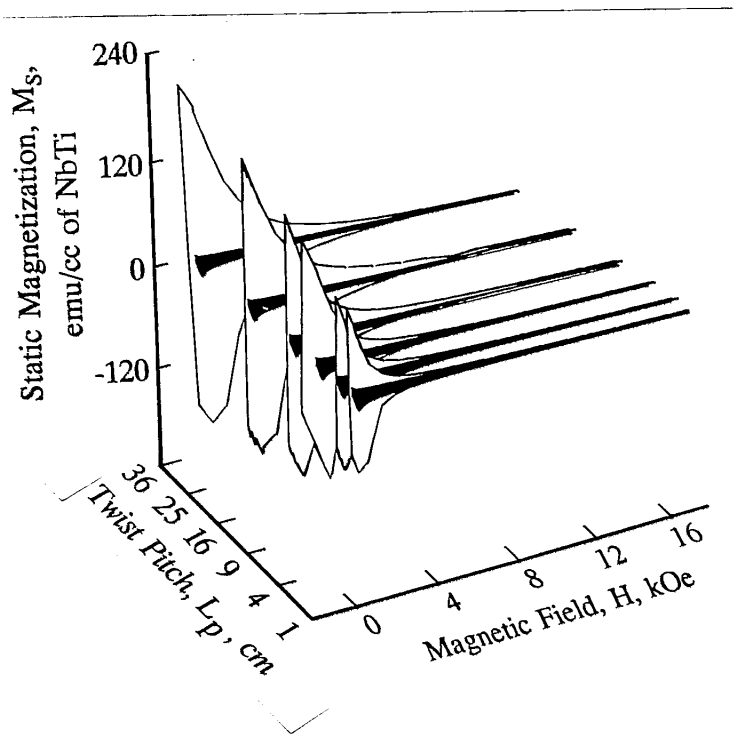

Fig. 4.1.1.1 Static M-H versus L_p for Cu matrix VP coils made from the strand NTCU20

via the stepping M-H loop method, we take these to be the static M-H loops (cf. App. B). Looking at Fig. 4.1.1.1, and also at Fig. 4.1.1.2 where we have re-plotted these data as ΔM_S versus L_p, we can see the main features of these loops, viz: (1) For a given H, ΔM_S increases with L_p, and (2) For a given L_p, ΔM_S decreases with increasing H.

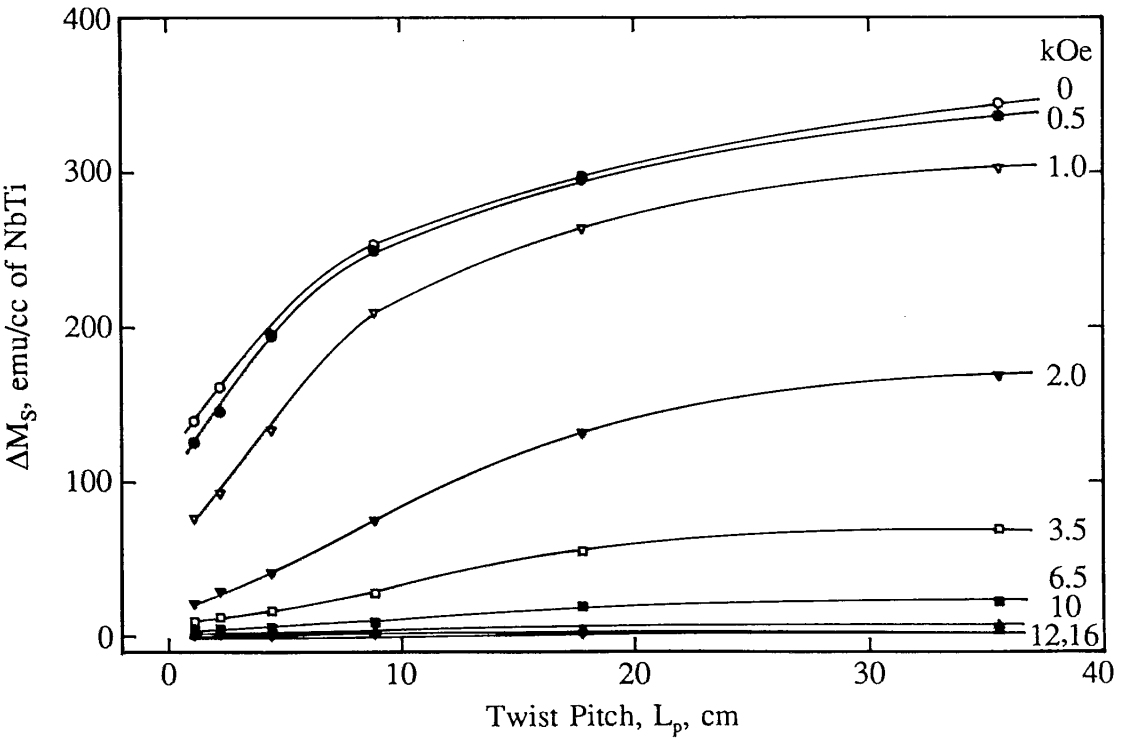

Fig. 4.1.1.2 ΔM_S versus L_p at various fields for Cu matrix VP coils made from the strand NTCU20 (small L_p)

Expanding upon point one, above, we notice that ΔM_S is linearly proportional to L_p for small L_p, with a subsequent saturation (cf. Sec. 5.1.3). ΔM_S also has a zero L_p intercept which is close to ΔM_h (the ΔM from the NbTi), indicating that it is in fact ΔM_{PE} which

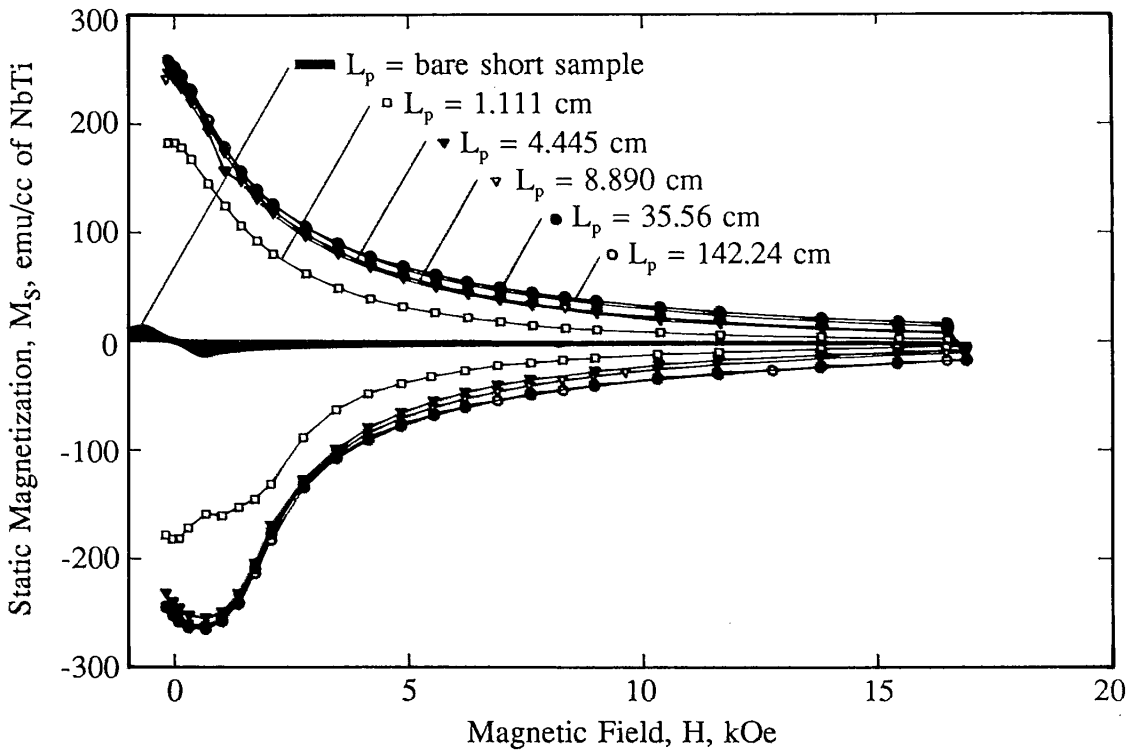

Fig. 4.1.1.3 Static M-H for several Cu matrix VP coils of different L_p made from the strand NTCU07

is proportional to L_p. The connecting curves in Fig. 4.1.1.2 (and all subsequent ΔM_S versus L_p figures) are guides to the eye. In Fig. 4.1.1.3 are displayed the M-H half loops for the 0.7 μm Cu VP coils. Here we see that ΔM_S for high fields appears to be proportional to L_p, and that PEs extend out to the full extent of the field sweep. Figs.

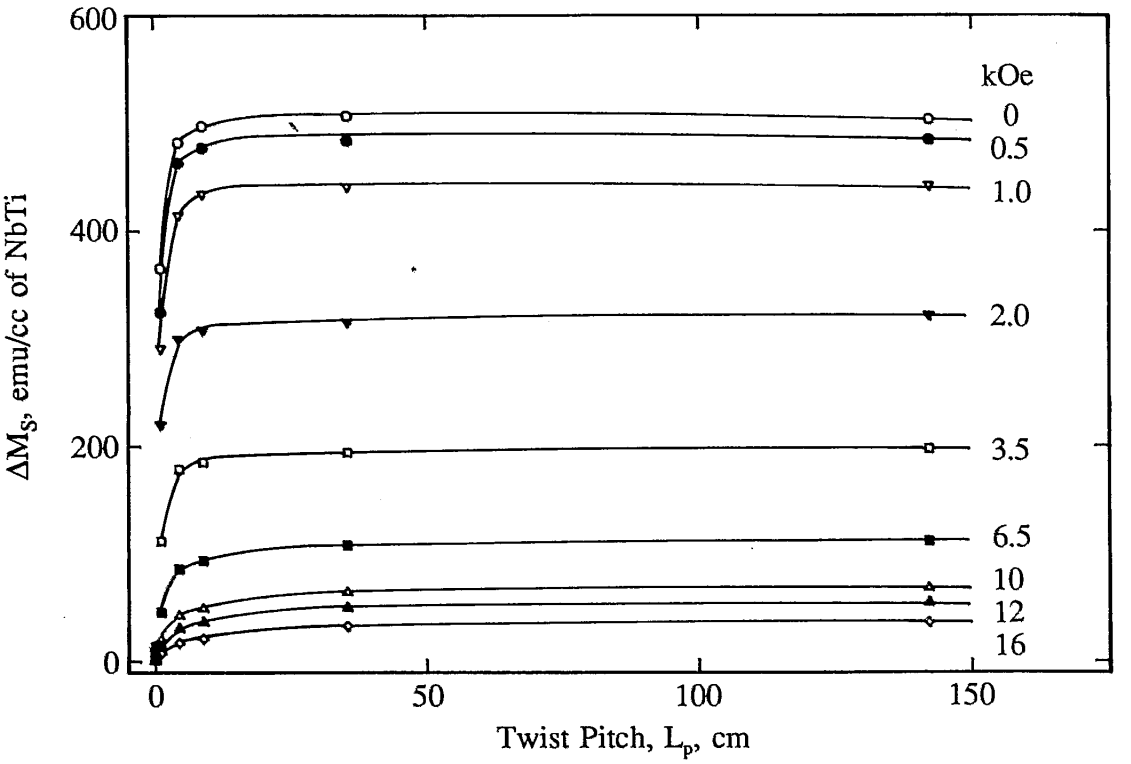

Fig. 4.1.1.4 ΔM_S versus L_p at various fields for Cu matrix VP coils made from the strand NTCU07 (large L_p)

4.1.1.4 and 4.1.1.5 indicate that the magnetization begins to saturate at very low L_p and at a rather large value as compared to that of the bare sample. In comparing the two sets of Cu coils we can see that: (1) in the fine filament strands the PEs extend out to much higher field, and (2) the low field magnetizations are similar in size.

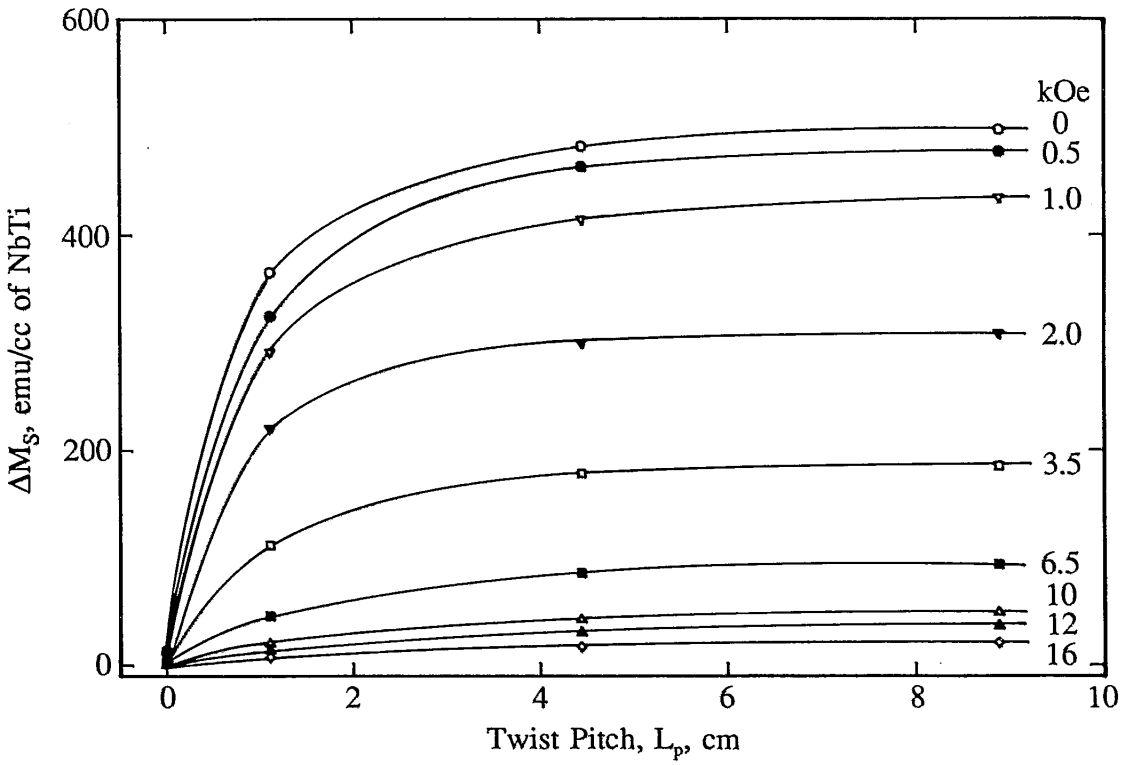

Fig. 4.1.1.5 ΔM_S versus L_p at various fields for Cu matrix VP coils made from the strand NTCU07 (small L_p)

Large H_m static M-H loops for the CuMn matrix VP coils from strand NTCM20 are shown in Fig. 4.1.1.6 (for a list of sample codes see Table 3.3.2.1). The bare sample M-H loop is also shown in this figure. In Fig. 4.1.1.7 we re-plot the data as ΔM_S versus L_p. We note that the CNTCM20-X coils display the same ΔM_S dependence on L_p as was

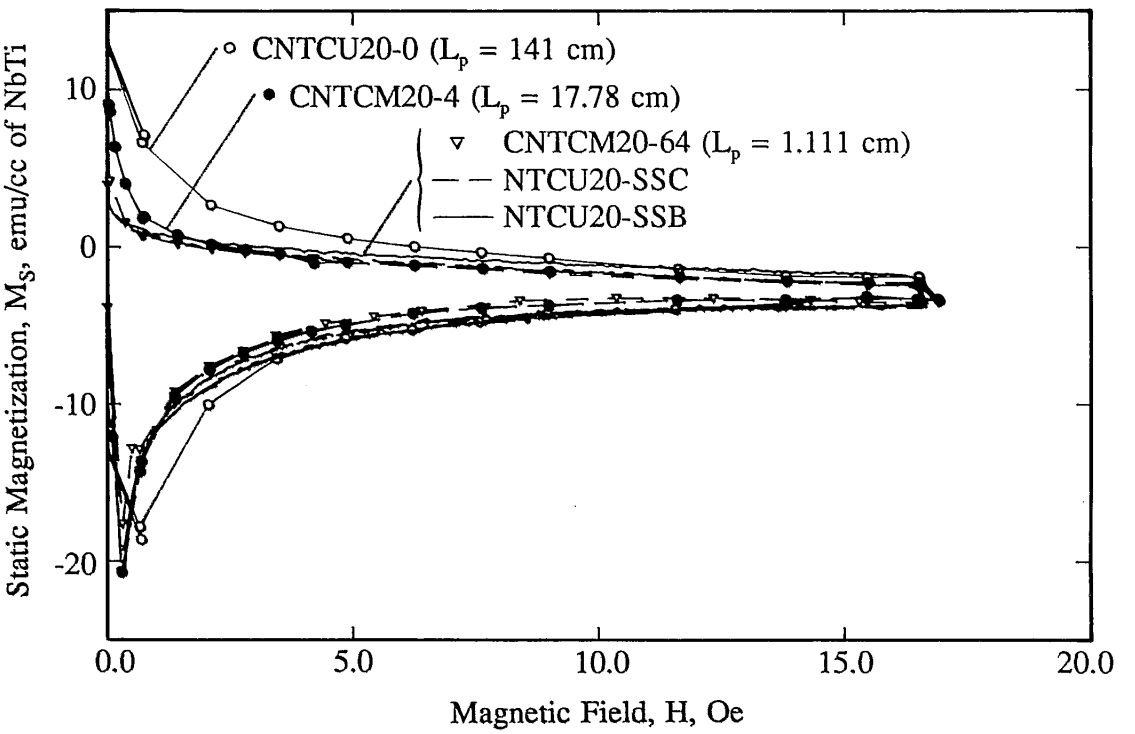

Fig. 4.1.1.6 Static M-H for several CuMn matrix VP coils of different L_p made from the strand NTCM20

seen in the Cu coils, although it is very much weaker here. Also, the absolute value of the magnetization is much lower than those in the CNTCU20 coils, being very much closer to that of the bare NbTi. This brings out the fact that it is the ΔM_{PE} portion of ΔM_S that is proportional to L_p. These results are consistent with the well known weaker

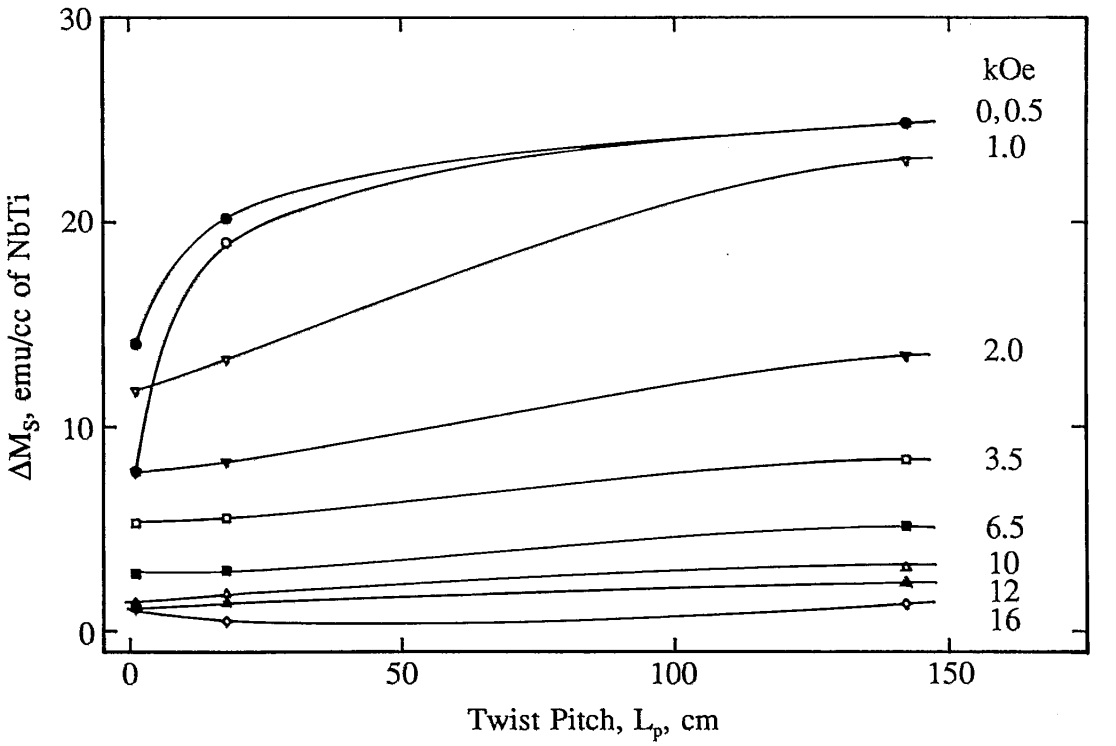

Fig. 4.1.1.7 ΔM_S versus L_p at various fields for CuMn matrix VP coils made from the strand NTCM20 (large L_p)

PE in the CuMn matrix material. In Figs. 4.1.1.8-10 the results for the CNTCM07 coils are shown. These results show a magnetization, and a dependence of this magnetization on L_p, which is greater at all fields than that of the CNTCM20 coils. In comparing these results to those of CNTCU07 (Fig. 4.1.1.3-5) we can see that the dependence of the

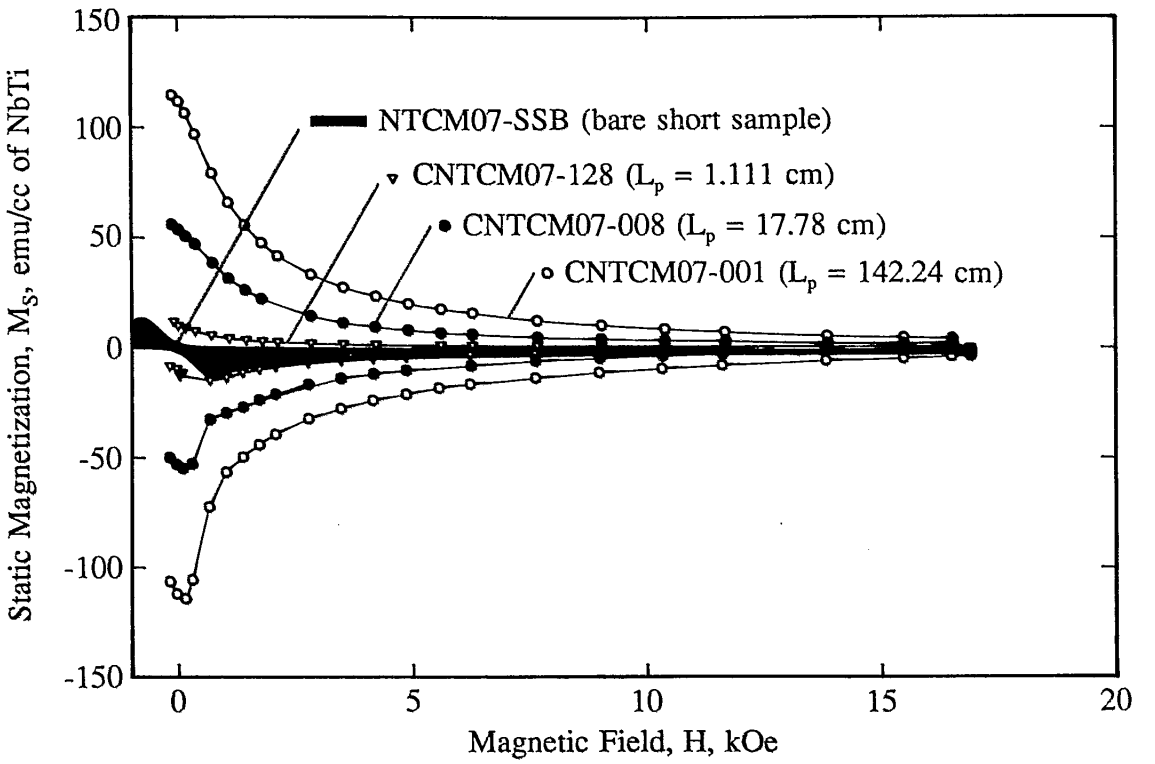

Fig. 4.1.1.8 Static M-H for several CuMn matrix VP coils of different L_p made from the strand NTCM07

magnetization on L_p is greater in the CNTCM07 coils, but that the absolute value of the magnetization is not as high as the CNTCU07 coils. This seems to suggest that the PE for the CNTCM07 coils is strong enough to have large PE, but not strong enough to be fully saturated.

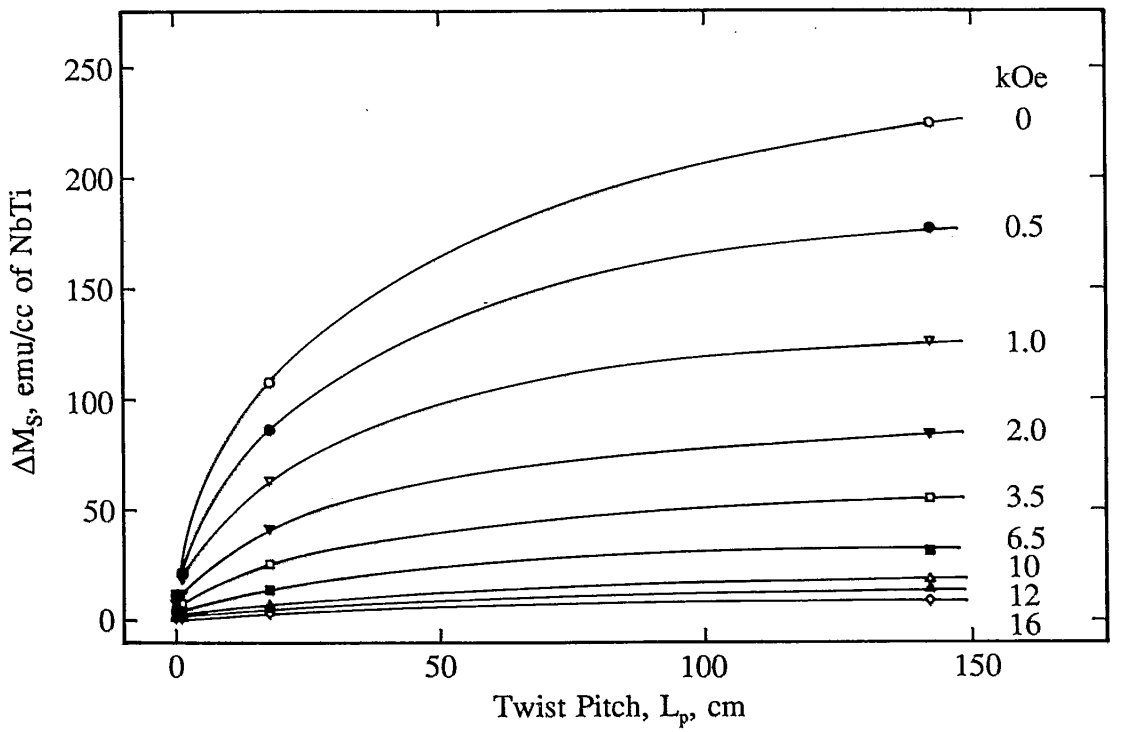

Fig. 4.1.1.9 ΔM_S versus L_p at various fields for CuMn matrix VP coils made from the strand NTCM07 (large L_p)

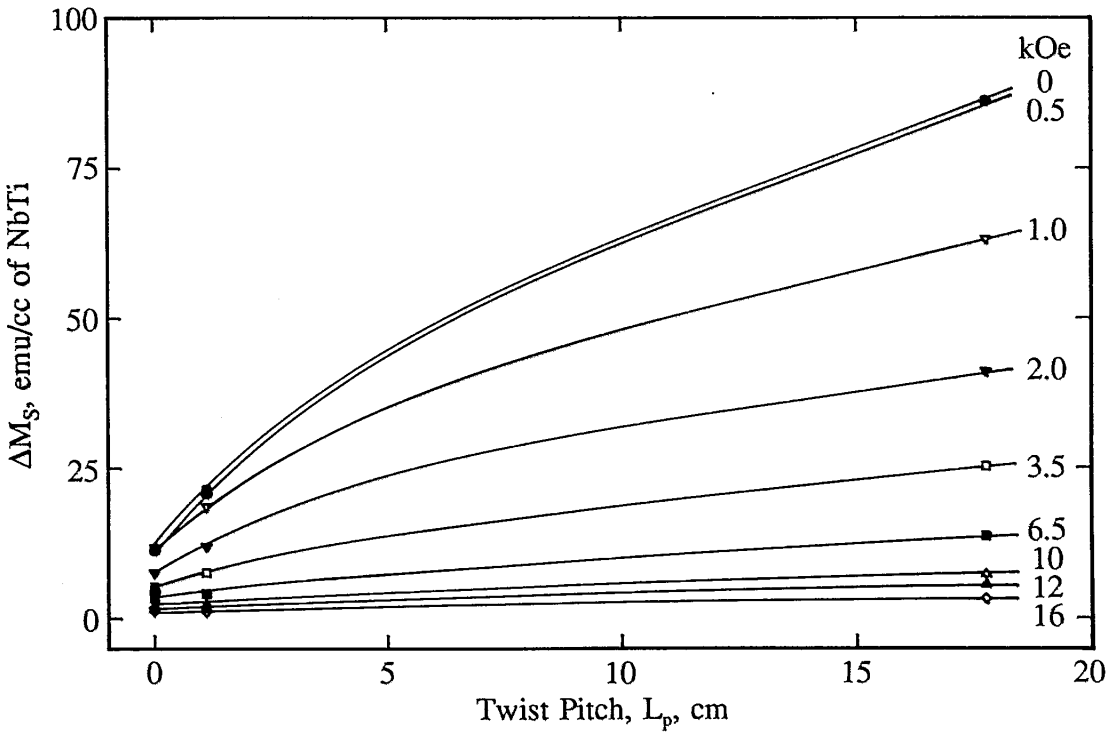

Fig. 4.1.1.10 ΔM_S versus L_p at various fields for CuMn matrix VP coils made from the strand NTCM07 (small L_p)

In summary we suggest that the coil sets can be listed in order of increasing PE coupling strength as; CNTCM20 < CNTCM07 < CNTCU20 < CNTCU07. The PE is very weak in CNTCM20, giving a weak linear dependence of ΔM_{PE} on L_p and no saturation. CNTCM07 and CNTCU20 are moderately coupled, giving an initial linear dependence of ΔM_{PE} on L_p, with a later saturation to relatively high values of ΔM_{PE}. CNTCU07 is almost fully coupled at these L_ps giving a saturated, high PE enhanced ΔM_{PE}. These ΔM_{PE} are superimposed on a constant ΔM_h.

4.1.2 Variable Length (VL) Coil Results

Displayed in Fig. 4.1.2.1 and 4.1.2.2 are the M-H half-loops for VNTCU20-X and VNTCU07-X respectively. Inside these graphs are displayed the short-sample bare M-H of the appropriate filament diameter. We note four common features associated with both of these graphs: (1) the static M-H is proportional to L, paralleling the L_p dependence shown above, (2) the H-extent of the proportionality of ΔM_{PE} to L increases with L, similar to the increase with L_p seen in the VL coils, (3) while M_{ex} is similar for samples where $L_p \approx 2L$ (the condition for near-equivalence of L and L_p eddy-current effects in the Morgan model[45]) the H-extent of the effect is smaller in the VL samples, (4) as L is decreased the M_{NbTi} and M_{PE} peaks become distinct, and tend toward the separation

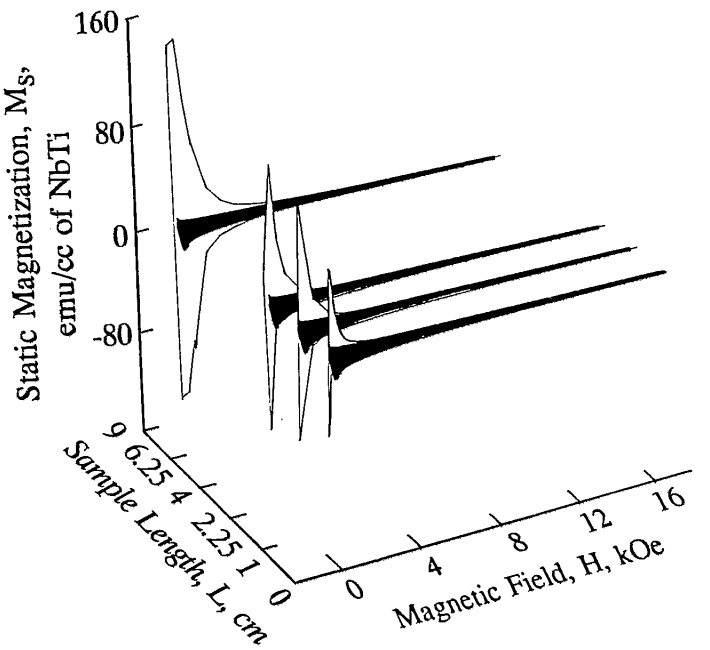

Fig. 4.1.2.1 Static M-H versus L_p for Cu matrix VL coils made from the strand NTCU20

characteristic of the short samples (cf. Sec 4.3). If we compare the VNTCU07 coils to the VNTCU20 coils we see that, as with the VP coils, the smaller filament samples have greater PE enhanced magnetizations, and these magnetizations extend to higher fields. We also note that for all except the shortest samples there is only one magnetization peak, i.e. the PE peak is sufficiently broad so that it overlaps the NbTi peak.

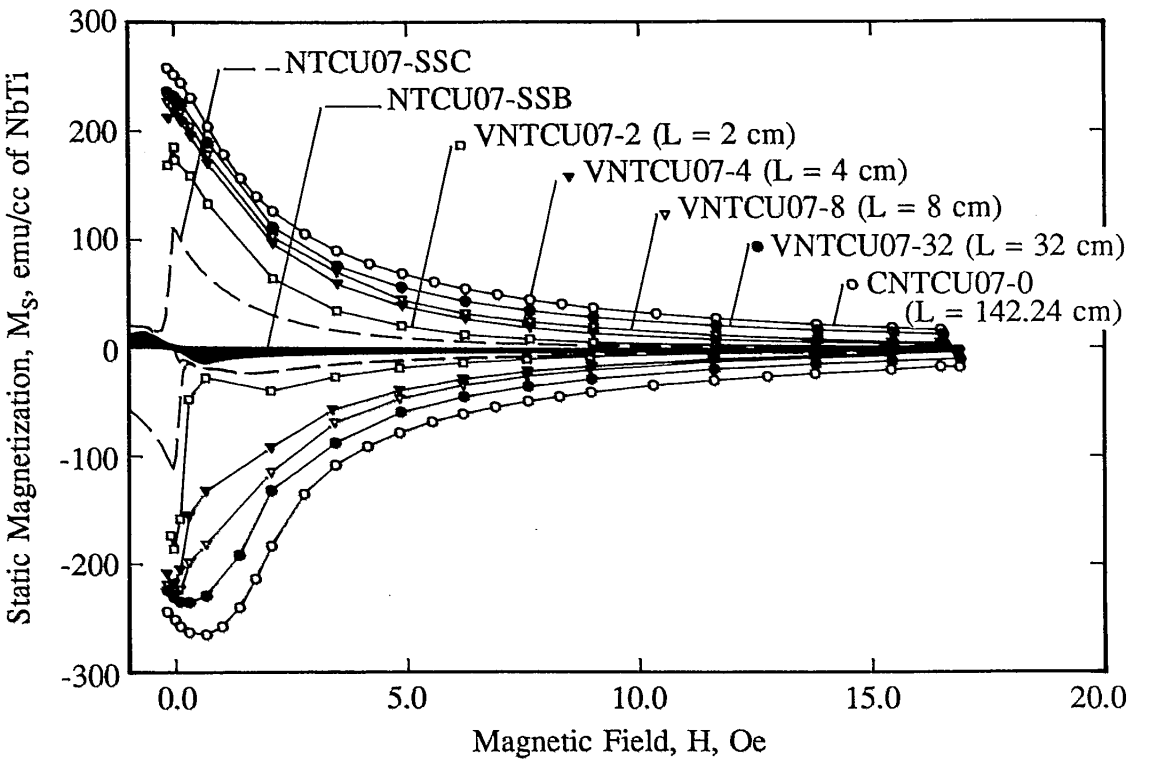

Fig. 4.1.2.2 Static M-H for several Cu matrix VL coils of different L made from the strand NTCU07

4.2 Small H_m M-H and IM for the VP and VL Coils

Both initial magnetization and low field M-H loops were taken for all Cu matrix samples. In general, the coil samples exhibited no deviation from linearity (indicating complete flux exclusion) up to $H_{c1,NbTi}$. The short and VL samples had $H_{c1,prox}$s, distinct from $H_{c1,NbTi}$. A set of these curves is shown in Fig. 4.2.1. We can see that as the length increases, $H_{c1,prox}$ seems to increase. We believe that this is a manifestation of an end effect. For isotropic superconductors, if RJ_c (where R is the strand diameter) is large, H_{c1}

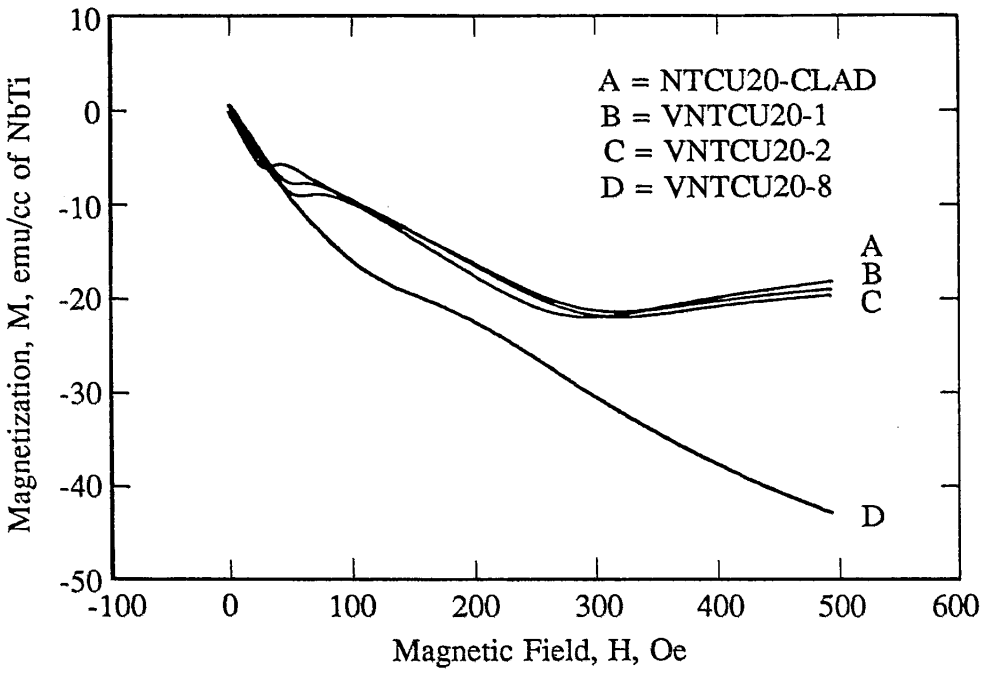

Fig. 4.2.1 IM for selected Cu matrix VL coils made from the strand NTCU20

is artificially enhanced. But in this case we interpret the observed increase in $H_{c1,prox}$ in terms of current transfer at the ends of the strands. End-induced current transfer causes the maximum shielding current which can flow down the conductor to be proportional to the sample length (cf. Sec. 5.2). Note that there does seem to be a tendency, even at small lengths, for a non-zero $H_{c1,prox}$, which we will interpret below as a true $H_{c1,prox}$. M-H loops for these samples, along with that for the coil sample CNTCU20-32 are shown in Fig. 4.2.2. The figure indicates that at these field sweeps the coil sample is barely penetrated, since $H_{c1,NbTi}$ has been only slightly exceeded.

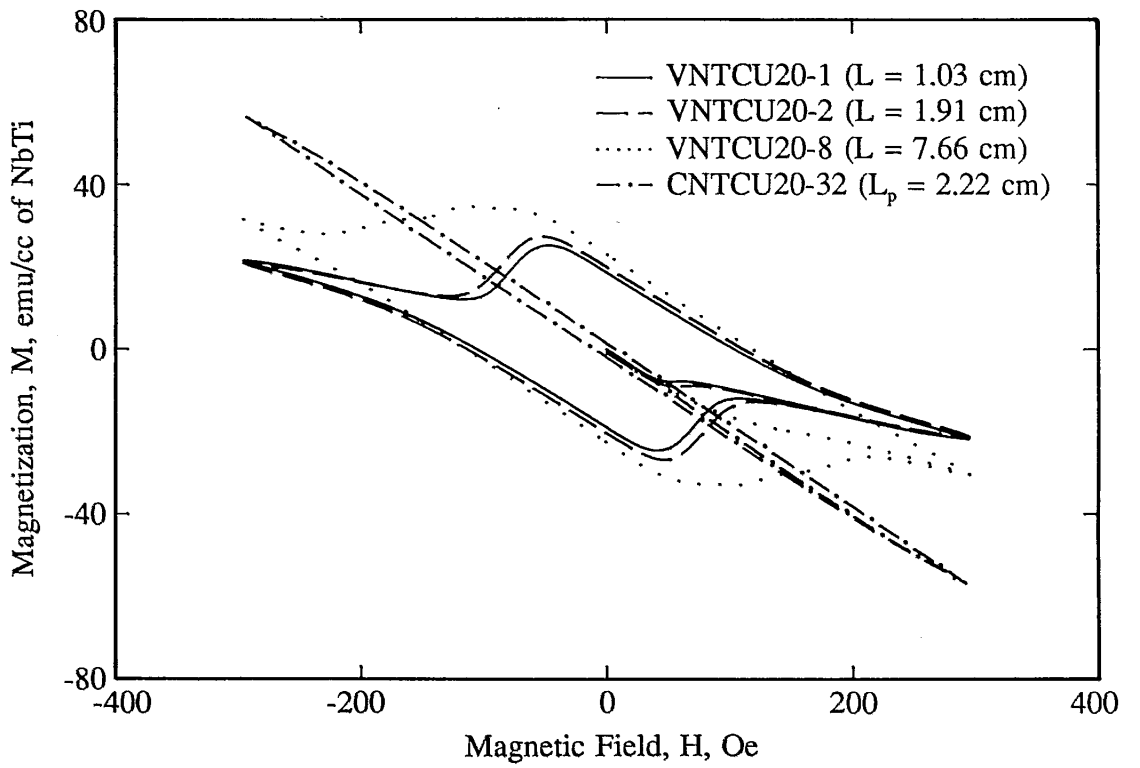

Fig. 4.2.2 Small H_m M-H for various Cu matrix VL and VP coils made from the strand NTCU20

4.3 Large H_m M-H as well as $H_{c1,prox}$ and J_{cp} for the Short Samples

Short samples measurements had three purposes: (1) a quick overview of the variation of the PE with diameter and matrix type, (2) investigation of the angular dependence of the PE, (3) measurement of the intrinsic properties of the proximity-effected copper. Short samples were mounted in holders like that shown in Fig. 3.4.1, which permitted rotation of the strand about an axis perpendicular to the field direction. For these samples, the decay time constants were sufficiently small that 10 minutes runs (IM and M-H) were slow enough to ensure that only the static curve was being measured.

4.3.1 Large H_m M-H for the short samples

The M-H loops for the Cu matrix material in a perpendicular-field orientation are displayed as a function of filament diameter in Fig. 4.3.1.1. The bare M-H loops (filled in) are superimposed on the clad. We note that PE, which is significant even for the largest filaments (2.0 μm), increases with decreasing filament diameter (and hence smaller interfilamentary spacing). From a comparison of Figs. 4.1.2.1 (VL), 4.1.1.1 (VP), and the curve for NTCU20-SSC from Fig. 4.3.1.1, we note that while the zero field M_{ex}s are comparable, the short sample ΔM decreases most rapidly with increasing field.

Note that for these short samples there are two local magnetization maxima on both the positive-, and the negative M branches of the M-H curve. For the more weakly coupled samples, the low-field peak is uniquely associated with PE, and the higher field peak corresponds closely to the magnetization maximum of the bare NbTi. As the PE

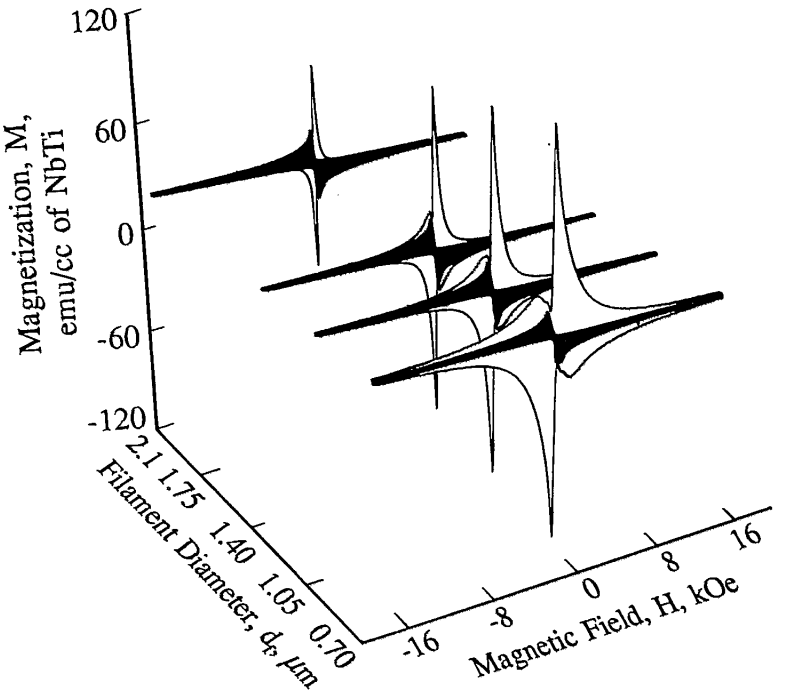

Fig. 4.3.1.1 M-H versus d_f for short samples of Cu matrix material ($\theta_\perp$ orientation, dark is bare)

becomes stronger, however, we can see that this higher field peak is enhanced as well for PE samples (as compared to bare). The question should really be rephrased as: why is there a dip? This will be investigated further in Section 5.3.2.

M-H loops for the CuMn matrix strands are shown in Fig. 4.3.1.2. Here the bare curves appear as dashed lines. They indicate a significantly smaller PE than do the Cu matrix short samples of similar d_f (filament diameter). The CuMn curves show a tilt for the clad (with respect to the bare) samples; this is due to the paramagnetism of the matrix.

In Figs. 4.3.1.3 (Cu) and 4.3.1.4 (CuMn) we note, in these large H_m loops, the

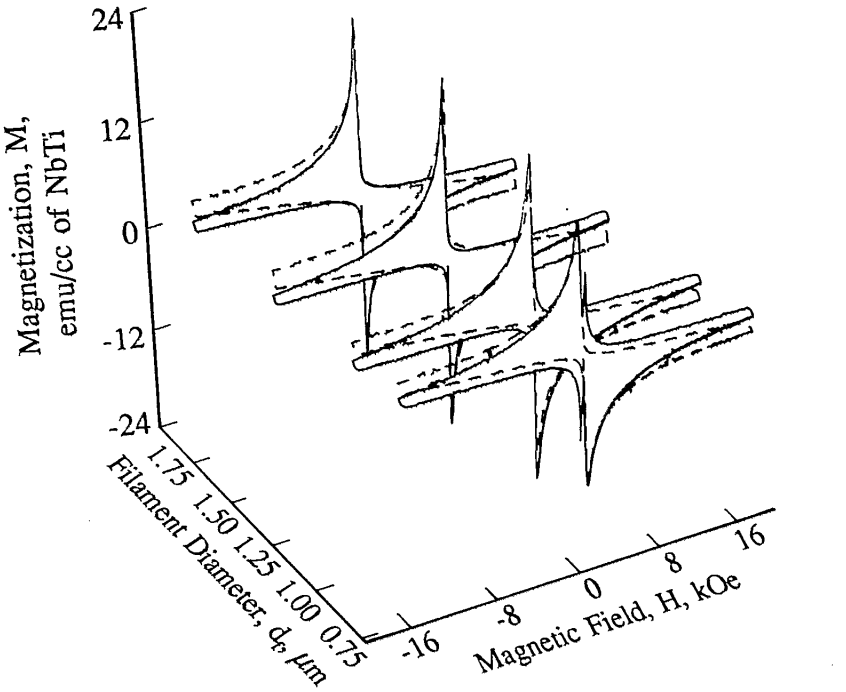

Fig. 4.3.1.2 M-H versus d_f for short samples of CuMn matrix material ($\theta_\perp$ orientation, dashed is bare)

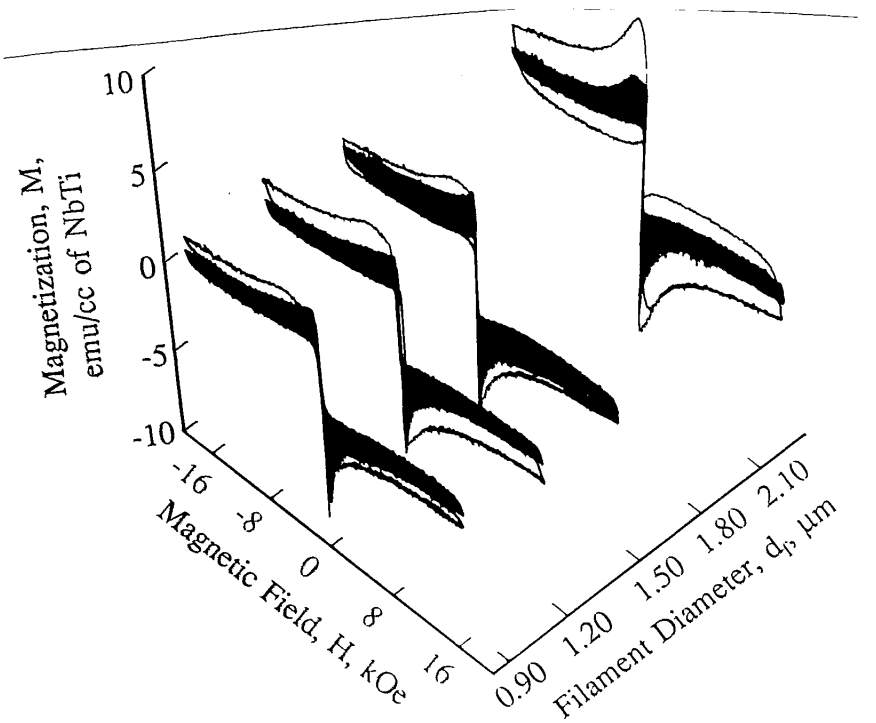

Fig. 4.3.1.3 M-H versus d_f for short samples of Cu matrix material ($\theta_\parallel$ orientation, dark is clad)

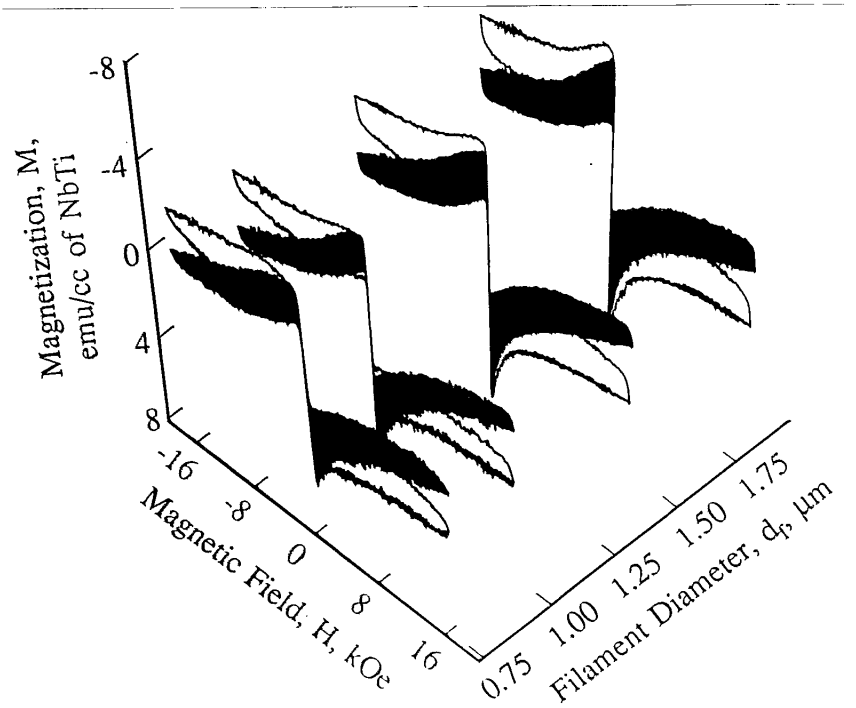

Fig. 4.3.1.4 M-H versus d_f for short samples of CuMn matrix material ($\theta_{\parallel}$ orientation, dark is clad)

complete absence of any measurable PE for the longitudinal field orientation measurements. Noticeable, however, is the discrepancy in magnetization between bare and clad samples (here we have filled in the clad curves). This is due to the existence of surface pinning and/or sheath effects, which are damped in the presence of a metal (conductive) overlayer[4,5,16,17,46,47]. That some small PE does exist for these samples in this field orientation can be most clearly seen in the very low-H_m loops (not shown here), where the NbTi is in its Meissner state.

4.3.2 PE lower critical field, $H_{c1,prox}$

These short samples exhibit critical fields and currents associated with the PE. There seem to be two critical fields just as in type II superconductors, and also a critical current. We have measured the lower critical field, $H_{c1,prox}$, in both the transverse- and longitudinal orientations, in an attempt to distinguish the true critical field (rather than one that is artificially enhanced, dependent on the geometry and the flux pinning properties of the composite).

Experimentally, $H_{c1,prox}$ was determined by numerically subtracting an extrapolation of the very low field slope of the IM curve from the curve itself, and then looking for the deviation of that difference from zero. $H_{c1,prox}$s for both the perpendicular-field and parallel-field orientations are shown in Fig. 4.3.2.1 for the Cu matrix NTCU20 sample as a function of temperature. Both are fit to the equation

$$H_b = \left(\frac{A_1}{d_N}\right)\exp\left(-T\frac{d_N}{A_2}\right)$$

which Mota et al. used to describe their data[24]. In our work we identify Mota's H_b with our $H_{c1,prox}$. Mota's data was for relatively thick NbTi monofilaments (tens of micrometers) with a Cu overlayer. In Mota's work, d_N was metal overlayer thickness, but here we identify it with one half of the interfilament separation. The dotted curve represents a fit to the data using their values of A_1 (viz., 19 Oe μm) and A_2 (viz., 0.6 K μm), and letting d_N vary. The best fit occurs for d_N = 0.226 μm, which is very reasonable, since $d_N \approx s/2$, and s/d = 0.2 (where s is the interfilament spacing for strand

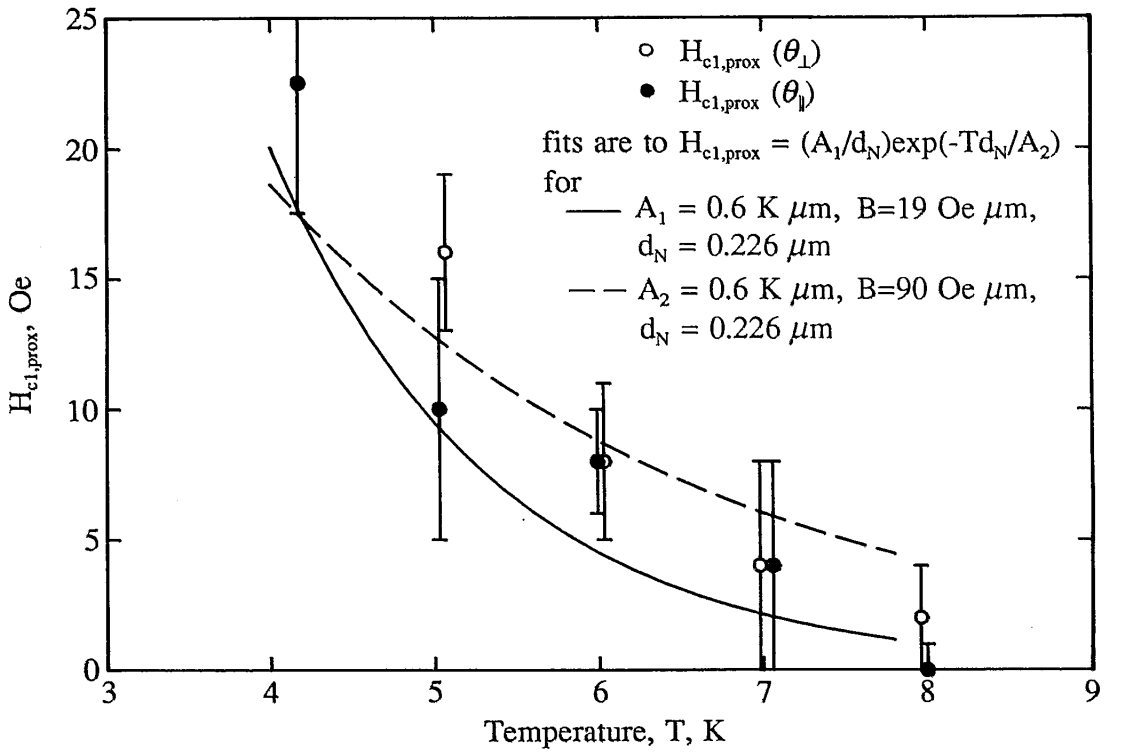

Fig. 4.3.2.1 $H_{c1,prox}$ versus T, measured in $\theta_\perp$ and $\theta_\parallel$ orientations for the short sample NTCU20-SSC

NTCU20). The solid curve represents a fit with all three parameters free which gives A_1 = 90 Oe μm, A_2 = 0.3 K μm, and d_N = 0.226 μm. This is not as good, but nevertheless reasonable, since our geometry is significantly different than that of the monofilament case.

Ordinarily, it would be expected that the $H_{c1,prox}$ values for the perpendicular orientation would be half those of the parallel orientation (because of demagnetization), but our data show them to be nearly equal. However, since at these fields the NbTi filaments are still in the Meissner state, first flux entry will occur at the sample ends.

Here the demagnetization factor would be difficult to calculate in detail, but it clearly must be nearly 1.

Fig. 4.3.2.2 shows $H_{c1,prox}$ as a function of d_f for the Cu samples. Here again the data has been fit to the above expression for H_b, but with less success. In Fig. 4.3.2.2 are plotted the results for both the field-parallel and the field-perpendicular orientations. We can see that there is some scatter, but they both fall below the expected result, which we have calculated to zeroth order by setting $d_N = s/2$, and using the values from Mota et al. for A_1 and A_2 (this curve is shown solid). These data do not fit the equation well, but

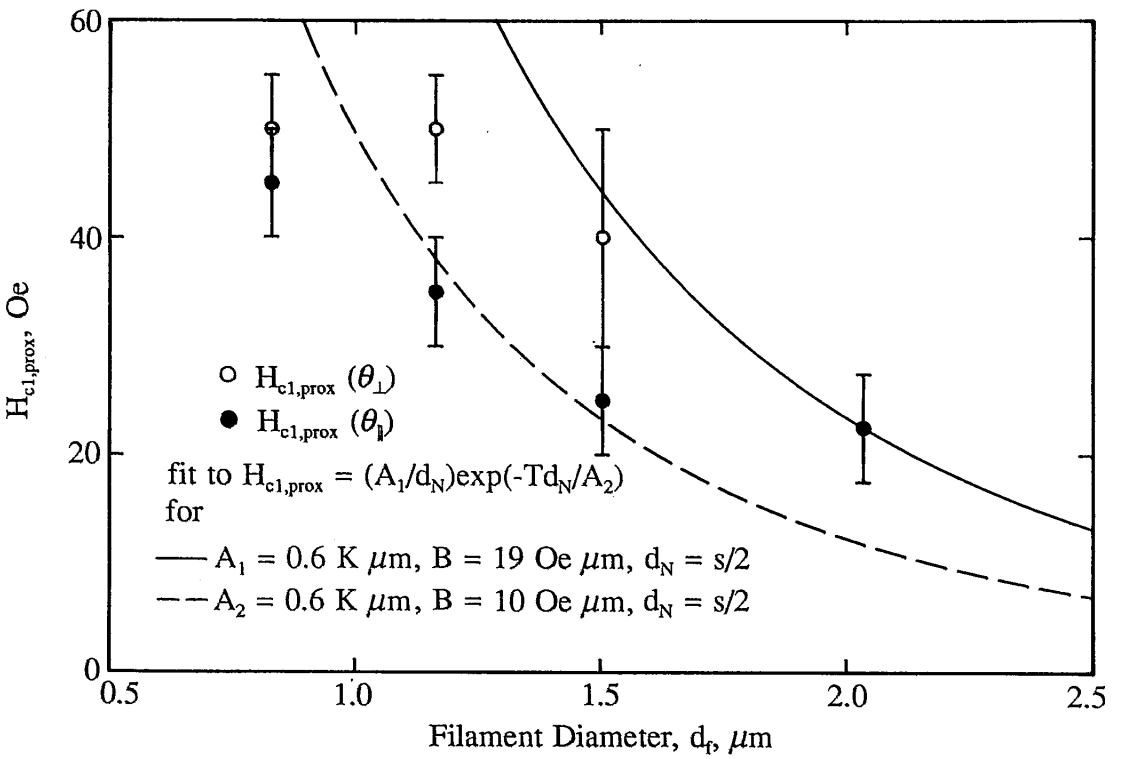

Fig. 4.3.2.2 $H_{c1,prox}$ versus d_f, measured in $\theta_\perp$ and $\theta_\parallel$ orientations for the Cu matrix short samples (T = 4.2 K)

a forced fit is shown for A_1 = 0.6 K μm, A_2 = 10 Oe μm, and d_N = s/2, which does seem to fit the data better. The $H_{c1,\ prox}$s for the CuMn samples were too small to be noticeable, with the exception of NTCM07-SSC, which had a critical field of about 3 Oe.

4.3.3 PE critical current, J_{cp}

In order to measure the J_{cp} of the proximity effect, we decided to look at the low-H_m, longitudinal M-H loops of these samples (field along the filament axis of symmetry), because J_{cp} should be easiest to extract from these measurements ($J_{c\theta}$ should be the only current flowing, and it should be equal to J_{cp}). A Bean model approximation was used, giving the expression $H_{p0,proxL} = (4\pi/10)J_{cp}R$, in our case, where R = strand radius. $H_{p0,proxL}$ is used since the distance over which we develop the flux gradient is just R, so that this field is less than $H_{c1,NbTi}$, as is necessary from the definition of $H_{p0,proxL}$ (cf. Sec. 5.1.1). J_{cp} versus temperature data was taken for sample NTCU20 (shown in Fig. 4.3.3.1) as well as J_{cp} versus d_f for all four the Cu short samples at T = 4.2 K (shown in Fig. 4.3.3.2). Both sets of data were fit simultaneously to the equation

$$J_{cp} = C_1 \exp\left(-\frac{Td_N}{C_2}\right)$$

These fits are shown along with the data in Figs. 4.3.3.1 and 4.3.3.2 where the parameters used were C_1 = 19700 A/cm^2, and C_2 = 0.25 μm K. Data fits were attempted for models

assuming an exponential dependence of J_{cp} on field, but the results were disappointing. This is probably because the PE matrix geometry is not simple as we have assumed -- it is in fact a multiply connected region. However, these values of J_{cp} should provide an interesting comparison to those J_{cp}s garnered from transverse high field measurements.

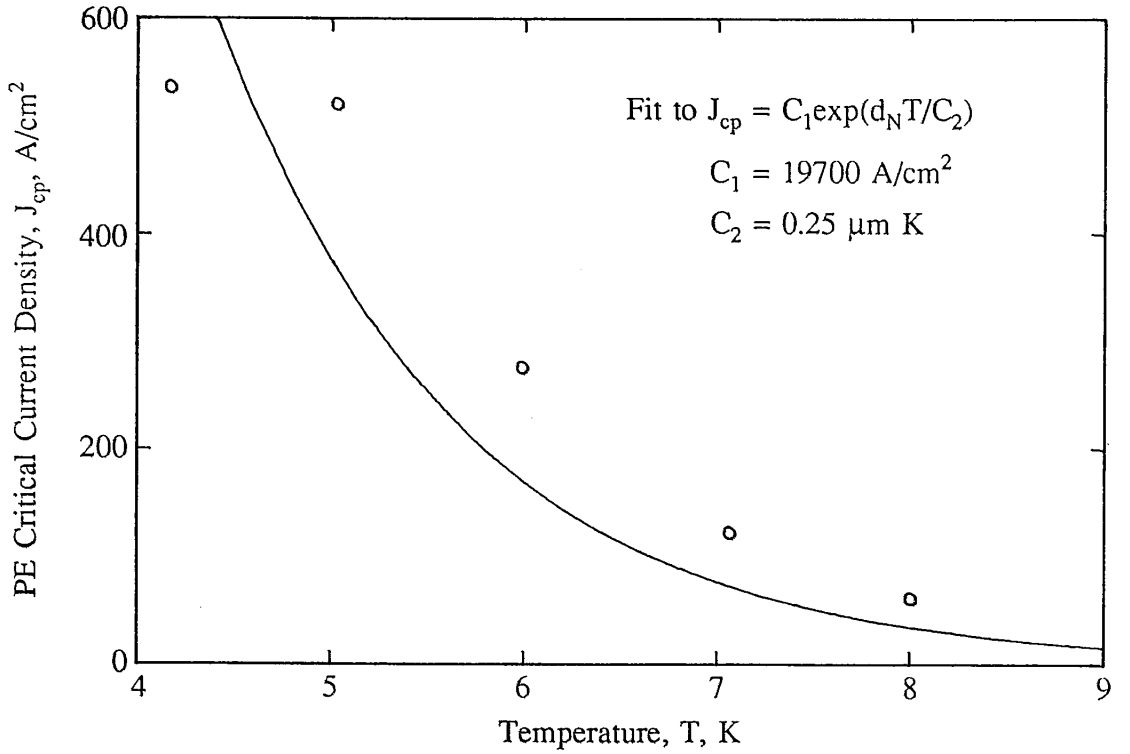

Fig. 4.3.3.1 PE critical current density (J_{cp}) versus T for the short sample NTCU20-SSC

4.4 M-H versus H_m

M-H loops were taken as a function of H_m for several different samples. The results for the Cu matrix are shown in Figs. 4.4.1-2 (NTCU07-SS), 4.4.3-4 (CNTCU07-128), 4.4.5-6 (CNTCU07-001). For these loops there are two common features, viz: (1) for large H_m, all curves follow an envelope for fields sufficiently away from field reversals, (2) for lower H_m, the curves blossom outward with increasing H_m. Of course just such a thing occurs for ordinary superconductors, with the H_m which separates these

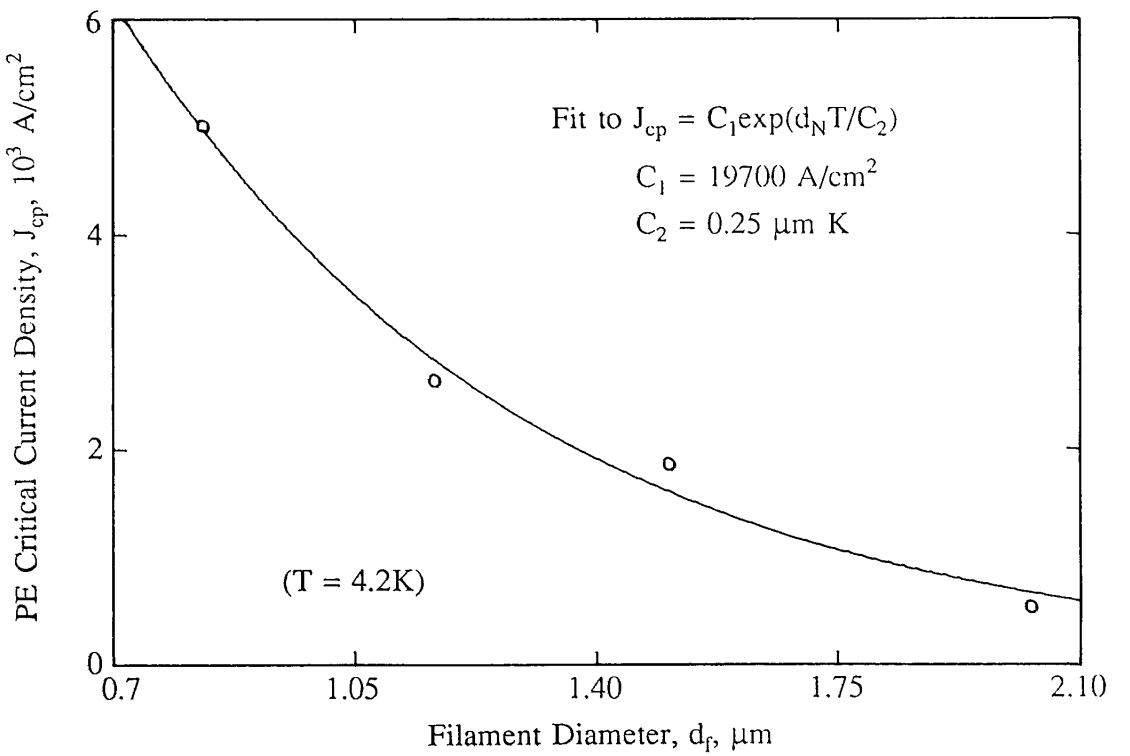

Fig. 4.3.3.2 PE critical current density (J_{cp}) versus d_f for the Cu matrix short samples (T = 4.2 K)

two regimes just equal to the penetration field. We pointed out, in an earlier paper, that the H_m defining the two loss regimes for proximity effected materials seemed to be just twice the penetration field of our NbTi filaments[44]. This was true because $H_{p,prox} \approx H_{p,NbTi}$ in these samples, because of their short length (a lower penetration field, $H_{p,proxL}$ also exists, see Sec. 5.1.1). In general, the appropriate penetration field from which to determine the "crossover" field sweep is determined by one of two PE penetration depths (cf. Sec. 5.2).

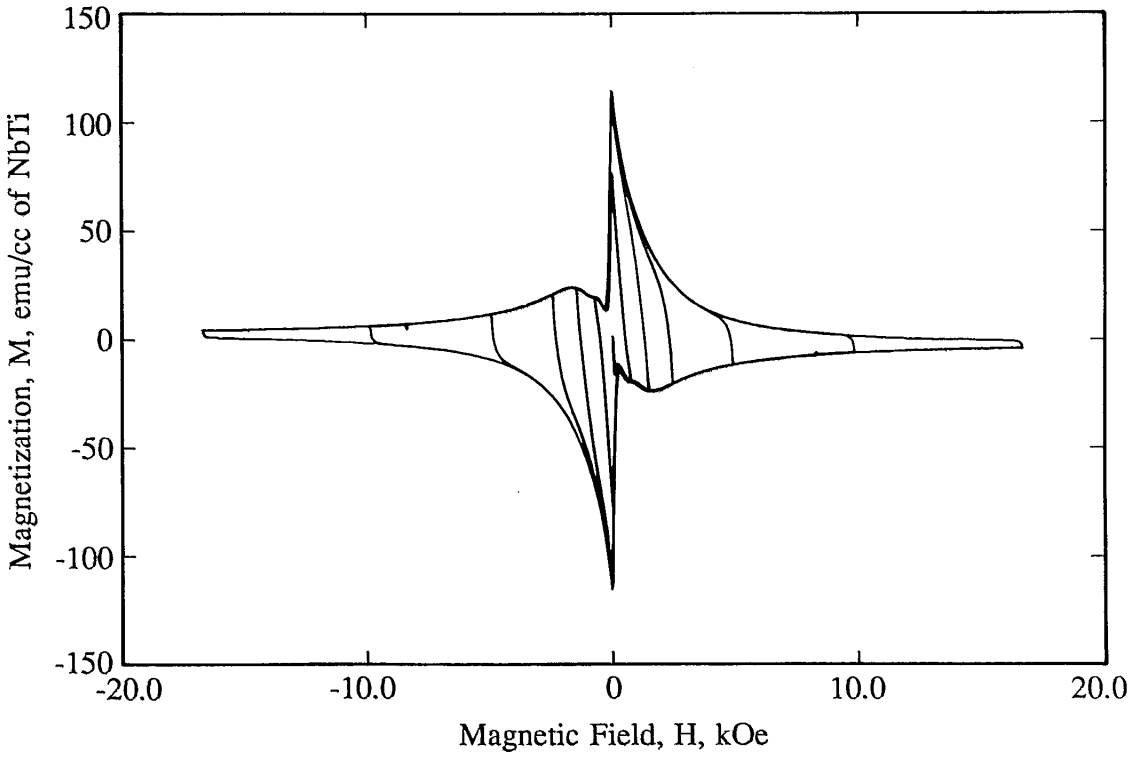

Fig. 4.4.1 M-H versus H_m for NTCU07-SSC, for large H_m range

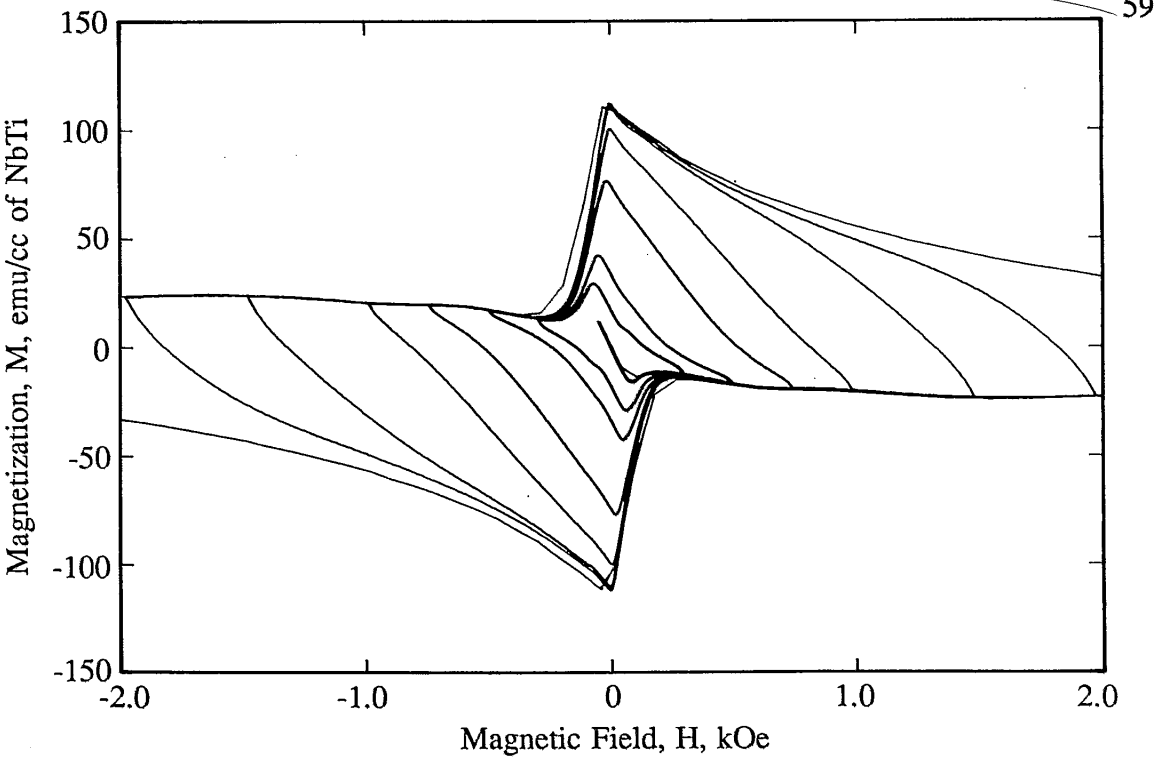

Fig. 4.4.2 M-H versus H_m for NTCU07-SSC, for small H_m range

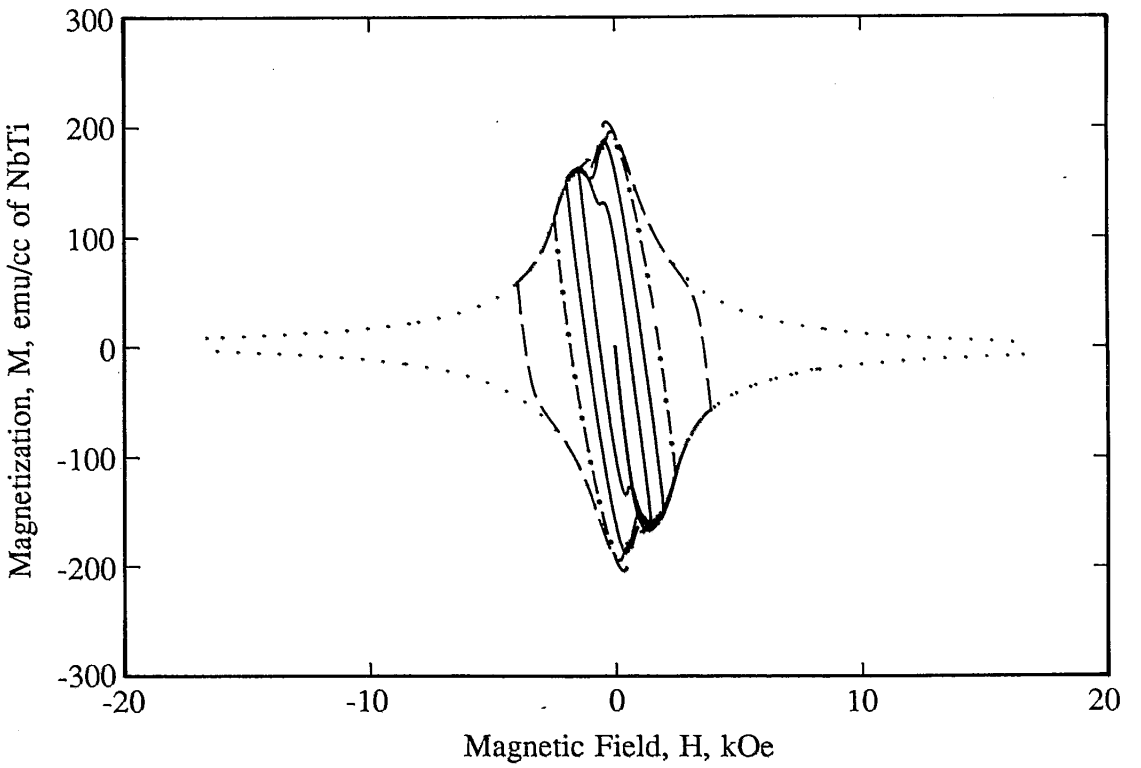

Fig. 4.4.3 M-H versus H_m for CNTCU07-128, for large H_m range (L_p = 1.111 cm)

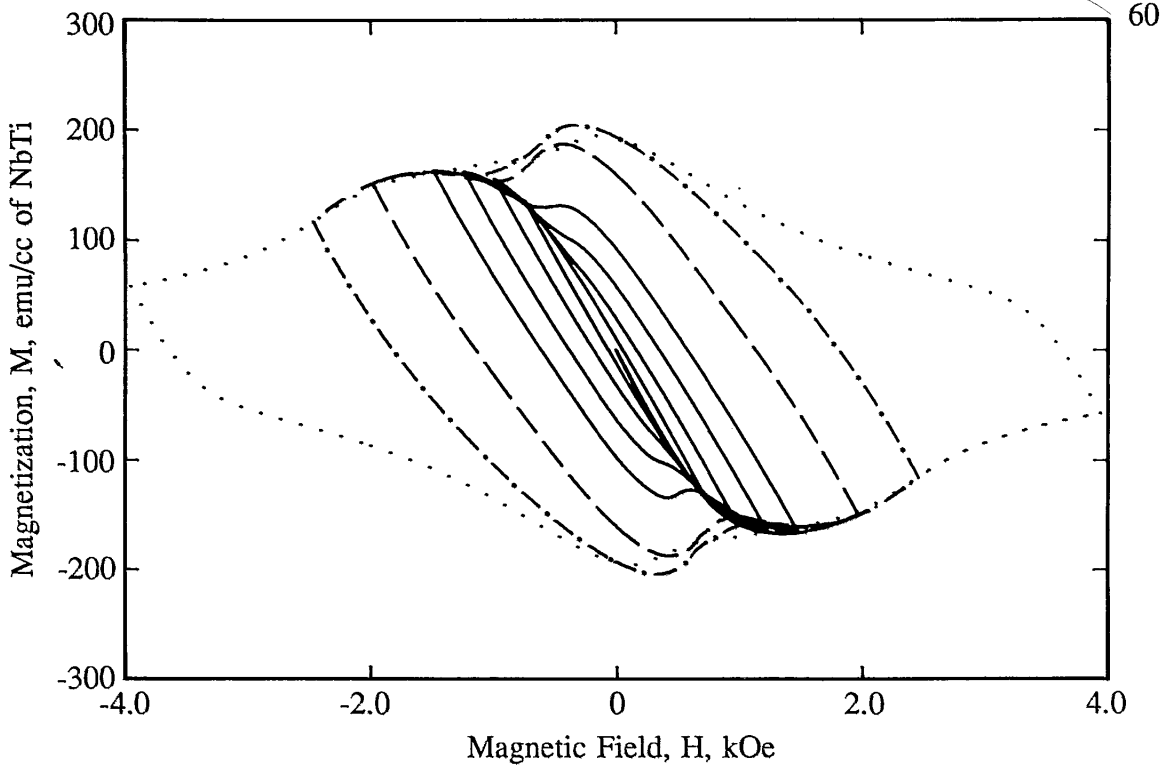

Fig. 4.4.4 M-H versus H_m for CNTCU07-128, for small H_m range (L_p = 1.111 cm)

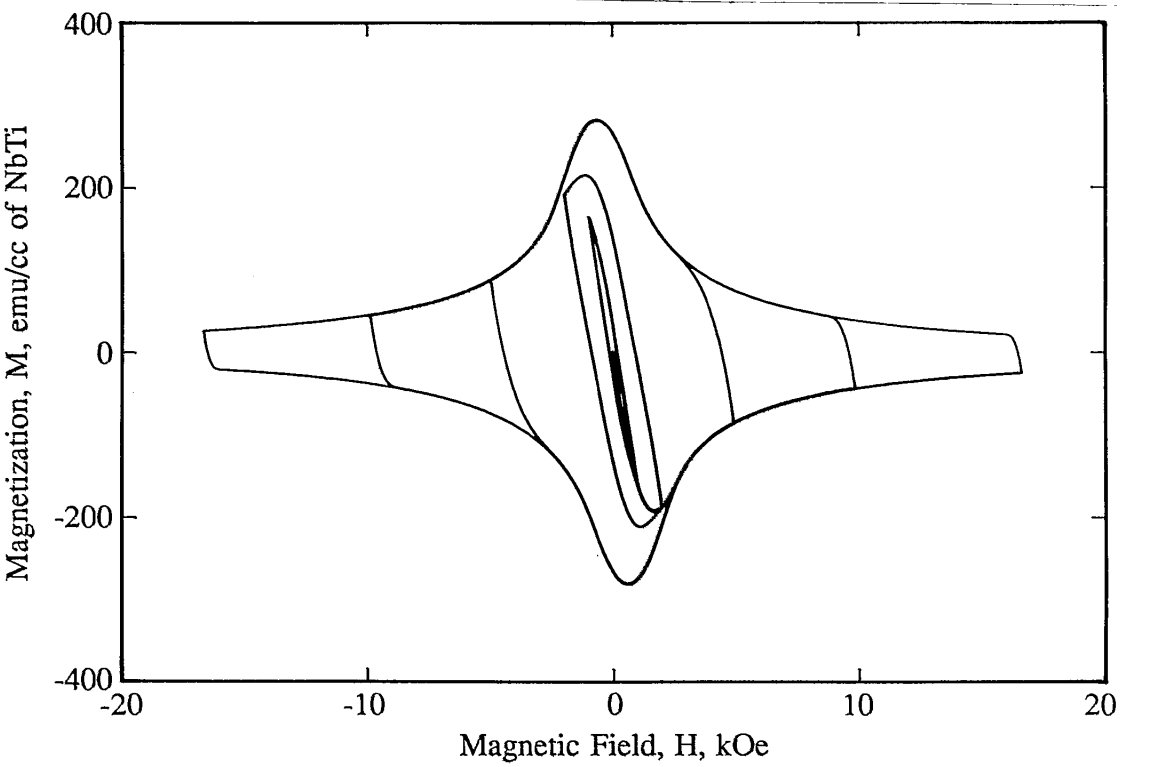

Fig. 4.4.5 M-H versus H_m for CNTCU07-1, for large H_m range (L_p = 142.24 cm)

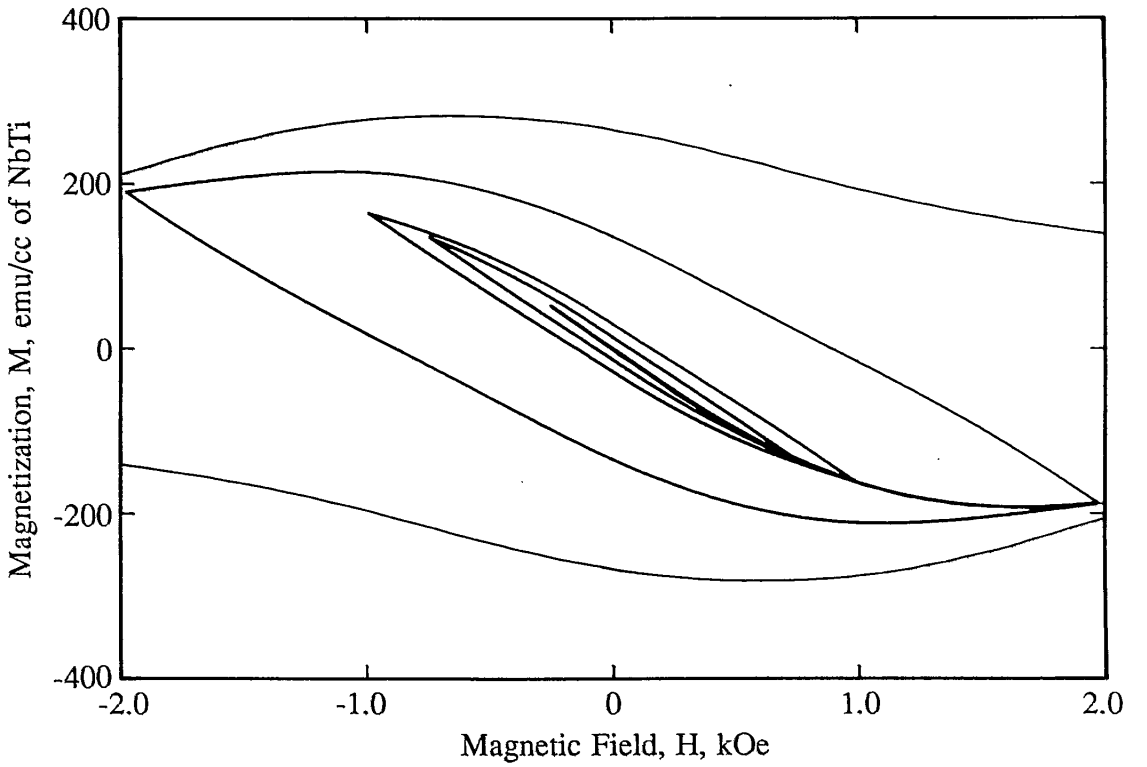

Fig. 4.4.6 M-H versus H_m for CNTCU07-1, for small H_m range (L_p = 142.24 cm)

4.5 Angular Behavior of Large H_m M-H for the Short Samples

Large H_m M-H loops were taken as a function of the angle of the field with respect to the filament axis on two short cylindrical samples (NTCU20 clad and bare). Here $\theta_s = 90°$ indicates that the field is transverse to the filaments. These loops had 1000 points and were taken via a continuous H sweep, with a dH/dt = 141.7 Oe/s. We know from previous experiments that these samples are too short to support significant eddy currents. The M-H loops are shown in Fig. 4.5.1, where both clad and bare sample

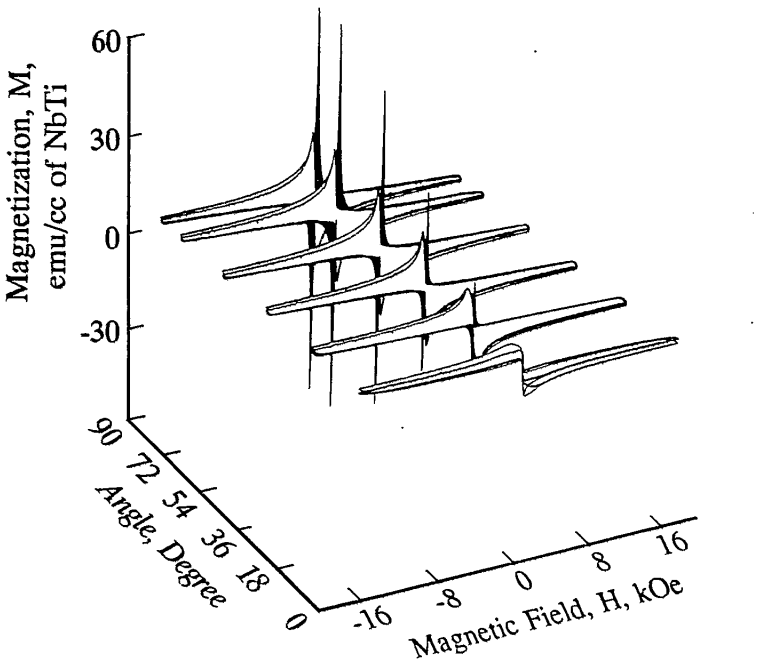

Fig. 4.5.1 M-H versus θ_s for Cu matrix short sample NTCU20-SSC

results are plotted together. Where the bare results exceed the clad (as in $\theta_s = 0°$ case, because of surface currents[46,47]) we have not filled in the region. Where clad results exceed bare (via PE) we have filled in that region. We can see the gradual evolution of a sharp proximity peak as the angle goes from 0° to 90°. This is due to the existence of a larger J_c along the z-axis of the strand (J_{cz}) than for J_c about the strand ($J_{c\theta}$) (cf. Sec. 5.1.2).

4.6 Loss versus L_p, L, and H_m

This section looks at loss versus L_p, L, and H_m. The Q_T versus H_m results are presented in Figs. 4.6.1 and 4.6.2 for several Cu VP coil samples of different L_p and d_fs, as well as that for the bare and clad short samples of the same filament diameters. These Q_T values were calculated from M-H loops which were 10 minutes in duration, and had in some cases significant eddy currents.

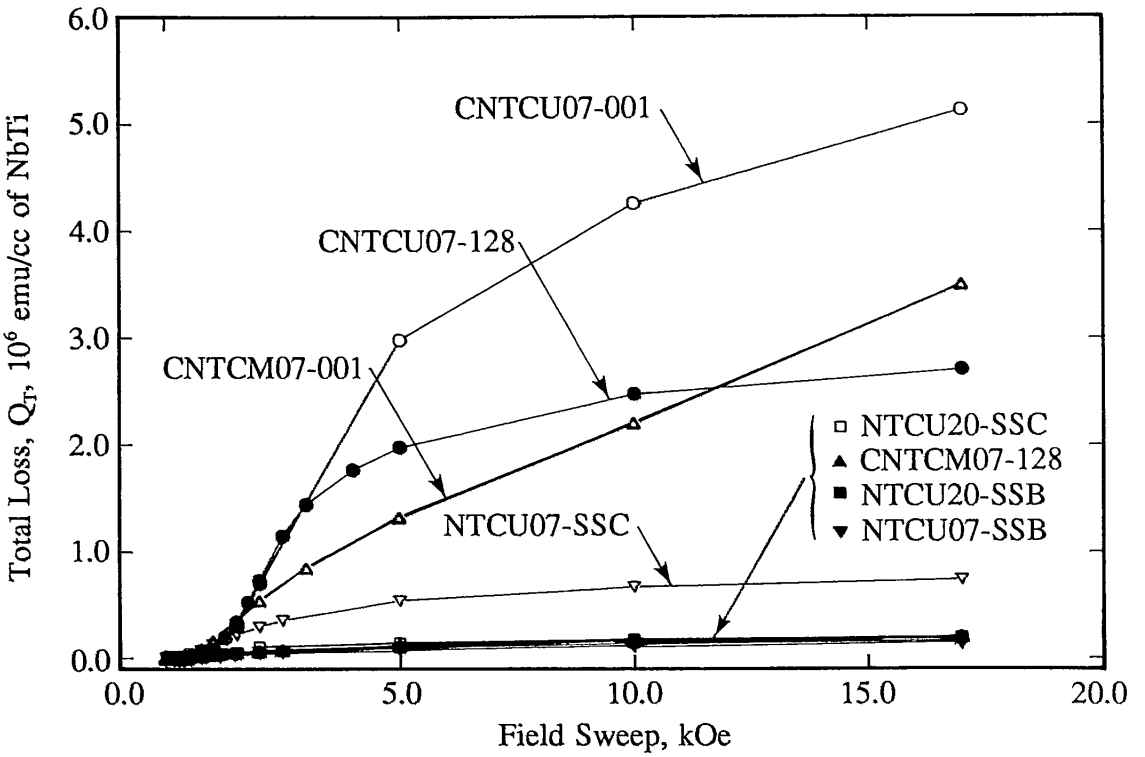

Fig. 4.6.1 Total loss (Q_T) versus H_m for several samples, large H_m range

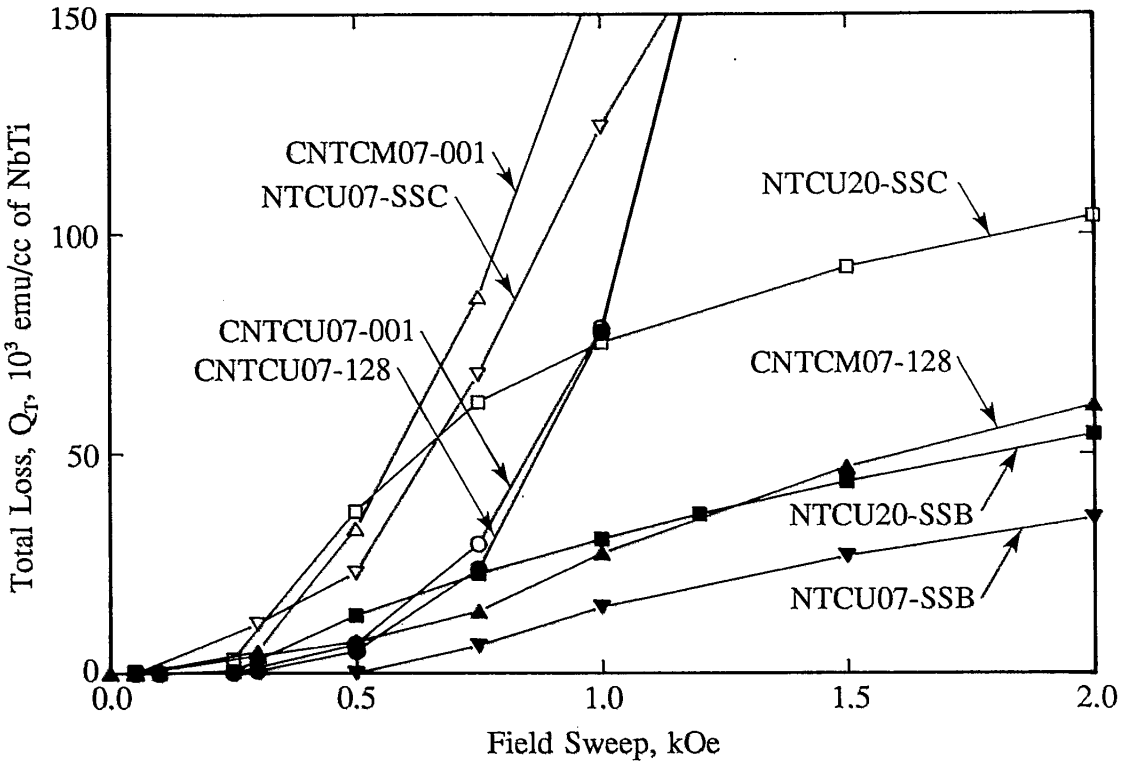

Fig. 4.6.2 Total loss (Q_T) versus H_m for several samples, small H_m range

Figs. 4.6.3 and 4.6.4 show Q_S versus L_p for all of the VP coil samples (for H_m = 17 kOe). These results closely parallel the ΔM results shown earlier. The more weakly coupled strands (CuMn matrix) have lower losses and a more linear relationship between the losses and L_p. The more strongly coupled materials have higher losses and show a saturation with increasing L_p. We have included the losses from the bare short sample as the zero L_p point. Fig. 4.6.5 shows Q_S versus L for the VL samples. The results here

are similar to those above, with a linear dependence of Q_S on L for weakly coupled samples, and a saturation with L for more strongly coupled ones. Here also the bare short samples are included as the zero L samples.

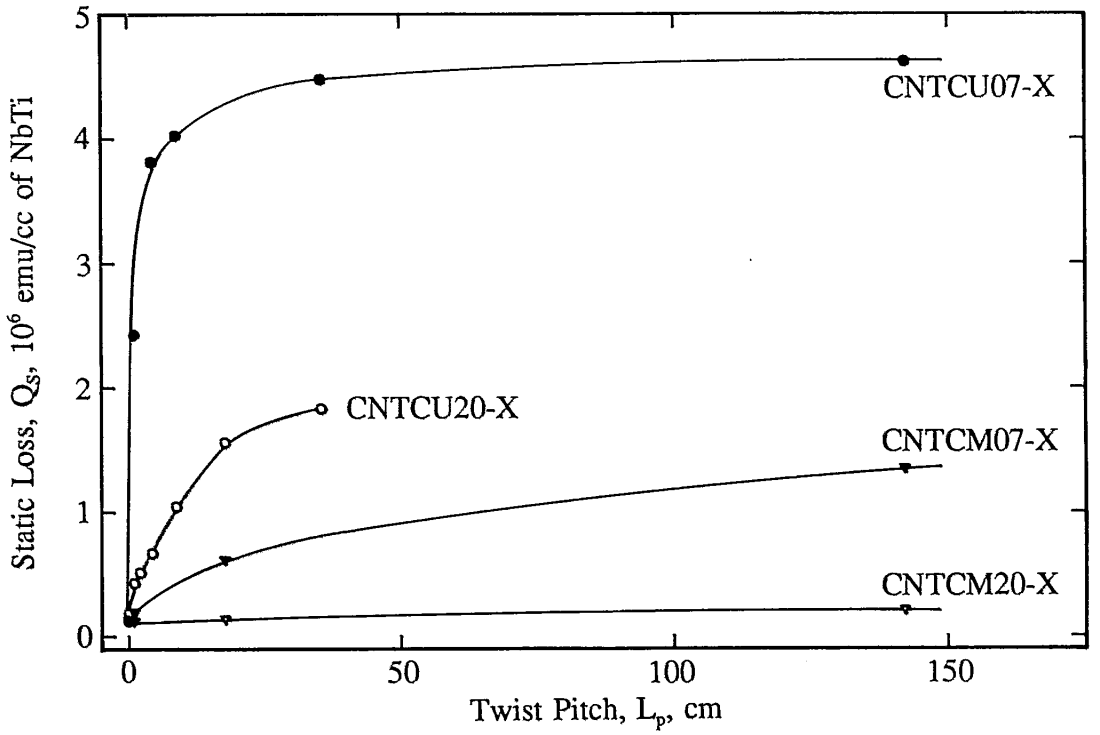

Fig. 4.6.3 Static loss (Q_S) versus L_p for the VP coils, large L_p range (H_m = 17 kOe)

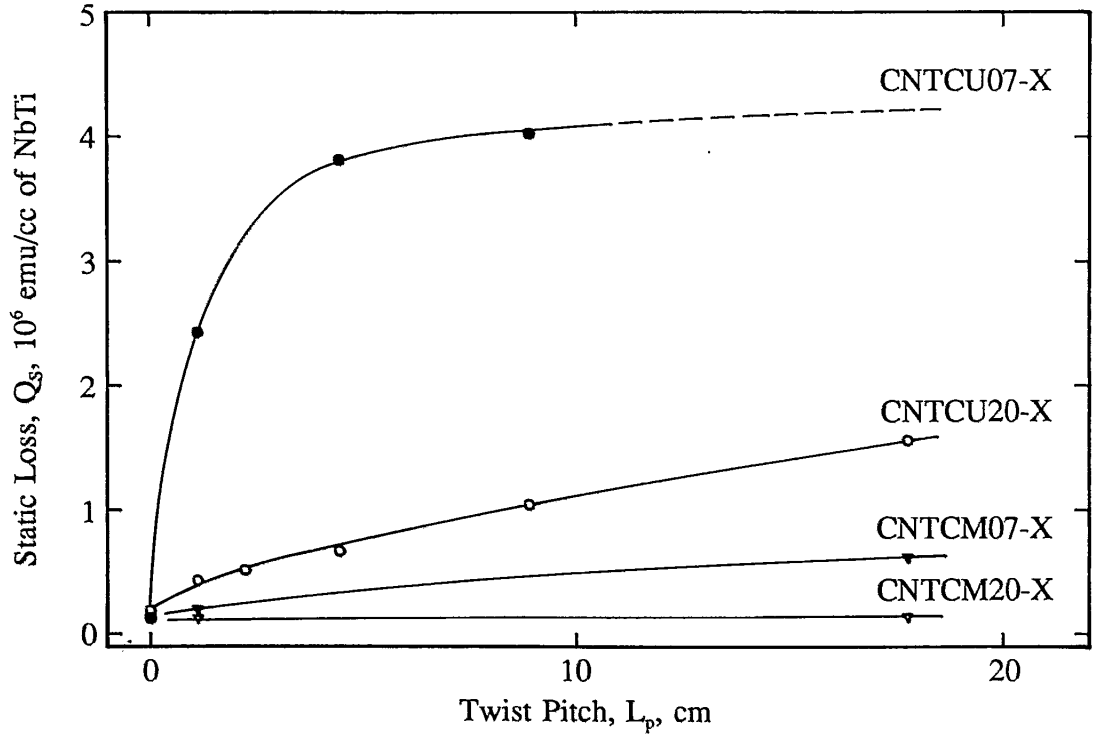

Fig. 4.6.4 Static loss (Q_S) versus L_p for the VP coils, small L_p range (H_m = 17 kOe)

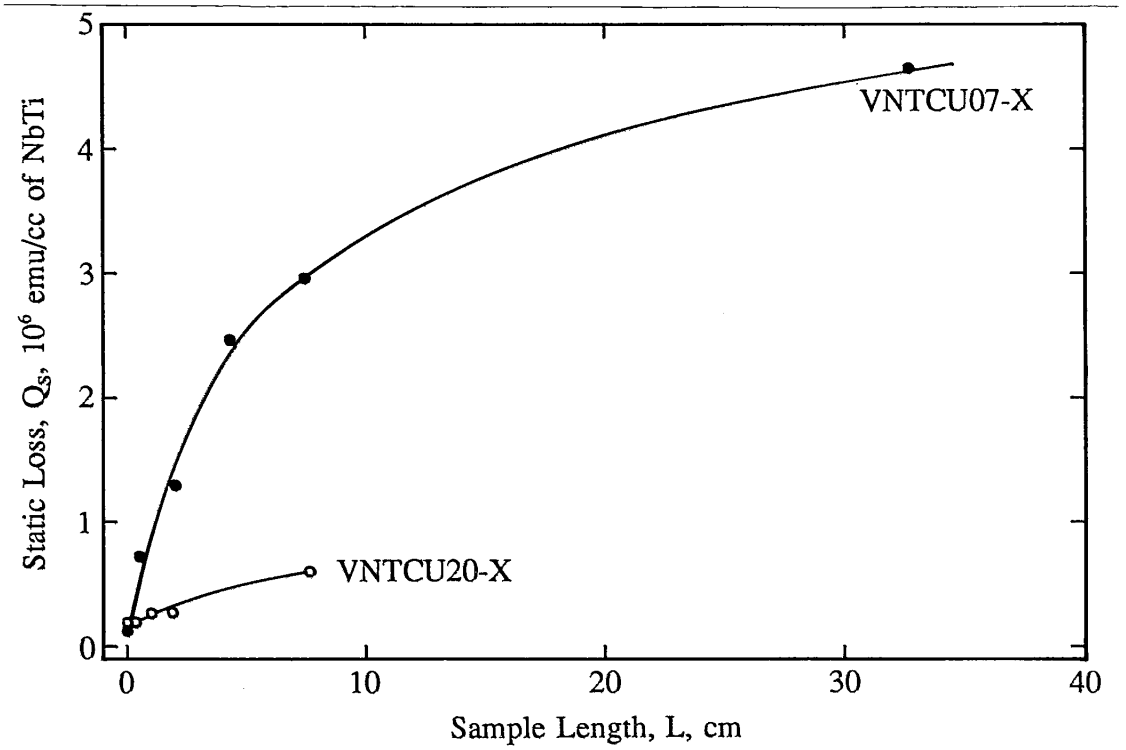

Fig. 4.6.5 Static loss (Q_S) versus L for the VL coils (H_m = 17 kOe)

CHAPTER 5: INTERPRETATION OF RESULTS: PHENOMENOLOGICAL THEORY

5.1 Critical Currents, Magnetization, and Penetration Fields in Multifilamentary Superconductive Composites

5.1.1 The Extended Critical State Model

In order to describe proximity-effected multifilamentary superconductive composites, the critical state model must be extended. This is because the proximity-effected strand is a macroscopically inhomogeneous composite material. It is aptly described as an intertwining of two materials with different critical fields and currents to form a honeycomb pattern. It order to clarify some ideas about magnetization and loss, consider the case of a number of semi-infinite layers of superconductive material, as shown in Fig. 5.1.1.1. We let these layers alternate with high (NbTi) and low (proximity-effected matrix) J_c, and apply a magnetic field parallel to these layers. If the PE is weak the field profiles are as indicated by the solid line. This is just the profile that would be found for an insulating matrix, or a metallic matrix in the limit of dH/dt = 0. For strongly PE coupled materials the profile is that shown by the dashed line. This is similar to the profile that would be generated for the case of a non-superconducting metallic matrix where significant eddy currents are present (dH/dt is large). Generally, a gradient

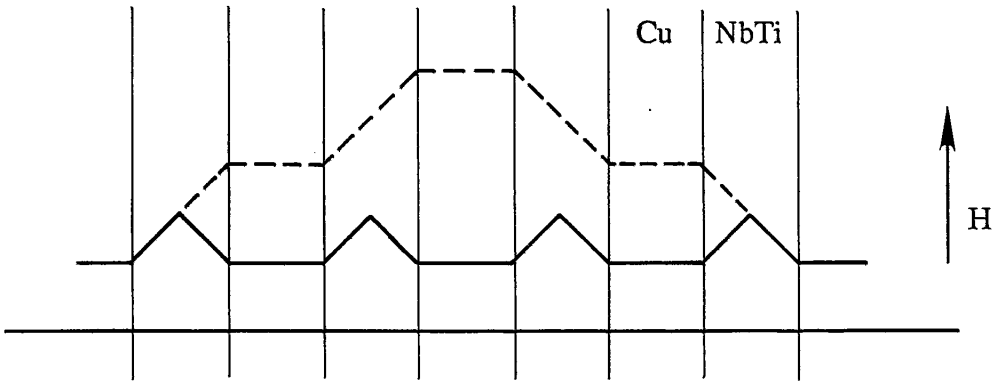

Fig. 5.1.1.1 Flux profiles for a multilayer composite consisting of alternating high and low J_c layers

in B will form across the proximity-effected copper, but here we consider that gradient to be negligibly small.

Traditionally in the description of eddy currents the magnetization has been separated in the following way (where we ignore PE for the moment):

$$M_T \{L_p, \frac{dH}{dt}\} = M_h + M_E \{L_p, \frac{dH}{dt}\} \qquad \text{Eq. 5.1.1.1}$$

Here M_T is the total loss, M_E is the eddy current loss, M_h is the NbTi loss, and the brackets denote functional dependence. Note, however, that M_E defined in this way has a contribution which is due to the difference between B and H in the matrix, and a part which is due to the shielding of the inner NbTi filaments.

In a similar way, we can now include the PE and write

$$M_T \{L_p, \frac{dH}{dt}\} = M_h + M_E \{L_p, \frac{dH}{dt}\} + M_{PE} \{L_p\} \qquad \text{Eq. 5.1.1.2}$$

as have Harada et al.[40], where M_{PE} is the PE magnetization, and $M_{PE} + M_h = M_S$ (the static magnetization). As above, M_{PE} is partly due to the difference in B and H in the matrix, but also to the shielding of the filaments. Note that we have adopted the view of B-H relations which says that H, the applied field, is constant throughout the superconductor. In this view all gradients are in B, and all magnetization currents contribute directly to B (rather than H)[48].

Since

$$Q = \int M \, dH$$

it follows that

$$Q_T \{L_p, \frac{dH}{dt}\} = Q_S \{L_p\} + Q_E \{L_p, \frac{dH}{dt}\} \qquad \text{Eq. 5.1.1.3}$$

as well as

$$Q_S \{L_p\} = Q_h + Q_{PE} \{L_p\} \qquad \text{Eq. 5.1.1.4}$$

where the various components of Q are defined analogously to those of M, above. We can see that Q_{PE}, as well as M_{PE}, will have a component due to the shielding of the filaments. It is for this reason that the Q_{PE} seen in the small H_m regime for the short samples is so much smaller than the Q_{PE} in the large H_m regime[44].

We can see from above that PEs have great topological similarity to eddy current effects. If we now consider the case of a multifilamentary composite in a transverse field, the fields and their gradients will become more complicated. If such additional complications as L_p and L are considered, the picture becomes quite involved. However, this picture can be simplified enormously by considering the composite to be an

anisotropic continuum. In this point of view (used by Carr to describe eddy currents, and implied in his PE work[38]) the currents in a given coordinate direction are average properties, but they may be different in the various directions. This is the perspective used in the rest of Chapter 5. In Sections 5.1.2-5.1.4 critical currents, ΔM_{PE}, and $H_{p,prox}$ are determined for long, twisted, multifilamentary strands. In Section 5.2 the additional complication of sample length is considered. Throughout Chapter 5 $H_{c1,NbTi}$ and $H_{c1,prox}$ are set to zero.

While in general this approach is quite successful, it is useful to point out several situations in which it breaks down. This failure occurs primarily because of the influence of traditional reversible magnetization effects. If $H_{c1,NbTi}$ was the same as $H_{c1,prox}$ reversible magnetization effects could be accounted for by simply by "tacking on" a H_{c1} related field jump (possibly field dependent) to the surface of the strand. However, when $H_{c1,NbTi} > H_{c1,prox}$ three things occur: (1) there are two H_{c1}s, one denoting the initial flux penetration into the matrix, one initial penetration into the filament, (2) the loss when $H_{c1,prox} < H_m < H_{c1,NbTi}$ is due to the difference in B and H in the matrix alone, as mentioned above, and (3) $H_{p,prox}$ may, depending on sample length, have two values. While effects (1) and (2) are clear enough, the penetration field effects demand further consideration.

Let us take $H_{c1,prox} << H_{c1,NbTi}$ and describe the length over which flux gradients form in the proximity-effected matrix by the parameter L_g. Then there are two cases (illustrated in Fig. 5.1.1.2): (1) $J_{cp} \times L_g > H_{c1,NbTi}$: only one penetration field exists, and for $J_{cp}L_g >> J_{cfil}\,\lambda R$ it is similar conceptually to the value calculated in Section 5.1.4,

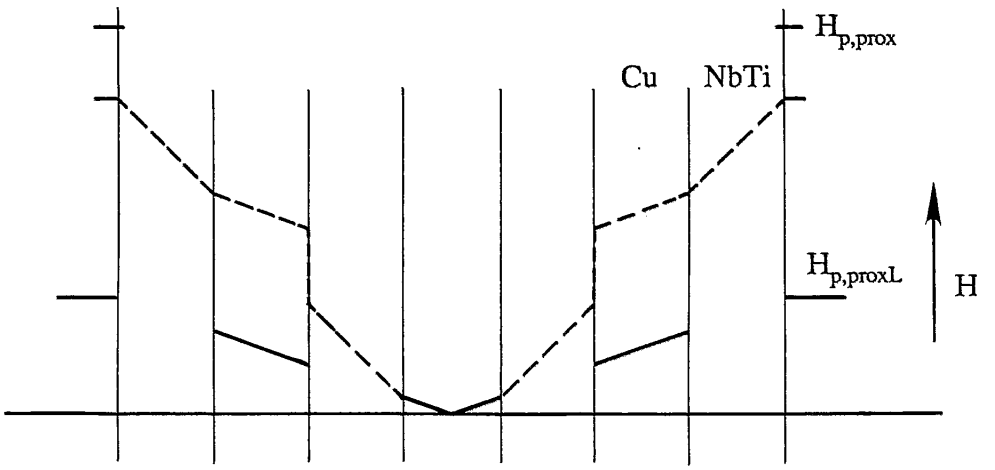

Fig. 5.1.1.2 Flux profiles for a multilayer composite when $H_{c1,NbTi} \neq 0$

below, where the assumption was made that there were no reversible magnetization effects. The flux profile for this case is shown as a dashed line in Fig. 5.1.1.2. (2) J_{cp} x $L_g < H_{c1,NbTi}$: Two penetration fields exist. The larger one is analogous to case 1, above, where flux is present in both the matrix and the filaments. A second, lower one appears, due solely to the gradients in the matrix (the flux gradient is shown here as the solid line). This is the $H_{p,proxL}$ used for the calculation of J_{cp} in Section 4.3.3. We will denote the higher value simply $H_{p,prox}$.

5.1.2 Critical Currents in Multifilamentary Composites

Consider a cylindrical, multifilamentary strand with the field applied perpendicular to the cylindrical axis. We take this strand to be fully filamentary, with a constant filament spacing. We will also ignore the reversible magnetization effects (i.e. $H_{c1,prox} = H_{c1,NbTi} = 0$). Below, in Fig. 5.1.2.1, we see a schematic representation of this strand and the currents it sustains.

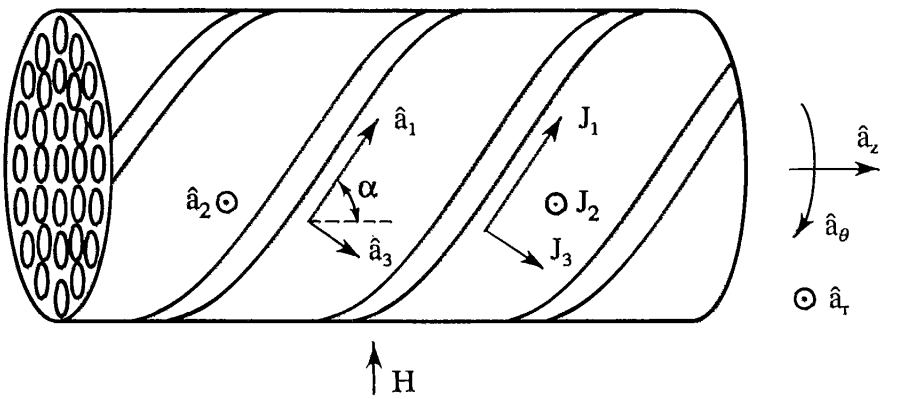

Fig. 5.1.2.1 Helically twisted strand, showing critical currents and unit vector definitions

When an H-field is applied perpendicular to the z-axis of the conductor, shielding currents (or trapping currents, depending upon field history) are induced to flow along the z-axis, just as for a monolithic conductor. Following Carr[38], we model this system as an anisotropic continuum. Carr has assumed the following critical current densities in his model:

$$J_{c1} = \lambda J_{cfil}$$
$$J_{c2} = 0 \qquad \text{Eq. 5.1.2.1}$$
$$J_{c3} = J_{cp}$$

Here λ is the NbTi filling factor. Carr originally created this model for in-situ conductors, and had a multiplicative factor of two in the J_{c1} equation. $J_{c3} = J_{cp}$ since the current in this direction must flow through filamentary regions and matrix regions in series. J_{c2} was set to zero in Carr's original model because of the morphology of his

filaments, but this radial current turns out only to be important in end effects (cf. Sec 5.2), at least to a first approximation (cf. App. D). It is shown in App. C that the critical current in the z-direction is given by

$$\text{(a)} \qquad J_{cz} = J_{cfil}\lambda\left[1 + \left(\frac{2\pi\rho}{L_p}\right)^2\right]^{1/2} \qquad \alpha < \alpha_c$$

$$\text{(b)} \qquad J_{cz} = J_{cp}\left(\frac{L_p}{2\pi\rho}\right)\left[1 + \left(\frac{2\pi\rho}{L_p}\right)^2\right]^{1/2} \qquad \alpha > \alpha_c$$

Eq. 5.1.2.2

where ρ is the radial distance in the strand,

$$\cos\alpha = \frac{L_p/2\pi\rho}{(1 + (L_p/2\pi\rho)^2)^{1/2}}, \quad \text{and}$$

$$\cos\alpha_C = \frac{\lambda J_{cfil}/J_{cp}}{(1 + (\lambda J_{cfil}/J_{cp})^2)^{1/2}}.$$

Eq. 5.1.2.3

Here α is the angle between the filament and the z-axis (see Fig. 5.1.2.1) and α_C (the critical angle) is the parameter which determines which of the 5.1.2.2 equations is valid. These equations are determined from the requirements of the critical state model that J is either $\pm J_c$ or zero, so that only one of the equations above can be satisfied for a

particular set of L_p and ρ values. Since the critical current in a given direction can not be exceeded, the lower of the two J_cs in a particular region is the limiting one, and current in the other direction is assumed to be a critical current, but to flow through a restricted region (Carr uses another approach[38]). This is illustrated in Fig. 5.1.2.2 where we have plotted Eqs. 5.1.2.2 (a) and 5.1.2.2 (b) (normalized to λJ_{cfil}) as a function of the dimensionless parameter β_ρ ($\equiv L_p/2\pi\rho$). We can see that at there is indeed a crossover in these equations at the point where $\beta_\rho = \beta_C$ ($\equiv \lambda J_{cfil}/J_{cp}$). We describe the regions with

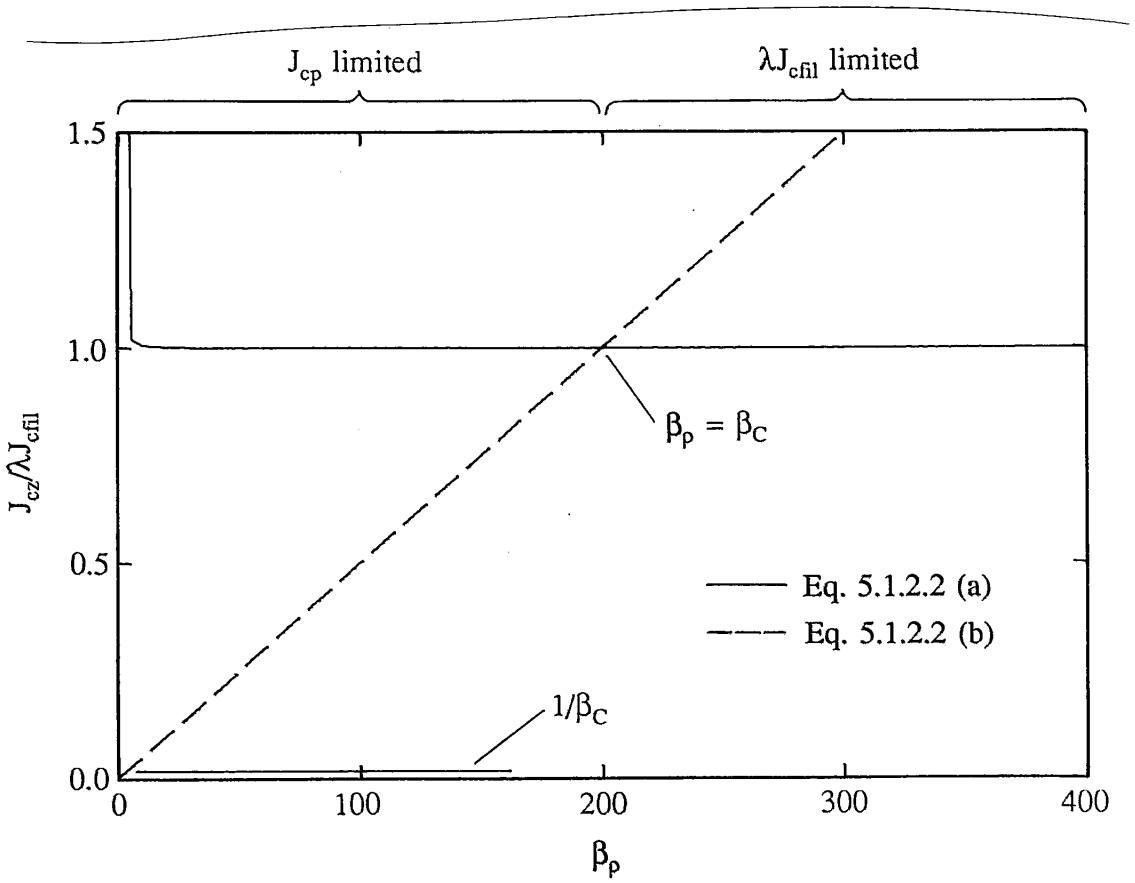

Fig. 5.1.2.2 Calculated J_{cz} versus β_ρ from Eqs. 5.1.2.2 (a) and 5.1.2.2 (b)

$\beta_\rho < \beta_C$ as J_{cp} limited, and the regions with $\beta_\rho > \beta_C$ we call λJ_{cfil} limited. This crossover occurs, for a given ρ, at a certain critical L_p given by

$$L_{pc} = \frac{2\pi\rho\lambda J_{cfil}}{J_{cp}}$$

Conversely, for a given L_p, the crossover occurs at a given critical radius

$$\rho_c = \frac{J_{cp}L_p}{2\pi\lambda J_{cfil}}$$

Both of these parameters come from Carr's original work[38] (cf. App. C).

5.1.3 Magnetization at Full Penetration

Looking at Fig. 5.1.2.2 above we note a sharp transition from Eq. 5.1.2.2 (b) to 5.1.2.2 (a). Although it is not apparent from Fig. 5.1.2.2, J_{cz} is in fact a maximum at $\beta_\rho = \beta_C$. One might expect the magnetization and loss to have similar maximums at L_{pc}, but in fact, this is not the case, since $J_{cz} = J_{cz}(\rho,L_p)$, and the magnetization is an integral of r x J over the whole strand. If we consider the equation for ρ_c we can see that in a conductor of a given L_p two regions exist, as shown in Fig. 5.1.3.1. In the outer region Eq. 5.1.2.2 (b) determines the critical current, while in the inner region

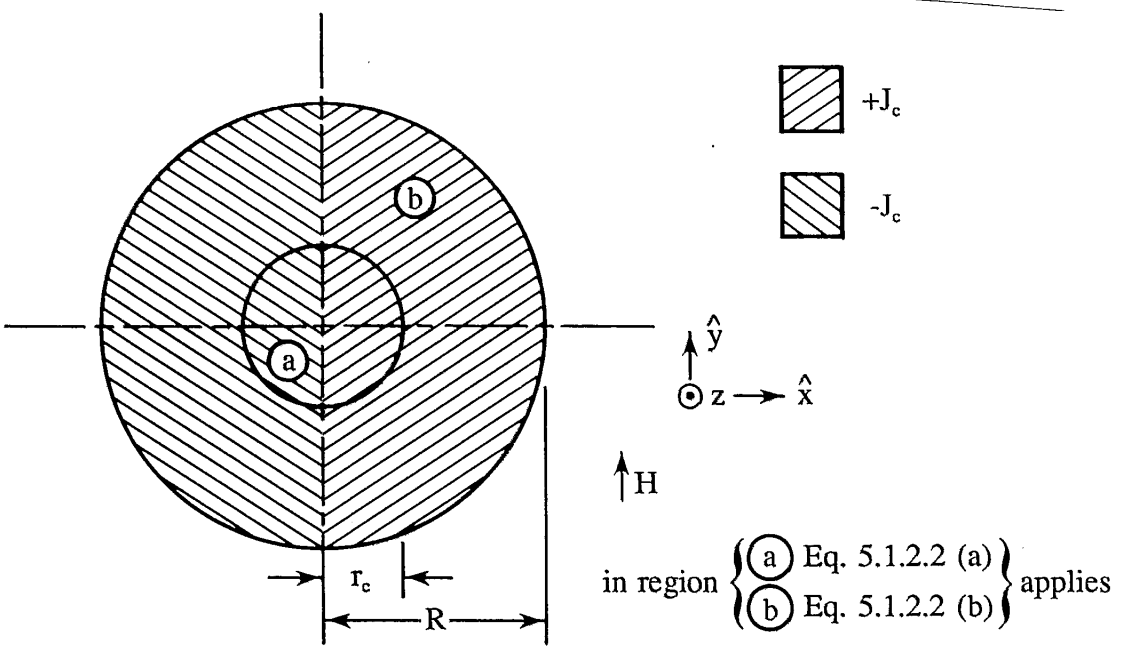

Fig. 5.1.3.1 Illustration of the critical radius and the two separate current regions in a fully penetrated strand with $L_p < L_{pcm}$

Eq. 5.1.2.2 (a) applies. The magnetic moment of this arrangement can be found by calculating M from

$$M = \left(\frac{1}{V}\right)\left[\frac{1}{20}\int \vec{r} x J(\rho) d\tau\right] \qquad \text{Eq. 5.1.3.1}$$

the relevant component of which is given by

$$M_y = \left(\frac{1}{20\pi R^2 L}\right)\int \hat{y} \cdot (\vec{r} x J)\rho d\rho d\theta dz \ . \qquad \text{Eq. 5.1.3.2}$$

Integrating over z and θ, and inserting the relevant J_cs

$$M_y = \left(\frac{2}{5\pi R^2}\right)\left\{ \int_0^{\rho'} \lambda\rho^2 J_{cfil}\left[1 + \left(\frac{2\pi\rho}{L_p}\right)^2\right]^{1/2} d\rho \right.$$

$$\left. + \int_{\rho'}^{R} \left(\frac{\rho J_{cp} L_p}{2\pi}\right)\left[1 + \left(\frac{2\pi\rho}{L_p}\right)^2\right]^{1/2} d\rho \right\}. \qquad \text{Eq. 5.1.3.3}$$

If we integrate this expression we get

$$\Delta\mu = 3\left\{ \frac{(1+\beta_R^2)^{3/2}}{3\beta_C} - \frac{\beta_R^3}{8\beta_C^2}(1+\beta_C^2)^{1/2} - \frac{\beta_R^3}{12\beta_C^4}(1+\beta_C^2)^{3/2} \right.$$

$$\left. - \frac{\beta_R^3}{8}\log\left[1 + (1+\beta_C^2)^{1/2}\right] + \frac{\beta_R^3}{8}\log\beta_C \right\} \qquad \text{Eq. 5.1.3.4}$$

for $L < L_{pcm}$ and

$$\Delta\mu = 3\left\{ -\frac{\beta_R}{8}(1+\beta_R^2)^{1/2} + \frac{1}{4\beta_R}(1+\beta_R^2)^{3/2} \right.$$

$$\left. - \frac{\beta_R^3}{8}\log\left[1 + (1+\beta_R^2)^{1/2}\right] + \frac{\beta_R^3}{8}\log\beta_R \right\} \qquad \text{Eq. 5.1.3.5}$$

for $L > L_{pcm}$

where

$$L_{pcm} = \frac{2\pi\lambda R\, J_{cfil}}{J_{cp}} \qquad \text{Eq. 5.1.3.6}$$

is just L_{pc} evaluated at the strand radius. For details of this calculation see App. E. Note that we have defined $\beta_p(\rho = R) \equiv \beta_R$ and have normalized the magnetization by its saturation value ($\Delta M_{sat} = 4\lambda J_{cfil} R/15\pi$). While Eq. 5.1.3.4 has contributions from both terms of Eq. 5.1.3.3, Eq. 5.1.3.5 (describing the saturated branch of the proximity-effected magnetization curve) comes solely from the first term of Eq. 5.1.3.3. The second term does not enter in because, for a given sample radius (R), there is an L_p beyond which the whole superconductor is described by Eq. 5.1.2.2 (a). This L_{pc} is just the L_{pcm} defined above.

These equations have the limits $\Delta\mu\ (L_p \rightarrow 0) = J_{cp}/\lambda J_{cfil}$, and $\Delta\mu\ (L_p \rightarrow \infty) = 1$, just as would be expected. $\Delta\mu$ is plotted below, in Fig. 5.1.3.2, as a function of β_R for some representative β_C values ($\beta_C \approx 200$ for NTCU20 and 20 for NTCU07). In Fig. 5.1.3.2 the contribution of the outer region of the strand (region (b) in Fig. 5.1.3.1) is shown by the dotted line, while the contribution of the inner region (a) is shown by the dashed line. We can see that initially (for small L_p), the second term of Eq. 5.1.3.3 is all that is necessary to describe $\Delta\mu$. For higher L_p the first term is necessary as well.

For $\beta_C >> \beta_R >> 1$ (i.e. $J_{cfil} >> J_{cp}$ as well as small to intermediate L_p), this expression has a linear approximation given by

$$\Delta\mu \approx \frac{3}{2}\frac{\beta_R}{\beta_C}$$

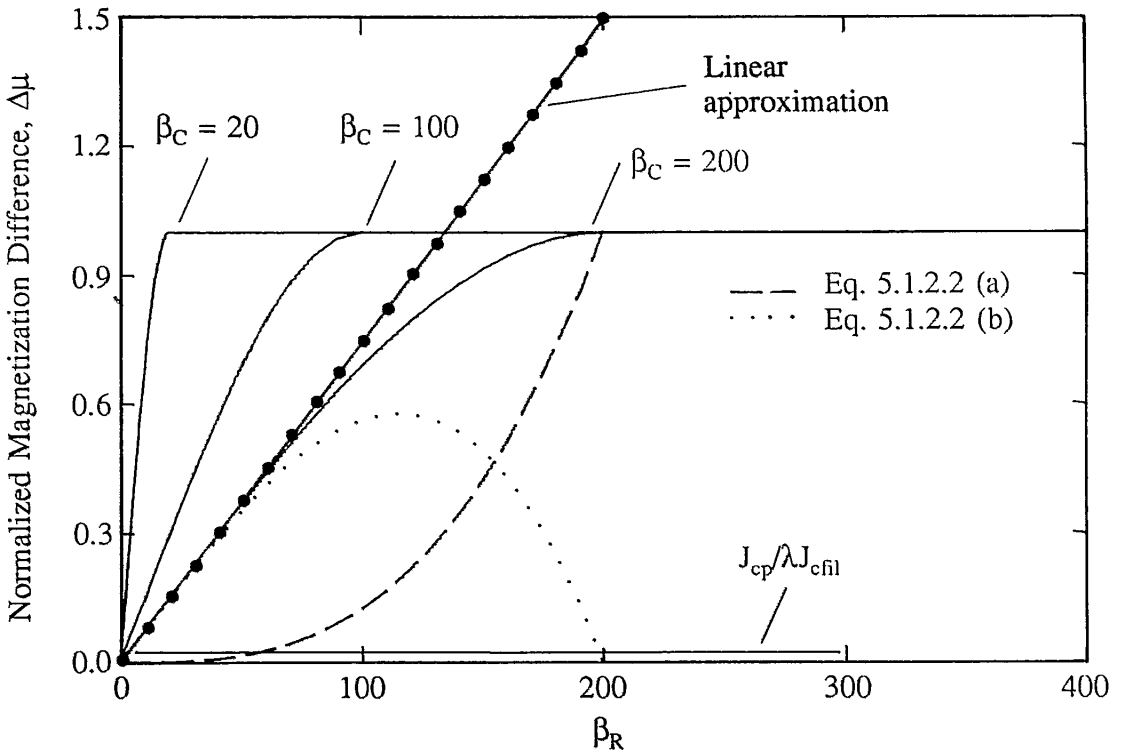

Fig. 5.1.3.2 Calculated $\Delta\mu$ versus β_R for several β_C values. For $\beta_C = 200$ the contributions from parts of the strand described by equations 5.1.2.2 (a) and (b) are separated

Written in cgs-practical units this is

$$\Delta M_S \approx \frac{J_{cp} L_p}{5\pi^2}$$

where the magnetization is normalized to the composite volume. This is just the first

term of the expression that Harada et al. have derived for ΔM by using Eq 5.1.2.2 (b) to describe the entire strand (their second term becomes significant when $L_p \approx R$)[40]. The linear approximation is good for the constraints mentioned above, but both at very low L_p, and in saturation, the full form of Eqs. 5.1.3.4 and 5.1.3.5 should be used. A comparison of this approximation to the full form of the equations is shown in Fig. 5.1.3.2. Harada et al. also introduce an H dependence for J_c via a semi-Bean approximation. In this approximation, variations in B(ρ) inside the superconductor, due to magnetization currents, are considered small compared to the variations of the external field H[49]. Practically, this amounts to replacing J by J(H) in any given equation. The above equations can be written in the same approximation, however, ρ_c will have to be calculated with J = J(H) as well.

5.1.4 $H_{p,prox}$ at Full Penetration

This problem is equivalent to finding the field created at the center of the conductor by the currents that flow in the saturated state. This field can be found from

$$B(\vec{r}') = \frac{1}{10}\int J(\vec{r}) \times \frac{(\vec{r}'-\vec{r})}{|\vec{r}'-\vec{r}|^3} d\vec{r}^3 \ . \qquad \text{Eq. 5.1.4.1}$$

The relevant component of the field is

$$B_y = \frac{1}{10}\int \frac{\hat{y}\cdot(J \times \vec{r})}{r^3} \rho d\rho d\theta dz \ . \qquad \text{Eq. 5.1.4.2}$$

We then find that

$$H_{p,prox} = \frac{8}{10}\int_0^R J_{cz}(\rho)d\rho \qquad \text{Eq. 5.1.4.3}$$

and when we take into account 5.1.2.2 (a) and 5.1.2.2 (b)

$$H_{p,prox} = \left(\frac{8}{10}\right)\left\{ \int_0^{r_c} \lambda J_{cfil}\left[1 + \left(\frac{2\pi\rho}{L_p}\right)^2\right]^{1/2} d\rho \right. \qquad \text{Eq. 5.1.4.4}$$

$$\left. + \int_{r_c}^R \frac{J_{cp}}{\rho}\left[\left(\frac{L_p}{2\pi}\right)^2 + \rho^2 \right]^{1/2} d\rho \right\}$$

This integrates to

$$h = \beta_R\left\{\frac{1}{\beta_R\beta_C}(1+\beta_R^2)^{1/2} - \frac{1}{2\beta_C^2}(1+\beta_C^2)^{1/2} \right. \qquad \text{Eq. 5.1.4.5}$$

$$\left. + \frac{1}{\beta_C}\log\left[\frac{\beta_C + (1+\beta_C^2)^{1/2}}{\beta_R + (1+\beta_R^2)^{1/2}}\right] + \frac{1}{2}\log\left[\frac{1}{\beta_C} + \frac{(1+\beta_C^2)^{1/2}}{\beta_C}\right]\right\}$$

for $L < L_{pcm}$, while for $L > L_{pcm}$

$$h = \frac{1}{2}\left\{\frac{1}{\beta_R}(1+\beta_R^2)^{1/2} + \beta_R \log\left[1 + (1+\beta_R^2)^{1/2}\right] - \beta_R \log\beta_R\right\} \qquad \text{Eq. 5.1.4.6}$$

where for $L_p > L_{pcm}$ only the first term of Eq. 5.1.4.4 contributes. For the details of these calculation see App. F. Note that these equations have been normalized to the saturation value of the penetration field, $H_{p,prox,sat} = 0.8J_{cfil}\lambda R$. They have the limits that as $L_p \rightarrow 0$, $h \rightarrow J_{cp}/\lambda J_{cfil}$, and as $L_p \rightarrow \infty$, $H_{p,prox} \rightarrow 1$. h has been plotted in Fig. 5.1.4.1 as a function of β_R for several β_C. The contribution from the inner region of the strand (described by Eq. 5.1.2.2 (a)) is shown as a dotted line, while that of the outer region

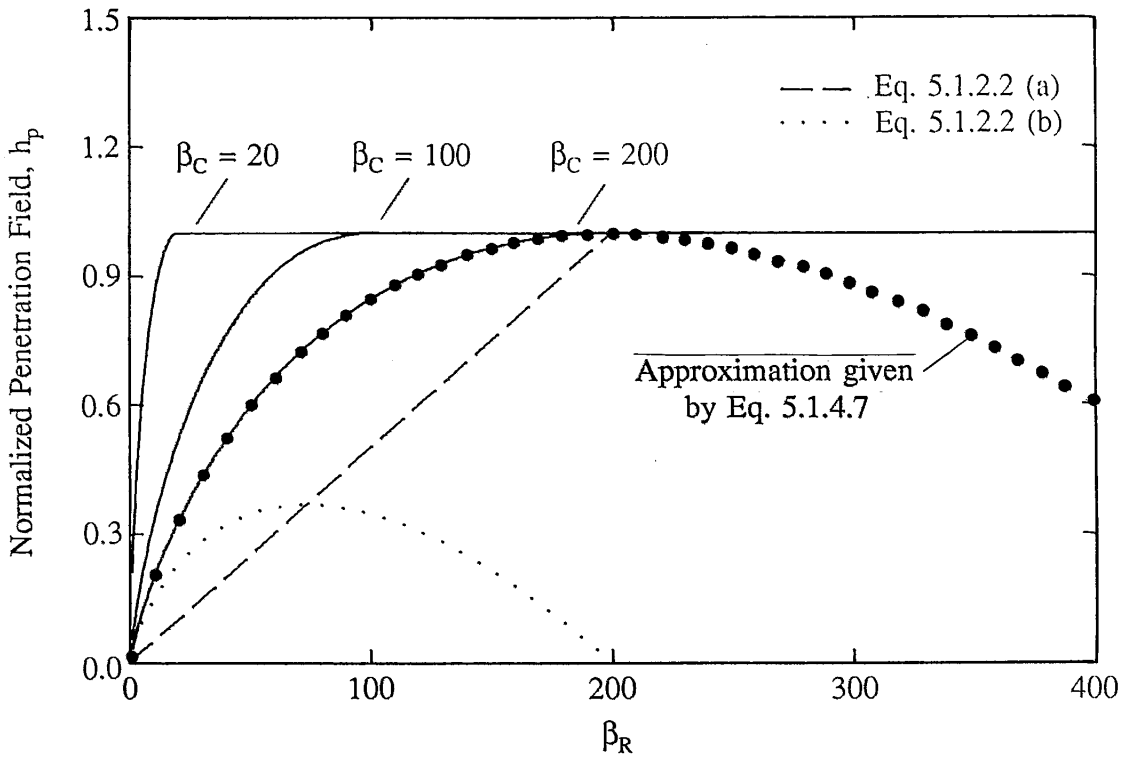

Fig. 5.1.4.1 Calculated h versus β_R for several β_C values. For β_C = 200 the contributions from parts of the strand described by equations 5.1.2.2 (a) and (b) are separated

(described by Eq. 5.1.2.2 (b)) is shown as a long dashed line. We can see that for all L_p except for the lowest both sections of the strand contribute significantly to $H_{p,prox}$.

For $\beta_C >> \beta_R >> 1$, a good approximation to the above expressions is given by

$$h \approx \frac{\beta_R}{\beta_C}\left[\, 1 + \log \frac{\beta_C}{\beta_R} \,\right] \qquad \text{Eq. 5.1.4.7}$$

If we now write this in cgs-practical units it becomes

$$H_{p,prox} \approx \left(\frac{0.8\, J_{cp} L_p}{2\pi}\right)\left[\, 1 + \log\left(\frac{\lambda\, J_{cfil}\, 2\pi R}{J_{cp} L_p}\right)\right]$$

The first term of this is the expression used by Harada et al[40]. The Harada approximation (i.e. the linear term alone), although not plotted above, is difficult to distinguish from the contribution from the inner section of the strand alone (described by Eq. 5.1.2.2 (a)). This agreement is apparently accidental, and the approximation seems to be too low. If we now include the second, logarithmic term (due to the outer region of the strand), we get the curve represented by the dotted line in Fig. 5.1.4.1, which is a very good approximation.

5.2 Effects of Finite Strand Length: Transfer Length

5.2.1 General Introduction to Short Sample Effects

Because of the saturation of J_{cz} when L_p becomes infinite, a different criterion is needed to describe the length dependence of short, untwisted samples. This condition comes from the necessity of having a large enough length over which the filamentary currents can cross over the matrix (via PE) -- a PE transfer length. The above model does not address the issue of a transfer length, although one might be expected in analogy with eddy currents. A calculation for this is outlined below. So far in this Chapter, following the Carr prescription[38], we have set all non-axial currents to zero. These currents are, at least to a first approximation, irrelevant for long conductors, but they are the essence of PE transfer length effects. Yamafuji et al. initially described the PE coupled conductor via currents which flowed exclusively down the filaments and then crossed over across the matrix, entailing θ and ρ currents[9]. These currents, however, were used to describe the L_p dependence (see App. D). They have subsequently adopted Carr's prescription for J_{cz}[40], which ignores the possibility of θ and ρ currents.

5.2.2 Heuristic Result for Cylindrical (Strand) Geometry

This transfer length is a consequence of two things: (1) an anisotropy in J_c, and (2) Kirchhoff's law (the condition of current continuity). Crudely, these requirements become

$$J_{cz} A_z = 2RL_T J_{cp}$$

Here A_z is the cross sectional area through which J_{cz} flows down the strand (see Fig. 5.2.2.1).

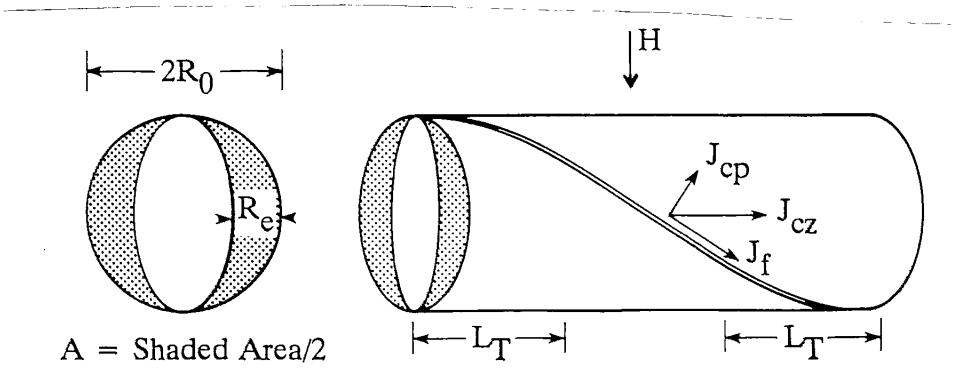

Fig. 5.2.2.1 Illustration of the transfer length effect in a short sample

First, consider the case for $H < H_{p,prox}$. Generally, the penetration field for the transverse case is $H_p = 0.8RJ_c$, which can be re-written to find the penetration distance, R_e as a function of the external field, giving $R_e = 1.25H/J_{cz}$. Combining this with the area $A_Z = RR_e\pi/2$ we get

$$L_T = (const)\left(\frac{H}{J_{cp}}\right)$$

where the constant incorporates both the geometrical factor and a dependence of J_{cp} on field. Notice that the PE L_T, in analogy to the eddy current transfer lengths dependence

on dH/dt, is a function of H. However, as shown by Carr[50], eddy current L_Ts are proportional to $1/(dH/dt)^{1/2}$, as opposed to PE induced L_Ts, which are directly proportional to H. Also, there is an inverse dependence on J_{cp}, which can be seen as analogous to conductivity in the normal matrix in eddy current problems. When $H > H_{p,prox}$ the transfer length becomes

$$L_T = (const)R\left(\frac{J_{cz}}{J_{cp}}\right)$$

The field sweep dependence of L_T is no doubt connected to the H_m dependence of the effect seen in Ref. 44.

5.2.3 Exact Results for the Rectangular Geometry, $J_{cp} \neq J_{cp}(H)$

5.2.3.1 M-H Equations for Short Samples of Rectangular Geometry: This section lists the equations for an M-H loop for a semi-infinite, rectangular slab of superconductor with anisotropic J_cs, where $J_c \neq J_c(B)$. This theory was originally formulated in the context of high T_c superconductors, and was used to describe crystals and thin films[51-53]. I have merely re-interpreted these equations in terms of low T_c PE multifilamentary composites in order to describe short sample effects. These equations are similar to those of Sec. 5.2.2, and represent the exact result for a rectangular geometry. We display the branch-by-branch M-H expressions which come from this model, and calculate M-H loops and Q_S as a function of H_m to qualitatively show that this model describes low T_c PE composites.

In this modified critical state model the flux gradients develop in more than one

direction because of the finiteness of the sample. In addition, the J_cs for these two directions are not the same. The two penetration depths encountered in this model are the generalizations of the transfer length (L_T) described in Sec 5.2.2 (but in this case for a rectangular geometry). Below is the summary of the expressions for M-H. For convenience the details of the calculations of the M-H loops in this form are given in App. G, but see[51-53].

Summary of equations for rectangular short sample

There are two cases: (1) $LJ_{cp} > \lambda J_{cfil}(d/2)$, and (2) $LJ_{cp} < \lambda J_{cfil}(d/2)$

Case A, $LJ_{cp} > \lambda J_{cfil}(d/2)$ (i.e. $L > L_T$)

Initial magnetization $H < H_{p,prox}$

$$M_z = \left(\frac{-H}{4\pi}\right)\left\{1 - H\left[\left(\frac{30}{12}\right)\left(\frac{1}{\lambda J_{cfil} d\pi}\right)+\left(\frac{15}{12}\right)\left(\frac{1}{J_{cp}\pi L}\right)\right] + \frac{50}{12}H^2\left(\frac{1}{J_{cfil}J_{cp}L\pi^2 d\lambda}\right)\right\}$$

Initial magnetization for $H \geq H_{p,prox}$

$$M_z = -\frac{d\lambda J_{cfil}}{40}\left(1 - \frac{d J_{cfil}\lambda}{6 J_{cp} L}\right)$$

Initial reversal region for

$H_m > 2H_{p,prox}$ and $|H| > H_m - 2H_{p,prox}$

$$M_{\frac{1}{2}} = \mp \left(\frac{J_{cfil} d \lambda}{40} - \frac{J_{cfil}^2 d^2 \lambda^2}{280 J_{cp} L} - \frac{(H_m \mp H)}{4\pi} \right.$$

$$\left. + \frac{15(H_m - H)^2}{96\pi^2} \left(\frac{1}{L J_{cp}} + \frac{1}{\lambda J_{cfil} d} \right) \right.$$

$$\left. - \frac{25}{96} \frac{(H_m - H)^3}{\pi^3} \frac{1}{dL J_{cfil} J_{cp} \lambda} \right)$$

Major trapping/shielding branches for $H_m > 2H_{p,prox}$ and $|H| < H_m - 2H_{p,prox}$

$$M_{\frac{1}{2}} = \pm \frac{d J_{cfil} \lambda}{40} \left(1 - \frac{d J_{cfil} \lambda}{6 J_{cp} L} \right)$$

Trapping/shielding branches for $H_m < H_{p,prox}$

$$M_{\frac{1}{2}} = \mp \left[\frac{1}{96 J_{cfil} J_{cp} L \pi^3 d \lambda} \right] \left\{ -100 H_m^3 + 60 H_m^2 J_{cp} L \pi \right.$$

$$+ 30 H_m^2 J_{cfil} \pi \lambda d \mp 24 H_m J_{cfil} J_{cp} L \pi^2 \lambda d + 24 J_{cfil} J_{cp} L \pi^2 \lambda d (H_m \mp H)$$

$$\left. - (30 J_{cp} L \pi + 15 J_{cfil} \pi \lambda d)(H_m \mp H)^2 + 25 (H_m \mp H)^3 \right\}$$

Case B, $J_{cp}L < \lambda J_{cfil}(d/2)$ (i.e. $L < L_T$)

Initial Magnetization for $H > H_{p,prox}$

$$M_z = -\left(\frac{H}{4\pi}\right)\left\{1 - H\left[\left(\frac{30}{12}\right)\left(\frac{1}{\lambda J_{cfil} d\pi}\right) + \left(\frac{15}{12}\right)\left(\frac{1}{J_{cp}\pi L}\right)\right] + \left(\frac{50}{12}\right)H^2\left(\frac{1}{J_{cfil}J_{cp}L\pi^2\lambda d}\right)\right\}$$

Initial magnetization for $H > H_{p,prox}$

$$M_z = \left(\frac{-J_{cp}L}{20}\right)\left(1 - \left(\frac{2}{3}\right)\frac{J_{cp}L}{J_{cfil}\lambda d}\right)$$

Initial reversal region for $H_m > 2H_{p,prox}$ and $|H| > H_m - 2H_{p,prox}$

$$M_z = \left(\frac{\mp 1}{480 J_{cfil}J_{cp}L\pi^3\lambda d}\right)\left\{-16J_{cp}^3L^3\pi^3 + 24J_{cfil}J_{cp}^2L^2\pi^3\lambda d - 120J_{cfil}J_{cp}L\pi^2\lambda d(H_m \mp H) + (150J_{cp}L\pi + 75J_{cfil}\pi\lambda d)(H_m \mp H)^3 - 125(H_m - H)^3\right\}$$

Major trapping/shielding branches for $H_m > 2H_{p,prox}$, $H < 2H_{p,prox}$

$$M_z = + \left(\frac{-J_{cp}L}{20} \right) \left(1 - \left(\frac{2}{3} \right) \frac{J_{cp}L}{J_{cfil}\lambda d} \right)$$

Trapping/shielding branches for $H_m < H_{p,prox}$

$$M_{\frac{1}{2}} = \left(\frac{-1}{96 J_{cfil} J_{cp} L \pi^3 d\lambda} \right) \left\{ + 25H^3 - 75H^2 H_m + 75HH_m^2 + 75H_m^3 \right.$$

$$+ 30H^2 J_{cp} L\pi - 60HH_m J_{cp} L\pi - 30H_m^2 J_{cp} L\pi + 15H^2 J_{cfil} \pi d\lambda$$

$$\left. - 30HH_m J_{cfil} \pi d\lambda - 15H_m^2 J_{cfil} \pi d\lambda + 24HJ_{cfil} J_{cp} L\pi^2 d\lambda \right\} .$$

The above expressions have been used to construct M-H loops, and these loops are shown in Figs. 5.2.3.1.1 and 5.2.3.1.2. Conductor parameters comparable to those for the VNTCU20-X samples were chosen; J_{cp} = 600 A/cm^2, J_{cfil} = 1.85 x 10^5 A/cm^2, λ = 0.645, and R = 0.026 cm. Fig. 5.2.3.1.1 shows the M-H for a $H_m >> H_{p,prox}$ at a variety of sample lengths. Here we can see the same L dependence observed in the VL coils.

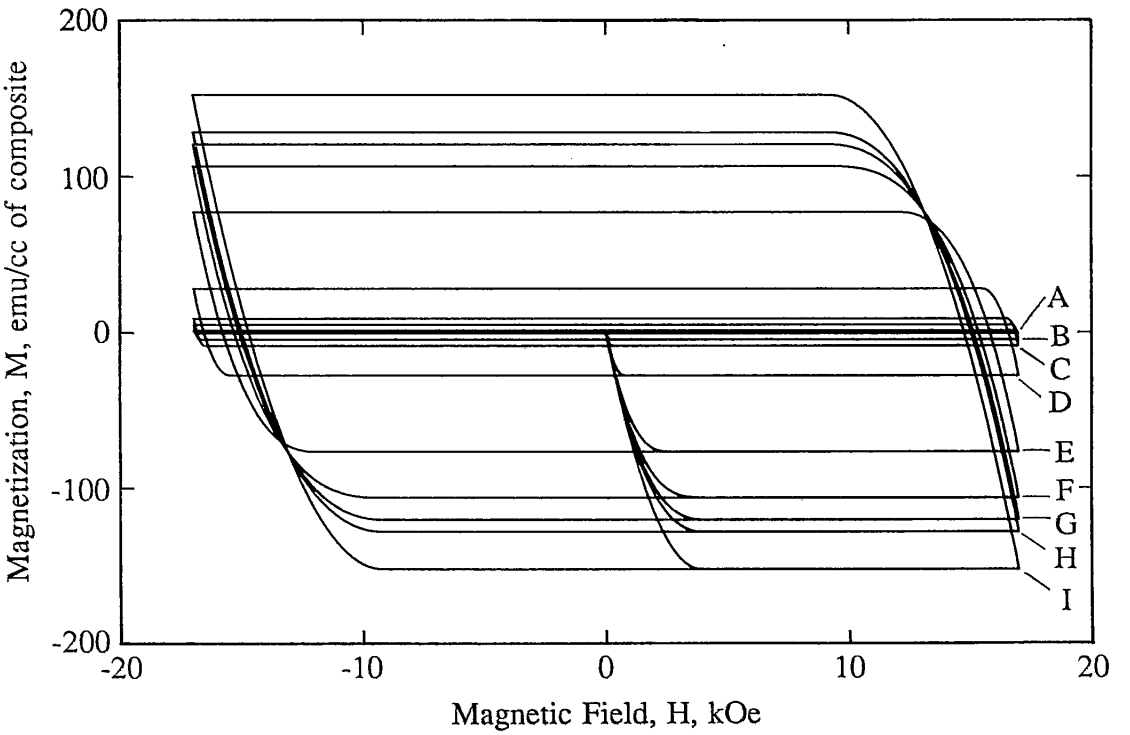

Fig. 5.2.3.1.1 Calculated M-H for the rectangular short sample model, large H_m, at several sample lengths. L (cm) is equal to A = 0.030, B = 0.165, C = 0.30, D = 1.00, E = 3.25, F = 5.50, G = 7.75, H = 10.0, I = 100

Note too that ΔM_S, at 150 emu/cc of composite, agrees roughly with the result for ΔM_{sat} for CNTCU20 coils at H = 0 (where $J_{cp} \approx 600$ A/cm^2). The calculated M-H for $H_m \approx H_{p,prox}$ are shown in Fig. 5.2.3.1.2. Here we can see an initial opening up of the M-H with L, followed by a coalescence down to a line of slope $1/4\pi$ for the longer lengths (as $H_{p,prox}$ begins to exceed H_m).

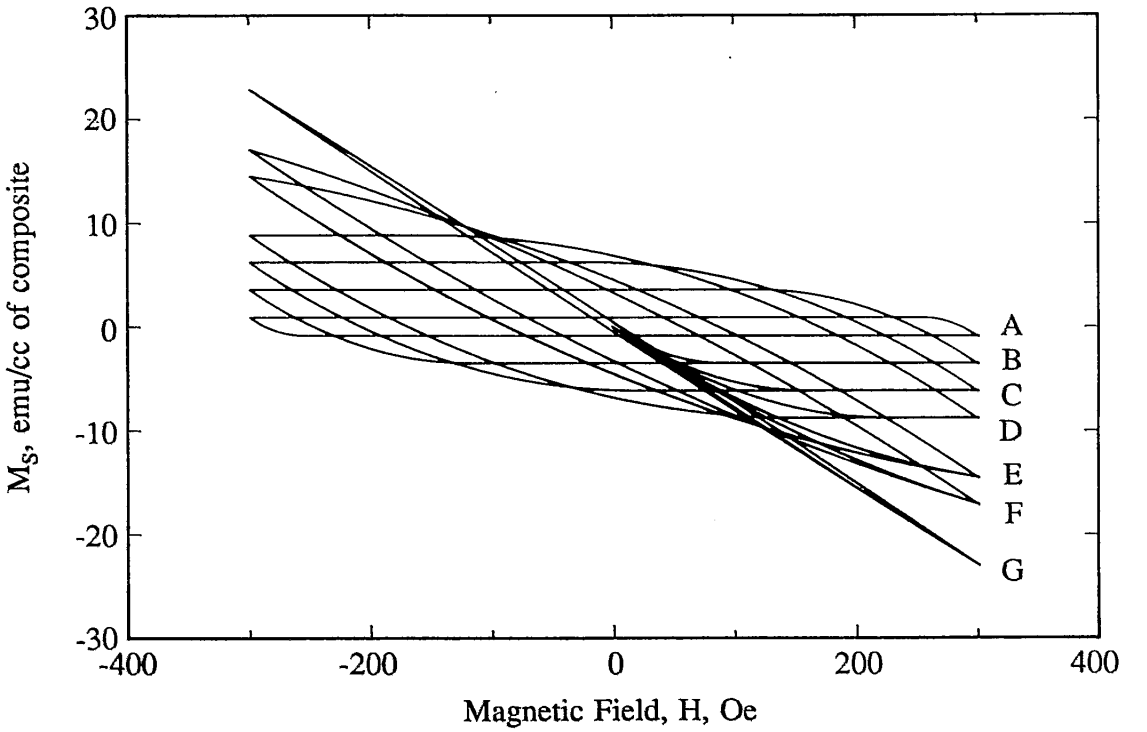

Fig. 5.2.3.1.2 Calculated M-H for the rectangular short sample model, small H_m, at several sample lengths. L (cm) is equal to A = 0.030, B = 0.120, C = 0.210, D = 0.300, E = 0.533, F = 0.766, G = 100

5.2.3.2 Q_S versus H_m for Short Samples of Rectangular Geometry

The variation of Q_S with field sweep is shown in Figs. 5.2.3.2.1 and 5.2.3.2.2. Here we notice a very strong similarity to the results from the data in Chapter 4 (Figs. 4.6.1 and 4.6.2). We can see in Fig. 5.2.3.2.1 that the loss for some of the shortest samples (e.g. those with L = 0.12, 0.21, 0.3, and 1 cm) initially exceeds that of the longer samples. However, in Fig. 5.2.3.2.2 we note that these low L curves fall under the curves

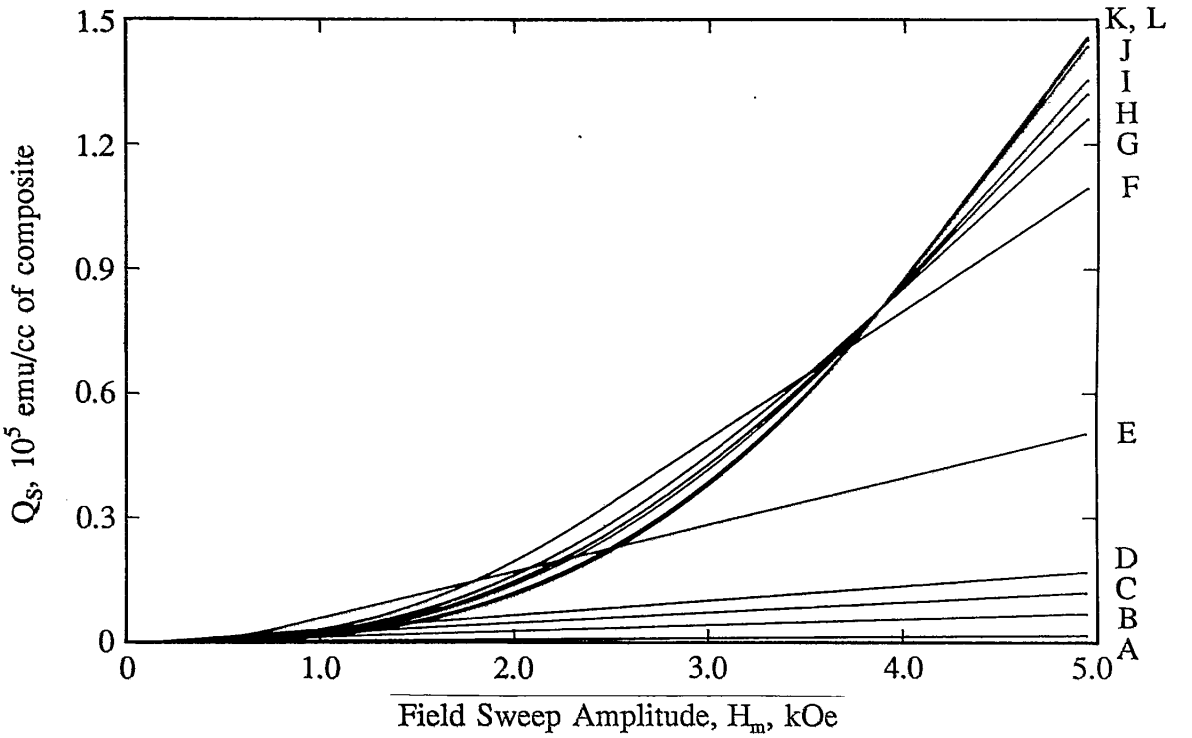

Fig. 5.2.3.2.2 Calculated Q_S versus H_m for rectangular short sample model, large H_m. L (cm) is equal to A = 0.030, B = 0.120, C = 0.210, D = 0.300, E = 1.00, F = 3.25, G = 5.50, H = 7.75, I = 10.0, J = 33.3, K = 66.6, L = 100

for the longer lengths. This shows that $H_{p,prox}$ is proportional to L. These curves are reminiscent of those from Ref 44, but no characteristic lower H_m plateau occurs. This is because $H_{c1,NbTi}$ has been set to zero in this approximation.

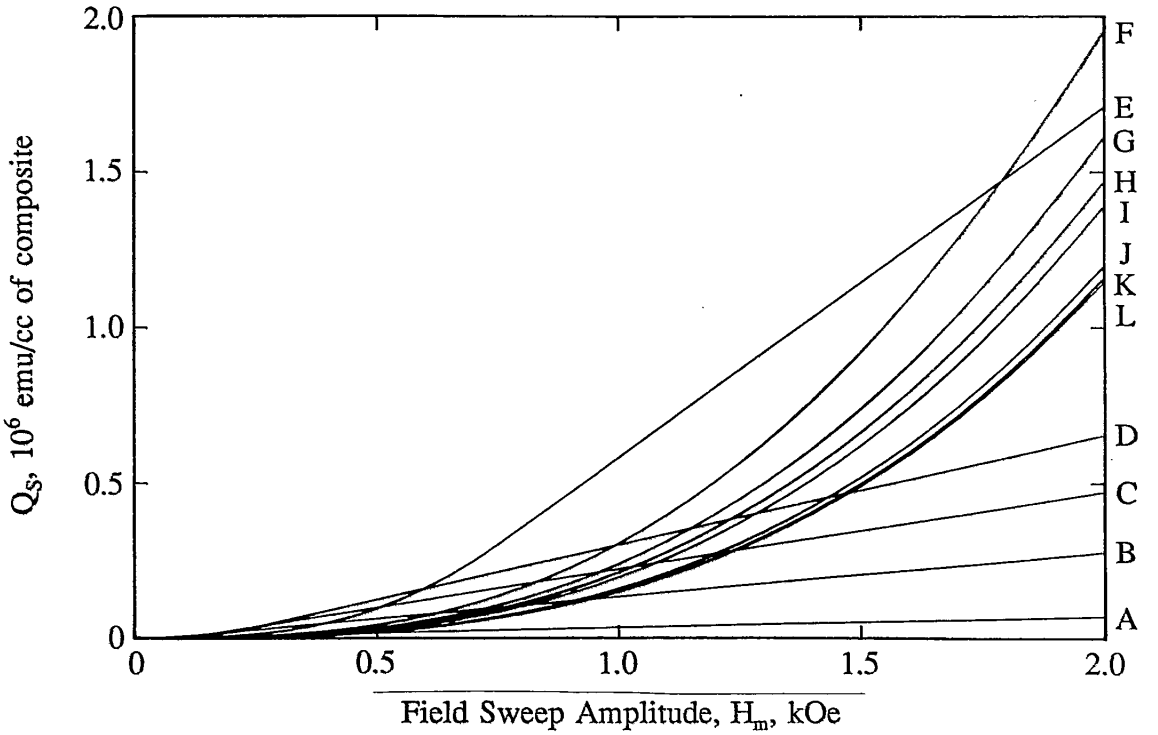

Fig. 5.2.3.2.1 Calculated Q_S versus H_m for rectangular short sample model, small H_m. L (cm) is equal to A = 0.030, B = 0.120, C = 0.210, D = 0.300, E = 1.00, F = 3.25, G = 5.50, H = 7.75, I = 10, J = 33.3, K = 66.6, K = 100

5.3 Discussion

5.3.1. The Pinning Centers

Chapter 5 has detailed a phenomenological theory based only on the assumption that the copper can sustain flux gradients. This is the same as asserting that it has a non-zero J_c. The real question, however, is what is the nature of the flux in these interfilamentary regions? There are really two main parts to this question: (1) what is the value of $\kappa_N(x_N)$ in the regions of the matrix that are superconducting, and (2) does the existence of S-N-S type Josephson junctions play an important role? We believe that there is no direct, concrete evidence to answer either of these two questions. The first question is complicated by the fact that $\lambda_N(x_N)$ varies over the interfilamentary distance, and this distance is comparable to the radius of the fluxon. It makes more sense to ask whether the field along the matrix/filament boundary exists as a continuous gradient, or a discrete set of fluxons with a varying spacing as we travel along the length.

Viewing the composite as an arrangement of S-N-S type Josephson junctions seems to provide a convenient explanation for having very dissimilar fields for initial bundle penetration versus high field extinction. This is because we can view $H_{c1,prox}$ as being due solely to PE current shielding, for which there is very good evidence (see Sec. 4.3.2). The upper critical field could then be explained in terms of Josephson junctions. However, none of the signature Josephson oscillations that would be expected from this rather regular array have been observed. Additionally, the field dependence of J_{cp} can be fit to exponential (a PE signature) as well as Josephson junction type forms. While it

wound be interesting to quantitatively explore this, it will not change the main features of this phenomenological model since it is based solely on the assumption that the copper regions are able to support a flux gradient.

As noted above, the phenomenological models describing the L dependence of the short sample M-H are just those that are used for high T_c superconductors. The reason for this is that the two systems have a common feature, viz: the presence of an anisotropy in J_c. In the case of low T_c multifilamentary PE samples this secondary, lower J_c is due to the fact that the copper constitutes a superconductive "weak link" between the filaments. This can be either described by PE or S-N-S links (which is to say PE + Josephson junctions). In the case of high T_c this anisotropy occurs on a much smaller scale (the individual layers or unit cells). The models used for the coupling between these layers are similar. The real difference is the scale and strength of these effects.

5.3.2 Comparison of Model to Experiment

Qualitatively, the model detailed in Chapter 5 describes the experimental data well. Taking the VP coil data first, ΔM_{PE} and Q_{PE} do seem to be initially linear with L_p. They also have a later saturation, to a value comparable to that predicted by the model (see Table 5.3.2.1, below). The model for the short samples (both the cylindrical and the rectangular geometries) also describes the L dependence seen in the VL samples, and of course the saturation value is the same as that predicted for the VP samples. The loss versus H_m characteristics are also quite similar, qualitatively. The basis for this similarity

is the length dependence of the penetration fields for short samples. The penetration fields for the CNTCU20 coils have been previously published[41], and show the predicted behavior with L_p. Lastly, the M-H versus θ_s characteristics are understandable, since $\Delta M_{PE} \propto J_{cp}L$ for short samples in the transverse orientation, but $\Delta M_{PE} \propto J_{cp}R$ in the longitudinal orientation. This implies that the ratio of transverse to longitudinal ΔM_{PE} is about 20 for the short samples.

As a preliminary semi-quantitative test for the theory presented in Chapter 5 we have listed values of some of the central parameters as calculated from this theory, along with their experimentally determined values. This is done for strands NTCU20 and NTCU07, and the values are listed in Table 5.3.2.1. J_{cp} values are from the short sample measurements, and J_{cfil} values were calculated from the ΔM of the bare samples at 10 kOe.

In general, the correlation between calculated and measured values is rough, with the agreement for strand NTCU20 somewhat better than that for NTCU07. Note that we have defined a $\Delta M_{sat}(H = 0)$ as the saturation value of ΔM (as with L_p) at zero applied field. The largest contributor to these discrepancies is probably the strong field dependence of the PE. It is somewhat surprising that no field dependence for L_{pcm} is seen in the data. The reason for the existence of the PE dip remains unanswered. As mentioned above (cf Sec. 4.3), the anomaly refered to is certainly a dip-like feature since the existence of an excess PE magnetization throughout this region of the loop is predicted by the above model. It is evident that all (or most) of the PE coupling is disappearing, and we are returned to the bare NbTi magnetization. Takàcs described a

5.3.2.1: Model parameters from Experiment and Theory

Quantity	CNTCU07-1 Calculated	CNTCU07-1 Measured	CNTCU20-1 Calculated	CNTCU20-1 Measured
J_{cp} (A/cm^2)	---	6000	---	600
J_{cfil} (A/cm^2)	---	1.85×10^5	---	1.85×10^5
L_T (cm)	0.2	4-8	5	> 10
L_{pcm} (cm)	1	4 to 8	33	≈> 35
$\Delta M_{sat}(H = 0)$ (emu/cc NbTi)	130	500	410	350
$H_{p,prox}$ (kOe)	0.8	2-3	2.5	2.0-2.5

similar dip in his M-H loops as the interaction between new and frozen-in flux lines, i.e, he believed that there was an anomalous canceling of anti-aligned flux near zero field[25]. This mechanism does not seem to require PE, and so the comparison between Cu and CuMn materials seems to rule this, and any other non-PE assisted mechanisms, out (at least in our samples). Even though we do not understand the cause of this dip, we can make some worthwhile comments about it: (1) It only occurs when significant PE trapping exists, (2) The filaments must be in the mixed state, (3) It always occurs near zero field on the trapping branch, and (4) It is sample length dependent.

CHAPTER 6: CONCLUSIONS

6.1 Summary

This thesis gives detailed data on the magnetization and loss behavior of PE coupled multifilamentary superconductive composites for both high and low H_m. The dependence of PEs on strand design (filament diameter, matrix type, and L_p), as well as sample geometry (L and field orientation) have been investigated. The proximity effect critical current (J_{cp}) and critical field ($H_{c1,prox}$) have been measured directly from longitudinal experiments on short samples.

Expressions for ΔM and $H_{p,prox}$ which are valid in saturation as well as the small L_p regime have been derived for long samples. Expressions for the M-H of finite length anisotropic superconductors, originally developed in the context of high T_c superconductors, have been applied to describe finite length effects in PE multifilamentary materials. A heuristic model based on the same principles but applied to the cylindrical geometry is proposed. From an experimental point of view this work demonstrates: (1) the complementary nature of matrix etching and L_p studies, and (2) an experimental technique which allows measurement of low $(dH/dt)_{eff}$ M-H loops.

These experiments have confirmed the L_p dependence of M_{PE} and Q_{PE} which was described by Harada et al.[40], and show that proximity-effected multifilamentary strands

with CuMn matrices have a similar, but weaker, dependence on L_p. In addition, an analogous dependence of Q_{PE} and M_{PE} on L exists. Both of these quantities vary linearly with L_p (or L), for relatively low levels of PE coupling. Q_{PE} and M_{PE}, while they can become quite large, saturate with increasing PE coupling strength. Also, measurements on short samples show that PEs are stronger when H is applied transverse to the filament axis as opposed to when H is applied along the filament axis.

From the longitudinal short sample measurements, we note that $H_{c1,prox}$ and J_{cp} are exponentially dependent on the interfilamentary distance and the temperature, and can be fit to equations describing PEs in monofilamentary NbTi in Cu. Additionally, these effects are very sensitive to the presence of Mn, as would be expected. However, it is noted that PEs persist to fields very much higher than $H_{c1,prox}$, indicating that the PE seen in multifilamentary strands are significantly different from those seen in monofilaments or thin films.

In seeking to describe the magnetization and loss as a function of H_m, there are several important parameters, $H_{c1,prox}$, $H_{c1,NbTi}$, $H_{p,proxL}$ and $H_{p,prox}$. For conductors with a large enough J_{cp}(Length) product such that no $H_{p,proxL}$ exists, the conductor behaves as a conventional superconductor with a large J_c. For these conductors the losses in the low ($H_{c1,prox} < H_m < H_{c1,NbTi}$) and intermediate H_m regime ($H_{c1,NbTi} < H_m < H_{p,prox}$) are inversely proportional J_c, but directly proportional to J_c in the high H_m regime ($H_m > H_{p,prox}$). As the length (or alternately J_{cp}) of a strand decreases the loss versus H_m characteristics in these regimes, as well as the boundaries of these regimes, change. For conductors such that J_{cp} (Length) < $H_{c1,prox}$ the loss is proportional to J_{cp} in all regimes.

These conductors can be quite well understood in terms a model in which the proximity-effected copper is capable of supporting a flux gradient (or, equivalently, has a non-zero J_{cp}), and has critical fields H_{c1} and H_{c2}. The multifilamentary composite can then be viewed in terms of an anisotropic continuum, where the different continuum J_cs (eg. $J_{c\rho}$, $J_{c\theta}$, J_{cz} (z is along the filament axis)) are functions of J_{cfil}, J_{cp}, and strand design (e.g. L_p). For simplicity we have chosen to ignore the lower critical field of this anisotropic continuum composite. Short samples, then, are aptly described as cylinders with anisotropic J_cs, and flux gradients which form across the whole strand diameter, as well as along the length of the cylinder. For longer samples, the flux gradients along the cylinder are not important, and the strand can simply be described as a homogenous conductor of effective $J_c = J_{cz}(\rho)$. Generally, this simple model describes the magnetization and loss, but for samples short enough that J_{cp} (Length) < $H_{c1,NbTi}$, the inhomogeneous nature of the strand becomes noticeable. For these samples low H_m sweeps will induce flux gradients in the matrix alone, but will not enter the NbTi filaments. For higher H_m the situation is still described by the above model where we have ignored reversible magnetization effects.

In either of the above cases, it is the anisotropy in J_c that is the basis of these unusual PE properties. It is this anisotropy that is the cause of the initial linear dependence of M_{PE} and Q_{PE} on L and L_p. The saturation with large L and L_p is due to: (1) the field dependence of the proximity effect, and (2) the approach to "full coupling", analogous to eddy current saturation.

We note that in some ways, these proximity effects can be seen as "super eddy currents". "Super" because these are in fact supercurrents which do not decay (or have significant decay times[42]), and whose driving force is an H field, rather than a dH/dt. "Eddy currents" because they travel the same paths that are associated with ordinary eddy current coupling. This point of view will be especially useful when the dynamic properties of these materials are more fully investigated. This is because these proximity effects have saturation values similar to their eddy current counterparts[42], due to the similarity in current paths mentioned above.

6.2 Technological Implications of This Work

As shown by Harada et al.[40], and confirmed by this work, small L_p is very important in minimizing excess PE magnetization and loss. Additionally, the use of magnetic scatterers is a very effective method of PE reduction. Magnetic scatterers are much more effective than nonmagnetic scatterers in reducing the PE at a given impurity level, thus the thermal stability of the strand is not degraded. Technologically useful strands, then, will have both CuMn matrices and small L_p to reduce unwanted loss and magnetization. Ni could be added in the form of barriers or as a solute to independently control eddy currents. As noted above, there is some suggestion that PE are associated with excess creep/drift, so that reduction of M_{PE} might reduce magnetization creep/drift as well.

We have also noted a strong topological similarity between the PE and eddy

current effects. In an appended paper (App. K), we can see that this extends to a competition for paths between their associated currents. The consequence of this is that many of the engineering calculations for eddy currents will need to be revisited with proximity effect currents (e.g. cable and twist pitch interaction (App. H), L_p, and L).

6.3 Directions for Future Research

There are two interesting directions for future research. The first of these is a further investigation of static properties of the PE. One of the first questions that should be addressed is the validity of (or the error associated with) the assumption that currents are restricted to flow along the z-axis for long samples. Next, a branch-by-branch calculation of an M-H loop should be completed, as this will be necessary for a more exact treatment which includes the field dependence of the PE. An investigation of the asymmetry of the short sample ΔM_{PE} would be interesting, as well as a better estimation of L_T. In addition, approximate analytic expressions for the loss of long conductors should be sought. Experimentally, matrix composition (e.g. CuMn +Ni barriers) should be optimized for low loss. It might be of interest to study the transition from "local" PEs (PE currents do not couple from one filament to another) to "distributed" PEs by studying relatively weakly coupled multifilamentary strands. Also, the role of PE versus Josephson junction coupling should be addressed. Here, perhaps a non-electromagnetic approach such as specific heat could prove interesting.

The second avenue of interest is in understanding the dynamic aspects of the PE.

The dynamic properties include both short term and long term effects. In the short term regime, there are apparent interactions between proximity currents and eddy currents[42], which would be of interest for any AC applications. In the long term regime, some researchers[9,43] seem to have found a correlation between magnetization creep/drift and proximity effect coupling. These effects are important in regard to the precision magnet applications for which these strands were designed, and promise to be a topic of considerable interest.

REFERENCES

1. E. Gregory, T.S Krelick, J. Wong, E.W. Collings, K.R. Marken Jr., R.M. Scanlan, and C.E. Taylor, "A Conductor with Uncoupled 2.5 μm Diameter Filaments, Designed for the Outer Cable of SSC Dipole Magnets", IEEE Trans. Magn. 25, 1926 (1989).

2. I. Hlásnik, S. Tákacs, V.P. Burjak, M. Majoros, J. Krajcik, L. Krempasky, M. Polak, M. Jergel, T.A. Korneeva, O.N. Mironova, and I. Ivan, "Properties of Superconducting NbTi Superfine Filament Composites with Diameters < 0.1 μm", Cryogenics 25, 558 (1985).

3. L.R. Motowidlo, H.C. Kanithi, and B.A. Zietlin, "NbTi Superconductors with Artificial Pinning Structures", Adv. Cryo. Eng. 36, 311 (1989).

4. G.L. Dorofejev, E.Y. Klimenko, S.V. Frolov, E.V. Nikulenkov, E.I. Plashkin, N.I. Salunin, and V.I. Filkin, "Current Carrying Capacity of a Superconductor with Artificial Pinning", Conference Proceedings of the 9th International Conference on Magnet Technology, Zurich, 564 (1985).

5. G.L. Dorofejev, S.V. Frolov, E.Y. Klimenko, V.Y. Filkin, E.V. Nikulenkov, E.I.

Plashkin, and N.I. Salunin, "Niobium-Titanium Superconducting Strands with Ultrafine Filaments (A Role of Superconductive Boundaries), IEEE Trans. Magn. 24, 1138 (1988).

6. Y. Yamafuji, N. Harada, Y. Mawatari, K. Funaki, T. Matsushita, K. Matsumoto, O. Miura, and Y. Tanaka, "Achievement of High Current Density in NbTi Superconducting Multifilamentary Wires by Introducing Artificial Pins", Cryogenics 31, 431 (1991).

7. W.S. Gilbert, R.F. Althaus, P.J. Barale, R.W. Benjegerdes, M.A. Green, M.I. Green, and R.M. Scanlan, "Magnetic Field Decay in Model SSC Dipoles", IEEE Trans. Magn. 25, 1459 (1989).

8. H. Bruck, D. Gall, G. Knies, J. Krzywinski, R. Lange, R. Meinke, H. Preibner, P. Schmuser, and Y. Zhao, "Time Dependent Field Distortions From Magnetization Currents in the Superconducting HERA Magnets", Cryogenics 30, 608 (1990).

9. K. Yamafuji, Y. Mawatari, N. Harada, E.S. Otabe, and T. Fujiyoshi, "Effect of Flux Creep on the SSC Diploe Magnets", Cryogenics 30 (Suppl.), 615 (1990).

10. R.W. Cross, "Transport Current Effects on Flux Creep and Magnetization in NbTi Multifilamentary Cable Strands", to be published in Adv. Cryo. Eng. 38.

11. S. Tákacs and A.M. Campbell, "Hysteresis Losses in Superconductors with Very Fine Filaments", Supercond. Sci. Technol. (U.K.) 1, 53 (1988).

12. F. Sumiyoshi, M. Matsuyama, M. Noda, T. Matsushita, K. Funaki, M. Iwakuma, and K. Yamafuji, "Anomalous Magnetic Behavior Due to Reversible Fluxoid Motion in Superconducting Multifilamentary Wires with Very Fine Filaments", J. Appl. Phys. 25, L148 (1986).

13. E.W. Collings, A.J. Markworth, J.K. McCoy, K.R. Marken Jr., M.D. Sumption, E. Gregory, and T.S. Kreilick, "Critical Field Enhancement Due to Field Penetration in Fine-Filament Superconductors", Adv. Cryo. Eng. 36, 255 (1990).

14. P. Estop, J.P. Tavergnier, C. Agnoux, and A. Fevrier, "Magnetization and Critical Current Density of Ultra-Fine Multifilamentary Superconductive Wires", IEEE Trans. Magn. 27, 2170 (1991).

15. J.R. Cave and A.M. Campbell, "AC Losses in Ultra-Fine Filamentary Superconductors", Presented at the International Cryogenic Materials Conference, Huntsville, AL, June 11-14 (1991).

16. C.P. Bean and J.D. Livingston, "Surface Barrier in a Type-II Superconductor", Phys.

Rev. Lett. 12, 14 (1964).

17. M.A.R. Leblanc and J.P. Lorrian, "Effect of Field Independent Surface Barriers on Hysteresis Losses in Type-II Superconductors", Cryogenics 24, 143 (1984).

18. W.J. Carr, "Hysteresis Loss in Fine-Filament Superconductors", Presented at the International Cryogenic Materials Conference, Huntsville, AL, June 11-14 (1991).

19. E.W. Collings, "Stabilizer Design Considerations in Fine Filament Cu/NbTi Composites", Adv. Cryo. Eng. 34, 867 (1988).

20. A.K. Ghosh and W.B. Sampson, "The Effect of Magnetic Impurities and Barriers on the Magnetization and Critical Currents of Fine Filament NbTi Composites", IEEE Trans. Magn. 24, 1145 (1988).

21. E.W. Collings, K.R. Marken Jr., M.D. Sumption, E. Gregory, and T.S. Kreilick, "Magnetic Studies of Proximity-Effect Coupling in a Very Closely Spaced Fine-Filament NbTi/CuMn Composite Superconductor", Adv. Cryo. Eng. 36, 231 (1990).

22. E.W. Collings and K.R. Marken Jr., "Properties of Double Stacked Strands", Interim Technical Report to Lawrence Berkeley Laboratory, August 1, (1991).

23. G. Deutscher and P.G. DeGennes, in Superconductivity, edited by R.D.Parks (Dekker, New York, 1969), pp. 1005-1033.

24. A.C. Mota, P. Visani, and A. Pollini, "Magnetic Properties of Proximity-Induced Superconducting Copper and Silver", J. Low T. Phys. 76, 456 (1989).

25. S. Takács, "Properties of Superfine Filaments Imbedded in a Normal Matrix", Czech. J. Phys. B36, 524 (1986).

26. K. Yasohama, K. Morita, and T. Ogasawara, "Superconducting Properties of Cu-NbTi Composite Wires With Fine Filaments", IEEE Trans. Magn. 23, 1728 (1987).

27. J.R. Cave, A. Fevrier, and T. Verhaege, "Reduction of Losses in Ultra-Fine Multifilamentary Wires", IEEE Trans. Magn. 25, 1945 (1989)

28. P. Dubots, A. Février, and H.G. Ky, "Specific Properties of NbTi Filaments", Proceedings of International Symposium on Flux Pinning and Electromagnetic Properties in Superconductors", edited by T. Matusushita, K. Yamafuji, and F. Irie, Fukuoka, Japan, Nov 11-14, 255 (1985).

29. Y. Oda, G. Fujii, and H. Nagano, "Diamagnetic Transition Due To Proximity Effect

in a Multi-Filamentary Nb-Ti Superconductor", Jpn. J. Phys. 21, 137 (1982).

30. J.R. Cave, A. Fevrier, and H.G. Ky, "Calculation of AC Losses in Ultra Fine Filamentary Wires", IEEE Trans. Magn. 23, 1732 (1987).

31. K. Ohmatsu, M. Nagata, M. Kawashima, H. Tateshi, and T. Onishi, "AC Losses of NbTi Superconducting Wires With Fine Filament", IEEE Trans. Magn. 25, 2105 (1989).

32. P. Dubots, A. Février, J.C. Renard, and J.P. Tavergnier, "NbTi Wires with Ultra-Fine Filaments for 50-60 Hz use: Influence of the Filament Diameter on Losses", IEEE Trans. Magn. 21, 177 (1985).

33. I. Hlásnik, "Progress and Problems in Superconducting Composites for AC Applications", Proceedings of International Symposium on Flux Pinning and Electromagnetic Properties In Superconductors", edited by T. Matsushita, K. Yamafuji, and F. Irie, Fukuoka, Japan, Nov 11-14, 247 (1985).

34. A.K. Ghosh, W.B. Sampson, E. Gregory and T.S. Kreilick, "Anomalous Low Field Magnetization in NbTi Conductors", IEEE Trans. Magn. 23, 1724 (1987).

35. A.K. Gosh and W.B. Sampson "Magnetization and Critical Currents of NbTi Wires

with Fine Filaments", Adv. Cryo. Eng. 32, 809 (1986).

36. W.J. Carr Jr. and G.R. Wagner "Magnetic Behavior of a Very Fine Filament Continuous Superconductor", Adv. Cryo. Eng. 32, 801 (1986).

37. S. Takács, "Pinning on Grain Boundaries and in Superfine Filaments", Proceedings of the International Symposium on Flux Pinning and Electromagnetic Properties in Superconductors, edited by T. Matsushita, K. Yamafuji, and F. Irie, Fukuoka, Japan, Nov 11-14, 204 (1985).

38. W.J. Carr Jr., "Effect of Twist on Wires Made From in-situ Superconductors", J. Appl. Phys. 54, 6549 (1983).

39. V.M. Pan, S.I. Mukhin, V.S. Flis, M.G. Vasilenko, V.I. Latysheva, L.M. Fisher, and V.M. Dzugutov, "AC Losses in Untwisted in-situ Superconductors above the Percolation Threshold", IEEE Trans. Magn. 21, 408 (1985).

40. N. Harada, Y. Mawatari, O. Miura, Y. Tanaka, and K. Yamafuji, "Excess Magnetization due to Interfilamentary Proximity Coupling in Nb-Ti Multifilamentary Wires", Cryogenics 31, 183 (1991).

41. M.D. Sumption and E.W. Collings, "Effect of Twist Pitch, Sample Length, and Field

Orientation on the Proximity Enhanced Magnetization of Fine Filamentary Multifilamentary Strands", Presented at the International Cryogenic Materials Conference, Huntsville, AL, June 11-14 (1991).

42. M.D. Sumption and E.W. Collings, "Temperature and Field Dependence of Short Term Decay and Loss in Multifilamentary Superconductors-- A Proximity Effect Interpretation", Presented at the International Cryogenic Materials Conference, Huntsville, AL., June 11-14 (1991).

43. K.R. Marken Jr., M.D. Sumption, and E.W. Collings, "Magnetization Decay of SSC-Type Strands in Various Short Test Sample Configurations", Presented at the International Cryogenic Materials Conference, Huntsville, AL., Nov 11-14 (1991).

44. M.D. Sumption, K.R. Marken Jr., and E.W. Collings, "Position and Amplitude of Proximity Effect Peaks in the Magnetization Curves of NbTi/Cu and NbTi/CuMn Multifilamentary Strands", IEEE Trans. Magn. 27, 1129 (1991).

45. G.H. Morgan, "Theoretical Behavior of Twisted Multicore Superconducting Wire in a Time Varying Uniform Magnetic Field", J. Appl. Phys. 41, 3673 (1970).

46. M.D. Sumption, K.R. Marken Jr., and E.W. Collings, "Hysteretic Surface Effects in

Multifilamentary NbTi Wires Exposed to Transverse Applied Fields", IEEE Trans. Magn. 27, 2166 (1991).

47. D. Saint-James, G. Sarma, Type II Superconductivity, (Pergamon, New York, 1969) pp. 81-120.

48. D. Shoenburg, Superconductivity, (Cambridge Press, London 1962), pp. 20-22.

49. W.A. Fietz, "Reversible and Irreversible Magnetic Properties of Some Type-II Alloy Superconductors", Ph. D. Thesis, Cornell (1967).

50. W.J. Carr, "End Effects on the Loss for Short Superconductors", Adv. Cryo. Eng. 28, 581 (1982).

51. E.M. Gyorgy, R.B. VanDover, K.A. Jackson, L.F. Scheneemeyer, and J.V. Waszczak, "Anisotropic Critical Currents in $Ba_2YCu_3O_7$ Analyzed Using an Extended Bean Model", Appl. Phys. Lett. 55, 283 (1989).

52. S. Hu, H. Hojaji, A. Barkett, M. Boroomand, A.N. Thorpe, and S. Altersecu, "Anisotropic Electromagnetic Features of a Grain-Aligned $YBa_2Cu_30_x$ Bulk Superconductor", Phys. Rev. B 43, 2878 (1991).

53. F.M. Sauerzopf, H.P. Wiesinger, and H.W. Weber, "Anisotropic Current Flow and Demagnetization Corrections in the Bean Model", Cryogenics 30, 650 (1990).

54. M.N. Wilson, C.R. Walters, J.D. Lewin, P.F. Smith, and A.H. Spurway,"Experimental and Theoretical Studies of Filamentary Superconducting Composites", J. Phys. D: Apply. Phys. 3, 1517-1583 (1970).

55. W.J. Carr Jr., AC Loss and Macroscopic Theory of Superconductors, (Gordon and Breach, New York, 1983) pp. 106-111.

56. K.R. Marken Jr., A.J. Markworth, M.D. Sumption, E.W. Collings, and R.M. Scanlan, "Eddy Current Effects in Twisted and Wound SSC Strands", IEEE Trans. Magn. 27, 1791 (1990).

57. S. Tákacs, "Coupling Losses in Cables in Spatially Changing AC Fields", Cryogenics 22, 661 (1982).

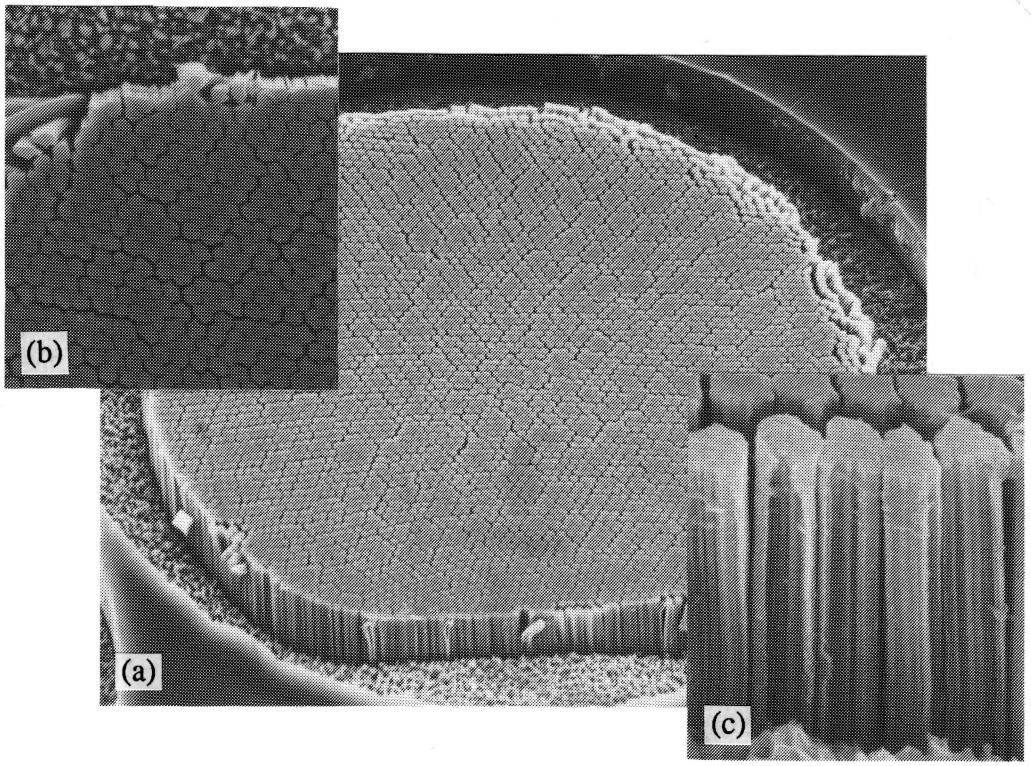

Fig. A1 SEM of strand NTCU07 at: (a) 1500 X, (b) 3000 X, (c) 10000 X

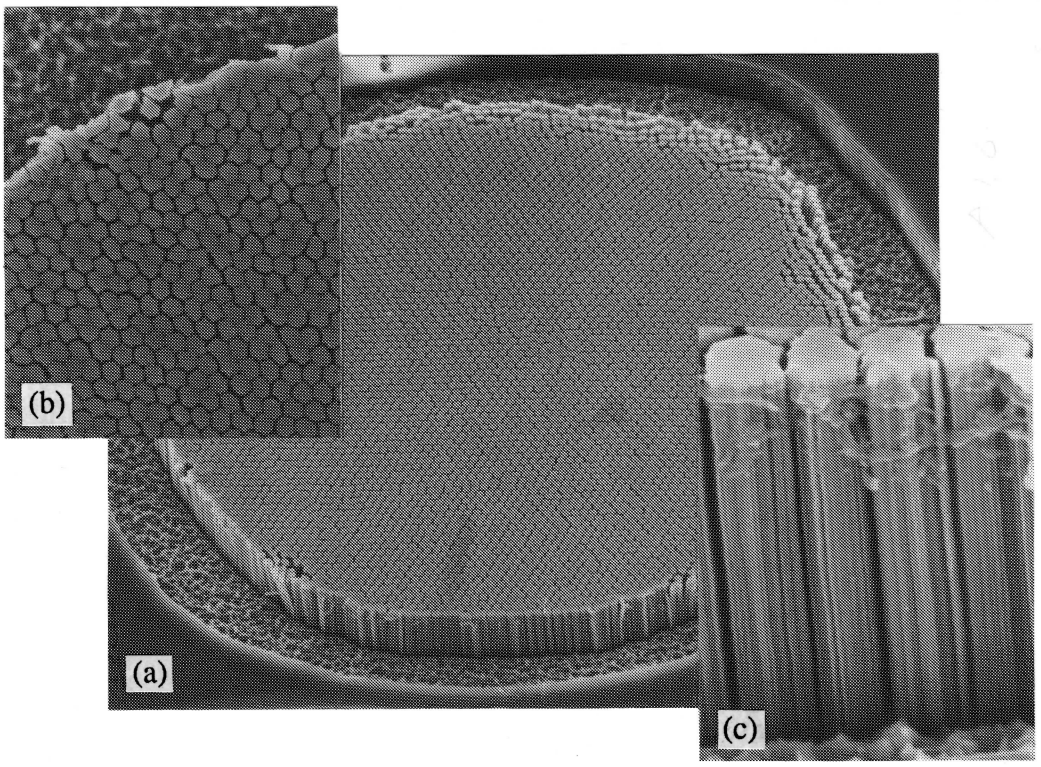

Fig. A2 SEM of strand NTCU10 at: (a) 1100 X, (b) 2500 X, (c) 9000 X

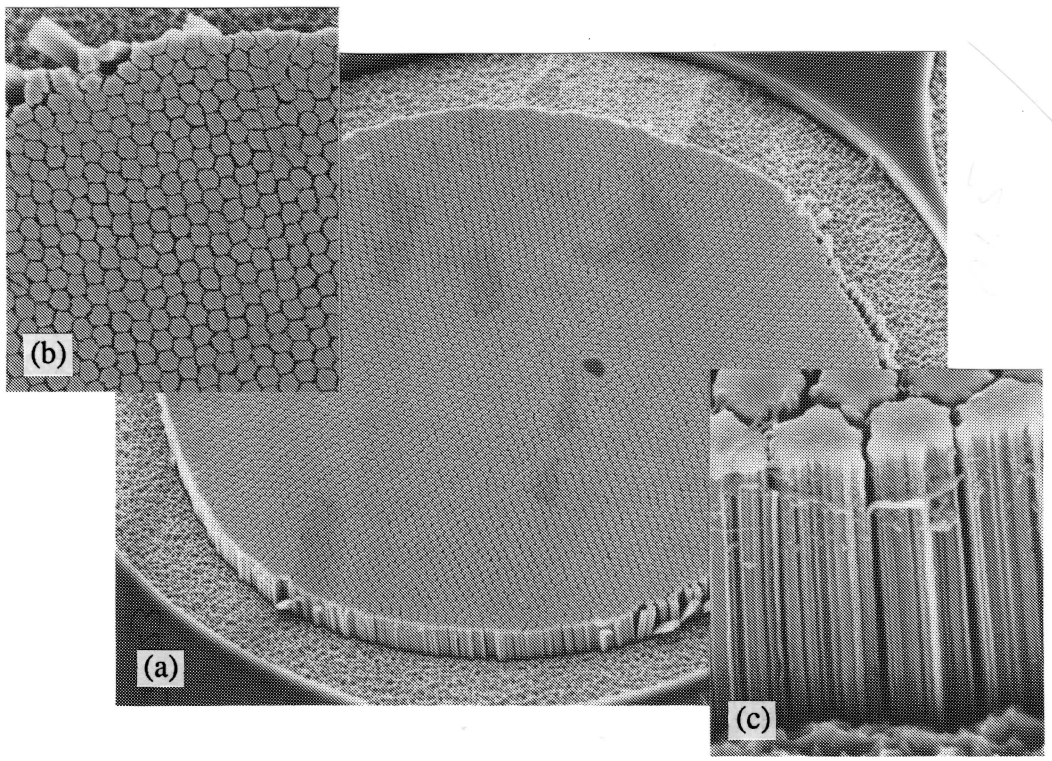

Fig. A3 SEM of strand NTCU14 at: (a) 750 X, (b) 1800 X, (c) 7500 X

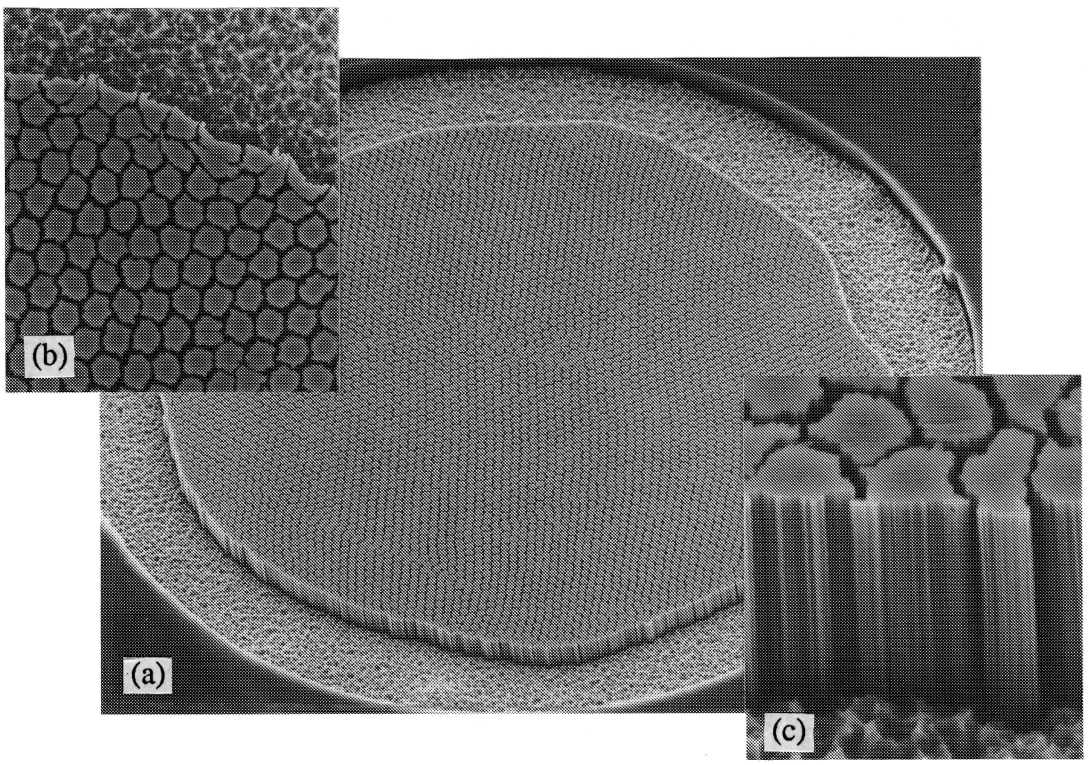

Fig. A4 SEM of strand NTCU20 at: (a) 550 X, (b) 2000 X, (c) 6000 X

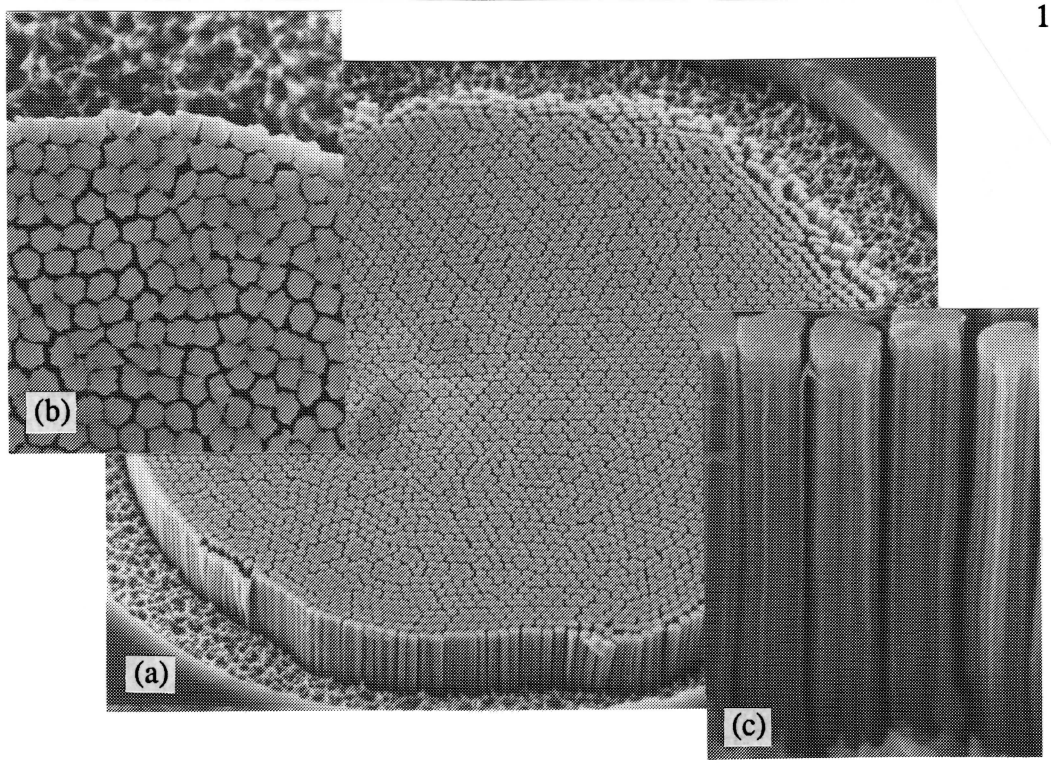

Fig. A5 SEM of strand NTCM07 at: (a) 1500 X, (b) 4000 X, (c) 10000 X

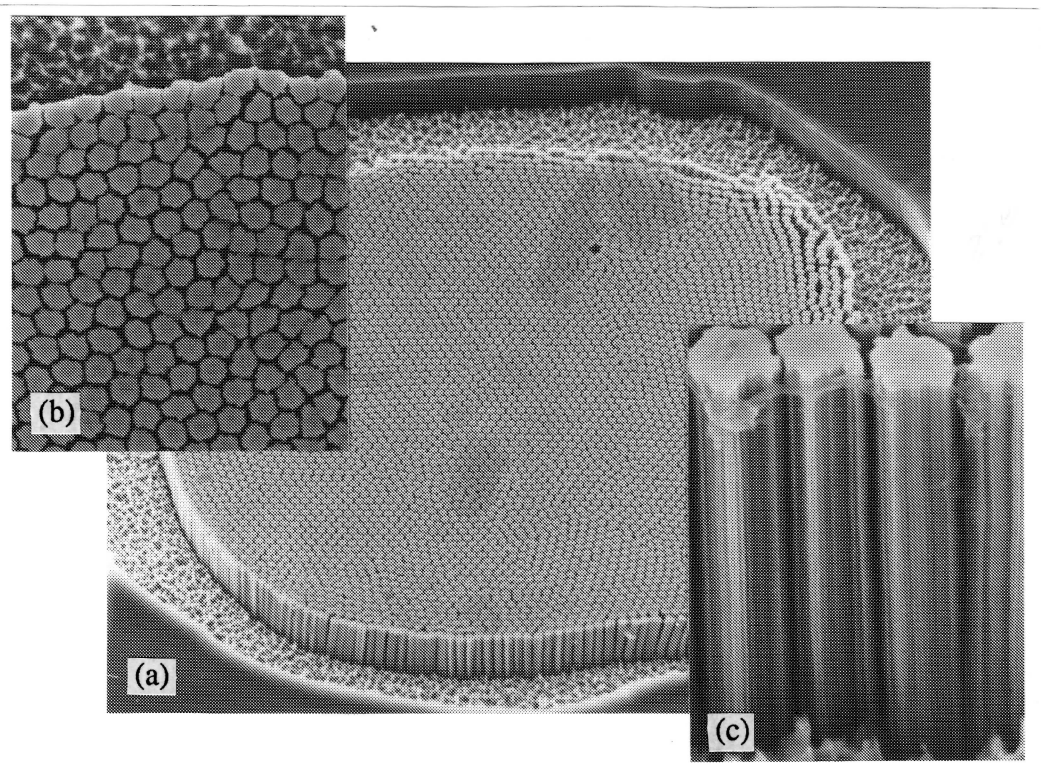

Fig. A6 SEM of strand NTCM10 at: (a) 1000 X, (b) 3000 X, (c) 9000 X

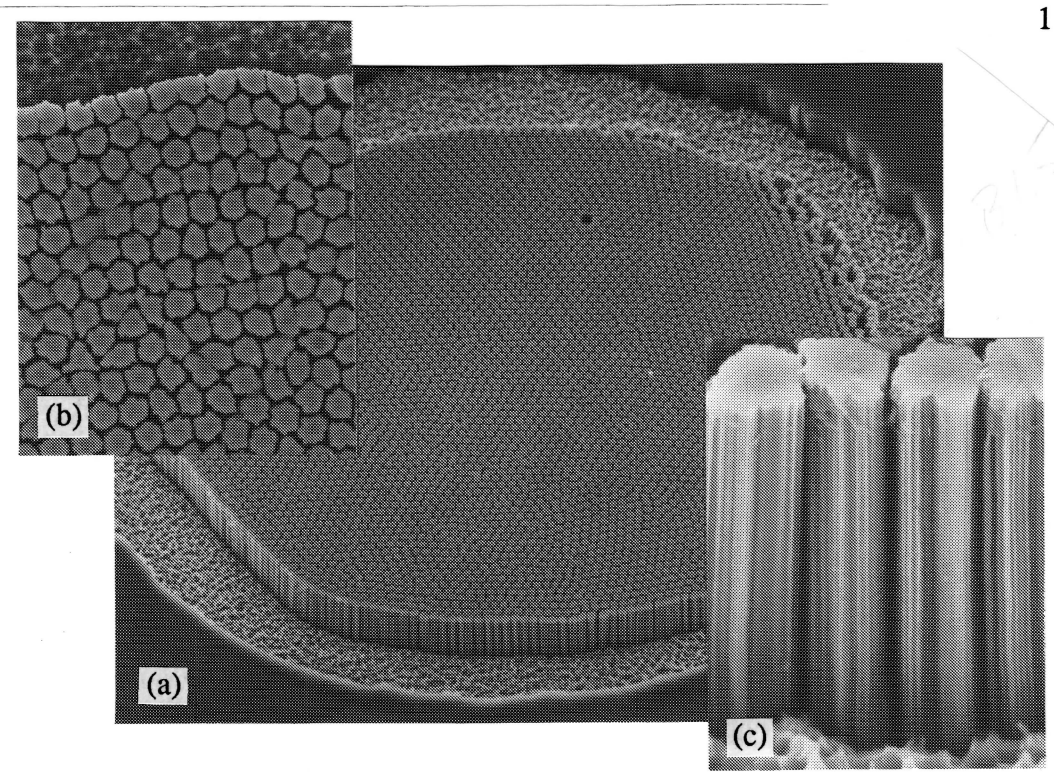

Fig. A7 SEM of strand NTCM14 at: (a) 800 X, (b) 2500 X, (c) 8000 X

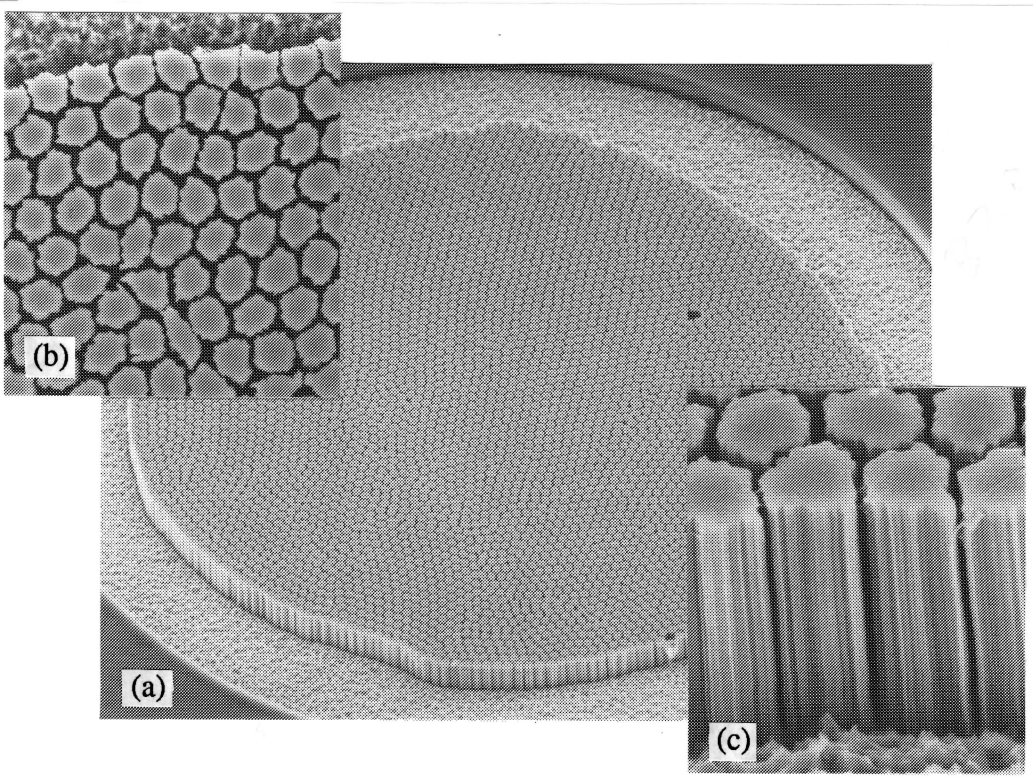

Fig. A8 SEM of strand NTCM20 at: (a) 600 X, (b) 2500 X, (c) 6000 X

Appendix B: Determination of the $(dH/dt)_{eff}$ for Stepping Field Sweep

This appendix compares the effective dH/dt for two different H-t profiles. The first is the standard continuous sweep, triangular wave H-t typically employed in a commercial VSM apparatus. The second profile is just that created by a ramp-and-hold procedure, where one M-H data point is taken per ramp-hold, at the end of the hold. This is the method that was employed in M-H measurements before the use of computerized equipment was common. To our knowledge this calculation of $(dH/dt)_{eff}$ has not appeared elsewhere. We include it here to show that the $(dH/dt)_{eff}$ reached by the stepping approach is much lower than that of the continuous sweep method, showing that data taken in this way approach static conditions.

Using the assumptions that:

(1) Dynamic PEs are negligible

(2) $M_T = M_S + M_E$ (in general)

(3) $M_E = M_{E0}\exp(-t/\tau_d)$ (following a single dH/dt pulse).

Where M_T is the total magnetization, M_S is the static magnetization (of any origin), and M_E is the eddy current magnetization. These last two expressions are just the condition that eddy current saturation does not occur (i.e. low frequency, low eddy current coupling). This expression for M_E is correct in general for the time following a dH/dt

pulse, and in particular we can use it for a time t_h. We can then imagine a sequence of ramp-hold M-H segments of hold time t_h, and we can describe the M value at the time t_h with the expression

$$M_T(t_h) = M_S + M_E(t_h) \qquad where \qquad M_E(t_h) = M_{E0}\exp(-t_h/\tau_d) \ .$$

Shown in Fig. B1 are the H-t diagrams of the two different M-H loops: (a) a continuous sweep loop, (b) a stepping loop.

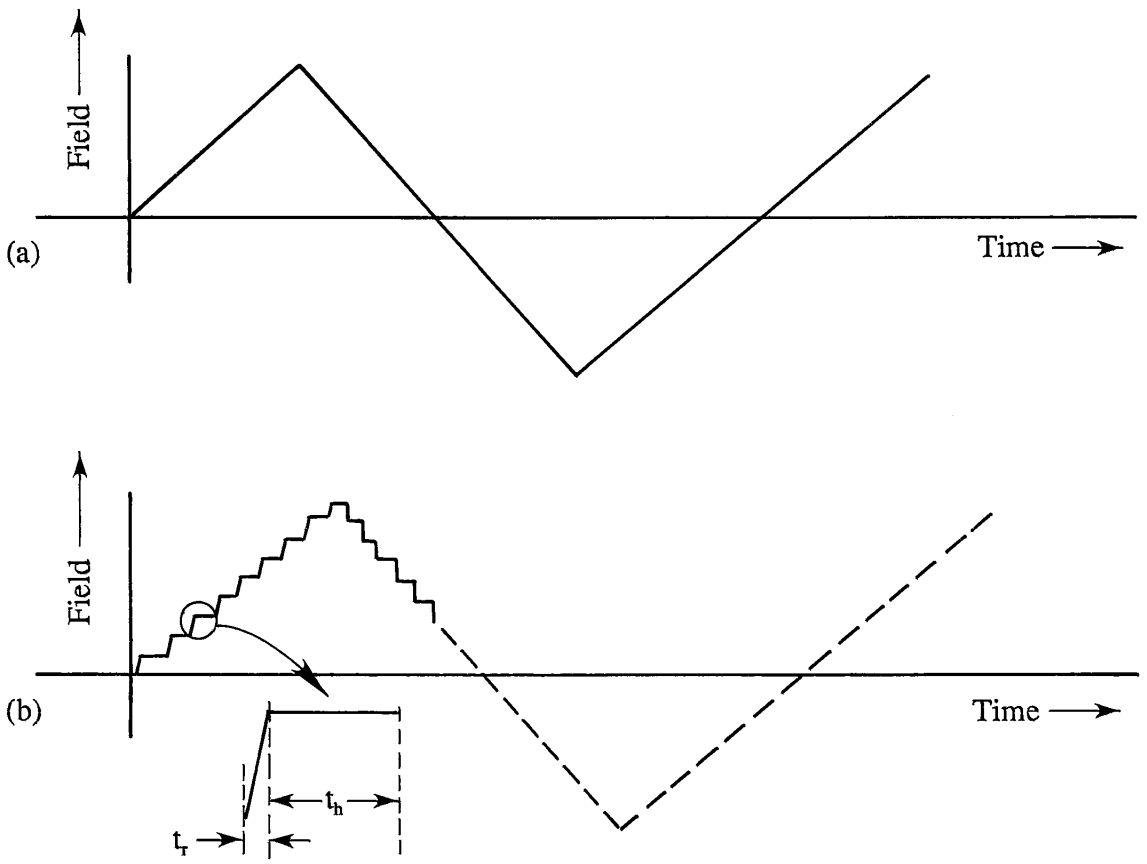

Fig. B1 H-t profiles for M-H loops taken in the

(a) continuous mode, and (b) stepping mode

For a direct comparison of these, we take a total loop measurement time of nt_{tot}, where n points are taken over a four segment M-H loop.

We can define

t_r = the time ramp per step-hold interval = $t_{tot}p$

t_h = the hold time per step-hold interval = $t_{tot}(1-p)$

and note that the field must jump $4H_m/n$ at each point in the stepping M-H loop.

It is known that $Q_E = GH_m^2(dH/dt)$ where G is a constant[54]. If we make the approximation $Q_E = 4H_mM_{EO}$ for a continuous loop, we can see that $M_{EO} = (H_m/4)G(dH/dt)$. M_E should be dependent, in a similar manner, on an effective dH/dt

$$M_E(t_h) \equiv \frac{GH_m}{4}\left(\frac{dH}{dt}\right)_{eff}$$

but remember that

$$M_{E0}\exp(-t_h/\tau_d) = M_E(t_h) = \frac{GH_m}{4}\left(\frac{dH}{dt}\right)_{eff}$$

then

$$\frac{GH_m}{4}\left(\frac{dH}{dt}\right)\exp(-t_h/\tau_d) = \frac{GH_m}{4}\left(\frac{dH}{dt}\right)_{eff}$$

which implies that

$$\left(\frac{dH}{dt}\right)_{eff}\{t_h, \tau_d, \ldots\} = \left(\frac{dH}{dt}\right)\exp(-t_h/\tau_d)$$

where the { } brackets enclose the variables that a function is dependent on. Note that the

dH/dt for M_{EO} is that of the ramp rate during the ramp time.

Now

$$\left(\frac{dH}{dt}\right)_r = \frac{4H_m}{t_{tot}\, pn}$$

so that

$$\left(\frac{dH}{dt}\right)_{eff}\{\, t_h,\ \tau_d,\ (dH/dt)_r \,\} = \frac{4H_m}{t_{tot}\, pn}\exp(-t_h/\tau_d)\ .$$

Note, however, that dH/dt for a continuous loop of the same total sweep time is

$$\left(\frac{dH}{dt}\right)_c = \frac{4H_m}{t_{tot}\, n}$$

so that

$$\left(\frac{dH}{dt}\right)_{eff} = \frac{1}{p}\left(\frac{dH}{dt}\right)_c \exp\left(\frac{-t_{tot}(1-p)}{\tau_d}\right)$$

where $(dH/dt)_c$ is the rate for a continuously ramped field, for a loop which has the same total sweep time and H_m.

In order to calculate a value for $(dH/dt)_{eff}$ it is somewhat easier to use the expression

$$\left(\frac{dH}{dt}\right)_{eff} = \left(\frac{dH}{dt}\right)_r \exp(-t_h/\tau_d)\ .$$

For our samples, τ_d's range from a few milliseconds to 30 seconds. In all of our step by

step measurements $t_r \approx 3$ seconds, while $t_h \approx 270$ seconds, giving a $p \approx 0.01$. For our long time constant samples, with $\tau_d \approx 30$ sec,

$$\left(\frac{dH}{dt}\right)_{eff} = \left(\frac{dH}{dt}\right)_r \exp(-t_h/\tau_d) \approx \frac{2000\ Oe}{3\ \text{sec}} \exp(-270/30) \approx 0.08\ Oe/s$$

which is a very low $(dH/dt)_{eff}$ indeed. With this method we could take half loops of 50 points for a H_m of 17 kOe in about 4 1/2 hours. If we double this to nine hours, the dH/dt of a continuous measurement of a full loop with the same field sweep would be (4 17000 Oe/3600 9 sec) = 2.09 Oe/s, larger by a factor of ~ 20. This ratio is, of course even more pronounced for the smaller τ samples.

We note several items. First, this calculation assumes that the magnetization and loss will decay exponentially. This is the reason that this step by step method is useful; other decay behavior (e.g. creep) requires different calculations. Second, $(dH/dt)_{eff}$ is material dependent. Thirdly, the actual loss induced in the sample will be proportional to the ramp rate, rather than the $(dH/dt)_{eff}$.

Appendix C: Critical Currents in a Helically Twisted, Proximity-Effected Multifilamentary Strand

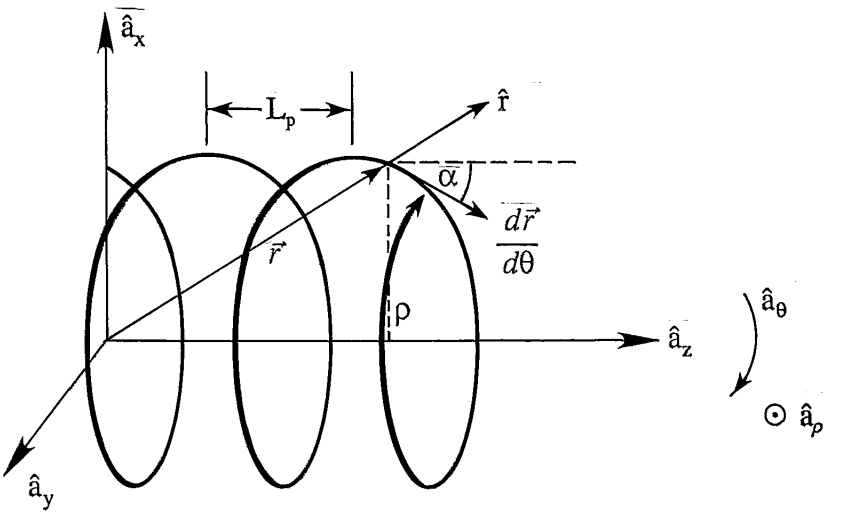

We want to find J_{cz} in terms of J_{cfil} and J_{cp}. In order to do this we need to find $\hat{a}_z$ in terms of $\hat{a}_1$ and $\hat{a}_3$.

From the diagram at right we can see that

(an expanded view of the above)

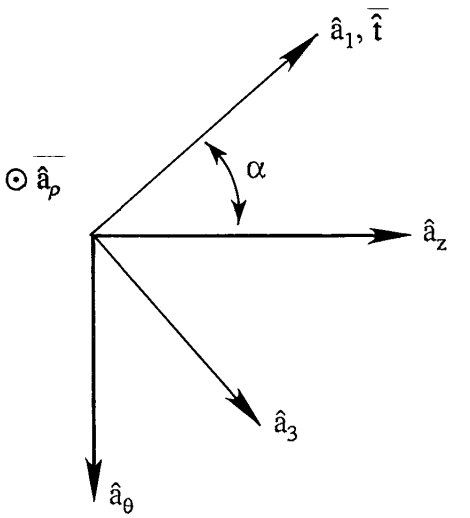

$$\hat{a}_\theta = -\hat{a}_1 \sin\alpha + \hat{a}_3 \cos\alpha$$

$$\hat{a}_z = \hat{a}_1 \cos\alpha + \hat{a}_3 \sin\alpha$$

In order to find α in terms of L_p and ρ, we need to dot multiply the tangential vector of the helix ($\hat{t}$) with $\hat{a}_z$. The radial vector of the helix is given by

$$\vec{r} = \rho\hat{a}_\rho + z\hat{a}_z$$

but since $z = \dfrac{-L_p\theta}{2\pi}$, $d\vec{r} = \rho d\hat{a}_\rho + \dfrac{L_p}{2\pi} d\theta \hat{a}_z$ and $d\hat{a}_\rho = \dfrac{d\hat{a}_\rho}{d\theta} d\theta = -\hat{a}_\theta d\theta$

this gives $d\vec{r} = \left(\rho\hat{a}_\theta + \dfrac{L_p}{2\pi}\hat{a}_z \right) d\theta$, $\left|\dfrac{d\vec{r}}{d\theta}\right| = \left(\rho^2 + \left(\dfrac{L_p}{2\pi}\right)^2\right)^{1/2}$.

Then the unit vector tangential to the helix is given by

$$\hat{t} = \frac{d\vec{r}}{d\theta} \Big/ \left|\frac{d\vec{r}}{d\theta}\right| = \frac{\rho\hat{a}_\theta + (L_p/2\pi)\hat{a}_z}{(\rho^2 + (L_p/2\pi)^2)^{1/2}}$$

and then $\cos\alpha$ can be found from

$$\hat{t} \cdot \hat{a}_z = \cos\alpha , \quad \cos\alpha = \frac{(L_p/2\pi\rho)}{(1 + (L_p/2\pi\rho)^2)^{1/2}} ,$$

but if we now let $\beta_\rho \equiv L_p/(2\pi\rho)$ we get

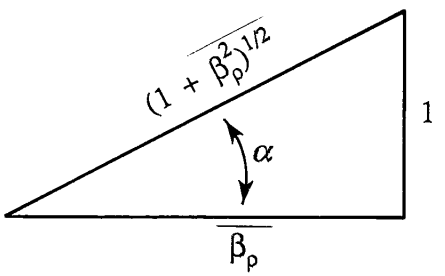

$$\cos\alpha = \frac{\beta_\rho}{(1 + \beta_\rho^2)^{1/2}} ,$$

$$\sin\alpha = \frac{1}{(1 + \beta_\rho)^{1/2}}$$

in which case

$$\hat{a}_z = \frac{\beta_\rho}{(1 + \beta_\rho^2)^{1/2}} \hat{a}_1 + \frac{1}{(1 + \beta_\rho^2)^{1/2}} \hat{a}_3 .$$

In order to get the J_cs we will introduce four plausible assumptions. The first of these is to describe the multifilamentary composite as a homogenous, anisotropic

continuum (cf. Sec. 5.1.1). Using the second assumption that $J_{cp} = 0$, we can write the J_cs in terms of the $\hat{a}_{1,2,3}$ unit vectors.

$$J_{c1} = \lambda J_{cfil}$$

$$J_{c2} = 0$$

$$J_{c3} = J_{cp} \ .$$

The third assumption is that the currents in both the $\hat{a}_1$ and $\hat{a}_3$ directions are described by the critical state model. The fourth assumption, originally employed by Carr[38] , is that if we project the currents on to the $\hat{a}_{\rho,\theta,z}$ directions, only currents along the $\hat{a}_z$ direction will be non-zero for a very long conductor. This is just the way in which the currents flow in an isotropic homogenous cylindrical superconductor (transverse applied H).

The setting up of a critical current in the z-direction allows only one of the critical currents J_{c1} and J_{c3} to flow in the direction of its associated unit vector (either $\hat{a}_1$, or $\hat{a}_3$). The current in the other direction will be on average less than J_c, although this can be seen as J_c flowing down only part of the cross sectional area (see Carr[38] for another description of this). Which of these currents is saturated will depend on the helix angle, α.

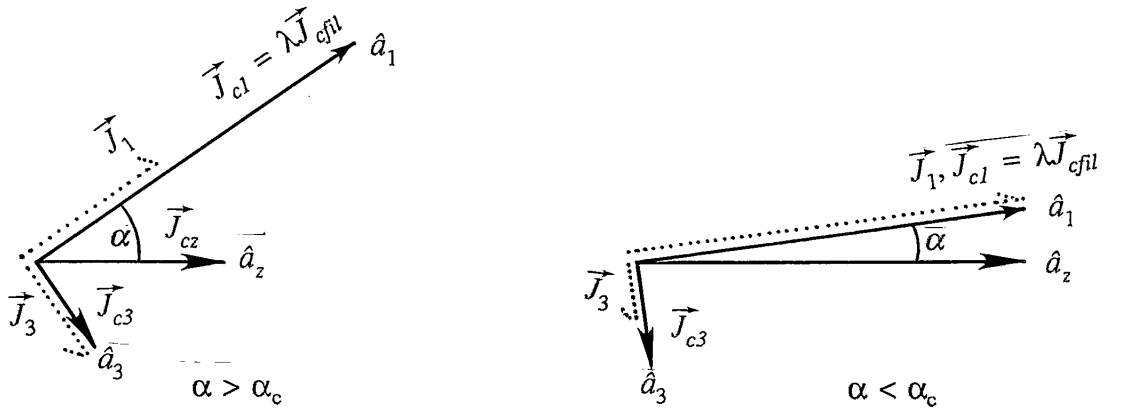

For $\alpha > \alpha_c$, J_{cz} is limited by the size of the J_{cp}, and $J_1 < J_{cfil}$. For $\alpha < \alpha_c$, J_{cz} is λJ_{cfil} limited, and $J_3 < J_{cp}$. At the critical angle α_c both J_1 and J_3 are saturated, and J_{cz} is a maximum. By projecting $\hat{a}_z$ along the $\hat{a}_1$ and $\hat{a}_3$ vectors we can see that

$$J_{cz} = \begin{cases} \dfrac{\lambda J_{cfil}}{\cos\alpha} & \alpha < \alpha_c \\ \text{for} & \\ \dfrac{J_{cp}}{\sin\alpha} & \alpha > \alpha_c \end{cases}$$

which can be rewritten in the form seen in Chapter 5

$$J_{cz} = \begin{cases} \lambda J_{cfil}\left(1 + \left(\dfrac{1}{\beta_\rho}\right)^2\right)^{1/2} & \alpha < \alpha_c \\ \text{for} & \\ J_{cp}\beta_\rho\left(1 + \left(\dfrac{1}{\beta_\rho}\right)^2\right)^{1/2} & \alpha > \alpha_c \end{cases} .$$

We can rewrite the critical criterion in terms of L_p and ρ by setting the two branches of the J_{cz} equation equal to each other at α_c. This gives

$$\lambda J_{cfil} = J_{cp}\beta_\rho$$

or

$$\lambda J_{cfil} = \frac{J_{cp} L_p}{2\pi\rho}$$

which can be rewritten to find a critical L_p at a given ρ, or vice versa.

Appendix D: Non-Axial Currents in Long Strands

Following Carr[38], we have taken the currents which flow to be such that if they were projected along the unit vectors $\hat{a}_{\rho,\theta,z}$, only the currents in the z-direction would be non-zero. In this appendix we argue that it is reasonable to expect non-axial currents, but that these can be treated as a correction term to the expressions calculated in Chapter 5. Let us now find the relation between the currents and the flux gradients, without the assumption that J_ρ and J_θ are zero. The Maxwell curl equation is

$$\vec{\nabla} \times \vec{B} = \begin{vmatrix} \frac{1}{\rho}\hat{\rho} & \hat{\theta} & \frac{1}{\rho}\hat{z} \\ \frac{\partial}{\partial\rho} & \frac{\partial}{\partial\theta} & \frac{\partial}{\partial z} \\ B_\rho & \rho B_\theta & B_z \end{vmatrix} = \left(\frac{4\pi}{10}\right)\vec{J} \quad \text{, in cgs-practical units.}$$

If we invoke the assumption of an anisotropic homogenous continuum, we get translational symmetry along the z-axis. The above equation then becomes

$$\frac{4\pi}{10}\vec{J} = \hat{\rho}\left(\frac{1}{\rho}\frac{\partial B_z}{\partial\theta}\right) - \hat{\theta}\frac{\partial B_z}{\partial\rho} + \hat{z}\frac{1}{\rho}\left(\frac{\partial(\rho B_\theta)}{\partial\rho} - \frac{\partial B_\rho}{\partial\theta}\right)$$

which has the components

$$J_\rho = \left(\frac{10}{4\pi\rho}\right)\left(\frac{\partial B_z}{\partial\theta}\right)$$

$$J_\theta = -\left(\frac{10}{4\pi}\right)\left(\frac{\partial B_z}{\partial\rho}\right)$$

$$J_z = \left(\frac{10}{4\pi\rho}\right)\left(\frac{\partial(\rho B_\theta)}{\partial\rho} - \frac{\partial B_\rho}{\partial\theta}\right) \quad .$$

Also, this anisotropic, homogenous, continuum helix is antisymmetric about the y-z plane (if the field is applied transverse to the strand, along the y-axis, as shown below). This means that $B_z(x,y) = -B_z(-x,y)$, which further implies that $B_z(y,x=0) = 0$. Additionally, from translational invariance

$$\frac{\partial B_z}{\partial z} = \frac{\partial J_\theta}{\partial z} = \frac{\partial J_\rho}{\partial z} = 0.$$

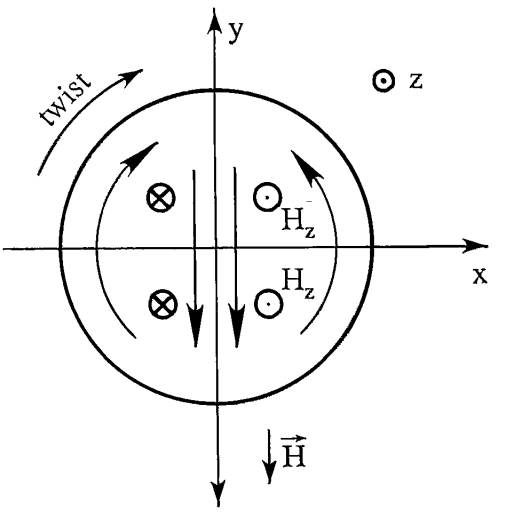

This means that in order for non-axial currents to flow: (1) an H_z field must exist, which is invariant in z, and has gradients in both θ and ρ, (2) the currents themselves must be antisymmetric about the y-z plane. This should give currents of the form seen above.

Note that this is consistent with the currents that would tend to flow in order to provide additional shielding (trapping). This is because currents that would provide additional shielding would flow down the filaments, and cross back along the axis of the applied field, as shown on the next page.

The above results follow simply from Maxwell's equations and symmetry arguments. It may be possible, however, to gain additional insight from the eddy current case, where a similar effect is seen[57].

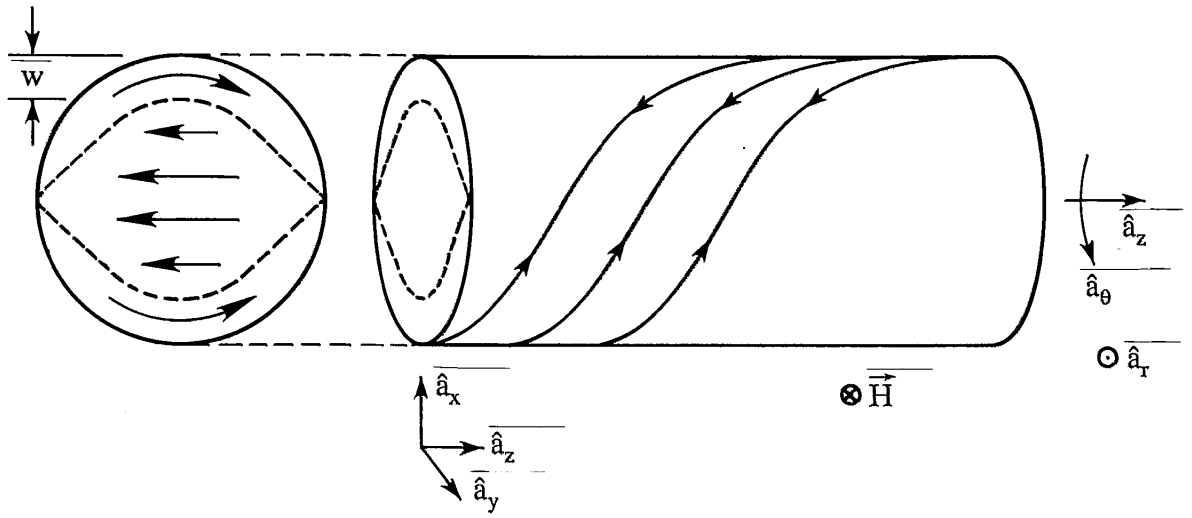

In this case Carr[57], from a consideration of the divergence of the total current, derives

$$\frac{\partial J_\rho}{\partial \rho} = -\frac{1}{\rho}\frac{\partial J_\theta}{\partial \theta} \quad . \qquad \text{Eq. 7.4.1}$$

Yamafuji et al.[9], in their first paper on PE L_p dependence, veiwed all strand sheilding currents as flowing down the $\hat{a}_1$ direction, and then crossing back along the axis of the applied field. If we take $J_\rho = -\lambda_p J_{cp}\sin\theta$ as Yamafuji et al. have in analogy with the eddy current case, then

$$\frac{1}{\rho}\frac{\partial J_\theta}{\partial \theta} = -\lambda_p J_{cp}\sin\theta$$

where we have used the equation 7.4.1, and then

$$J_z = \frac{L_p}{2\pi}\lambda_p J_{cp}\cos\theta \quad .$$

as a similar magnitude as the Carr equations for small L_p. This is because $J_{c3} = J_{c2} = J_{cp}$. It seems reasonable, as in the eddy current problem, to see the axial currents as the dominant terms, while the non-axial currents are the correction terms. We note, however, that in order to add this correction, it may be necessary to re-examine Carr's assumption that J_{c1}, J_{c2}, and J_{c3} are independent.

Appendix E: Calculation of ΔM for a Fully Penetrated PE Multifilamentary Strand

The total magnetization is given by

$$\vec{M} = \left(\frac{1}{V}\right)\left[\frac{1}{20}\int \vec{r}\, x\, \vec{J}_c(\vec{r})\, d\tau\right]$$

, in cgs-practical units where $\vec{M}$ represents an average magnetization, and

$$r = (\rho^2 + z^2)^{1/2}$$

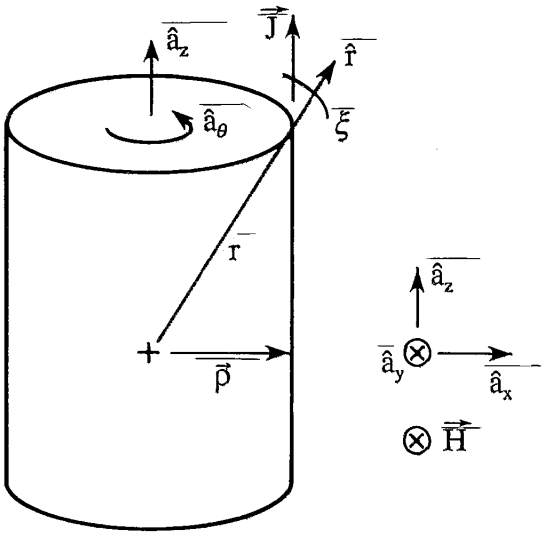

If we take into account the currents crossing the ends of the conductor at infinity[57], we get

$$\vec{M}_{tr} = \left(\frac{1}{V}\right)\left(\frac{1}{10}\right)\left[\int \vec{r}\, x\, \vec{J}_c(\vec{r})\, d\tau\right]$$

for the transverse magnetization.

Then

$$\vec{M} = \left(\frac{1}{V}\right)\left(\frac{1}{10}\right)\int \vec{r}\, x\, \vec{J}(\vec{r})\, \rho d\rho d\theta dz \quad .$$

$M_z = 0$ since $\hat{z}\cdot(\vec{r}\, x\, \vec{J}) = 0$ and $M_x = 0$ from symmetry in θ about x = 0.

This leaves

$$M_y = \left(\frac{1}{10\pi R^2 2L}\right)\int \hat{y}\cdot(\vec{r}\, x\, \vec{J})\, \rho d\rho d\theta dz$$

where, taking a cylinder 2L long, as $L \rightarrow \infty$, we get

$$M_y = \lim_{L\to\infty}\left(\frac{2}{10\pi R^2 2L}\right)\int_0^R\int_{-\pi/2}^{\pi/2}\int_{-L}^{L}\cos\theta\sin\xi J_c r\rho d\rho d\theta dz$$

$$= \lim_{L\to\infty}\left(\frac{8}{20\pi R^2 L}\right)\int_0^R\int_0^L rJ(r)\left(\frac{\rho}{r}\right)\rho d\rho dz$$

$$= \left(\frac{8}{20\pi R^2}\right)\int_0^R \rho^2\, J(\rho)\, d\rho = \left(\frac{2}{5\pi R^2}\right)\left[\int_0^R \rho^2\, J_{cz}(\rho)d\rho\right]$$

$$= \left(\frac{2}{5\pi R^2}\right)\left[\int_0^{\rho'}\lambda\rho^2 J_{cfil}\left(1+\left(\frac{2\pi\rho}{L_p}\right)^2\right)^{1/2} d\rho + \int_{\rho'}^R\left(\frac{\rho J_{cp}L_p}{2\pi}\right)\left(1+\left(\frac{2\pi\rho}{L_p}\right)^2\right)^{1/2} d\rho\right]$$

where

$$\rho' = \begin{cases} \rho_c = \dfrac{L_p J_{cp}}{2\pi\lambda J_{cfil}} & L_p \leq \\ & (for) \quad \left(\dfrac{2\pi\lambda R J_{cfil}}{J_{cp}}\right) = L_{pcm} \\ R & L_p \geq \end{cases} .$$

For $L_p < L_{pcm}$

$$\Delta M = \left(\frac{L_p^3}{240\pi^4 R^2}\right)\left\{8J_{cp}\left(1+\left(\frac{2\pi R}{L_p}\right)^2\right)^{3/2} - 3J_{cp}\left(1+\left(\frac{J_{cp}}{\lambda J_{cfil}}\right)^2\right)^{1/2}\right.$$

$$- 2J_{cp}\left(1 + \left(\frac{J_{cp}}{\lambda J_{cfil}}\right)^2\right)^{3/2} - 3J_{cfil}\lambda \log\left[\left(1+\left(\frac{J_{cp}}{\lambda J_{cfil}}\right)^2\right)^{1/2} + \frac{J_{cp}}{\lambda J_{cfil}}\right]\Bigg\}$$

while for $L_p > L_{pcm}$

$$\Delta M = \left(\frac{J_{cfil}L_p^2}{80\pi^4R^2}\right)\Bigg\{- 2\pi\lambda R\left(1+\left(\frac{2\pi R}{L_p}\right)^2\right)^{1/2} + 4\pi\lambda R\left(1+\left(\frac{2\pi R}{L_p}\right)^2\right)^{3/2}$$

$$- L_p\,\lambda\,\log\left[\left(1+\left(\frac{2\pi R}{L_p}\right)^2\right)^{1/2} + \frac{2\pi R}{L_p}\right]\Bigg\}\ .$$

This second equation comes from

$$\Delta M = \left(\frac{4}{5\pi R^2}\right)\left[\int_0^R \lambda\rho^2 J_{cfil}\left(1+\left(\frac{2\pi\rho}{L_p}\right)^2\right)^{1/2} d\rho\right]\ .$$

Note that

$$\Delta M\ \{\ limit\ as\ L_p \to 0\ \} = \frac{4J_{cp}R}{15\pi}$$

$$\Delta M\ \{\ limit\ as\ L_p \to \infty\ \} = \frac{4\lambda J_{cfil}R}{15\pi}$$

just as would be expected.

These two expressions are rewritten in their dimensionless form in Chapter 5. Note that ΔM for $L_p < L_{pcm}$ has two components, these are

$$\Delta M = \Delta M_A + \Delta M_B$$

$$\Delta M_A = \left(\frac{L_p^3}{80\pi^4 R^2}\right)\left\{ - J_{cp}\left(1+\left(\frac{J_{cp}}{\lambda J_{cfil}}\right)^2\right)^{1/2} + 2J_{cp}\left(1+\left(\frac{J_{cp}}{\lambda J_{cfil}}\right)^2\right)^{3/2} - \lambda\, J_{cfil} \log\left[\left(1+\left(\frac{J_{cp}}{\lambda J_{cfil}}\right)^2\right)^{1/2} + \frac{J_{cp}}{\lambda J_{cfil}}\right]\right\}$$

and

$$\Delta M_B = \left(\frac{J_{cp} L_p^3}{30\pi^4 R^2}\right)\left\{\left(1+\left(\frac{2\pi R}{L_p}\right)^2\right)^{3/2} - \left(1+\left(\frac{J_{cp}}{\lambda J_{cfil}}\right)^2\right)^{3/2}\right\} .$$

Appendix F: Calculation of $H_{p,prox}$ for a Proximity-Effected Multifilamentary Strand

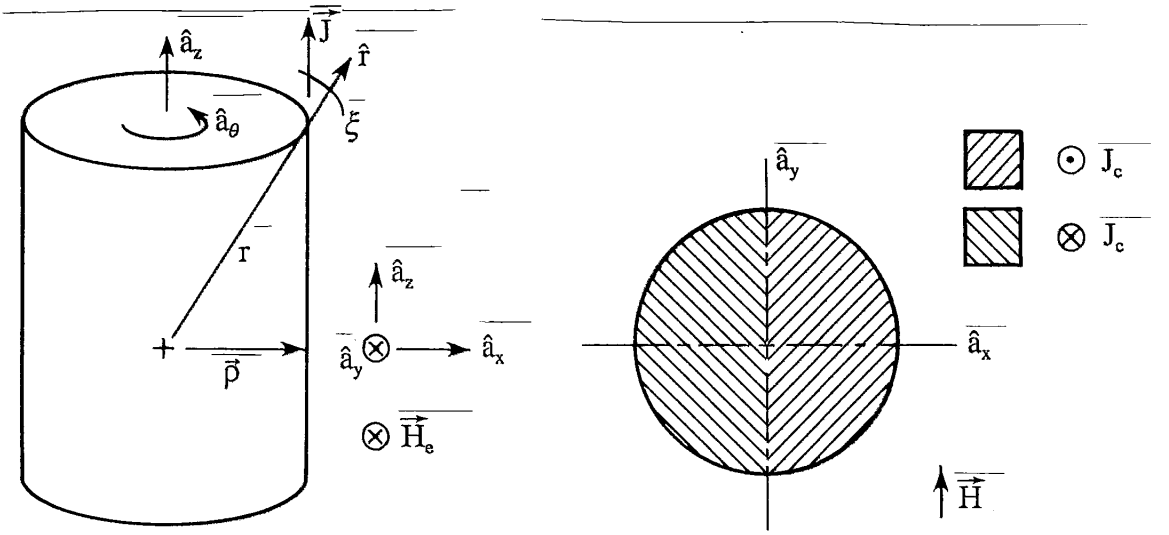

This problem turns out to be equivalent to finding the field generated by a fully penetrated sample at x, y = 0. The fact that B(x,y = 0) ≡ 0 when H = $H_{p,prox}$ implies that the contribution to B (at x,y = 0) from Bean currents is equal to - $H_{p,prox}$. Assume that the field is applied along the $\hat{a}_y$ direction. We want to find B_y for a fully penetrated sample (in the shielding mode). This can be found from

$$\vec{B}(\vec{r}') = \frac{1}{10} \int \vec{J}(\vec{r}) \, x \, \frac{(\vec{r}' - \vec{r})}{|\vec{r}' - \vec{r}|^3} \, d\vec{r}^3 \qquad \text{(in cgs-practical units)}$$

where $\vec{r}'$ denotes the point at which we wish to measure the field, and $\vec{r}$ denotes a vector describing the position of a given bit of current density. Since r' = 0,

$$\vec{B}\,(x{=}y{=}0) = \frac{1}{10} \int \frac{\vec{J} \, x \, \vec{r}}{r^3} \rho d\rho d\theta dz \quad .$$

where

$$r = (z^2 + \rho^2)^{1/2}$$

$$\Rightarrow \vec{B} = \frac{1}{10}\int \frac{\vec{J} \times \vec{r}}{r^3}\, \rho d\rho d\theta dz$$

now

$$B_z = 0 \quad \text{since} \quad \hat{z} \cdot (\vec{J} \times \vec{r}) = 0$$

and $B_x = 0$ since the θ integral cancels out

$$B_y = \left(\frac{1}{10}\right)\int \frac{\hat{y} \cdot (\vec{J} \times \vec{r})}{r^3}\, \rho d\rho d\theta dz$$

which leaves

$$\hat{y} \cdot (\vec{J} \times \vec{r}) = -\sin\xi\cos\theta Jr$$

where

$$\Rightarrow H_{p,prox} = \left(\frac{2}{10}\right)\int_0^R \int_{-\pi/2}^{\pi/2} \int_0^{\infty} \frac{\sin\xi\cos\theta Jr\, dz\, \rho d\rho d\theta}{r^3} \qquad \text{but } \sin\xi = \rho/r$$

$$= \left(\frac{4}{10}\right)\int_0^R \int_{-\pi/2}^{\pi/2} \int_0^{\infty} \frac{\cos\theta J\rho^2}{(\rho^2 + z^2)^{3/2}}\, d\rho\, d\theta dz$$

$$= \left(\frac{8}{10}\right)\int_0^R J\rho^2 \left[\frac{z}{\rho^2(\rho^2 + z^2)^{1/2}}\right]_0^{\infty} d\rho = \left(\frac{8}{10}\right)\int_0^R J d\rho \ .$$

Then

$$\overline{H_{p,prox}} = \left(\frac{8}{10}\right) \int_0^R J_{cz}(\rho) d\rho \ ,$$

and when we take into account both Eq. 5.1.2.2.(a) and (b)

$$\overline{H_{p,prox}} = \left(\frac{8}{10}\right) \left\{ \int_0^{\rho_c} \lambda J_{cfil} \left(1 + \left(\frac{2\pi\rho}{L_p}\right)^2\right)^{1/2} d\rho + \int_{\rho_c}^R \frac{J_{cp}}{\rho} \left(\left(\frac{L_p}{2\pi}\right)^2 + \rho^2\right)^{1/2} d\rho \right\}$$

where

$$\rho_c = \frac{J_{cp} L_p}{2\pi\lambda J_{cfil}} \quad \text{for } L_p < L_{pcm} \text{ and } \rho_c = R \text{ for } L_p > L_{pcm} \ .$$

Integrating, we get for $L_p < L_{pcm}$

$$\overline{H_{p,prox}} = \left(\frac{J_{cp} L_p}{5\pi}\right) \left\{ \frac{4\pi}{L_p} \left(R^2 + \left(\frac{L_p}{2\pi}\right)^2\right)^{1/2} + \left(1 + \left(\frac{J_{cp}}{\lambda J_{cfil}}\right)^2\right)^{1/2} - \frac{2}{\lambda J_{cfil}} (J_{cp}^2 + \lambda^2 J_{cfil}^2)^{1/2} \right.$$

$$- 2\log \left[\frac{L_p + 2\pi(R^2 + (L_p/2\pi)^2)^{1/2}}{2\pi R}\right] + 2\log \left[\frac{\lambda J_{cfil} + (J_{cp}^2 + \lambda^2 J_{cfil}^2)^{1/2}}{J_{cp}}\right]$$

$$\left. + \frac{J_{cfil}\lambda}{J_{cp}} \log \left[\left(1 + \left(\frac{J_{cp}}{J_{cfil}\lambda}\right)^2\right)^{1/2} + \frac{J_{cp}}{\lambda J_{cfil}}\right] \right\}$$

and for $L_p > L_{pcm}$ we get

$$\overline{H_{p,prox}} = \left(\frac{\lambda J_{cfil}}{5}\right)\left\{2R\left(1+\left(\frac{2\pi R}{L_p}\right)^2\right)^{1/2} + \frac{L_p}{\pi}\log\left[\frac{2\pi R}{L_p} + \left(1+\left(\frac{2\pi R}{L_p}\right)^2\right)^{1/2}\right]\right\}.$$

The last calculation (H_p for $L_p > L_{pcm}$) was obtained from

$$\overline{H_{p,prox}} = \left(\frac{8}{10}\right)\int_0^R \lambda J_{cfil}\left(1+\left(\frac{2\pi\rho}{L_p}\right)^2\right)^{1/2} d\rho$$

For $L_p < L_{pcm}$ these equations have the limit that as $L_p \rightarrow 0$, $\overline{H_{p,prox}} \rightarrow 0.8J_{cp}R$ and for $L_p > L_{pcm}$ they have the limit $L_p \rightarrow \infty$, $\overline{H_{p,prox}} \rightarrow 0.8J_{cfil}\lambda R$.

The above equations can be re-written in dimensionless parameters to give the result in Chapter 5. If we calculate the contributions from the two different regions of the strand ($\rho <$ and $> \rho_c$) individually, we get

$$\overline{H_{p,prox}} = H_{PA} + H_{PB}\ , \text{ where}$$

$$H_{PA} = \left(\frac{8}{10}\right)\int_0^{\rho_c} \lambda J_{cfil}\left(1+\left(\frac{2\pi\rho}{L_p}\right)^2\right)^{1/2} d\rho$$

and

$$H_{PB} = \left(\frac{8}{10}\right)\int_{\rho_c}^R J_{cp}\left(\frac{L_p}{2\pi\rho}\right)\left(1+\left(\frac{2\pi\rho}{L_p}\right)^2\right)^{1/2} d\rho\ .$$

These become

$$H_{PA} = \left(\frac{1}{5\pi}\right)\left\{ J_{cp}L_p\left(1+\left(\frac{J_{cp}}{\lambda J_{cfil}}\right)^2\right)^{1/2} + J_{cfil}L_p\lambda\log\left[\left(1+\left(\frac{J_{cp}}{\lambda J_{cfil}}\right)^2\right)^{1/2} + \left(\frac{J_{cp}}{\lambda J_{cfil}}\right)\right]\right\}$$

and

$$H_{PB} = \left(\frac{J_{cp}L_p}{5\pi}\right)\left\{ \frac{4\pi}{L_p}\left(R^2 + \left(\frac{L_p}{2\pi}\right)^2\right)^{1/2} - \frac{2}{\lambda J_{cfil}}(J_{cp}^2 + \lambda^2 J_{cfil}^2)^{1/2} \right.$$

$$\left. - 2\log\left[\frac{L_p + 2\pi(R^2 + (L_p/2\pi)^2)^{1/2}}{2\pi R}\right] + 2\log\left[\frac{\lambda J_{cfil} + (J_{cp}^2 + \lambda^2 J_{cfil}^2)^{1/2}}{J_{cp}}\right]\right\}.$$

Appendix G: Calculation of M-H for the Short Samples

This appendix calculates the M-H loop for short samples of proximity-effected NbTi/matrix multifilamentary strand. We use ideas which are directly adopted from work by several authors describing high T_c conductors[51-53]. First, let us list the solution for the well known problem of a semi-infinite superconductive sheet, finite in only one direction. ΔM can be found directly from Maxwell's curl equation

$$\vec{\nabla} \times \vec{B}(\vec{r}) = \frac{4\pi}{10} J_c, \text{ which in 1-D is } \frac{dB(x)}{dx} = \frac{4\pi}{10} J_c,$$

which can be integrated to find, for a fully penetrated sample on the field increasing branch,

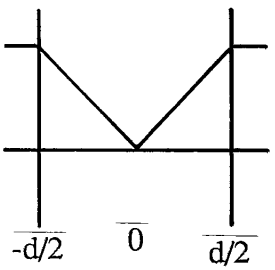

$$B(x) = H - \frac{4\pi}{10} J_c (d/2 - |x|) .$$

as shown above. If we combine this with the relation $\langle B \rangle = H + 4\pi M$, we find that

$$M = \frac{\langle B \rangle - H}{4\pi} \qquad \Rightarrow \Delta M = \frac{J_c d}{20},$$

where the penetration field is given by

$$\boxed{H_p = \frac{4\pi}{20} J_c d .}$$

This becomes more complicated if the sheet is finite in two dimensions, because flux gradients will form in both of these directions. If we additionally let the J_cs be anisotropic, we can adequately describe the magnetization of high T_c crystals[51-53]. In this appendix will show that the essential features of the magnetization of short samples of proximity-effected multifilamentary strand are described by a model of this type, if certain additional assumptions are made. These are (1) the strand is treated as an anisotropic homogenous continuum, and (2) reversible magnetization effects are ignored. These assumptions can later be relaxed to qualitatively describe the reversible magnetization effects in the loss vs field sweep amplitude of short samples (cf. Sec. 5.1.1, 5.2.3.2, and 5.3). The rest of this appendix will be devoted to adapting the model mentioned above to calculate the M-H loops branch-by-branch for the short samples of proximity-effected strand.

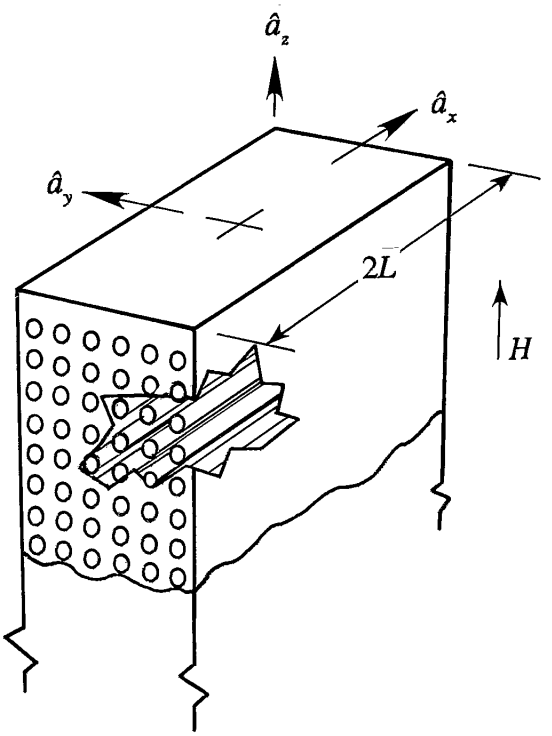

Imagine a semi-infinite slab of PE conductor as shown below.

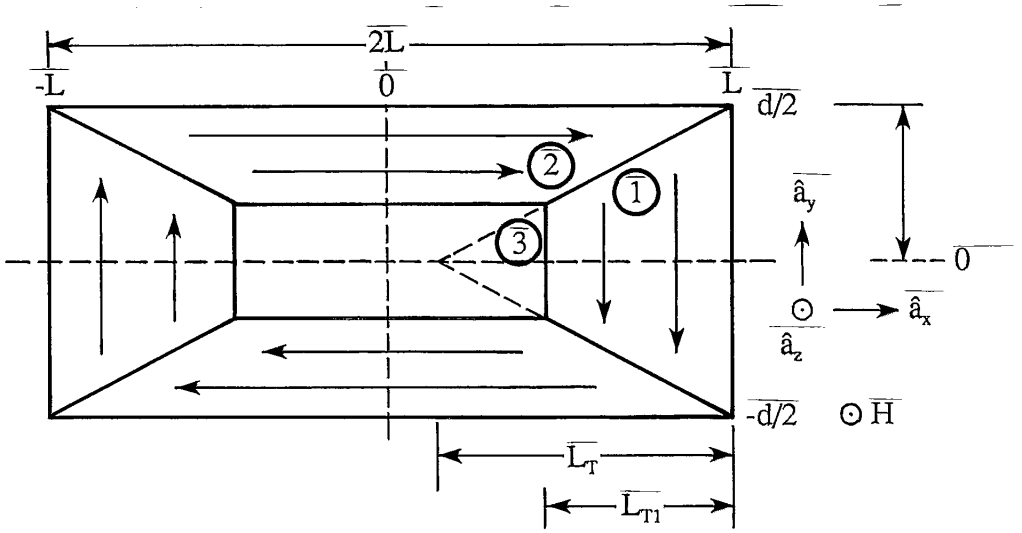

We now let L_p --> ∞, and set the critical currents to be $J_{cx} = \lambda J_{cfil}$, $J_{cy} = J_{cp}$, and $J_{cz} = J_{cp}$.

From Maxwell's equations

$$\vec{\nabla} \times \vec{B} = \left(\frac{4\pi}{10}\right)\vec{J} \qquad \text{(cgs-practical)}$$

which, in rectangular coordinates, is

$$\vec{\nabla} \times \vec{B} = \begin{vmatrix} \hat{a}_x & \hat{a}_y & \hat{a}_z \\ \frac{\partial}{\partial x} & \frac{\partial}{\partial y} & \frac{\partial}{\partial z} \\ B_x & B_y & B_z \end{vmatrix} = \frac{4\pi}{10}\vec{J} \ .$$

If we apply field along the z axis only, we get

$$\hat{a}_x \left(\frac{\partial B_z}{\partial y}\right) - \hat{a}_y \left(\frac{\partial B_z}{\partial x}\right) = \left(\frac{4\pi}{10}\right)(\hat{a}_x J_x + \hat{a}_y J_y + \hat{a}_z J_z) \ ,$$

which gives us

$$\frac{\partial B_z}{\partial y} = J_x\left(\frac{4\pi}{10}\right), \quad \text{and} \quad \frac{\partial B_z}{\partial x} = -J_y\left(\frac{4\pi}{10}\right).$$

Since, however, J_x is either $\pm \lambda J_{cfil}$ or 0, and J_y is either $\pm J_{cp}$ or 0, then

$$\frac{\partial B_z}{\partial y} = \pm\lambda J_{cfil}\left(\frac{4\pi}{10}\right)$$

$$\frac{\partial B_z}{\partial x} = \pm J_{cp}\left(\frac{4\pi}{10}\right) \quad . \qquad \text{Eq. 7.7.1}$$

These equations show the relation between the dual flux gradients and the anisotropic J_cs mentioned above. If we now apply the condition of current continuity, we get

$$\vec{\nabla} \cdot \vec{J} = \frac{\partial J_x}{\partial x} + \frac{\partial J_y}{\partial y} = 0 \quad .$$

Following the above-mentioned authors[51-53], we guess the following solutions

$$\left\{ \begin{array}{ll} \vec{J} = -J_{cp}\hat{a}_y & \textit{in region } 1 \\ \vec{J} = \lambda J_{cfil}\hat{a}_x & \textit{in region } 2 \\ \vec{J} = 0 & \textit{in region } 3 \end{array} \right\}$$

where the listed regions are shown above. Notice that these equations satisfy the continuity equation within each region. We can now require that the continuity equation is valid at the boundaries as well, in order to find these boundaries. Looking at the diagonal between regions 1 and 2, we find that for full penetration

$$\frac{\partial J_x}{\partial x} = -\frac{\partial J_y}{\partial y} \quad \Rightarrow \quad \int_0^{d/2} \lambda J_{cfil} dy = \int_{L-L_T}^{L} J_{cp} dx$$

$$\Rightarrow \quad \lambda J_{cfil} d/2 = J_{cp} L_T$$

which gives us the length to which the flux penetrates along the x-axis. This is also the length that is required for the current to transfer across the weaker J_c material. By an analogy to the eddy current case, we will call this the transfer length, L_T. There are two general cases; (A) the flux fronts along the x-direction meet at full penetration, (B) the flux fronts along the y-direction meet at full penetration. Integrating Eqs. 7.7.1 we find that these two cases have the penetration fields

$$H_{p,prox} = \left(\frac{4\pi}{10}\right) J_{cfil} \lambda (d/2) \qquad \text{for} \qquad L J_{cp} > \lambda J_{cfil} (d/2)$$

and

$$H_{p,prox} = \left(\frac{4\pi}{10}\right) L J_{cp} \qquad \text{for} \qquad L J_{cp} < \lambda J_{cfil} (d/2) \quad .$$

We can find the magnetization from

$$\vec{M} = \left(\frac{1}{20}\right)\left(\frac{1}{V}\right)\left[\int \vec{r}\, x\, \vec{J}_c(\vec{r}) d\tau\right] .$$

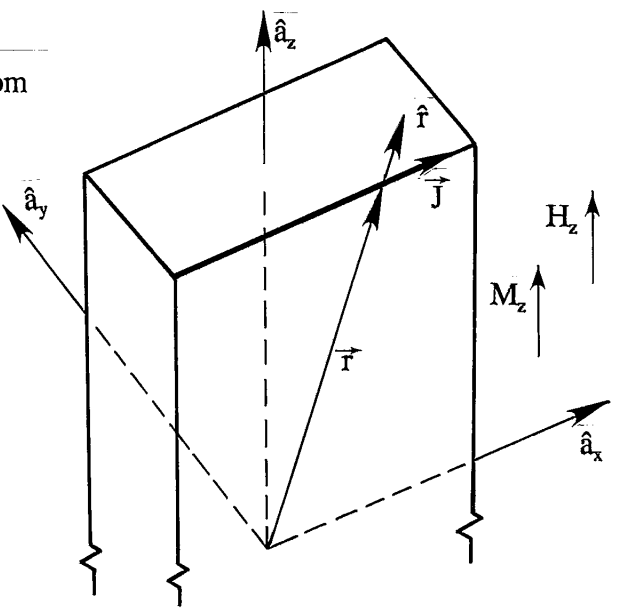

It can be shown that M_x and M_y vanish by symmetry, so that we are interested in M_z. This is given by

$$M_z = \left(\frac{1}{20}\right)\left(\frac{1}{V}\right)\left[\int \hat{a}_z \cdot (\vec{r}\, x\, \vec{J})d\tau\right]$$

where

$$\vec{r}\, x\, \vec{J} = \begin{vmatrix} \hat{a}_x & \hat{a}_y & \hat{a}_z \\ x & y & z \\ J_x & J_y & J_z \end{vmatrix} = \hat{a}_x(yJ_z - zJ_y) + \hat{a}_y(zJ_x - xJ_z) + \hat{a}_z(xJ_y - yJ_x)$$

and

$$\hat{a}_z \cdot (\vec{r}\, x\, \vec{J}) = xJ_y - yJ_x .$$

This gives

$$M_z = \left(\frac{1}{20}\right)\left(\frac{1}{V}\right)\left[\int_{-L}^{L}\int_{-d/2}^{d/2}\int_{-s_L}^{s_L} (xJ_y - yJ_x)\, dx\, dy\, dz\right]$$

where s_L is the length from 0 to ∞ along the z-direction, making the total length along z-axis = $2s_L$. Integrating along the z-direction we get

$$M_z = \left[\frac{1}{40dL}\right]\left[\int_{-L}^{L}\int_{-d/2}^{d/2} (xJ_y - yJ_x)dx\, dy\right] .$$

Below, the magnetization as a function of H is calculated for both case A and B, for all branches of the M-H loop. The results are summarized in Sec. 5.2.3.1.

CASE A: $LJ_{cp} > \lambda J_{cfil}(d/2)$ (i.e. $L > L_T$)

Initial Magnetization for $H < H_{p,prox}$, Case A

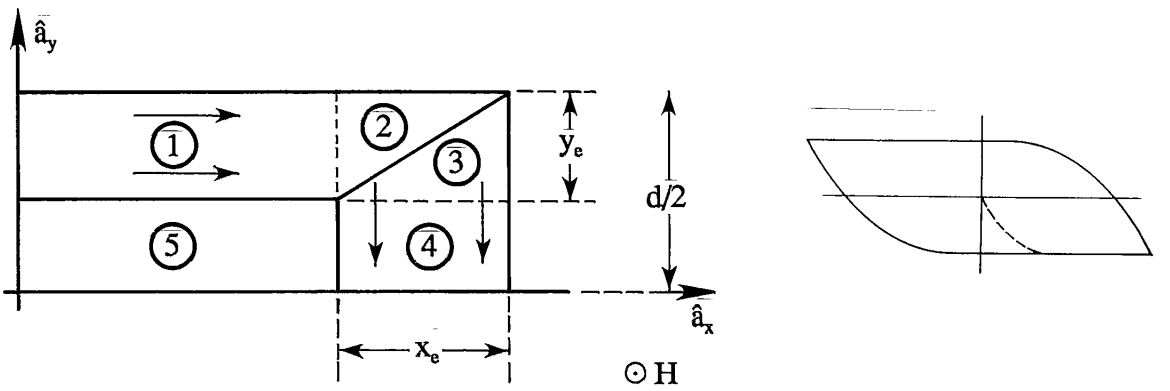

Let us define two parameters x_e and y_e as the distance the flux fronts advance in the x and y direction respectively, for the case of less than full penetration, as

$$y_e = \left(\frac{10}{4\pi}\right)\left(\frac{H}{J_{cfil}\lambda}\right)$$

and

$$x_e = \left(\frac{10}{4\pi}\right)\left(\frac{H}{J_{cp}}\right).$$

Note that when $H = H_{p,prox}$ the above expressions become $y_e = d/2$ and $x_e = L_T$. Since the four quadrants are symmetric, we can find M_z from

$$M_z = \left[\frac{1}{10dL}\right]\left\{I_1 + \cdots I_5\right\}$$

where I_1, I_2, etc. stand for

$$\int\int (xJ_y - yJ_x)dx\,dy$$

and the integration is only over the first quadrant. Then

$$M_z = \left[-\frac{1}{10dL}\right]\left\{\int_{d/2-y_e}^{d/2}\int_0^{L-x_e} y\lambda J_{cfil}\,dy\,dx + \int_{L-x_e}^{L}\int_{d/2+(\frac{y_e}{x_e})(x-L)}^{d/2} y\lambda J_{cfil}\,dy\,dx\right.$$

$$\left. + \int_{d/2-y_e}^{d/2}\int_{L+(\frac{x_e}{y_e})(y-d/2)}^{L} xJ_{cp}\,dx\,dy + \int_0^{d/2-y_e}\int_{L-x_e}^{L} xJ_{cp}\,dy\,dx\right\}$$

$$= \left(\frac{-H}{48J_{cfil}J_{cp}L\pi^3\lambda d}\right)\left\{50H_e^2 - 30H\,J_{cp}L\pi - 15H\,J_{cfil}\pi\lambda d + 12J_{cfil}J_{cp}L\pi^2\lambda d\right\}$$

$$= \left(\frac{-H}{4\pi}\right)\left\{1 - H\left[\left(\frac{30}{12}\right)\left(\frac{1}{\lambda J_{cfil}d\pi}\right) + \left(\frac{15}{12}\right)\left(\frac{1}{J_{cp}\pi L}\right)\right]\right.$$

$$\left. + \frac{50}{12}H^2\left(\frac{1}{J_{cfil}J_{cp}L\pi^2\lambda d}\right)\right\}.$$

This has the limit that as $H \rightarrow 0$, $M_z \rightarrow 0$. Also, as $H \rightarrow H_{p,prox}$

$$M_z \longrightarrow -\frac{dJ_{cfil}\lambda}{40}\left(1 - \frac{dJ_{cfil}\lambda}{6J_{cp}L}\right).$$

Note that if we let $L \rightarrow \infty$ in the second limit we get back the result for the slab which is finite in only one dimension.

Major Trapping/Shielding Branches and IM for $H > H_{p,prox}$, Case A

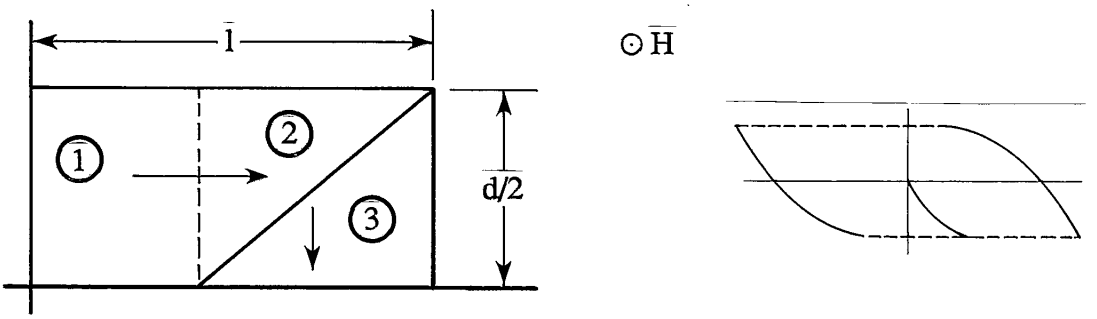

Here

$$M_z = \left[\frac{1}{10dL}\right]\left\{ I_1 + I_2 + I_3 \right\}$$

$$= \left[-\frac{1}{10dL}\right]\left\{ \int_0^{d/2} \int_0^{L-L_T} y J_{cfil}\,\lambda\, dy\, dx \right.$$

$$\left. + \int_{L-L_T}^{L} \int_{\left(\frac{d}{2L_T}\right)(x-(L-L_T))}^{d/2} y\lambda\, J_{cfil}\, dy\, dx + \int_0^{d/2} \int_{L-\left(\frac{L_T}{d/2}\right)(d/2-y)}^{L} x J_{cp}\, dx\, dy \right\}.$$

Integrating we find

$$M_z = -\frac{dJ_{cfil}\lambda}{40}\left(1-\frac{dJ_{cfil}\lambda}{6J_{cp}L}\right).$$

Initial Reversal Region for $H_m > 2H_{p,prox}$ and $|H| > H_m - 2H_{p,prox}$, Case A

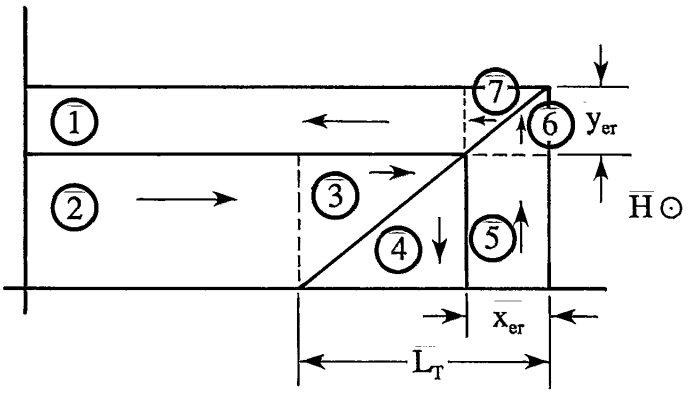

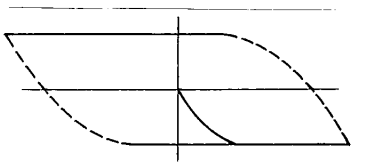

Here $$M_z = \left[\frac{1}{10dL}\right]\left\{I_1 + \ldots I_7\right\}.$$

For this calculation we need to find x_{er} and y_{er}, the position at which the current directions switch for the x and y axes, respectively. We can find y_{er} from

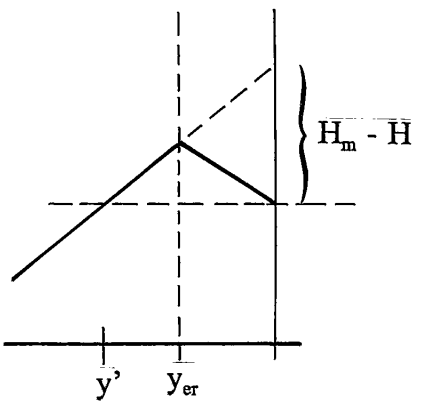

$$\frac{\partial B}{\partial y} = \left(\frac{4\pi}{10}\right) J_c$$

$$\Rightarrow \quad \Delta B = \left(\frac{4\pi}{10}\right) \Delta y \; \lambda J_c$$

so that

$$H_m - H = \left(\frac{4\pi}{10}\right) y' \; \lambda J_{cfil}$$

$$\Rightarrow \quad y_{er} = \left(\frac{5}{4\pi}\right)\left(\frac{H_m - H}{\lambda J_{cfil}}\right).$$

Similarly,

$$x_{er} = \left(\frac{5}{4\pi}\right)\left(\frac{H_m - H}{J_{cp}}\right).$$

Then

$$M_z = \left[-\frac{1}{10dL}\right]\Bigg\{ -\int_0^{L-x_{er}} \int_{d/2-y_{er}}^{d/2} \textcircled{1}\, y\lambda J_{cfil}\, dy\, dx$$

$$+ \int_0^{L-L_T} \int_0^{d/2-y_{er}} \textcircled{2}\, y\lambda J_{cfil}\, dy\, dx + \int_{L-L_T}^{L-x_{er}} \int_{(d/2-y_{er})\frac{(x-(L-L_T))}{(L_T-x_{er})}}^{d/2-y_{er}} \textcircled{3}\, y\lambda J_{cfil}\, dy\, dx$$

$$+ \int_0^{d/2-y_{er}} \int_{L-L_T+\frac{(L_T-x_{er})}{(d/2-y_{er})}(y)}^{L-x_{er}} \textcircled{4}\, x\, J_{cp}\, dx\, dy - \int_0^{d/2-y_{er}} \int_{L-x_{er}}^{L} \textcircled{5}\, xJ_{cp}\, dx\, dy$$

$$- \int_{d/2-y_{er}}^{d/2} \int_{L-x_{er}+(\frac{x_{er}}{y_{er}})(y-(d/2-y_{er}))}^{L} \textcircled{6}\, xJ_{cp}\, dx\, dy$$

$$- \int_{L-x_{er}}^{L} \int_{d/2-y_{er}+(\frac{y_{er}}{x_{er}})(x-(L-x_{er}))}^{d/2} \textcircled{7}\, y\lambda J_{cfil}\, dy\, dx \Bigg\}.$$

When integrated, this gives

$$M_z = -\left(\frac{J_{cfil}\lambda d}{40} - \frac{J_{cfil}^2 d^2 \lambda^2}{240 J_{cp} L} - \frac{(H_m - H)}{4\pi} + \frac{15(H_m-H)^2}{96\pi^2}\left(\frac{1}{LJ_{cp}} + \frac{2}{\lambda J_{cfil} d}\right)\right.$$

$$\left. -\frac{25}{96}\frac{(H_m-H)^3}{\pi^3}\frac{1}{dLJ_{cfil}J_{cp}\lambda}\right).$$

In the limit that H --> $H_{p,prox}$,

$$M_z = -\frac{dJ_{cfil}\lambda}{40}\left(1-\frac{dJ_{cfil}\lambda}{6J_{cp}L}\right),$$

and as H --> H_m - $2H_{p,prox}$

(where $H_{p,prox} = (4\pi/10)J_{cfil}\lambda(d/2)$)

$$M_z = \frac{dJ_{cfil}\lambda}{40}\left(1 - \frac{dJ_{cfil}\lambda}{6J_{cp}L}\right).$$

Trapping/Shielding Branches for $H_m < H_{p,prox}$, Case A

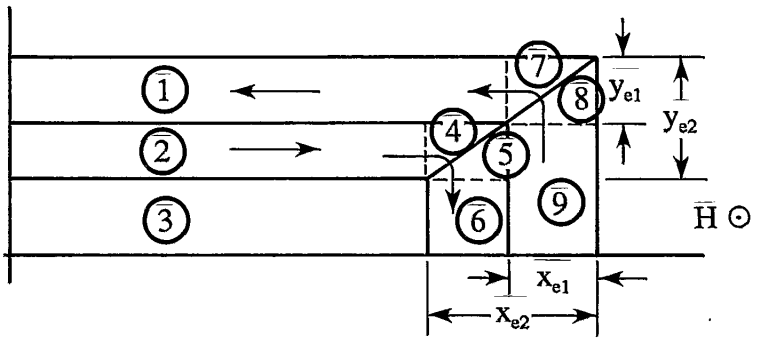

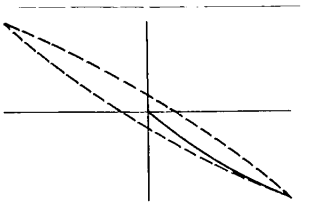

Here

$$M_z = \left[\frac{1}{10dL}\right]\left\{I_1 \ldots I_9\right\}.$$

To get M_z we need to find both the distance to which the flux penetrates (x_{e2} and y_{e2}) and the point at which the Bean currents reverse (x_{e1} and y_{e1}). These are given by the expressions

$$x_{e2} = \left(\frac{10}{4\pi}\right)\left(\frac{H_m}{J_{cp}}\right),$$

$$y_{e2} = \left(\frac{10}{4\pi}\right)\left(\frac{H_m}{J_{cfil}\lambda}\right),$$

$$x_{e1} = \left(\frac{5}{4\pi}\right)\left(\frac{H_m - H}{J_{cp}}\right), \quad \text{and} \quad y_{e1} = \left(\frac{5}{4\pi}\right)\left(\frac{H_m - H}{\lambda J_{cfil}}\right).$$

We find that

$$M_z = \left(-\frac{1}{10dL}\right)\Bigg\{ \int_0^{L-x_{s1}} \int_{d/2-y_{s1}}^{d/2} y J_{cfil}\lambda\, dy\, dx \quad (1)$$

$$- \int_0^{L-x_{s2}} \int_{d/2-y_{s2}}^{d/2-y_{s1}} y J_{cfil}\lambda\, dy\, dx \quad (2)$$

$$- \int_{L-x_{s2}}^{L-x_{s1}} \int_{(d/2-y_{s2})+\frac{(y_{s2}-y_{s1})}{(x_{s2}-x_{s1})}(x-(L-x_{s2}))}^{d/2-y_{s1}} y J_{cfil}\lambda\, dy\, dx \quad (4)$$

$$- \int_{d/2-y_{s2}}^{d/2-y_{s1}} \int_{L-x_{s2}-\frac{(x_{s2}-x_{s1})}{(y_{s2}-y_{s1})}(y-(d/2-y_{s2}))}^{L-x_{s1}} x J_{cp}\, dx\, dy \quad (5)$$

$$- \int_0^{d/2-y_{s2}} \int_{L-x_{s2}}^{L-x_{s1}} x J_{cp}\, dx\, dy \quad (6)$$

$$+ \int_{L-x_{s1}}^{L} \int_{(d/2-y_{s1})+(\frac{y_{s1}}{x_{s1}})(x-(L-x_{s1}))}^{d/2} y\lambda J_{cfil}\, dy\, dx \quad (7)$$

$$+ \int_{d/2-y_{s1}}^{d/2} \int_{(L-x_{s1})+(\frac{x_{s1}}{y_{s1}})(y-(d/2-y_{s1}))}^{L} x J_{cp}\, dx\, dy \quad (8)$$

$$+ \int_0^{d/2-y_{s1}} \int_{L-x_{s1}}^{L} x J_{cp}\, dx\, dy \Bigg\}. \quad (9)$$

Integrating, we get

$$M_z = \left[\frac{1}{96 J_{cfil} J_{cp} L\pi^3 \lambda\, d}\right]\Big\{ -100 H_m^3 + 60 H_m^2 J_{cp} L\pi$$

$$+ 30 H_m^2 J_{cfil}\pi\lambda\, d - 24 H_m J_{cfil} J_{cp} L\pi^2 \lambda\, d + 24 J_{cfil} J_{cp} L\pi^2 \lambda\, d(H_m - H)$$

$$-(30 J_{cp} L\pi + 15 J_{cfil}\pi\lambda\, d)(H_m - H)^2 + 25(H_m - H)^3 \Big\}.$$

This has the limit that as H_m - H --> 0, and H_m --> $H_{p,prox}$, M_z --> the shielding results for H > $H_{p,prox}$. Also, as H_m --> and $H_{p,prox}$, H --> $-2H_{p,prox}$, M_z --> the trapping results for H > $H_{p,prox}$.

CASE B: $J_{cp}L < J_{cfil}\lambda(d/2)$ (i.e. $L < L_T$)

Initial Magnetization for $H < H_{p,prox}$, Case B

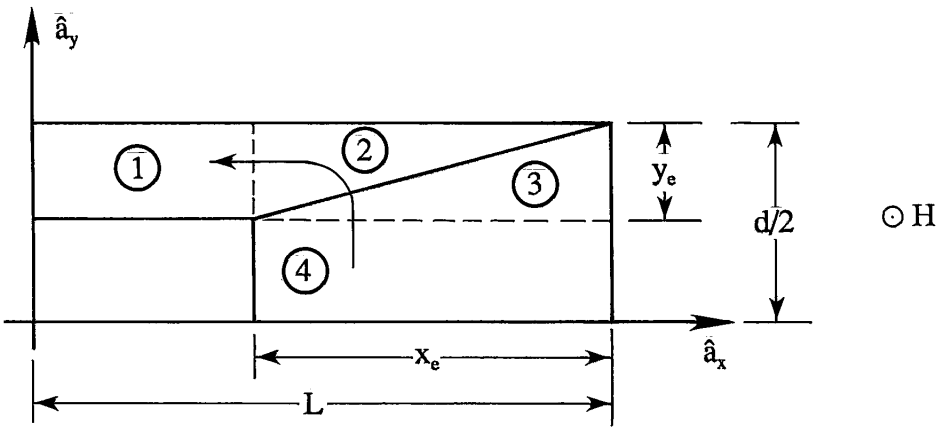

Here

$$M_z = \left[\frac{1}{10dL}\right]\left\{I_1, + \cdots I_4\right\}.$$

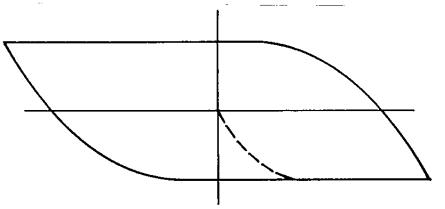

In order to find M_z, we need to find the expressions

$$x_e = \left(\frac{10}{4\pi}\right)\left(\frac{H}{J_{cp}}\right) \quad \text{and} \quad y_e = \left(\frac{10}{4\pi}\right)\left(\frac{H}{J_{cfil}\lambda}\right).$$

We then find that

$$M_z = \left[\frac{-1}{10Ld}\right]\left\{ \underbrace{\int_0^{L-x_e}\int_{d/2-y_e}^{d/2} y\lambda J_{cfil}\,dy\,dx}_{①} + \underbrace{\int_{L-x_e}^{L}\int_{(d/2-y_e)+(\frac{y_e}{x_e})(x-(L-x_e))}^{d/2} y\lambda J_{cfil}\,dy\,dx}_{②} \right.$$

$$\left. + \underbrace{\int_{d/2-y_e}^{d/2}\int_{L-x_e+(\frac{x_e}{y_e})(y-(d/2-y_e))}^{L} xJ_{cp}\,dx\,dy}_{③} + \underbrace{\int_0^{d/2-y_e}\int_{L-x_e}^{L} xJ_{cp}\,dx\,dy}_{④} \right\}.$$

This can be integrated to find

$$M_z = -\left(\frac{H}{48J_{cfil}J_{cp}L\pi^3\lambda\, d}\right)\left\{ 50H^2 - 30H\,J_{cp}L\pi \right.$$

$$\left. - 15H\,J_{cfil}\pi\lambda\, d + 12J_{cfil}J_{cp}L\pi^2\lambda d \right\}$$

which can be re-written as

$$M_z = \left(-\frac{H}{4\pi}\right)\left\{ 1 - H\left[\left(\frac{30}{12}\right)\left(\frac{1}{\lambda J_{cfil} d\pi}\right) + \left(\frac{15}{12}\right)\left(\frac{1}{J_{cp}\pi L}\right)\right] \right.$$

$$\left. + \left(\frac{50}{12}\right)H^2\left(\frac{1}{J_{cfil}J_{cp}L\pi^2\lambda\, d}\right)\right\}.$$

Note that this is the same as the result for $L > L_T$. This has the limits that as

$$H \longrightarrow \left(\frac{4\pi}{10}\right) L J_{cp},\ M_z \longrightarrow = -\left(\frac{J_{cp} L}{20}\right)\left(1 - \left(\frac{2}{3}\right)\frac{J_{cp} L}{J_{cfil}\lambda d}\right),$$

and for H $\rightarrow$ 0, $M_z \rightarrow 0$, as would be expected.

Major Trapping/Shielding Branches and IM for $H > H_{p,prox}$, Case B

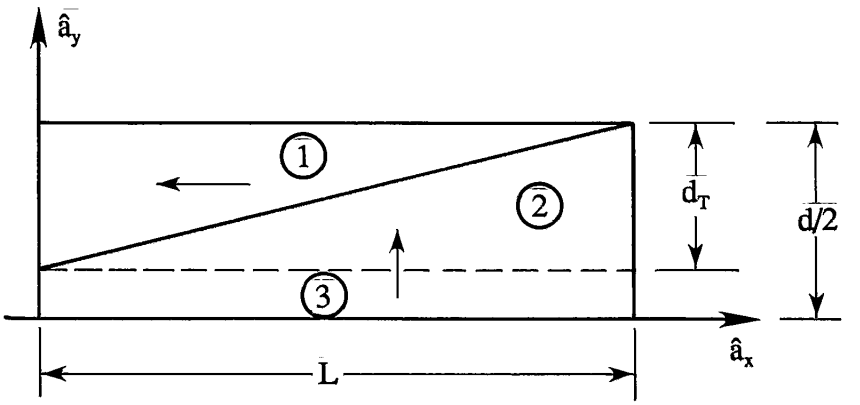

Here

$$M_z = \left[\frac{1}{10Ld}\right]\left\{I_1 + I_2 + I_3\right\}.$$

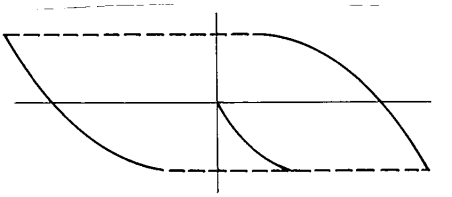

In order to find M_z, we need the expression

$$d_T = \frac{LJ_{cp}}{\lambda J_{cfil}}.$$

We then find

$$M_z = \left[\frac{-1}{10Ld}\right]\left\{ \underbrace{\int_0^L \int_{d/2-d_T+\frac{d_T}{L}(x)}^{d/2} y\lambda J_{cfil}\,dy\,dx}_{①} + \underbrace{\int_{d/2-d_T}^{d/2} \int_{\frac{L}{d_T}(y-(d/2-d_T))}^{L} xJ_{cp}\,dx\,dy}_{②} + \underbrace{\int_0^L \int_0^{d/2-d_T} xJ_{cp}\,dx\,dy}_{③} \right\}$$

Integrating we get

$$= \frac{J_{cp}L}{60J_{cfil}\lambda d}(2J_{cp}L - 3J_{cfil}\lambda d)$$

$$\Longrightarrow \quad \boxed{M_z = -\left(\frac{J_{cp}L}{20}\right)\left(1-\left(\frac{2}{3}\right)\frac{J_{cp}L}{J_{cfil}\lambda d}\right).}$$

Note that if we define L' = 2L, and d' = d/2, (note the normalizing area is unchanged)

M_z becomes

$$M_z' = -\frac{J_{cp}L'}{40}\left(1-\frac{2}{3}\frac{J_{cp}L'}{4J_{cfil}\lambda}\right)$$

which is just the result for case A, showing the consistency of these expressions.

Initial Reversal Region for $H_m > 2H_{p,prox}$ and $|H| > H_m - 2H_{p,prox}$, Case B

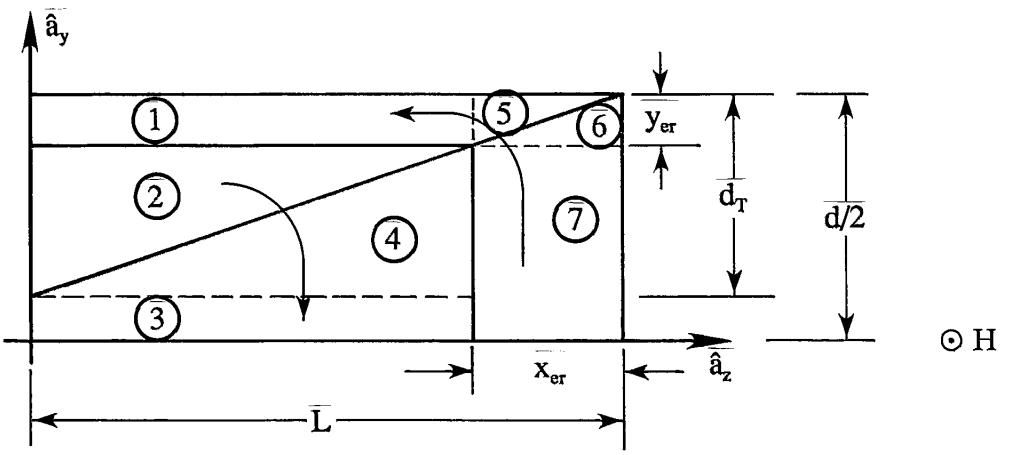

Here

$$M_z = \left[\frac{1}{10dL}\right]\left\{I_1 \cdots I_7\right\},$$

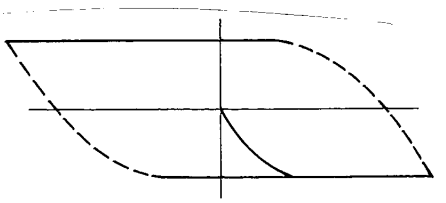

which gives

$$M_z = \left[\frac{-1}{10Ld}\right]\left\{ -\int_0^{L-x_{er}}\int_{d/2-y_{er}}^{d/2} y\lambda J_{cfil}\,dy\,dx \quad +\int_0^{L-x_{er}}\int_{d/2-d_T+\frac{(d_T-y_{er})}{(L-x_{er})}(x)}^{d/2-y_{er}} y\lambda J_{cfil}\,dy\,dx \right.$$

$$+\int_0^{d/2-d_T}\int_0^{L-x_{er}} xJ_{cp}\,dx\,dy+\int_{d/2-d_T}^{d/2-y_{er}}\int_{\frac{(L-x_{er})(y-(d/2-d_T))}{(d_T-y_{er})}}^{L-x_{er}} xJ_{cp}\,dx\,dy$$

$$-\int_{L-x_{er}}^{L}\int_{(d/2-y_{er})+\left(\frac{y_{er}}{x_{er}}\right)(x-(L-x_{er}))}^{d/2} y\lambda J_{cfil}\,dy\,dx$$

$$\left. -\int_{d/2-y_{er}}^{d/2}\int_{L-x_{er}+\left(\frac{x_{er}}{y_{er}}\right)(y-(d/2-y_{er}))}^{L} xJ_{cp}\,dx\,dy \quad -\int_{L-x_{er}}^{L}\int_0^{d/2-y_{er}} xJ_{cp}\,dx\,dy \right\}.$$

Integrating, and using the expressions

$$d_T = \frac{LJ_{cp}}{\lambda J_{cfil}},$$

$$x_{er} = \left(\frac{5}{4\pi}\right)\left(\frac{H_m - H}{J_{cp}}\right), \quad \text{and} \quad y_{er} = \left(\frac{5}{4\pi}\right)\left(\frac{H_m - H}{\lambda J_{cfil}}\right),$$

we find that

$$M_z = \left(\frac{-1}{480 J_{cfil} J_{cp} L \pi^3 \lambda d}\right)\Big\{-16 J_{cp}^3 L^3 \pi^3 + 24 J_{cfil} J_{cp}^2 L^2 \pi^3 \lambda d$$

$$-120 J_{cfil} J_{cp} L \pi^2 \lambda d (H_m - H)$$

$$+ (150 J_{cp} L \pi + 75 J_{cfil} \pi \lambda d)(H_m - H)^2 - 125 (H_m - H)^3 \Big\}.$$

Taking the limit $H_m \rightarrow H$, we find

$$M_z = \frac{J_{cp} L (2 J_{cp} L - 3 J_{cfil} \lambda d)}{60 J_{cfil} \lambda d}$$

$$= -\left(\frac{J_{cp} L}{20}\right)\left(1 - \left(\frac{2}{3}\right)\frac{J_{cp} L}{J_{cfil} \lambda d}\right).$$

Taking the limit as $H_m \rightarrow H_{p,prox}$, $H = -H_{p,prox}$, we find that

$$M_z = \left(\frac{J_{cp}L}{20}\right)\left(1-\left(\frac{2}{3}\right)\frac{J_{cp}L}{J_{cfil}\lambda d}\right)$$

as expected.

Trapping/Shielding Branches for $H_m < H_{p,prox}$, Case B

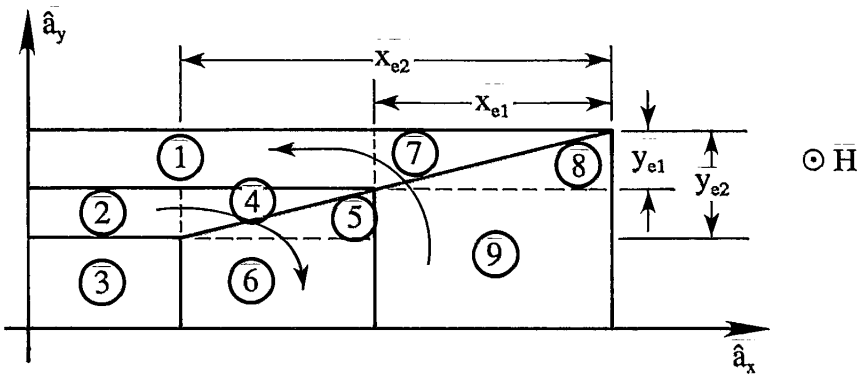

Here

$$M_z = \left[\frac{1}{10Ld}\right]\left\{ I_1 \cdots I_9 \right\},$$

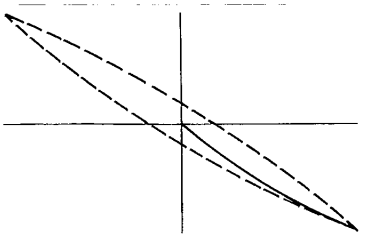

In order to find M_z, we need the expressions

$$x_{e1} = \left(\frac{5}{4\pi}\right)\left(\frac{H_m - H}{J_{cp}}\right), \quad \text{and} \quad y_{e1} = \left(\frac{5}{4\pi}\right)\left(\frac{H_m - H}{\lambda J_{cfil}}\right),$$

$$H_{p,prox} = \left(\frac{4\pi}{10}\right)LJ_{cp},$$

$$x_{e2} = \left(\frac{10}{4\pi}\right)\left(\frac{H_m}{J_{cp}}\right), \quad \text{and} \quad y_{e2} = \left(\frac{10}{4\pi}\right)\left(\frac{H_m}{\lambda J_{cfil}}\right).$$

We then find that

$$M_z = \left[\frac{-1}{10Ld}\right] \left\{ -\int_{d/2-y_{s1}}^{d/2} \int_{0}^{L-x_{s1}} y\lambda J_{cfil}\, dx\, dy \quad (1) \right.$$

$$+ \int_{d/2-y_{s2}}^{d/2-y_{s1}} \int_{0}^{L-x_{s2}} y\lambda J_{cfil}\, dx\, dy \quad (2)$$

$$+ \int_{L-x_{s2}}^{L-x_{s1}} \int_{(d/2-y_{s2})+\frac{(y_{s2}-y_{s1})}{(x_{s2}-x_{s1})}(x-(L-x_{s2}))}^{d/2-y_{s1}} y\lambda J_{cfil}\, dy\, dx \quad (4)$$

$$+ \int_{d/2-y_{s2}}^{d/2-y_{s1}} \int_{(L-x_{s2})+\frac{(x_{s2}-x_{s1})}{(y_{s2}-y_{s1})}(y-(d/2-y_{s2}))}^{L-x_{s1}} x J_{cp}\, dx\, dy \quad (5)$$

$$+ \int_{0}^{d/2-y_{s2}} \int_{L-x_{s2}}^{L-x_{s1}} x\, J_{cp}\, dx\, dy \quad (6)$$

$$- \int_{L-x_{s1}}^{L} \int_{(d/2-y_{s1})+(\frac{y_{s1}}{x_{s1}})(x-(L-x_{s1}))}^{d/2} y\lambda J_{cfil}\, dy\, dx \quad (7)$$

$$- \int_{d/2-y_{s1}}^{d/2} \int_{(L-x_{s1})+(\frac{x_{s1}}{y_{s1}})(y-(d/2-y_{s1}))}^{L} x J_{cp}\, dx\, dy \quad (8)$$

$$\left. - \int_{0}^{d/2-y_{s1}} \int_{L-x_{s1}}^{L} x J_{cp}\, dx\, dy \right\} . \quad (9)$$

Integrating we get

$$M_z = \left(\frac{-1}{96 J_{cfil} J_{cp} L \pi^3 d\lambda}\right)\Big\{ +25H^3 - 75H^2 H_m + 75H H_m^2 + 75H_m^3$$

$$+ 30H^2 J_{cp} L\pi - 60H H_m J_{cp} L\pi - 30H_m^2 J_{cp} L\pi$$

$$+ 15H^2 J_{cfil} \pi\lambda d - 30H H_m J_{cfil} \pi\lambda d - 15H_m^2 J_{cfil} \pi\lambda d$$

$$+ 24H J_{cfil} J_{cp} L_T^2 \lambda d \Big\}.$$

This has the limit that as both H and $H_m \rightarrow H_{p,prox}$,

$$M_z = \frac{J_{cp} L (2 J_{cp} L - 3 J_{cfil} \lambda d)}{(60 J_{cfil} \lambda d)}$$

$$= -\left(\frac{J_{cp} L}{20}\right)\left(1 - \left(\frac{2}{3}\right)\frac{J_{cp} L}{J_{cfil} \lambda d}\right).$$

Also, as $H \rightarrow -H_{p,prox}$, and $H_m \rightarrow H_{p,prox}$,

$$M_z = \left(\frac{J_{cp} L}{20}\right)\left(1 - \left(\frac{2}{3}\right)\frac{J_{cp} L}{J_{cfil} \lambda d}\right).$$

Appendix H: The L_{eff} Dependence of PEs

This appendix presents experimental data which, with the aid of a simple phenomenological model, demonstrate that Q_{PE} and M_{PE} are modified by interactions between cable pitch (L_c) and strand twist pitch (L_p), just as eddy currents effects are[56]. The model described below was originally used to describe eddy current effects in helical coils wound from SSC-type strands similar to those used for this thesis. A similar but non-equivalent model has been published for eddy current effects in cables[57]. The strands used in Ref. 56 were multifilamentary strand of NbTi in CuMn, made from a single stack procedure with a total of 10,830 filaments. The strands were 0.81 mm in diameter, with a d_f of 5.07 μm. The filament diameter and matrix type suggest that these strands should have weak PE coupling. In order to try to simulate possible magnet conditions, the strands were wound into long (≈ 140 cm total strand length) helical coils and exposed to slight field gradients. In addition, only a small portion of the helix was measured by the apparatus. However, even though this setup is less than optimal for the present purpose, an interesting point can made by intercomparison of the results for these helices. Here we revisit the data from Ref. 56, in conjunction with some previously unpublished results on the same materials, in order to explain some of the PEs which where not understood at the time.

We will assume a model for the static PE losses of the form:

$$Q_{PE} \propto L_{eff}$$

where $$L_{eff} = \left(\frac{1}{2}\right)^{1/2}\left(\frac{1}{(1/L_c - 1/L_p)^2} + \frac{1}{(1/L_c + 1/L_p)^2}\right)^{1/2} .$$

This has the limits:

$$L_{eff} \rightarrow L_p \quad as \quad L_c \rightarrow \infty \ (L_p \rightarrow 0)$$

$$L_{eff} \rightarrow L_c \quad as \quad L_p \rightarrow \infty \ (L_c \rightarrow 0)$$

$$L_{eff} \rightarrow \frac{1}{\sqrt{2}}\left(\frac{1}{|1/L_c - 1/L_p|}\right) \quad when \quad L_p \approx L_c .$$

This indicates, sensibly, that when $L_p << L_c$, L_p is the limiting pitch, and vice versa. It also shows that as these two pitches become comparable, L_{eff} becomes large, along with the losses. We can see in Table H1 that there is a positive correlation between the Q_S losses (extrapolations of Q versus f to zero f) and larger values of L_{eff}, even if there are only four data points, and noting that Q_S is greater for LQB rather than LQD (the above model would predict the $Q_{S,D} > Q_{S,B}$ based on L_{eff}). Also, we can see in Fig. H1 the direct comparison of the M-H loops for these four coils. These runs were 30 min. long, giving a loop frequency of 0.04167 min^{-1}. Notice that not only are the losses

greater for the samples with greater L_{eff} (with the above exception), but that this is especially true in the low field region, where a new, significantly larger peak emerges.

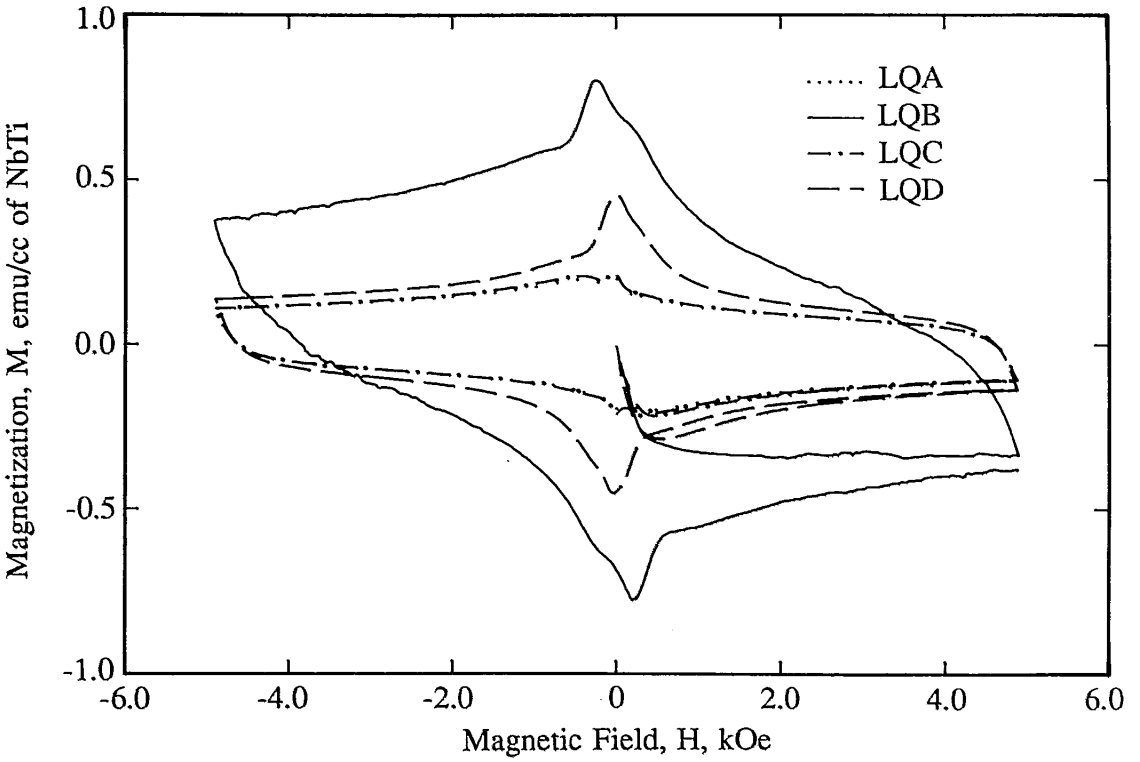

Fig. H1 M-H for various long helices

These loops, of course, are experiencing eddy current losses as well as Q_S (= Q_h + Q_{PE}) losses, and this is exacerbated for samples with a large L_{eff}. However, as we can see in Fig. H2, the losses at 0.04167 min^{-1} have a relatively small eddy current component, if we assume a linear dependence of eddy current losses on frequency (expected in the low frequency regime, and shown in the figure). The fact that $Q_{S,B} > Q_{S,D}$ can be attributed to experimental errors, since L_c is difficult to determine precisely and the function is very sensitive to the difference between L_c and L_p (in fact has a singularity) near their equivalence.

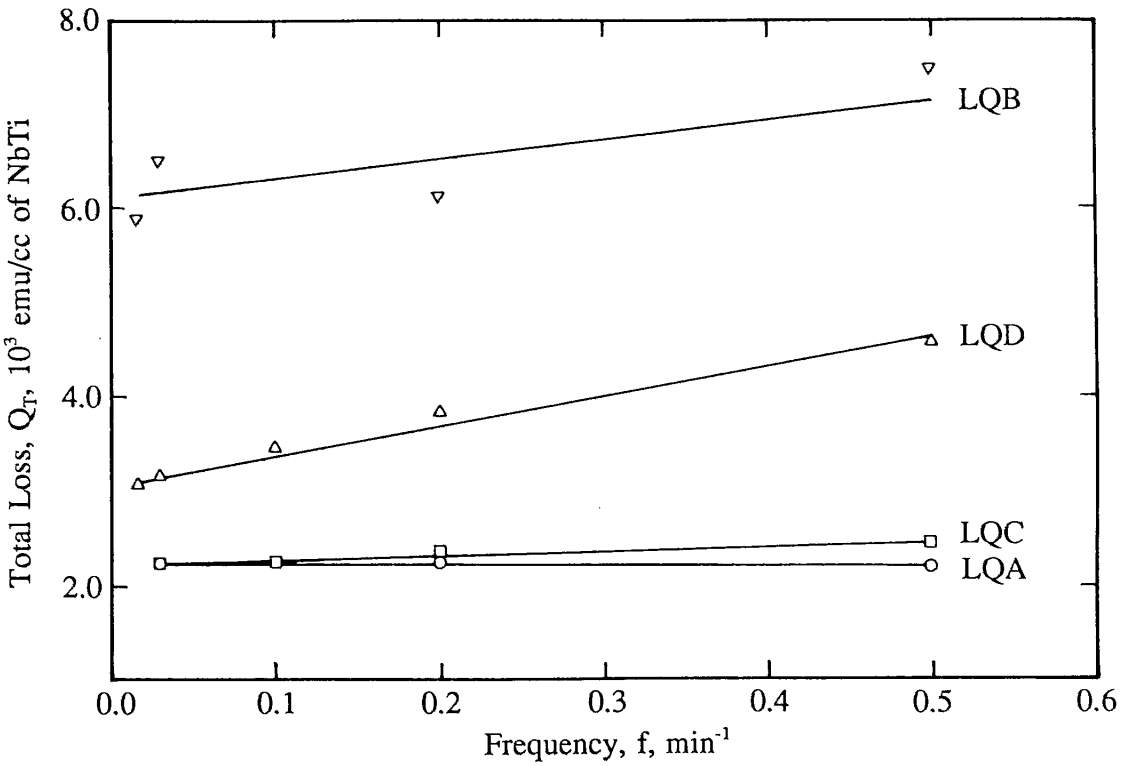

Fig. H2 Total loss as a function of field sweep frequency in samples LQA through LQD

Thus, these few measurements suggest that the situation where $L_p \approx L_c$ should be avoided. In fact, this is avoided in practice because of eddy current enhancement near this pole. PE L_c/L_p interaction, however, is an additional effect which should be kept in mind, and it emphasizes the analogy between eddy currents and proximity effects in these composites.

Table H1: Q_s versus L_{eff} for helical strands in a transverse field

Sample code	L_c (cm)	L_p (cm)	L_{eff} (cm)	Q_S (ergs)
LQA	0.79	∞	0.79	2200
LQB	0.79	0.75	10.5	6000
LQC	0.79	1.50	1.24	2200
LQD	0.79	0.76	14.2	3000

MAGNETIC STUDIES OF PROXIMITY-EFFECT COUPLING IN A VERY CLOSELY SPACED FINE-FILAMENT NbTi/CuMn COMPOSITE SUPERCONDUCTOR

E. W. Collings*, K. R. Marken Jr*., M. D. Sumption*†, E. Gregory**††, and T. S. Kreilick**

* Battelle Memorial Institute, Columbus, OH 43201
† Permanent address: Ohio University, Athens, OH 45701
** Supercon, Inc., Shrewsbury, MA 01545
†† Present address: IGC Advanced Superconductors, Waterbury, CT 06704

ABSTRACT

Magnetization studies have been conducted on a 23,000-filament composite (with a filament-spacing/filament-diameter ratio, s/d, of about 0.19) drawn down to d = 11.5 to 0.5 μm. Various techniques have been used to explore the occurrence and properties of proximity-effect coupling between the filaments across the Cu-0.5wt.%Mn matrix. This coupling, which sets in at d < 1.5 μm -- much smaller than 2.5 μm intended for superconducting supercollider (SSC) magnet applications -- is studied both at low fields (well below the H_{c1} of the NbTi) and at high fields (of up to 1.5 tesla (15 kG)).

INTRODUCTION

When a superconductor is subjected to a time-varying external magnetic field the "height" of the M(H) hysteresis loop is proportional to the critical current density, J_c, and the thickness, d, of the superconductor. Thus in order to minimize the residual magnetization retained in a partially de-energized coil, such as an SSC magnet following de-excitation from an operating field of 6.6 tesla to a beam-injection field of 0.3 tesla, it has been recommended that the filaments of the cable strands should be made as small as possible. The preservation of a high J_c under these conditions dictates the use of a filament-spacing/filament-diameter ratio, s/d, of some 0.13-0.17. A consequence of this is that filaments less than 3-4 μm in diameter are coupled by proximity effect (even at 0.3 tesla) which contributes an unwanted excess magnetization [1,2,3] to at least a portion of the M(H) hysteresis loop. Interfilamentary coupling can be suppressed by alloying the matrix with a high concentration of Ni (e.g. 30 wt.%) or, preferably, a low concentration of Mn (e.g. 0.5 wt.%)[1,2,3,4]. For the multifilamentary strands prepared for this study, an interfilamentary alloy of Cu-0.5wt.% Mn was used. As a result, filaments as small as d = 2.5 μm (hence s = 0.5 μm, at the design s/d of 0.19 in this case[3]) were successfully decoupled.

The purpose of the study was: (a) to determine for Cu-0.5wt.%Mn the coupling-threshold value of d (hence s); (b) to examine the manner in which coupling magnetization manifested itself both in the low-field regime below the H_{c1} of NbTi as well as in the high-field regime up to about 15 kG.

Advances in Cryogenic Engineering (Materials), Vol. 36
Edited by R. P. Reed and F. R. Fickett
Plenum Press, New York, 1990

Table 1. Specifications of 23,000-Filament Strands

Sample Code	Strand Diam. (nom.), mils	Strand Diam. (actual), μm	Avg. Fil. Diam.* μm	Cu/SC Ratio†	A_{tot}/A_{SC}
CMN-115	119	2998.7	11.556	1.941	2.940
CMN-25	25	635.0	2.459	1.912	2.912
CMN-21	21	529.4	2.051	1.909	2.909
CMN-15	15	385.0	1.495	1.897	2.897
CMN-10	10	274.5	1.086	1.885	2.885
CMN-5	5	127.2	0.4995	1.831	2.831

* Obtained by etching using measured density of bulk Nb-46.5Ti (= 6.097).
† Obtained from measured strand and filament diameters.

EXPERIMENTAL

Magnetization Measurements

Magnetization was measured as function of temperature up to the T_c of NbTi with field sweep amplitudes of from a few tens of gauss up to 15 kgauss on cylindrical bundles of multifilamentary strand. Measurements were taken with the applied field transverse to the sample axis. A computerized PAR-EG&G vibrating-sample magnetometer (VSM) was used, in association with a 17-kG iron-core electromagnet powered by a ± 65 A field-controlled bipolar power supply. In completing a full hysteresis loop, including the initial branch from the origin, the instrument records 1,023 data pairs. Thus the field resolution in any experiment is about $1/200^{th}$ of the field-sweep amplitude, which enables all fine structure associated with coupling magnetization to be fully recorded.

Sample Material

Samples were prepared from high-homogeneity Nb-46.5wt%Ti rods clad with a thin barrier-layer of Nb (whose presence was ignored in the data analyses) and enough Cu-0.5wt.%Mn to provide an s/d ratio of 0.19 [5]. The strand design called for an annulus of 22,902 filaments encased in Cu and surrounding a Cu core for a total matrix/superconductor ratio of about 1.9. Photomicrographs illustrating this configuration have been presented elsewhere[3] (see also Table 2). The strands under study, whose filament diameters ranged from 11.5 μm (CMN-115) down to 0.5 μm (CMN-5), had not been twisted or heat treated (except for a final 4h/225°C anneal). Some of their specifications are listed in Table 1. Some further critical dimensions of CMN-5 are listed in Table 2.

Magnetometer-Sample Preparation

The samples consisted of cylindrical bundles, about 3 mm in diameter and 6 mm in length, of parallel multifilamentary strands imbedded in epoxy. Depending on the strand diameter, the number of strands in the bundle varied from about 15 (2.5 μm filaments) to 200 (0.5 μm filaments) so as to keep the volume of superconductor roughly constant at about 0.01 cm^3. Specifications of the magnetometer samples, including that of a sample prepared from unclad CMN-5 (i.e. CMN-5B, in which the Cu and Cu-Mn matrices had been removed by etching), are given in Table 3.

Table 2. Configuration of CMN-5

D_0	D_B	D_{IB} (μm)
128.0	98.04	39.62
126.5	101.35	39.62
125.5	98.04	38.10
125.0	97.79	36.58
126.3	98.81	38.48

Length of magnetization sample = 0.588 cm
Tot. Bundle Volume (incl. core) = 4.509×10^{-5} cm^3.
Tot. Bundle Vol./(n x fil. vol.) = 1.709

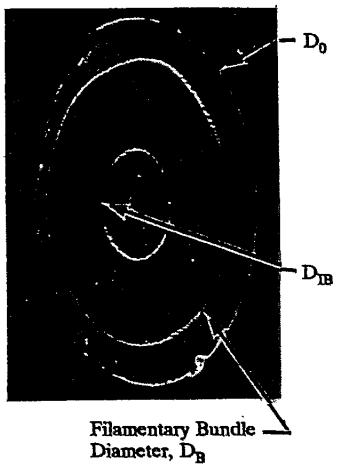

Table 3. Magnetization Sample Specifications

Sample Code	Fil. Diam., μm	Number of Strands	Sample Length, mm	NbTi Filament Volume, 10^{-3}cm^3
CMN-115	11.556	1	5.892	14.15
CMN-25	2.459	15	5.64	9.201
CMN-21	2.051	21	6.15	9.772
CMN-15	1.495	33	5.60	7.429
CMN-10	1.068	58	5.736	6.826
CMN-5	0.4995	200	5.88	5.278
CMN-5B*	0.4995	200	5.734	5.147

* All the matrix material removed by etching -- 4.5804×10^6 independent filaments.

LOW-FIELD MAGNETIZATION

Provided that the field-sweep amplitude remains below the H_{c1} of NbTi, the magnetic susceptibility of a cylindrical composite or its filamentary components in a transverse magnetic field, is given by the Meissner (flux-exclusion) value: $\chi = dM/dH = (-1/2\pi)P$. Here P, the "flux-exclusion" volume fraction, is given by: $P = 1-(2/x)I_1(x)/I_0(x)$, where x represents the ratio of filament radius (R = d/2) to the penetration depth, (λ_L), and I_0 and I_1 are modified Bessel functions of the first kind of order 0 and 1, respectively (see Ref. 6 and the companion paper in this proceedings[7]). For large-diameter cylinders, P = 1; on the other hand significant temperature-dependent departures from unity are noted for very fine filaments when the radius becomes comparable to λ_L.

The low-field magnetization loops for the entire series of clad multifilamentary specimens are presented in Fig. 1. Two features are immediately noted: (a) a decrease in overall dM/dH slope in going from CMN-115 to CMN-5; (b) for CMN-10, a slight opening of the loop near the origin, and for CMN-5, a pronounced hysteresis. The susceptibility decrease is due to the increasing influence of field penetration as R/λ_L decreases with decreasing R (see Ref. 7 for a full account of this effect). The first appearance of magnetic hysteresis with decreasing R (hence decreasing s) signifies the onset of coupling.

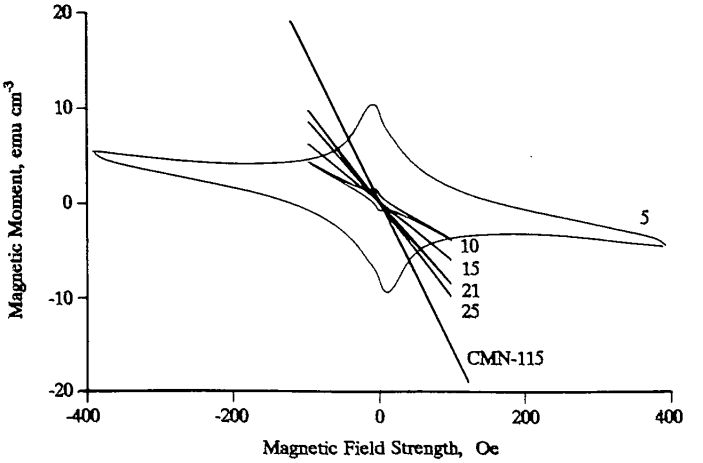

Fig. 1 Low-field ($<H_{c1}$) hysteresis loops for samples CMN-115 to CMN-5 at 4.2 K.

The initial magnetization for CMN-5, throughout the superconducting temperature range above 4.2 K, is shown in Fig. 2. The slope of the initial branch is -1.26×10^{-3} emu/G which, normalized to the exclusion-volume of the 200 filamentary bundles each of diameter 9.88×10^{-3} cm (see Table 2) that make up the sample, yields a volume susceptibility of -0.140. Comparing this with the ideal value of $-1/2\pi = -0.160$ for a cylinder in a transverse field, we note that in fields of up to about 8 or 9 G the filamentary bundle excludes (or screens out due to proximity-effect-permitted circulating supercurrents) about 88% of the applied field.

In CMN-5 at 4.2 K, departures from dM/dH linearity begin to occur as the applied field exceeds about 9 G. Above that field, flux begins to penetrate the bundle just as if it were a type-2 superconductor with a lower critical field, "H_{c1B}", of about 9 G. From the intercept of a plot of H_{c1B} versus temperature a T_c of 8.95 K for the fine-filamentary NbTi is deduced (a value agrees well with the 8.93 K obtained from the susceptibility temperature dependence of the bare filaments[7]). A plot of H_{c1B} versus t^2, where $t = T/T_c$, the reduced temperature, is presented in the inset to Fig. 2. We note that H_{c1B} has a quadratic temperature dependence and a zero-K value of 10.5 G.

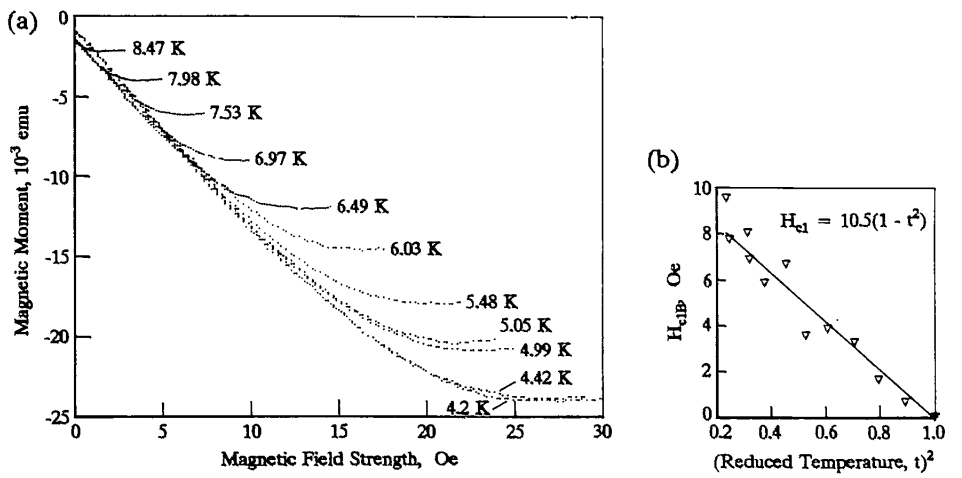

Fig. 2 Temperature dependence of (a) the initial magnetization of CMN-5; (b) the lower critical field, H_{c1B}, of the filamentary bundle.

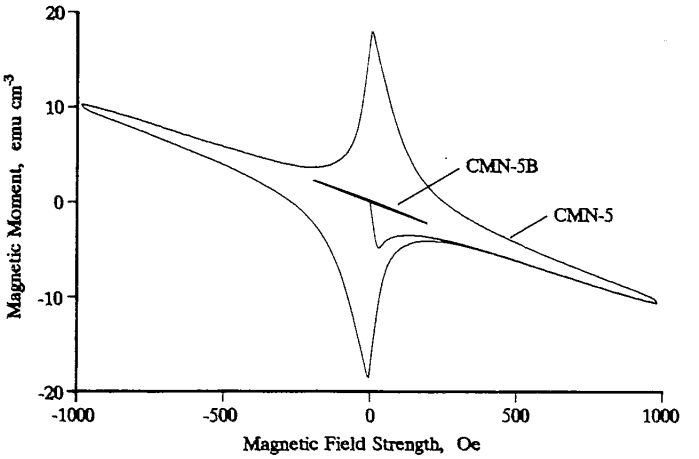

Fig. 3 Low-field ($<H_{c1}$) hysteresis loops for CMN-5 and the unclad CMN-5B at 4.2 K.

The full magnetization loop for CMN-5, at 4.2 K and with field amplitude less than the H_{c1} of the NbTi filaments*, is shown in Fig. 3. Inserted is the magnetization loop (closed line) for the corresponding bare-filamentary sample CMN-5B, the slope of which approximates the between-wings slope of the Cu-clad sample. The susceptibility of the bare CMN-5B, measured as part of a companion study[7], was found to be -0.0108 (a value which is a factor of 14.74 lower than it would be in the absence of field penetration, and which yields a 4.2-K penetration depth[7] $\lambda_L = R/x = 323$ nm). The measured ratio of the clad to bare low-field (<9 G) susceptibilities* is 0.140/-0.0108 = 13.0, which in itself is spectacular evidence for the existence of coupling. This comparison of the magnetizations of clad and unclad materials is exploited further in the high-field regime.

With decreasing d (hence s), coupling also manifests itself as a development of the M(H) line into a hysteresis loop, as indicated in Fig. 3 for CMN-5. This excess magnetization, say M_{ex}, which decreases monotonically with increasing field, can be thought of as being superimposed on an imaginary inclined line (drawn between the wings of the M(H) loop) representing the Meissner diamagnetism of the filaments themselves.

TRANSITION FROM THE LOW-FIELD- TO THE HIGH-FIELD MAGNETIZATION REGIMES

As the field-sweep amplitude, H_m, increases three new features of the coupling emerge: (1) The peak of M_{ex} moves away from H = 0. (2) As depicted in Fig. 4, the peak value of M_{ex} increases with H_m in two stages -- stage-i, for $H_m < H_{c1}$, corresponding to filaments in the Meissner state, and stage-ii, for $H_m > H_{c1}$, corresponding to filaments in the mixed state. (3) As will be seen below, whereas at low values of H_m, a coupling M_{ex} appears during both the increasing and decreasing sweeps of the applied field (Fig. 3), when H_m exceeds H_{c1} the coupling occurs predominantly during the field-decreasing (so-called "trapping") segments of the M(H) loop.

---

* As discussed in a companion paper[7], the critical field of fine filaments is strongly enhanced as a result of field-penetration effect. For example, the measured H_{c1} of CMN-5 at 4.2 K is 607 gauss[7].

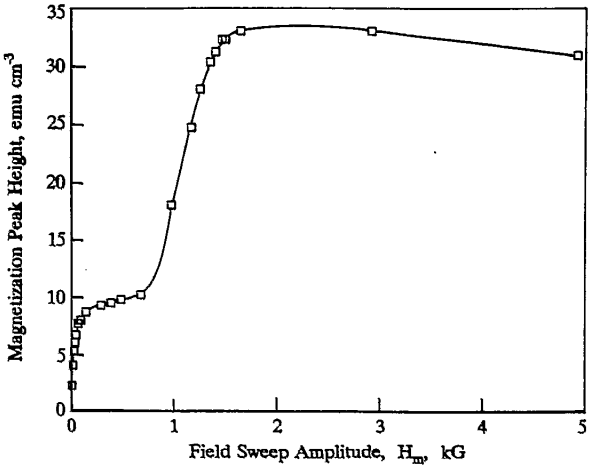

Fig. 4 Excess magnetization (clad-unclad, with respect to CMN-5 and CMN-5B) at the coupling peak in the positive M(H) quadrant, as function of the field-sweep amplitude.

HIGH-FIELD MAGNETIZATION

Clad-Filament/Critical Current Method

For a cylindrical superconducting composite in a transverse magnetic field sufficiently strong to place the filaments in the mixed state, the full height, ΔM, of the magnetic hysteresis loop (in emu/cm^3 based on the strand volume) is given by

$$\Delta M = (0.4/3\pi)\, L\, J_c\, d \qquad (1)$$

i.e.

$$\Delta M/(I_c/A_{strand}) = (0.4/3\pi)\, d \qquad (2)$$

where L is the filling factor ($= A_{SC}/A_{strand}$), J_c and I_c are the strand critical current density (A/cm^2) and critical current (A), respectively, and the strand diameter, d, is in cm. The conventional approach is thus to compare (as function of filament diameter, at constant applied field) the measured ΔM with the expected height based on Eqns. (1) or (2). General examples of the use of this approach have been presented elsewhere[1,4]. For the present material, the results of applying the Eqn.-(2) approach are given in Ref. [3]. From the plot of $\Delta M/(I_{SC}/A_{strand})$ versus d we noted that coupling was just beginning to appear in CMN-10, in agreement with the low-field conclusion (Fig. 1) and was more strongly present in CMN-5.

Clad-Filament/Bare-Filament Method

A second approach to the study of coupling uses magnetization only and eliminates the need for critical current measurement. It does, however, call for the preparation of a second set of samples in which all the matrix material has been removed by etching.

In analyzing the results of magnetization measurements performed on clad materials and their unclad counterparts, the left-hand side of Eqn. (2) may be essentially replaced by the height-ratio $(\Delta M)_{clad}/(\Delta M)_{bare}$. There are then two useful ways of dealing with this quotient: (1) Select a particular field strength, and plot the height-ratio versus d; (2)

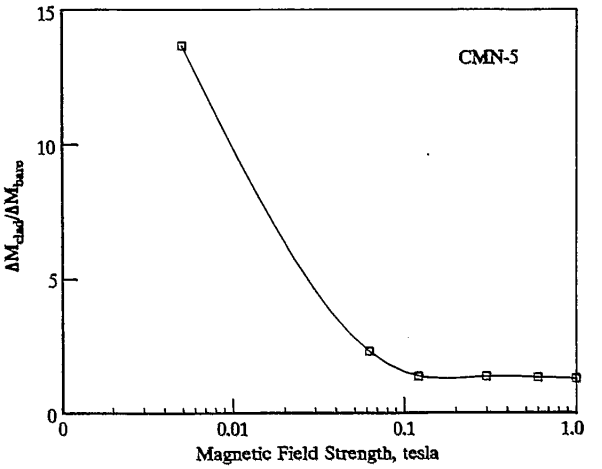

Fig. 5 Ratio of the hysteresis-loop height (clad/unclad) for CMN-5 and CMN-5B as function of the corresponding field.

select a particular strand, and plot the height-ratio versus applied field strength. The result of applying the second method is shown in Fig. 5 for the strand-pair CMN-5 and CMN-5B.

Finally, the availability of unclad-strand magnetization data sheds further light on the properties of the coupled strands. In Fig. 6 the high-field magnetization loops for CMN-5 and CMN-5B are superimposed. The former exhibits a tilt due to the paramagnetism of the Cu-0.5wt.%Mn interfilamentary matrix. But once this tilt is removed it can be seen that the curves superpose almost completely along the field-increasing (shielding) branches, while most of the coupling appears along the trapping segments of the M(H) loop.

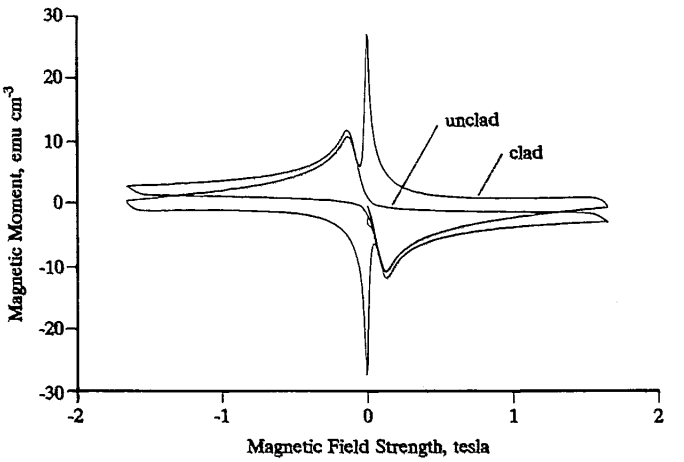

Fig. 6 High-field (mixed-state) hysteresis loops at 4.2 K for CMN-5 and CMN-5B, indicating the predominance of coupling along the trapping branches of the M(H) loop.

SUMMARY

In sample CMN-5, with an interfilamentary separation (across a Cu-0.5wt.%Mn matrix) of about 0.1 μm, the filamentary bundle at very low applied field strengths simulates a solid cylinder of superconductor with a zero-K lower critical field, H_{c1B}, of 10.5 G. Above H_{c1B}, but below the H_{c1} of NbTi, the hysteresis loop of the composite exhibits an excess magnetization, M_{ex}, symmetrically disposed about a line representing the Meissner diamagnetism of the uncoupled NbTi filaments. As the field sweep amplitude increases beyond H_{c1}, the height of the coupling peak increases in two steps separated by $H_m = H_{c1}$. During large H_m, M_{ex} is no longer symmetrical about the mixed-state magnetization of the NbTi. Instead, the coupling manifests itself predominantly during the "trapping" stroke of the hysteresis loop -- an effect which is being examined more extensively using more strongly coupled unalloyed-Cu-matrix composites.

ACKNOWLEDGEMENTS

The clad and unclad epoxy-potted magnetization samples were prepared by R. D. Smith, Battelle. The research was sponsored in full by the U.S. Department of Energy, Division of High-Energy Physics.

REFERENCES

1. A. K. Ghosh, W. B. Sampson, E. Gregory, and T. S. Kreilick, "Anomalous low field magnetization in fine filament NbTi conductors", IEEE Trans. Magn. MAG-23, 1724 (1987).

2. A. K. Ghosh, W. B. Sampson, E. Gregory, S. Kreilick, and J. Wong, "The effect of magnetic impurities and barriers on the magnetization and critical current of fine filament NbTi composites", Tenth Int. Conf. Magnet Tech., Boston, MA, Sept. 21-25 (1987).

3. E. Gregory, T. S. Kreilick, J. Wong, E. W. Collings, K. R. Marken Jr., R. M. Scanlan, and C. E. Taylor, "A conductor with uncoupled 2.5 μm diameter filaments designed for the outer cable of SSC dipole magnets", IEEE Trans. Magn. MAG-25, 1926 (1989).

4. E. W. Collings, "Stabilizer design considerations in ultrafine filamentary Cu/NbTi composites", Sixth NbTi Workshop, Madison, WI, Nov. 12-13, 1986; see also Adv. Cryo. Eng. (Materials) 34, 867 (1988).

5. P. Valaris, T. S. Kreilick, E. Gregory, and J. Wong, "Refinements in billet design for SSC strand", IEEE Trans. Magn. MAG-25, 1937 (1989).

6. E. W. Collings, A. J. Markworth, and K. R. Marken Jr., "Possibility of critical field enhancement in high-T_c sponges and thin films", IEEE Trans. Magn. MAG-25, 2491 (1989).

7. E. W. Collings, K. R. Marken Jr., A. J. Markworth, J. K. McCoy, M. D. Sumption, E. Gregory, and T. S. Kreilick, "Critical field enhancement due to field penetration in fine-filament conductors", Paper in this Proceedings.

TEMPERATURE AND FIELD DEPENDENCE OF SHORT TERM DECAY AND LOSS IN MULTIFILAMENTARY SUPERCONDUCTORS – A PROXIMITY EFFECT INTERPRETATION

by

M. D. Sumption[*†] and E. W. Collings[*]

[*]Battelle, Columbus, OH 43201, USA
[†]Physics Dept., Ohio University, Athens, OH 45701, USA

Pepared for the
CEC/ICMC Conference
Huntsville, AL
June 10-14, 1991

TEMPERATURE AND FIELD DEPENDENCE OF SHORT TERM DECAY AND LOSS IN MULTIFILAMENTARY SUPERCONDUCTORS -- A PROXIMITY EFFECT INTERPRETATION

M. D. Sumption*† and E. W. Collings*

*Battelle, Columbus, OH 43201, USA
†Physics Dept., Ohio University, Athens, OH 45701, USA

ABSTRACT

The temperature and field dependence of short term decay, as well as the frequency dependence of the loss, have been investigated in multifilamentary NbTi superconductors. We find that the total loss for two samples with widely different amounts of proximity effect coupling, while showing quite different low frequency losses, exhibit almost identical loss in the high frequency (saturation) regime. A field and temperature dependence of τ which is greater than can be accounted for by the variation of bulk matrix resistivity in this temperature regime is observed, being significantly greater for the more heavily proximity coupled strand. This, in combination with the qualitative difference in the decay between samples known to exhibit static proximity effects to varying degrees, indicates that the proximity effect does influence the short term decay and dH/dt dependent loss (at least below saturation).

BACKGROUND

Proximity effects in multifilamentary materials are well known, but typically only their contribution to the static magnetization is addressed. However, Yamafuji et al.[1], and others[2], have investigated the influence of proximity effects on long term decay. Very little work exists on the temperature dependence of eddy currents in general[3], and none that we know of for samples where the proximity effect is noticeable. With the recent interest in proximity effect, magnetization drift, and possible relations between them[4-6] we decided to study time dependent magnetization decay at short times (10 min. and less) in samples with strong proximity effect. In addition we have investigated the influence of proximity effects of dH/dt loss.

EXPERIMENTAL

Samples

A matched pair of superconductive strands with NbTi in Cu and CuMn were used in these experiments. The strands were fully filamentary, with approximately 5000 filaments, 2 μm in diameter, with s/d ratios = 0.2. No Nb sheaths were used to surround the filaments. Further details are listed in Tab. 1.

Table 1. Strand Specifications

Strand Code	NTCU20	NTCM20
Strand Diameter (10^{-2}cm)	2.174	2.190
Bundle Diam. (10^{-2}cm)	1.678	1.694
Filament No.	4395	5355
Filament Diam. (μm)	2.03	1.90
Matrix Composition	Cu	CuMn

Table 2. Coil Specifications

Strand Code	CNTCM20-0	CNTCU20-0
Coil Length, L (cm)	1.2-1.4	1.0-1.2
Coil Thickness, d (cm)	0.2-0.5	0.1-0.5
Coil Width, w (cm)	0.25	0.25
Total Strand Mass (mg)	235.36	207.23
Strand length (cm)	81.724	71.1
Fil. Region Vol. (10^{-3}cm^3)	18.428	15.731
NbTi Vol. (10^{-3}cm^3)	12.431	10.15
Fil. Filling factor, λ	0.675	0.645

One coil was wound from each of the above strands. These coils were ovals; a sketch is shown in Fig. 1., and further details are given in Tab. 2. These wires were nominally untwisted, and we chose the lengths to give sizable eddy currents and proximity effects. Throughout the paper these samples are assumed to have effective L_ps of $\approx$2L, for purposes of comparison.

Measurements

Two types of measurements were made for this set of experiments: M-H loops and moment vs time decay. The hysteresis measurements were 1000 point data sets, taken over times of from 2 to 120 minutes (including the initial magnetization). All measurements were made with the magnetic field applied along the axis of symmetry of the solenoid (as shown in Fig. 1.). The decay measurements were either 5 or 10 minutes in duration with a dH/dt of 300 Oe/s. Each of the decay measurements had 100 (for the 5 min.) or 200 (for the 10 min.) points. We used a protocol of waiting 5 minutes after reaching the initial field before applying the ΔH, so that all eddy current effects from the initial set up had decayed.

RESULTS

Loss

The per cycle dH/dt dependent loss (Q_e) vs frequency is compared for Cu and CuMn samples in Fig. 2. The loss is for a triangular field profile with a maximum amplitude (H_m) of 16.55 kOe, and is normalized to $(2L)^2$ (where L is the sample length) as well as the volume of the filamentary region (filaments and matrix, but excluding outer Cu shell). Here the zero

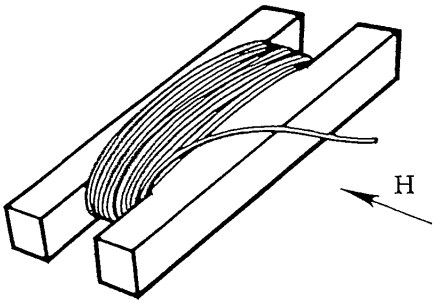

Fig. 1.
Illustration of sample coil.

frequency loss has been subtracted for each sample. The static loss was much greater for the Cu coil because of the proximity effect, and was determined via a set of M vs t decay experiments. These measurements were five minutes in duration, allowing the measurement of a loop with a very low effective dH/dt. The moment measured at the end of the run was taken as the dH/dt independent magnetization. This was taken as a compromise between the need to exclude eddy current effects, and a desire to minimize long term creep effects (we wished to examine the portion of the decay expected to be exponential). The measurements of static PE loss are detailed in a companion paper in this proceedings[5]. Q_e should be linear with f for sufficiently small frequencies, but as we can see, it is not linear for either of these samples over the range of M-H loop frequencies used. This figure shows that the Q_e losses of the Cu matrix sample are lower than those of the CuMn matrix sample for f greater than about 0.4 mHz (although the total losses are greater for the Cu sample at these relatively low frequencies).

Shown in Fig. 3 are the M-H loops for the Cu and CuMn coils at near zero frequency, and also their 2 min (saturation) hysteresis loops. This shows that the M-H loops for both samples at near full saturation (dH/dt = 710 Oe/s) are almost identical. It is clear from this that even though the zero frequency loss is very much greater for the Cu sample (by a factor of about 15), that the loss at full saturation is almost exactly the same. The proportion, then, of Q_e to total losses, as well as Q_e will be greater for the CuMn coil at saturation. This indicates that the proximity effect losses and the eddy current losses are to some extent competing phenomena, as would be expected from their topological similarity[4,6].

Although M-H loops with times greater than 120 minutes were not taken, it seems likely that the initial slope of the Q_e vs f curve for the Cu matrix material would be greater than that

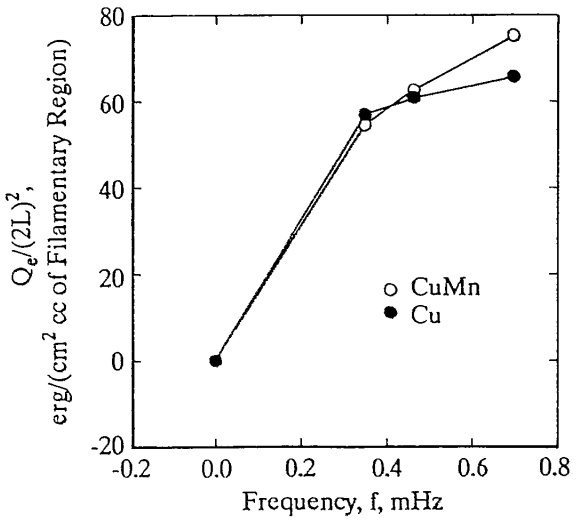

Fig. 2.
Normalized Q_e loss vs frequency for both coils.

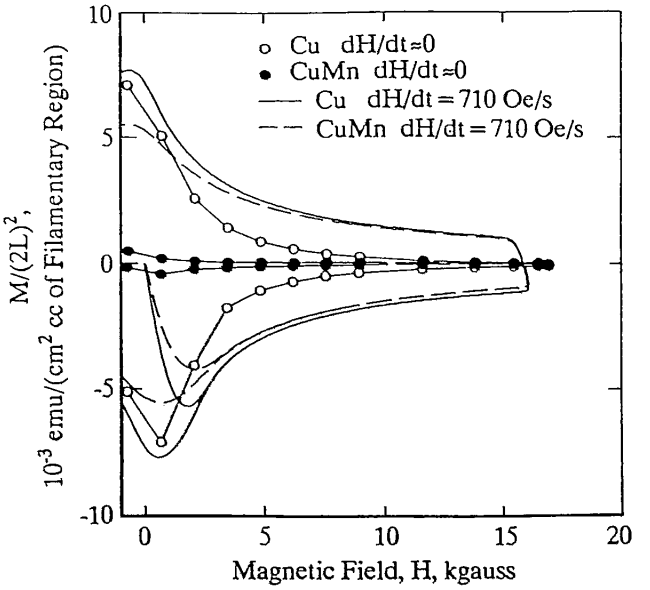

Fig. 3. Static and 2 minute Hysteresis loops for both coils.

of the CuMn matrix material (in order to avoid discontinuities in the derivative). This, in the conventional eddy current interpretation, would imply that the resistivity is lower[6] (and conversely, that the exponential decay time, τ, is greater) in the Cu sample, as would be expected from the increase in resistivity with a Mn addition. As the rest of the paper will describe, the decay constant is, indeed, larger for the Cu sample. However, the interpretation of this in terms of an eddy currents decay constant modified by the resistivity of the Mn is not as reasonable as it might at first seem.

M vs t Decay at Various Temperatures

Fig. 4 shows the moment decay for both samples at T=4.2K and H=10.28 kOe (here ΔH was from 8.94 kOe to 10.28 kOe, with a dH/dt=300 Oe/s). The moment has been normalized to $(2L)^2$ and the filamentary region volume as before, so that the initial M_0 is similar for these samples. Also, the NbTi critical state magnetization has been subtracted (taken to be the magnetization of the CuMn sample at the end of the M vs t decay). A third curve of the Cu

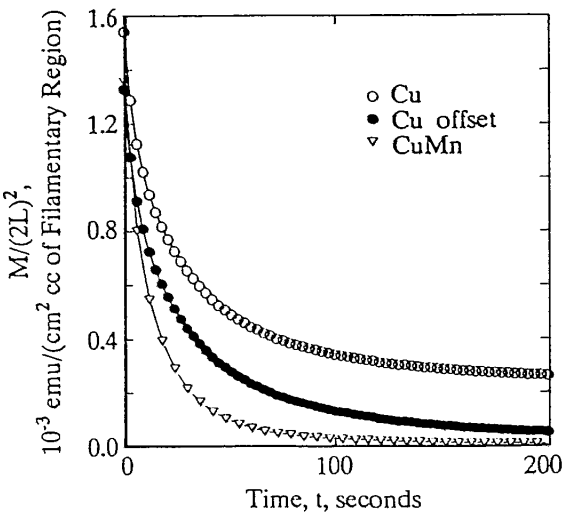

Fig. 4.
Magnetization decay at T=4.2K and H=10.28 kOe.

matrix decay with the static, excess proximity effect (PE) magnetization subtracted is also displayed. In this decay, the sample apparently does not reach complete saturation, since the Cu sample M_0 is higher (about the amount of the PE magnetization). Notice that while the initial slopes are very similar, the decay between 10 and 100 seconds is slower for the Cu matrix coil. This would be consistent with the higher τ inferred from the initial slope of Q_e vs frequency plots above. For all the following decay measurements, the final magnetization has been subtracted, so that purely exponential decay will appear linear when plotted as lnM(t).

Looking to Fig. 5, we can see that the M vs t decays for the CuMn material, taken for various temperatures, obey an exponential decay law reasonably well (ΔH and dH/dt are the same as above). The same cannot be said for the Cu matrix material, as can be seen in Fig. 6. The decays increasingly deviate from linearity with decreasing temperature. The τs extracted from these curves are displayed in Fig. 7. The data were fit to an exponential of the form $M = M_0 \exp(-t/\tau)$, where the constant term in the data (taken to be the value of M(t) at the end of the data run) was subtracted, as mentioned above. We can see that while τ for the CuMn

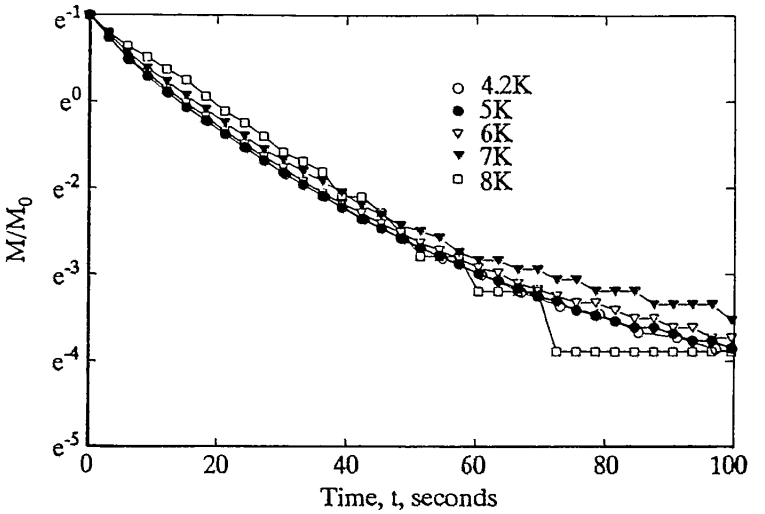

Fig. 5. Magnetization decay at H = 10.28 kOe and various temperatures for CNTCM20-0.

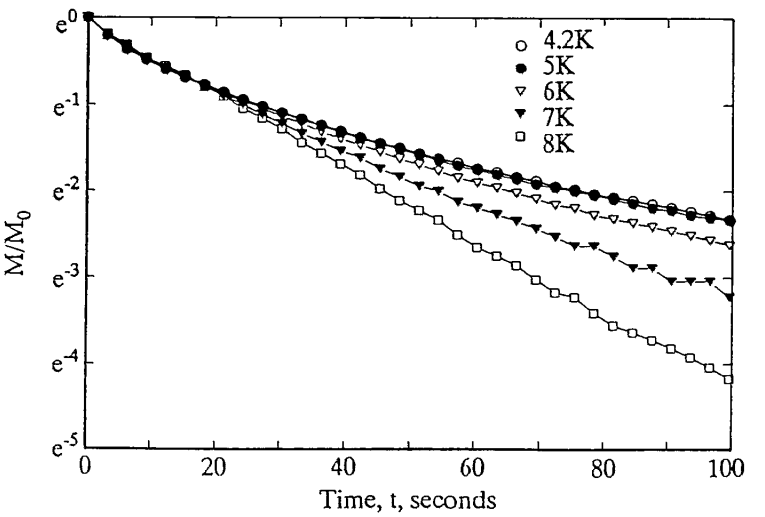

Fig. 6. Magnetization decay at H = 10.28 kOe and various temperatures for CNTCU20-0.

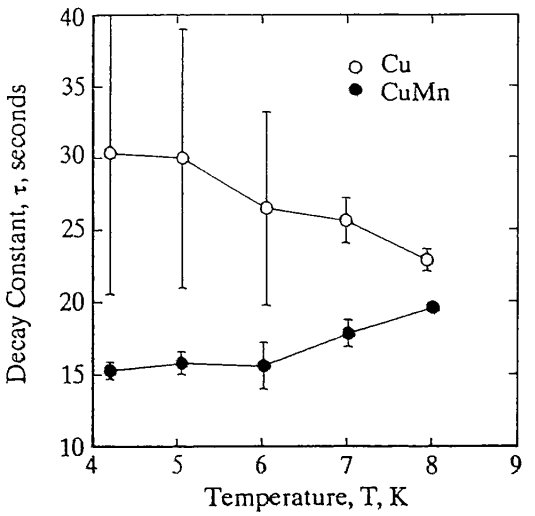

Fig. 7.
Decay constant, τ, vs temperature for both coils.

has a relatively small decrease as the temperature is dropped, the τ for the Cu increases significantly. However, as pointed out above, the curves are not really exponential, causing "uncertainty" in the measured τs. Notice, however, the similarity of the τs at 8K.

M vs t Decay at Various Fields

The M vs t decay at T = 4.2K for the CuMn and Cu matrix coils are shown for several different fields in Figs. 8 and 9. Here there were four different ΔHs: i) 16.95 kOe to 16.53 kOe, ii) 13.81 kOe to 11.72 kOe, iii) 6255 Oe to 4890 Oe, and iii) 2100 Oe to 720 Oe. dH/dt≈300 Oe/s for all ΔHs. The τs derived from these curves are displayed in Fig. 10. There seems to be an upward trend in τ as we go to lower fields in the CuMn matrix material. The τ for the Cu sample has rather large error bars, and no trend is apparent. This 720 Oe decay for the Cu matrix material had an anomalously low M_0 (after the static magnetization was subtracted), which is probably an indication of a rather complete proximity effect coupling.

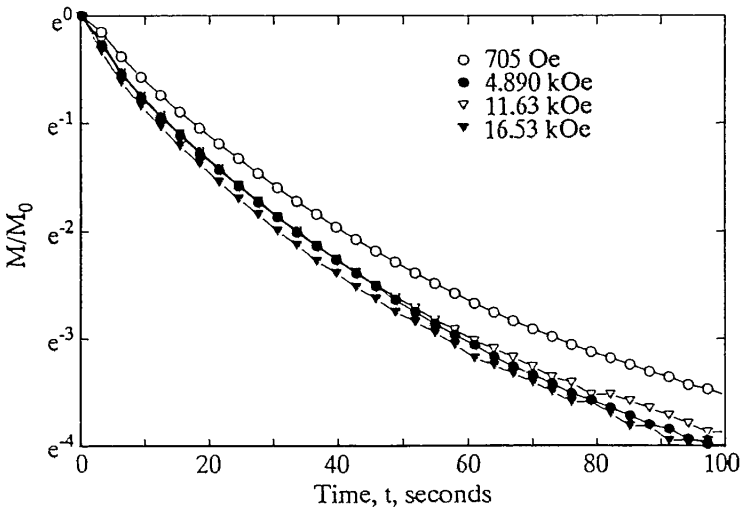

Fig. 8. Magnetization decay at T = 4.2K and various fields for CNTCM20-0.

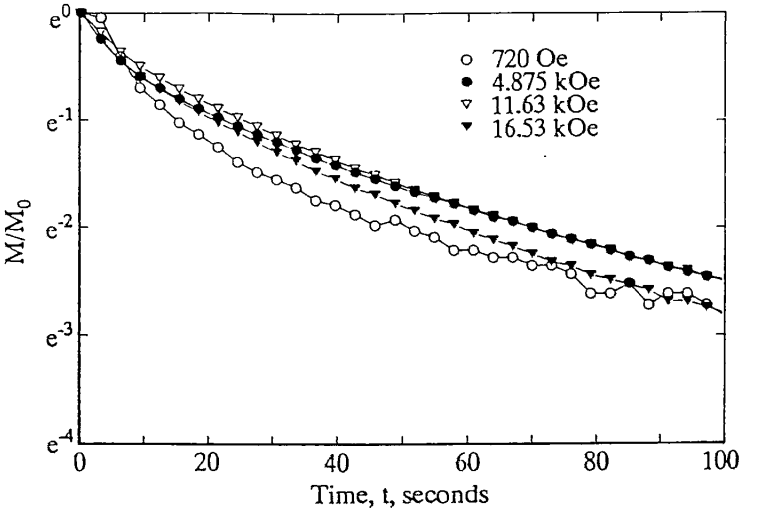

Fig. 9. Magnetization decay at T = 4.2K and various fields for CNTCU20-0.

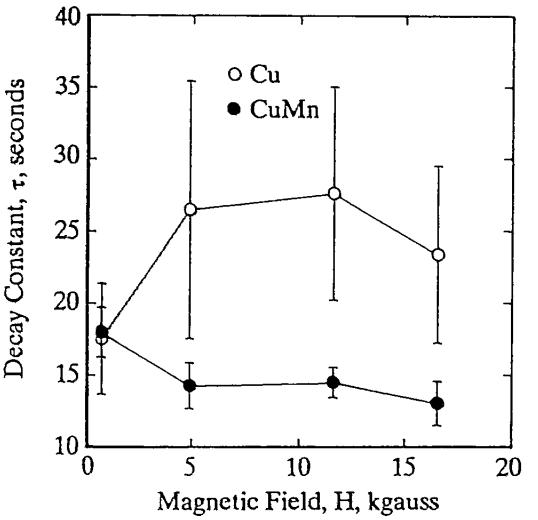

Fig. 10.
Decay Constant, τ, vs field for both coils.

DISCUSSION

The similarity in the τs measured for these samples (i.e. the fact that they are the same order of magnitude) indicates that the resistivity is dominated by the size effect rather than by the resistivity of the Mn additions. This size effect becomes larger at lower temperatures, and thus is unable to explain the τ variation with temperature seen in the Cu matrix sample. The variation of τ with temperature is too large to be accounted for by the temperature dependence of the bulk resistivity of Cu since it changes about 3% in this range, as compared to the factor of two change for τ in Fig. 7. τ increases only slightly with decreasing field for the CuMn sample, but this is left unexplained by a negative magnetoresistance[8]. The variation of NbTi J_c should not affect the measured resistivity, and note that, in any case, it would be the same for Cu and CuMn matrix samples. This leads to the consideration of the possibility of proximity effect creep on short time decay.

CNTCM20-0 is rather weakly proximity coupled even at 4.2K, and it exhibits little T-dependence, but some H-dependence at 4.2K is noted. CNTCU20-0 is much more completely coupled, and has therefore has a temperature dependence. No definite field dependence is

apparent at 4.2K, but at this temperature it may be too strongly coupled to exhibit such dependence. It seems likely that the decrease of Q_e with large amounts of proximity coupling is due to some sort of "volume erosion", where the volume of uncoupled conductor which can experience a dH/dt becomes less and less with stronger proximity effects, presumably becoming zero when the proximity coupling is complete.

There seem to be two possibilities for the initial increase in τ with increasing proximity effect: i) The proximity effect modifies the resistivity (either of the bulk or at the interface), and ii) Proximity assisted creep effects are significant, even at these short times. In fact, either or both of these may be occurring. From long term creep measurements on these samples we know that noticeable creep should be present during these decays[2]. For this reason, as well as the nonlinearity of the decay, we believe that at least the second mechanism is present. Preliminary analysis indicates that a simple summation of eddy currents and creep effects does not explain the resultant decay.

CONCLUSIONS

We are left with the rather interesting conclusion that proximity effects increase τ, but decrease the associated Q_e losses. Apparently, the competition between the two currents for the same paths cause the saturation magnetization to be almost identical for two comparable strands with varying degrees of proximity effect coupling. Hence, while larger τs and lower Q_e losses seem incompatible at first glance, it is just that the proximity effects reduce the amount of permissible eddy currents, but the proximity currents which are necessary to do this decay with a large creep, increasing the effective τ.

ACKNOWLEDGEMENTS

This Research was supported by Lawrence Berkeley Laboratory under P.O. No. 4558510.

REFERENCES

1. K. Yamafuji, Y. Mawatari, N. Harada, E.S. Otabe and T. Fujiyoshi, "Effects of Flux Creep on the SSC Dipole Magnets", Cryogenics 30, 615 (1990).

2. K. R. Marken, M. D. Sumption, E. W. Collings, R. M. Scanlan, "Magnetization Decay of SSC-Type Strands in Various Short Test Sample Configurations", Paper FY-3, this conference.

3. E. W. Seibt and D. Tabarsi, "Temperature Dependent AC Loss Measurements on NbTi and Nb_3Sn Superconductors Between 4.2K and 1.8K", J. Phys. C1, 475 (1984).

4. N. Harada, Y. Mawatari, O. Miura, Y. Tanaka, and K. Yamafuji, "Excess Magnetization due to Interfilamentary Proximity Coupling in Nb-Ti multifilamentary Wires", Cryogenics 31, 183 (1991).

5. M. D. Sumption, E. W. Collings, K. R. Marken, "Effect of Twist Pitch, Sample Length, and Field Orientation on the Proximity Effect Enhanced Magnetization of Fine Filament, Multifilamentary Strands", Paper AY-3, this conference.

6. E. W. Collings, M. D. Sumption, Studies of Magnetic Relaxation and Drift in SSC Magnet Materials-III, Report to Lawrence Berkeley Laboratory, January 10, 1991.

7. P. J. Ford and J. A. Mydosh, "Electrical Resistivity of Noble-Metal-Host-3-d Solute Spin-Glass Alloys", Phys. Rev. B 14, 2057 (1976).

8. S. P. McAlister and D. F. Kroeker, "Negative Magnetoresistance in a CuMn and AuFe Alloy", Physica B 108, 897 (1980).

T-MAG/27/2/2/43548

Position and Amplitude of Proximity Effect Peaks in the Magnetization Curves of NbTi/Cu and NbTi/CuMn Multifilamentary Strands

M. D. Sumption
K. R. Marken
E. W. Collings

Reprinted from
IEEE TRANSACTIONS ON MAGNETICS
Vol. 27, No. 2, March 1991

IEEE TRANSACTIONS ON MAGNETICS, VOL. 27, NO. 2, MARCH 1991

POSITION AND AMPLITUDE OF PROXIMITY EFFECT PEAKS IN THE MAGNETIZATION CURVES OF NbTi/Cu AND NbTi/CuMn MULTIFILAMENTARY STRANDS

M.D. Sumption, K.R. Marken, E.W. Collings
Battelle Memorial Institute
505 King Avenue
Columbus, OH, USA 43201

Abstract

The magnitude and position of proximity-effect-related magnetization peaks in the M-H loops of multifilamentary NbTi superconductive composites have been studied. M-H loops were taken at T=4.2 K as a function of field-sweep amplitude, H_M, for several specimens. Three regimes emerge: (i) low field, where proximity effects are mainly shielding in nature; (ii) high field, where there are anomalous trapping effects; (iii) an intermediate field region, corresponding to a crossover between these two regimes. Correlations are made between these regimes and the specimen parameters $H_{C1,NbTi}$ and $H_{p,NbTi}$. A relationship is found between the magnitude of the maximum of the high field magnetization (M_{EX}) and the breakdown field of the copper (H_{br}).

Introduction

The influence of the proximity effect in fine filament, multifilament superconductive wire has been studied by several authors[1-7]. These papers have shown that the proximity effect, in addition to providing excess low field Meissner screening, is associated with a mixed state, field trapping anomaly near zero field. It has also been shown that doping the interfilamentary matrix with Mn suppresses both the initial screening and the subsequent trapping segment anomaly. A recent paper from our group showed unexplained behavior in both the magnitude and position of the M-H anomaly[1].

The behavior of these anomalies is clearly important from the point of view of AC losses. Also, it is important for wire used in precision magnet (e.g. SSC) applications to minimize remanent magnetization.

Materials

The strands used for these experiments were fine filament, multifilamentary Nb-46.5 wt%Ti in a Cu or CuMn matrix. Three series of strands were included. All were constructed via a single stacking procedure. The CMN (Tab. 1 and Ref. 6) and RHIC (Ref. 1) strands have a central solid cylinder of copper for added stability. These strands have from 5000-23000 filaments with spacing/diameter (s/d) ratios of from 0.15 to 0.2. The ZTCU (Tab. 1) and CMN wires were not heat treated, and none of the wires in the three series were twisted. Samples consisted of some 10-300 wires in parallel and in epoxy, forming a cylinder about 5 mm long by 2 mm in diameter. Further sample specifications are available in Tab. 1.

Background/preliminary data

M-H loops taken on sample CMN-5 are displayed in Figs. 1 and 2 showing the anomaly in its high field (Fig. 1) and low field (Fig. 2) forms respectively. Notice that anomalous flux trapping is present in both regimes as evidenced by a comparison between the hysteresis of the bare and clad curves. This is in addition to the screening usually associated with proximity effects[3,7]. Notice as well that the magnitude of the trapping seems to be quite different in the two regimes. The reason for any proximity-effect-related trapping, especially in the low field regime, is not completely understood. Trapping and irreversibility are both contrary to the usual picture of proximity effect. However, some authors have reported superheating and supercooling for proximity-effected copper surrounding individual filaments[7]. Looking at the low field loop, a "penetration field" $H_{p,Cu}$ can be defined for this field regime in a multifilamentary composite, in analogy to the standard irreversible type-II superconductor. This field is distinct from the H_{br} defined by the first deviation from bundle exclusion, and it is likely that it is affected by other, possibly geometrical, factors. $H_{p,Cu}$ is probably related to the breakdown field of the Cu in regions near the filaments , while the H_{br} is associated with the regions of copper remote from the filament. It should be noted that neither of these fields are likely to be well described by a standard proximity- effect theory since they seem to be anisotropic with respect to the applied field orientation[4].

Data taken on sample CMN-5 and previously published in Ref. 1 are displayed in Fig. 3. The difference in magnetization at the maximum of the anomaly was extracted from hysteresis loops taken on clad/bare pairs of samples at various field sweeps. The size of this difference (denoted M_{EX}) and the H-field position of its occurrence (H_{EX}) are plotted as a function of field sweep amplitude. A detailed understanding of both H_{EX} and M_{EX} is lacking. However, it is clear that the increase in M_{EX} and the shift in H_{EX} are correlated with the field sweep exceeding the H_{C1} of the

TABLE 1. STRAND AND SAMPLE PARAMETERS

Sample Code	Filament Diameter, (μm)	NbTi Volume (Bare) ($cm^3 \times 10^{-3}$)	NbTi Volume (Clad) ($cm^3 \times 10^{-3}$)	Bare: Sample Length, (mm)	Bare: Number of Strands	Clad: Sample Length, (mm)	Clad: Number of Strands
CMN-5	0.4995	5.147	5.278	5.79	169	5.88	200
ZTCU-3	0.67	-----	3.206	----	---	5.395	60
ZTCU-9	2.00	-----	4.622	----	---	5.392	250

Manuscript received September 24, 1990.

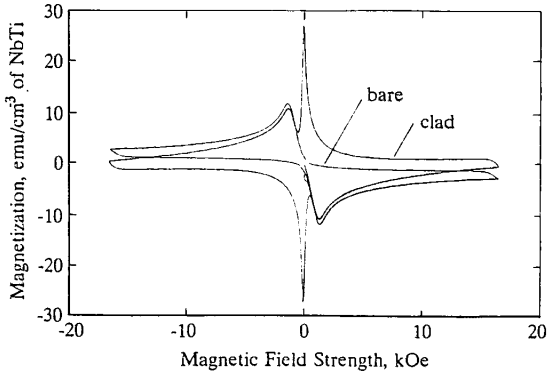

Figure 1. M-H loops for clad and bare CMN-5 at 4.2K illustrating magnetic behavior in the high field regime

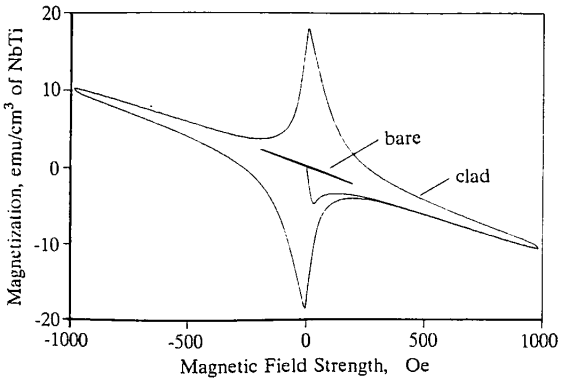

Figure 2. M-H loops for clad and bare CMN-5 at 4.2 K illustrating magnetic behavior in the low field regime.

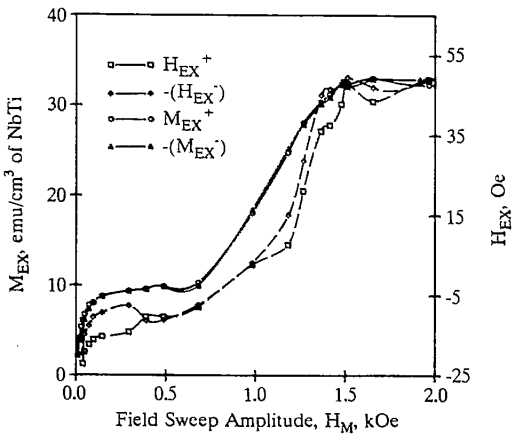

Figure 3. M_{EX} and H_{EX} vs. H_M for sample CMN-5 in the low H_M regime.

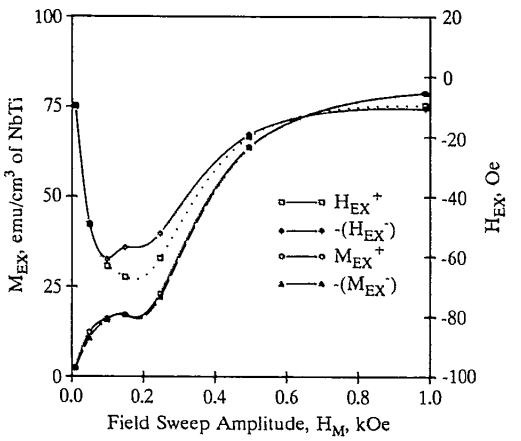

Figure 4. M_{EX} and H_{EX} vs. H_M for sample ZTCU-9 in the low H_M regime.

NbTi.[8] Along with the above data, that on several new samples, as well as some previously unpublished results, were analyzed in an attempt to understand the behavior of H_{EX} and M_{EX}.

Measurements

Hysteresis loops were taken for all samples at various field sweep amplitudes ranging from 50 Oe to 17 kOe, all at T = 4.2 K. The data were taken on a commercial vibrating sample magnetometer (VSM) with 1000 points per curve. For the experiments on the ZTCU samples, M_{EX} was measured as the maximum value of the anomalous magnetization (rather than the difference between bare and clad) because bare sample data are not yet available. The values of M_{EX} and H_{EX} were extracted from the clad curves and plotted vs. field sweep.

Figures 4 and 5 show the dependence of M_{EX} and H_{EX} on field sweep for sample ZTCU-9. In these figures we can see the same general dependence as in the CMN data; there are two plateaus, one at low fields corresponding to the NbTi filaments being in a Meissner state, and one at higher fields corresponding to an Abrikosov state for the filaments. Between these two regimes there is a transition region of finite width. We can define the transition

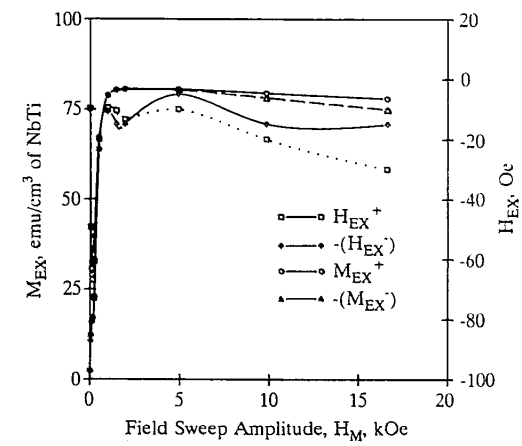

Figure 5. M_{EX} and H_{EX} vs. H_M for sample ZTCU-9 in the high H_M regime.

region (with increasing field) in terms of its onset field, H', and termination field, H". Figs. 6 and 7 show the corresponding curves for sample ZTCU-3; their behavior corresponds to those of ZTCU-9. The lowest field sections of both of these curves correspond to values of field-sweep amplitude, H_M, for which not only are the filaments in the Meissner state, but the matrix, as well, has not yet reached its "penetration field". In this region flux is almost totally excluded from the bundle, and the moments correspond to the Meissner response of $M=(-1/2\pi)H$ when M is normalized to total strand volume. For $H_{p,Cu}<H_M<H'$ M_{EX} and H_{EX} saturate at the values that could be described by a model which assumes a standard type-II irreversible superconductor with a field-dependent J_c of the appropriate magnitude. The actual mechanism by which flux is trapped is not known; it is possible that at low fields the trapping occurs in the proximity-effected copper or at the matrix/filament boundaries.

At high and intermediate values of H_M the magnitude of M_{EX} increases with the amount of field penetration into the filaments. In Tab. 2 several values from these curves, as well as some additional specimen data, are presented. It can be seen that in general the H' fields correspond to $H_{C1,NbTi}$, and that H" corresponds to $2H_{p,NbTi}$-$H_{C1,NbTi}$ (where H_p is understood to include Meissner effects). This indicates that the amount of flux trapping is dependent on the magnetic state of the filaments, as well as that of the matrix. At these higher sweep amplitudes the presence of flux in the filaments increases M_{EX} until H_M exceeds $2H_{p,NbTi}$-$H_{C1,NbTi}$. The saturation of M_{EX} at this point corresponds to an H_M above which the remanent magnetization of the filaments themselves at (or near) zero field is no longer changing with increasing field sweep amplitude.

Fig. 8 shows M_{EX} plotted as a function of H_{br}. Of course, there is a general tendency for M_{EX} to increase with H_{br}, as would be expected, but note that the increase is somewhat linear. Also, notice that the slope is close to the demagnetization factor for our sample. This relation could be interpreted crudely in the following terms : some volume close to the filament volume may retain an additional amount of field equal H_{br}, once that value is corrected for demagnetization.

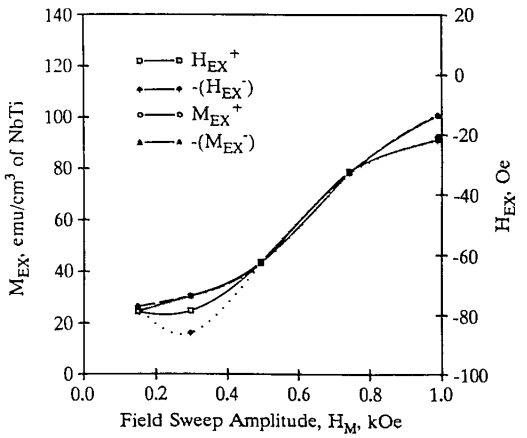

Figure 6. M_{EX} and H_{EX} vs. H_M for sample ZTCU-3 in the low H_M regime.

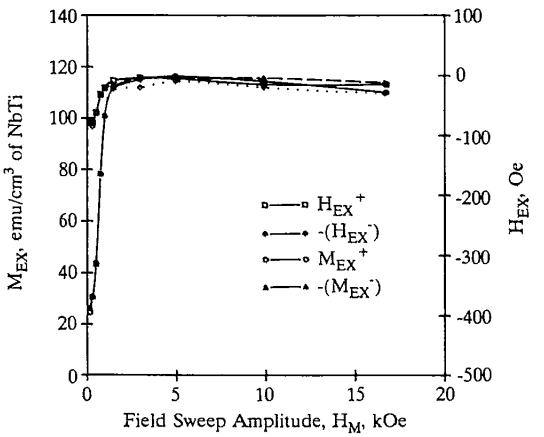

Figure 7. M_{EX} and H_{EX} vs. H_M for sample ZTCU-3 in the high H_M regime.

Table 2: Field regime correlations

Sample code	CMN-5	ZTCU-3	ZTCU-9
$H_{C1,NbTi}$	607	300	125
$H_{p,NbTi}$	1250	600	300
$2H_{p,NbTi}$-$H_{C1,NbTi}$	1900	900	475
H'	630	300	200
H"	1500	1000	600

All values in Oe

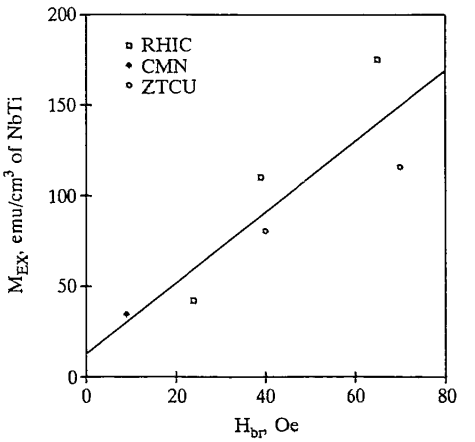

Figure 8. Saturation value of M_{EX} vs. H_{br} for all samples.

Discussion/conclusion

Several features of the behavior of H_{EX} and M_{EX} emerge from the above observations. For low fields, H_{EX} and M_{EX} are about the values that would be expected from shielding considerations, although this is only true to the extent that the anomalous trapping is small for this regime. At high fields we can see that the behavior of H_{EX} is anomalous; it is on the trapping branch for CMN, but on the shielding branch for the ZTCU samples (although the anomalies for all three samples extend a considerable distance into the trapping segment). Also, the high field value of H_{EX} seems to be the same for ZTCU-3 and 9. This may suggest that at high fields H_{EX} is to some extent dependent on geometrical factors other than filament diameter (e.g. s/d ratio or strand format such as Cu core or no Cu core (ZTCU)?). We have noted the scaling of M_{EX} with H_{br} but it can be seen that H_{EX} scales with M_{EX} as well.

It can be concluded that M_{EX} and H_{EX} are characterized by three regimes: (1) At low fields, these quantities are describable in terms of shielding currents. (2) At high fields, the anomalous trapping is enhanced by the entrance of the filaments into the mixed state. The value to which M_{EX} saturates scales with H_{br} and is about equal to the moment that would be generated by H_{br} (corrected for demagnetization) times the filamentary volume. (3) At intermediate fields there is transitional behavior with M_{EX} increasing with the level of field penetration into the filaments. Although it is possible that several mechanisms contribute to the above excess magnetization (M_{EX}) and its location in field (H_{EX}) we believe that two features central to any future theory will be: (1) a demagnetization effect; (2) flux trapping, due, either directly or indirectly, to proximity effects, and facilitated by the topography of the filaments themselves.

Acknowledgements

The clad and epoxy-potted magnetization samples were prepared by R.D. Smith, Battelle. The research was sponsored in full by the U.S. Department of Energy, Division of High-Energy Physics.

References

1. E.W. Collings, K.R. Marken Jr., M.D. Sumption, et al., "Magnetic Studies of Proximity-Effect Coupling in a Very Closely Spaced Fine-Filament NbTi/CuMn Composite Superconductor", *Adv. Cryo. Eng.(Materials)*, 36, 231-238, 1990.

2. A.K. Ghosh and W.B. Sampson, "The Effect of Magnetic Impurities and Barriers on the Magnetization and Critical Current of Fine Filament NbTi Composites", *IEEE Trans. Mag.*, 24, 1145-1149, 1988.

3. I. Hlásnik, S. Takács, V.P. Burjak, et al., "Properties of Superconducting NbTi Superfine Filament Composites With Diameters $\leq 1\mu m$ ", *Cryogenics*, 25, 558-565, 1985.

4. W.J. Carr, G.R. Wagner, "Magnetic Behavior of a Very Fine Filament Continuous Superconductor", *Adv. Cryo. Eng.(Materials)*, 32, 801-807, 1985.

5. S. Takacs, "Properties of Superfine Filaments in a Normal Matrix", *Czech. J. Phys.*, B36, 524-536, 1986.

6. E.W. Collings, K.R. Marken Jr., M.D. Sumption, et al., "Interfilament and Intrafilament Magnetizations in Fine Filamentary Composite Strands for Precision-Dipole Magnet Applications", *Presented at the 13th ICEC, Beijing, China*, April 24-27, 1990 - - to be published in Cryogenics.

7. A.C. Mota, P. Visani, and A. Pollini, "Magnetic Properties of Proximity-Induced Superconducting Copper and Silver", *J. Low T. Phys.*, 76, 456-512, 1989.

8. Because of the fine filament nature of this material H_{c1} is enhanced to 607 G, see Ref. 6.

EFFECT OF TWIST PITCH, SAMPLE LENGTH, AND FIELD ORIENTATION ON THE PROXIMITY EFFECT ENHANCED MAGNETIZATION OF FINE FILAMENTARY MULTIFILAMENTARY STRANDS

by

M. D. Sumption*† and E. W. Collings*

*Battelle, Columbus, OH 43201, USA
†Physics Dept., Ohio University, Athens, OH 45701, USA

Prepared for the
CEC/ICMC Conference
Huntsville, AL
June 10-14, 1991

EFFECT OF TWIST PITCH, SAMPLE LENGTH, AND FIELD ORIENTATION ON THE PROXIMITY EFFECT ENHANCED MAGNETIZATION OF FINE FILAMENTARY MULTIFILAMENTARY STRANDS

M. D. Sumption*† and E. W. Collings*

*Battelle, Columbus, OH 43201, USA
†Physics Dept., Ohio University, Athens, OH 45701, USA

ABSTRACT

The influence of twist pitch, sample length, and field orientation on the proximity effect (PE) induced excess magnetization in fine filamentary material is discussed. Small coils, elongated along one of the diameters of the coil, were wound from wires with lengths ranging from 1 cm to 80 cm, and with various twist pitches. M-H loops were then taken with the magnetic field applied parallel to the solenoidal axis. Our studies indicate that some of the static magnetic properties of these materials are twist pitch (L_p) dependent, including: i) The magnitude of the PE enhanced magnetization and loss ii) The H-field position of the PE magnetization maximum, and iii) The PE enhanced penetration field (H_{pp}). This dependence is, to a first approximation, independent of dB/dt. A similar dependence on sample length was found for these parameters. Additionally, this excess magnetization and loss was studied as a function of angle for a shorter sample, showing that the proximity effect anomaly is significantly weaker when the field is applied parallel to the filament axis.

INTRODUCTION

We have examined the topological dependence of the proximity effect (PE) related enhanced magnetization in fine filament NbTi superconductors. Our previous work investigated the properties of short samples, showing the relative strengths of the proximity effect in Cu and CuMn matrices, as well as the field sweep (H_m) dependence of the PE magnetization maximum (M_{ex}), and its H-field occurrence (H_{ex}) for short samples[1,2]. However, as Harada et al.[3,4] have recently shown, the composite topology (e.g. twist pitch) is a very important parameter. We now extend our measurements to samples with various lengths and twist pitches. Following the work of Harada et al.[3], we have further studied the effect of twist pitch on the proximity effect magnetization, looking not only at the loss, but also at the PE enhanced penetration field (H_{pp}) and H_{ex} as a function of L_p. In addition, we have studied the effects of sample length and field orientation. We have included materials with both Cu and CuMn matrices in our studies. Our results are interpreted in terms of Carr's model for in situ conductors[5], with some modifications.

SAMPLES

A matched pair of multifilamentary NbTi strands were used, one with a Cu matrix, and one with a CuMn (0.5%wt Mn) matrix. These strands were fully filamentary, with approximately 5000, 2 μm filaments drawn in a single stack procedure. The s/d ratio was 0.2, and no Nb barriers were present around the filaments. Further specifics are given in Tab. 1.

Three different types of samples were made from these strands: i) Short lengths of strand epoxied into cylinders, ii) 71 cm lengths of wire, given various twist pitches and wound into oval coils (VP samples), and iii) wires of various length and infinite L_p, wound into oval coils (VL samples). These coils were 1.2-1.4 cm in length, 0.2-0.5 cm wide and 0.25 cm thick (where thickness is taken along the axis of symmetry of the solenoid). The specifics of these samples are given in Tab. 2 and 3, where sample codes beginning with V denote variable length (VL) samples, and names beginning with C denote variable twist pitch (VP) samples. In all cases the strand code is submerged within the sample code. While no special precautions were taken with the VP sample ends, the ends of both the short samples and the coils of wire of various lengths were polished, and a representative sample end is shown in Fig. 1. This was done to avoid spurious end effects that might affect shorter samples (such as filament shorting), but no differences between equivalent polished and unpolished samples was seen.

Table 1. Strand Specifications

Strand Code	NTCU20	NTCM20
Strand Diam. (10^{-2}cm)	2.174	2.190
Bundle Diam. (10^{-2}cm)	1.678	1.694
Filament No.	4395	5355
Filament Diam. (μm)	2.03	1.90
Matrix Composition	Cu	CuMn

Table 2. Standard Sample Specifications

Strand Code/Type	NTCU20-Bare*	NTCU20-Clad
No. of Strands	59	60
Sample Length (mm)	5.40	3.66
NbTi Vol. (10^{-3}cm^3)	4.55	3.13

* These samples had the matrix etched away

Table 3. VL and VP Coil Specifications

Sample Name	V_{NbTi} (10^{-3}cm^3)	Total sample Length, L (cm)	L_p (cm)	No. of Wires
CNTCU20-2	10.15	71.1	35.6	1
CNTCU20-4	10.15	71.1	17.8	1
CNTCU20-8	10.15	71.1	8.89	1
CNTCU20-16	10.15	71.1	4.44	1
CNTCU20-32	10.15	71.1	2.22	1
CNTCU20-64	10.15	71.1	1.11	1
CNTCM20-0	12.431	81.724	∞*	1
CNTCM20-4	10.81	71.1	17.8	1
CNTCM20-64	10.81	71.1	1.11	1
VNTCU20-1	4.25	1.03	∞	29
VNTCU20-2	3.64	1.91	∞	13
VNTCU20-8	6.56	7.66	∞	6

* i.e. there is no twist of the filaments about the z-axis of the strand

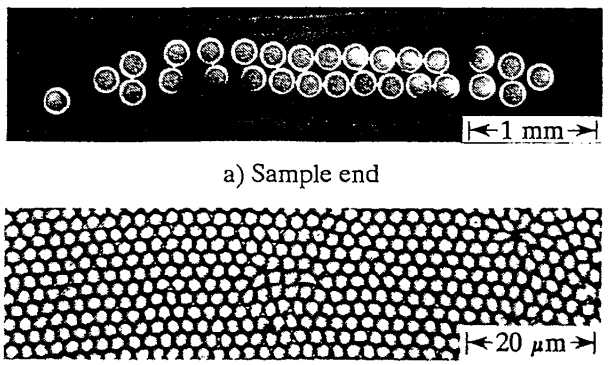

a) Sample end

b) Enlargement showing single strand

c) Enlargement showing individual filaments

Fig. 1. Micrograph showing a representative VL sample end (VNTCU20-1).

MEASUREMENTS AND RESULTS

High field M-H and loss vs L and L_p

M-H loops were taken for VP and VL Cu matrix samples, as well as VP CuMn matrix samples. In these, and all coil measurements in this paper, the field was applied along the axis of symmetry of the solenoid. Looking to Fig. 2, we see the M-H behavior for the Cu matrix strand as a function of L_p, which shows a substantial increase of hysteretic losses with increasing L_p, as seen by Harada et al.[3] Notice too the substantial increase in the extent of the effect along the H-axis. Inserted in each of these loops is the M-H of the short sample of bare filaments, so that we can clearly see the excess proximity effect magnetization. The hysteresis loops for the bare samples were 1000 points long, taken over a duration of ten minutes, with a constant dH/dt = 141.7 Oe/s. The loops for the coil samples, however, were taken as a series of M vs t decay experiments, where the field was first stepped, and then dH/dt = 0 for 5 min., during which the moment vs time was recorded. This procedure was used because significantly lower sweep frequencies (in fact, essentially f = 0) could be reached. This is important for long twist pitch samples, as τ's for our longest sample could be as long as 30 sec. We used this procedure, rather than extrapolations to zero frequency, because eddy current saturation effects may cause deviations from linearity in the ΔM vs f curve.

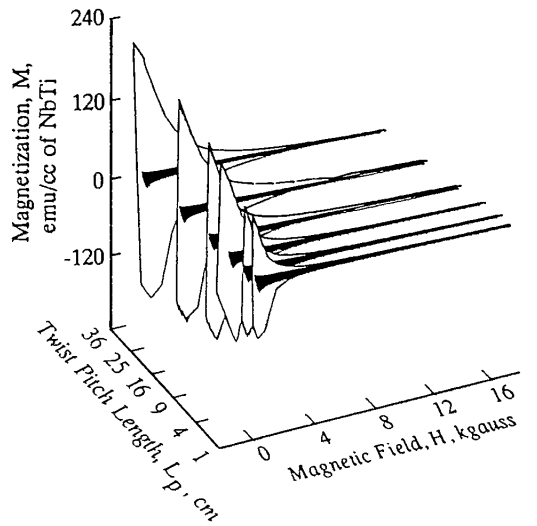

Fig. 2.
M-H vs L_p for Cu matrix VP samples.

An analogous dependence of the loss and magnetization on L can be seen in Fig. 3 for the Cu matrix VL samples. Just as in the eddy current problem, there is an analogy between L and L_p, as will be described below. Turning now to Fig. 4 we can see an L_p dependence in the CuMn matrix samples which is qualitatively very similar to, although very much smaller than, that of the Cu matrix samples.

Fig. 5 shows the high field (HF) loss (per cycle) vs L_p and L for the Cu matrix VP coils, and loss vs L_p for the CuMn matrix VP coils. Initially the dependence seems to be linear, although there is a saturation at high L_ps. The proportionality of the PE loss and magnetization to L and L_p is seen for all VL and VP samples, both Cu and CuMn, although it is most pronounced in the Cu matrix VP samples. Fig. 6 shows the differences between two Cu matrix coils; one a VP sample with $L_p = 2.222$ cm, and one a VL sample with $L = 1.026$ cm. If we were using Morgan's model for eddy currents[6] (where $L_{p,eff} = 2L$) these would be nearly equivalent samples. The magnitude of the maximum magnetization seems to be similar, although both the loss and the H-extent of the effect seem to be significantly smaller in the VL sample.

Various loop parameters vs L and L_p

In Fig. 7 we have plotted several loop parameters for the Cu matrix VP samples as a function of L_p. The height (M_{ex}), and the H-field position (H_{ex}) of the PE enhanced

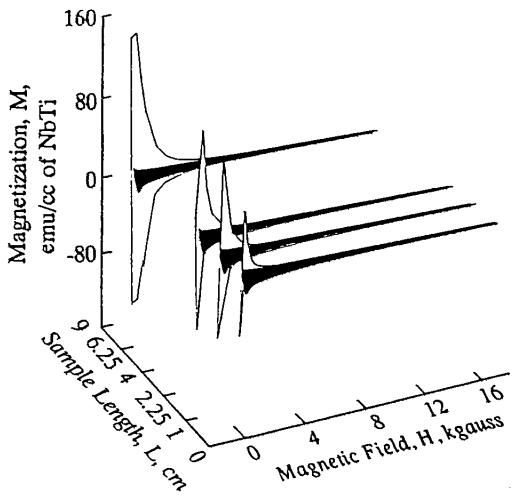

Fig. 3.
M-H vs. L for Cu matrix VL samples.

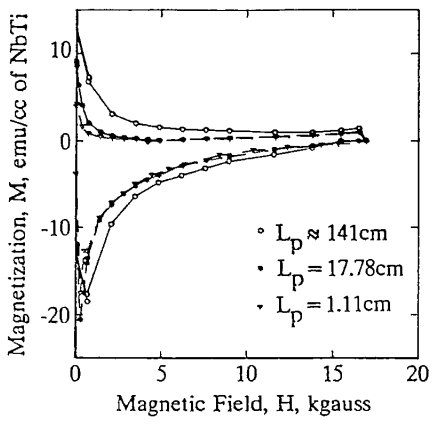

Fig. 4. M-H for several CuMn matrix coils of different L_p.

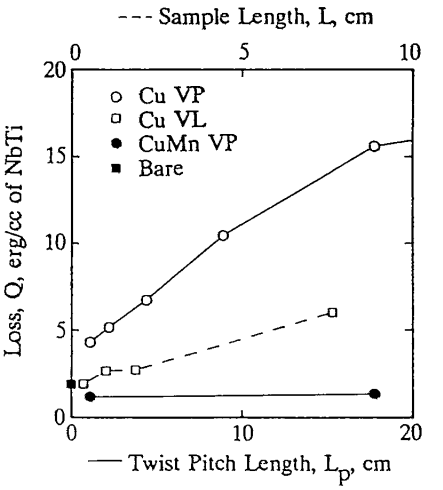

Fig. 5. High field sweep loss (per cycle) vs. L_p and L for Cu VL and VP samples.

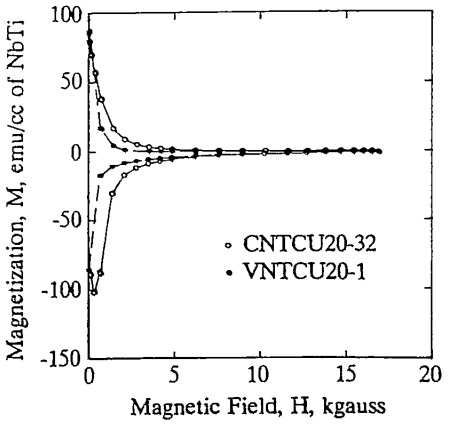

Fig.6. High field M-H for VNTCU20-1 and CNTCU20-32, comparing VL and VP samples.

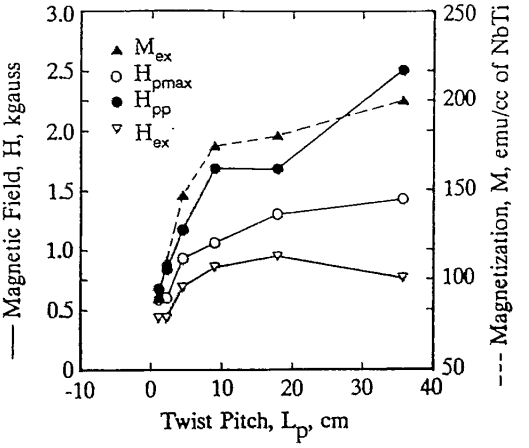

Fig. 7. Various loop parameters vs L_p for Cu matrix VP samples.

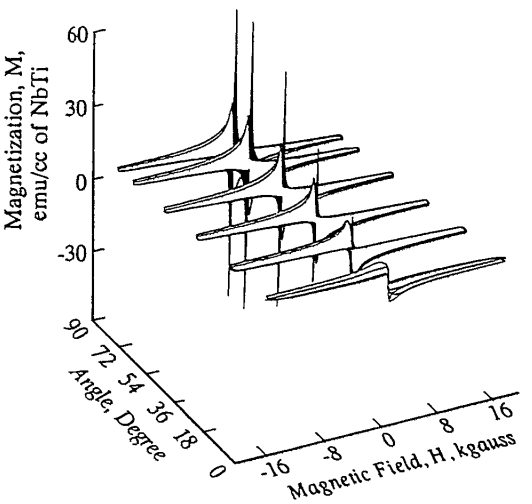

Fig. 8.
M-H vs θ for Cu matrix short samples (Both Bare and Clad) - darkened regions correspond to $M_{clad}| > |M_{bare}|$.

magnetization maximum are both initially proportional to L_p, although a saturation later sets in. Similarly, both the proximity effect assisted penetration field H_{pp}, and the maximum (negative) in the initial magnetization, which we define as H_{pmax}, are initially proportional to L_p with a subsequent saturation. Here we use H_{pp} to describe the actual penetration field of the PE multifilamentary composite (i.e. where the initial and subsequent magnetization curves join). H_{pmax} is included because it is easier to measure accurately. Modification of H_{pp} such as these have been seen in in situ material as well[7]. The saturations in these parameters, as well as that in the loss, may stem from uncertainties in the twist pitch (there may be some residual L_p in nominally untwisted wires), or they may be more fundamental in nature.

High field Characteristics vs Field Orientation

M-H loops were taken as a function of the angle of the field with respect to the filament axis on short cylindrical samples. Here $\theta = 90°$ defines the field to be transverse to the filaments. These loops had 1000 points, and a continuous sweep, with a dB/dt = 141.7 Oe/s. Because of the short nature of these samples, and previous experiments in similar samples, we know eddy currents to be negligible in these samples. These loops are shown in Fig. 8, where both clad (as received) and bare (Cu etched away) sample results are plotted together. Where the bare results exceed the clad (as in $\theta = 0°$ case, because of surface currents[8]) we have not

filled in the region. Where clad results exceed bare (via proximity effect) we have filled in that region. We can see the gradual evolution of a sharp proximity peak as the angle goes from 0° to 90°. This is due to the existence of a larger J_{ceff} for the transverse field orientation, as described below.

Low Field M-H and Initial Magnetization

H_{br} is defined as the field above which there is deviation from the straight line given by the initial magnetization. For these samples that initial slope corresponds to flux exclusion from 84% of the bundle volume (very close to this for all samples). dH/dt = 0.83 Oe/s or less for these runs, making eddy current effects unimportant. H_{br} is about 120-140 Oe for all of the Cu matrix VP samples. It has a generally upward tendency with increasing L for the Cu VL samples, being in the range of 25-50 Oe. Fig. 9 shows the initial magnetization for several of the variable length samples. It appears that there is some H_{br} that is independent of L for all samples, and that as J_{ceff} goes up, H_{br} is artificially enhanced (much the same as H_{c1} is difficult to determine for high J_cd conductors) until it is indistinguishable from $H_{c1,NbTi}$ (measured to be 150 Oe for the bare filaments in this orientation). Full low field loops are shown in Fig. 10 for two samples, with the length of the VL sample equal to about 1/2 of the L_p of the VP sample. This shows the strong difference between the low field properties for VL and VP samples. H_{br} may also be dependent on topology, as we have seen variations with field angle (unpublished data).

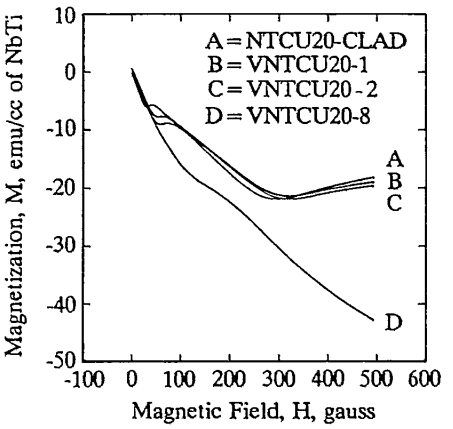

Fig. 9. Initial magnetization for the Cu VL samples.

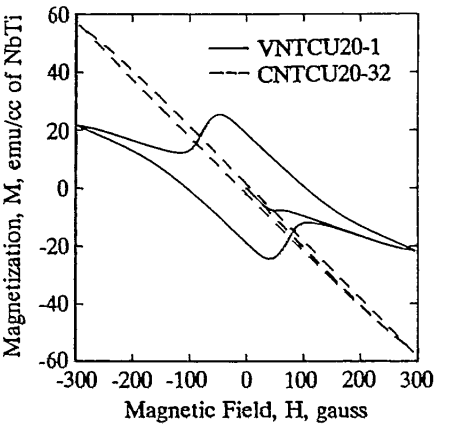

Fig. 10. Low field loops for CNTCU20-32 and VNTCU20-1.

THEORY

General

The recent work of the Harada[3,4] group was described using the model derived by Carr for proximity coupling in in-situ conductors[5], which is substantially correct for continuous filament material as well. Carr takes the currents which will flow along the z-axis of the conductor (J_{cz}), and decomposes them into currents along the filaments (J_{cfil}), and currents across the interfilamentary matrix (J_{cp}). This gives the two conditions:

$$J_{cz} = J_{cfil}(1 + (2\pi R/L_p)^2)^{1/2} \quad \text{(from limitation on filament current)}$$

and

$$J_{cz} = J_{cp}(L_p/2\pi R)(1 + (2\pi R/L_p)^2)^{1/2} \quad \text{(from limitation on matrix } J_c\text{)}$$

Here R is the strand diameter (see Fig. 11). Rather than violate either of these two conditions, the flux will encroach further into (or flow out of) the sample, keeping these J_c's (or more

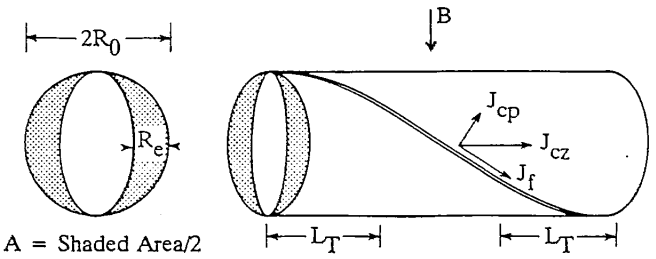

Fig. 11.
Illustration of transfer length.

generally one of them) at the critical value. The second criterion is typically the operative limitation, because it is the more stringent condition for shorter L_ps. For L_ps sufficiently short that this criteria will dominate, but long enough that $R/L_p << 1$, $J_{cz} \approx L_p J_{cp}/2\pi R$. However, as L_p is increased, eventually the first criterion becomes the more restrictive of the pair, causing a saturation at $J_{cz} \approx \lambda J_{cfil}/2$, (where λ = NbTi filling factor) as shown by Carr[5]. A second effect which will cause saturation is, of course, the field dependence of J_{cp}. This would keep the ratio of the proximity effect magnetization to bare filament magnetization from reaching its maximum (which would presumably be $\propto \lambda R_{strand}/R_{fil}$).

Because of the saturation of J_{cz} when L_p becomes infinite, a different criterion is needed to describe the length dependence of short, untwisted samples. This condition comes from the necessity of a transfer length. The above model does not address the issue of a transfer length, although one might be expected in analogy with eddy current effects. A calculation for this is outlined below. Also, because of the asymmetry of his filaments, Carr ignored radial currents. This consideration is apparently irrelevant for rather long conductors, although these currents will be important for the description of finite length conductors. Yamafuji et al.[4] do mention currents which flow radially, although these are not included in their model, nor is any motivation for their restriction that these currents flow parallel or antiparallel to the B field.

Transfer length

This transfer length, L_T, is a consequence of two things: i) an anisotropy in J_c, and ii) Kirchhoff's Law (the condition of current continuity). Crudely, these requirements become

$$J_{cz} A_1 = 2RL_T J_{cp}.$$

Here A_1 is the cross sectional area through which J_{cz} flows down the strand (see fig. 11). Generally, the penetration field for the transverse field case is $H_p = 0.8R_0 J_c$, which can be rewritten to find the penetration distance, R_e, as a function of the external field $R_e = 1.25H_m/J_{cz}$. Combining this with the area $A_1 = R_0 R_e \pi/2$ we get

$$L_T = \propto (\text{const})(H_m/J_{cp})$$

where the constant incorporates both the geometrical factor and a dependence of J_{cp} on field. Notice that this proximity effect transfer length, in analogy to eddy current transfer lengths dependence on dH/dt, is proportional to H_m (their respective driving forces). However, as shown by Carr[9], eddy current transfer length's are $\propto 1/(dB/dt)^{1/2}$, as opposed to proximity effect induced transfer lengths. Also, there is an inverse dependence on J_{cp}, which can be seen as analogous to conductivity in the normal matrix in eddy current problems. The field dependence of L_T is no doubt intimately connected to the H_m dependence of the effect seen in Ref. 2.

Application to H_{pp}, H_{pmax} and H_{ex}

As shown by Harada et al.[3], H_{pp} should also be proportional to L_p. In general, for transverse fields $H_p = 0.8R_0 J_c$. When $J_c = J_{cz}$, and we use the second criteria above:

$$H_p = (0.4/\pi) J_{cp} L_p.$$

This does not, however, include the effects of the strong field dependence of J_{cp}. If we interpret

H_{ex} and H_{pmax} in terms of the anisotropic continuum model (where the peak M_{ex} and its position H_{ex} come about because of the field dependence of J_{cp}) then these two should be also be $\propto L_p$, as seen in Fig. 7.

DISCUSSION

The dependence of the VP samples loss on L_p is well described by Carr's model, although we have not tried to quantitatively account for the apparent saturation. An additional criteria, $J_{cz} \propto LJ_{cp}/R$, essentially a re-write of the transfer length equation, explains the dependence of the VL sample loss on sample length. The loss as a function of field angle is also understandable, since the effective J_c varies as a function of angle, becoming essentially J_{cp} when the field is applied along the filament axis. Low field initial magnetization can be described by a H_{pr} (which may also be sample geometry dependent), which is being artificially enhanced by a $J_{ceff}d$ product which is increasing with sample length (a transfer length consideration).

CONCLUSIONS

We have found that the proximity effect magnetization has a great topological similarity to eddy current coupling. The dependence of the loss and magnetic moment on L_p for these continuous filament conductors is well described by Carr's model for in situ conductors. We have extended Carr's model to include end effects, as well as describing some loop features (H_{pp}, H_{pmax}, and H_{ex}).

From a practical point of view, several points should be made. First, clearly one should be careful about measurement of parameters such as the loss, the moment, τ, H_{c1}, and J_{cp}. Secondly, Mn suppression of proximity effects is evident throughout the range of L_ps investigated. This is as one would expect since $J_{cp} \propto 1/(\text{Mn concentration})$, and indicates that Mn addition will continue to be a good technique for proximity effect suppression. Lastly, all of the considerations which eddy currents necessitate (e.g. L_p, interactions between L_p and cable twist) will need to be revisited keeping the proximity effect in mind.

ACKNOWLEDGEMENTS

This research was supported by the U.S. Department of Energy, Division of High Energy Physics. Also we would like to thank W. J. Carr, R. L. Cappelletti, and K. R. Marken for some very helpful discussions.

REFERENCES

1. E. W. Collings, K. R. Marken Jr, M. D. Sumption, E. Gregory, and T. S. Kreilick, Adv. Cryo. Eng. 36, 231 (1990).
2. M. D. Sumption, K. R. Marken, E. W. Collings, IEEE Trans. Mag. 27, 1129 (1991).
3. N. Harada, Y. Mawatari, O. Miura, Y. Tanaka, and K. Yamafuji, Cryogenics 31, 183 (1991).
4. K. Yamafuji, Y. Mawatari, N. Harada, E. S. Otabe, and T. Fujiyoshi, Cryogenics 30 (Suppl.), 619 (1990).
5. W. J. Carr, J. Appl. Phys. 54, 6549 (1983).
6. G. H. Morgan, J. Appl. Phys. 41, 3673 (1970).
7. V. M. Pan, S. I. Mukhin, V. S. Flis, M. G. Vasilenko, V. I. Latysheva, L. M. Fisher, and V. M. Dzugutov, IEEE Trans. Mag. 21, 408 (1985).
8. M. D. Sumption, K. R. Marken, E. W. Collings, IEEE Trans. Mag. 27, 2166 (1991).
9. W. J. Carr, Adv. Cryo. Eng. 28, 581 (1982).